

Laser assisted micro-milling of titanium alloy

Zur Erlangung des akademischen Grades eines

Dr.-Ing.

von der Fakultät Maschinenbau
der Technischen Universität Dortmund
genehmigte Dissertation

Faramarz Hojati M.Sc.

aus

Iran

Tag der mündlichen Prüfung: 03.06.2024

1. Gutachter: Prof. Dr.-Ing. Prof. h.c. Dirk Biermann
2. Gutachter: Prof. Dr.-Ing. Bahman Azarhoushang

Dortmund, 2024

Acknowledgement

I wish to express my sincere appreciation to Prof. Biermann for his guidance and support throughout the journey of completing my PhD dissertation. I am deeply grateful to Prof. Azarhoushang, head of the KSF Institute at Furtwangen University for his encouragement and constructive feedback that have been instrumental in advancing my work and achieving the goals of this dissertation. I am also deeply thankful to Dr. Daneshi for the numerous discussions and scientific support. His insights and advice greatly contributed to the depth and quality of this work. Special appreciation is extended to Dr. Kadivar for his invaluable technical support throughout my research. His expertise was crucial to overcoming numerous challenges encountered during the experimental phase.

To my parents, whose unconditional love, support, and encouragement have been my foundation, I owe more than words can express. Thank you for believing in me and for your endless sacrifices that have allowed me to pursue my dreams.

Lastly, deep appreciation is extended to my partner, Arezou, for her unwavering support and understanding throughout this journey. Her patience, love, and encouragement have been my anchor during the most challenging times.

This dissertation is a testament to the collective support and guidance of all these remarkable individuals. I am deeply grateful for each one of you.

Dortmund, June 2024

Preface

This thesis is based on work performed at the KSF-Institute of Advanced Manufacturing at Furtwangen University (Germany).

Kurzfassung

Das Interesse an der Anwendung der additiven Fertigungstechnologie (AM) ist aufgrund ihrer Fähigkeit, komplexe Teile mit hoher Flexibilität als Alternative zu konventionellen Fertigungsverfahren herzustellen, gestiegen. Die schlechte Oberflächenqualität und begrenzte Form- und Maßgenauigkeit von AM-Teilen erfordern jedoch oft eine Nachbearbeitung, wie Zerspanung, Schleifen und Polieren. Unter den verschiedenen Materialien ist Titan eines der am häufigsten bearbeiteten Materialien in der AM-Technologie. In dieser Arbeit wurde Zerspanbarkeit von AM-Teilen aus einer Titanlegierung (Ti6Al4V), die mittels des Elektronenstrahlschmelzverfahrens (EBM) hergestellt wurden, mit der von stranggepressten Ti6Al4V-Teilen verglichen. Dabei lag der Schwerpunkt auf den Zerspanungskräften, der spezifischen Schneidenergie, der Gratbildung und der Oberflächenqualität im Mikrofräsverfahren. Trotz der höheren Härte von Ti6Al4V im EBM-Verfahren hergestellten im Vergleich zu stranggepresstem Ti6Al4V wurde kein bemerkenswerter Unterschied in den Schnittkräften der beiden Werkstoffe bei Spandicken zwischen 7,4 μm und 37,3 μm festgestellt. Allerdings wiesen die EBM-Teile im Vergleich zu den stranggepressten Teilen bei Spandicken unter 7,4 μm geringere Schnittkräfte und spezifische Schneidenergien auf. Außerdem zeigten die gefrästen EBM-Teile eine geringere Oberflächenrauheit (feinere Oberfläche). Beim Mikrofräsen beider Materialien (stranggepresstes und EBM-Ti6Al4V) bildeten sich kontinuierliche, wellenförmige Grate.

Die Untersuchung des Größeneffekts für beide Arten von Ti6Al4V-Werkstoffen in Bezug auf die spezifische Schneidenergie und die Gratbildung verdeutlicht die Problematik des Mikrofräsverfahrens. Trotz der hohen Flexibilität des Mikrofräsprozesses bei der Herstellung komplexer Mikroteile mit engen Toleranzen und hoher Genauigkeit schränken mehrere Schwierigkeiten wie Werkzeugablenkung, Größeneffekt und Werkzeugverschleiß seine Anwendung ein. Als Lösungseinsatz zur Umgehung der Probleme wurde die laserunterstützte Zerspanung (LAM) eingesetzt, die zur Reduzierung der Zerspanungskräfte führt und somit höhere Materialabtragsraten (MRR) ermöglicht. Im Gegensatz zur traditionellen LAM-Methode, bei der ein Laserstrahl als Wärmequelle verwendet wird, um die Materialfestigkeit vor dem Schneidwerkzeug zu verringern und somit die Schnittkräfte zu senken, wurden Ti6Al4V-Teile vor dem Mikrofräsen mit einem Pikosekundenlaser als Ultrakurzpulslaser (USPL) strukturiert und somit eine Änderung der Spandicke bei der nachfolgenden Zerspanung bewirkt.

Für ein grundlegendes Verständnis der Änderungen der Spandicke durch die Strukturierung und um die einflussreichen Parameter in diesem neu vorgestellten Ansatz zu finden, wurde ein kinematisches Modell entwickelt. In dem Modell wurden eine Vielzahl von Eingangsparametern in Bezug auf Struktur, Werkzeug und Prozessparameter untersucht. Das Modell zeigte eine Reduzierung der Spandicken durch die Strukturierung der Teile und identifizierte die Strukturichte als den wichtigsten Parameter für die Reduzierung und Veränderung der Spandicken. Basierend auf diesen Ergebnissen wurde der Einfluss der Strukturichte im vorgestellten LAM auf die Zerspanbarkeit von stranggepresstem Ti6Al4V hinsichtlich Zerspanungskräften und Oberflächenrauheit experimentell untersucht. Es wurde eine signifikante Reduktion der Zerspankräfte bei gleichbleibender Oberflächenrauheit

festgestellt. Die Orientierung der Strukturlinien in Bezug auf den Schrägungswinkel konnte als ein wichtiger Parameter für die Rauheitswerte der bearbeiteten Oberfläche ermittelt werden

Durch die Vorstrukturierung des Werkstücks mit USPL wird ein Teil des Materials abgetragen und eine kontrollierte Beschädigung der Oberfläche induziert. Dies führt zu einem geringeren Materialabtrag während des Mikrofräsens und folglich zu geringeren Schnittkräften, was die Zerspanbarkeit verbessert. In diesem Zusammenhang wurde das Verständnis der Wechselwirkung zwischen USPL und der Titanlegierung Ti6Al4V hinsichtlich der Oberflächenmorphologie, der Abtragsmechanismen und der geometrischen Merkmale näher untersucht.

Die experimentellen Untersuchungen wurden in drei Kategorien durchgeführt: Mehrfachpulse, einzelnes lineares Laserscanning und mehrfaches lineares Laserscanning für einen Pikosekundenlaser (ps) mit einer Pulsdauer von 12 ps. Bei Mehrfachpulsen hatte die Spitzenlaserfluenz ϕ_{L_peak} einen größeren Einfluss auf den Materialabtrag, die Veränderung der Oberflächenmorphologie und die Schmelzbildung. Im Falle des linearen Laserscannings wurde die Lasereingangsenergie E_{L_input} als Parameter definiert, der den Einfluss der aufeinanderfolgenden Pulse berücksichtigt. Beim einzelnen linearen Laserscanning wurde $E_{L_input} = 125 \text{ J/cm}^2$ als Schwellenwert festgelegt, bei dem die Abtragstiefe mit der Lasereingangsenergie bei $E_{L_input} > 125 \text{ J/cm}^2$ enorm anstieg, was einer wesentlichen Schmelzbildung auf der Oberfläche des gelaserten Profils entspricht. Bei einem $E_{L_input} < 125 \text{ J/cm}^2$ waren laserinduzierte periodische Oberflächenstrukturen (LIPSS) eine häufig auftretende Oberflächenmorphologie mit weniger oder gar keinem Schmelzen auf der Oberfläche. Beim mehrfachen linearen Laserscanning mit konstantem $E_{L_input} = 3.9 \text{ J/cm}^2$ führten niedrigere Scangeschwindigkeiten und Laserleistungen zu einer stärkeren Verschlechterung der Oberfläche, einem deutlicheren Anstieg der Ablationstiefe mit der Anzahl der Laserscans N_s , einer größeren Ablationstiefe, einem schmaleren gelaserten Profil, einer geringeren spezifischen Ablationsenergie und einer geringeren MRR.

Abstract

The interest in applying Additive Manufacturing AM technology has been growing due to its capability to produce complex parts with high flexibility as an alternative to conventional manufacturing processes. However, the poor surface quality of AM parts and their limited form and dimensional accuracy often require post-processing, such as machining, grinding, and polishing. Among different materials, titanium is one of the frequently working materials in AM technology. This work compared the machinability of AM Ti6Al4V titanium alloy parts produced by the Electron Beam Melting EBM technique and the extruded Ti6Al4V parts with a focus on cutting forces, specific cutting energy, burr formation, and surface quality in the micro-milling process. No remarkable difference in the cutting forces of both materials at chip thicknesses ranging from 7.4 μm and 37.3 μm was observed despite the higher hardness of the EBM Ti6Al4V compared to the extruded Ti6Al4V. However, the EBM parts exhibited lower cutting forces and specific cutting energies compared to the extruded parts in the chip thicknesses lower than 7.4 μm . Moreover, the milled EBM parts indicated lower surface roughness (finer surface). Continuous wavy-type burrs with comparable sizes were formed in the micro-milling of both materials, Extruded- and EBM Ti6Al4V.

Investigation of the size effect for both types of Ti6Al4V materials concerning specific cutting energy and burr formation highlighted the issue of the micro-milling process. Despite the high flexibility of the micro-milling process in manufacturing complex micro-parts with tight tolerances and high accuracies, several difficulties, such as tool deflection, size effect, and tool wear, limit its application. To tackle these issues, the significance of Laser-Assisted Machining LAM is highlighted by reducing machining forces and possibly using a higher Material Removal Rate MRR. Unlike the traditional LAM method that uses a laser beam as a heating source to reduce the material strength ahead of the cutting tool, and consequently decreasing the cutting forces, Ti6Al4V parts were structured using a pico-second laser as an Ultra-Short Pulse Laser USPL before micro-milling. The material was machined through laser structuring, affecting the uncut chip thicknesses during the micro-milling process.

A kinematic model has been developed to understand how structuring the workpiece changes the uncut chip thicknesses and find the influential parameters in this newly introduced approach. In the model, a variety of input parameters in terms of structure, tool, and process parameters were investigated. The model revealed a reduction of chip thicknesses through structuring the parts and considered the structure density and depth as the two most significant parameters in reducing and changing the chip thicknesses. In the experimental tests, the influence of structure density in the introduced LAM on the machinability of extruded Ti6Al4V concerning cutting forces and surface roughness was researched. A significant reduction in cutting forces was observed with no remarkable changing surface roughness. However, the orientation of structure lines with respect to the helix angle played an important role in the surface roughness values of the machined surface.

Pre-structuring the workpiece using USPL led to removing some part of the material and inducing controlled subsurface damages, followed by less material removal during the micro-milling process and consequently less resultant cutting forces, and better machinability. In this regard, the understanding of the interaction between

USPL and Ti6Al4V titanium alloy material concerning surface morphology, material removal mechanisms, and geometrical features must be taken into account.

The experimental studies were conducted in three categories: multiple pulses, single linear laser scanning, and multiple linear laser scanning for a picosecond laser with a pulse duration of 12 ps. For multiple pulses, the peak laser fluence ϕ_{L_peak} exhibited more influence on material ablation, changing surface morphology, and melting formation. In the case of linear laser scanning, laser input energy E_{L_input} was introduced as a parameter that includes the influence of successive pulses. In the single linear laser scanning, $E_{L_input} = 125 \text{ J/cm}^2$ is determined as a threshold in which the ablation depth tremendously increased with laser input energies at $E_{L_input} > 125 \text{ J/cm}^2$ that corresponds to the substantial melt formation on the surface of the lasered profile. At $E_{L_input} < 125 \text{ J/cm}^2$, Laser-Induced Periodic Surface Structures LIPSS were a frequently occurring surface morphology with less or even no melting on the surface. In multiple linear laser scanning, the introduction of a constant amount of laser input energy $E_{L_input} = 3.9 \text{ J/cm}^2$ through lower magnitudes of scan velocities and laser powers resulted in more surface degradation, a more significant rise in ablation depth with the number of laser scanning N_s , deeper ablation depth, narrower lasered profile, less specific ablation energy, and lower MRR.

Table of content

List of abbreviation	IV
List of formulas	VI
1 Introduction and motivation	1
2 State of art.....	3
2.1 Titanium alloys.....	3
2.2 Additively manufactured titanium alloys.....	4
2.3 Micro-machining	6
2.4 Micro-milling of titanium alloys.....	8
2.4.1 Tools	8
2.4.2 Cutting forces and specific cutting energy	11
2.4.3 Surface roughness.....	12
2.4.4 Burr formation	14
2.4.5 Tool wear	16
2.5 Machining of additively manufactured parts	17
2.6 Laser-assisted machining.....	18
2.6.1 Laser-assisted micro-machining	20
2.7 Laser material processing	22
2.7.1 Ultra short pulse lasers and ablation.....	23
2.7.2 Surface morphology in laser-titanium alloys interaction	24
2.8 Modelling and simulation of laser-assisted machining.....	25
3 Objectives and approach.....	27
4 Experimental equipment and plan	29
4.1 Experimental setup.....	29
4.1.1 Machine tool.....	29
4.1.2 Laser device.....	30
4.2 Workpiece materials and tool	31
4.2.1 Workpiece materials	31
4.2.2 Cutting tool.....	31
4.3 Measurements and analysis.....	32
4.3.1 Cutting forces.....	32
4.3.2 Surface roughness and topography	33
4.3.3 Tool wear and burr analysis.....	33
4.3.4 Material characterization.....	34
4.4 Experimental design	35

5	Comparison between machinability of additively manufactured and conventional titanium Ti6Al4V	38
5.1	Uncut chip thickness.....	38
5.2	Cutting forces	38
5.3	Specific cutting energy	40
5.4	Surface roughness	43
5.5	Burr formation.....	45
5.6	Tool wear.....	51
6	Interaction between laser and titanium Ti6Al4V	53
6.1	Multiple laser pulses	53
6.2	Single linear laser scanning.....	60
6.3	Multiple linear laser scanning	68
7	Laser assisted micro-milling	76
7.1	Modelling of the uncut chip thickness	76
7.1.1	Influence of structure parameters on the uncut chip thickness	87
7.1.2	Influence of tool geometry on the uncut chip thickness.....	89
7.1.3	Influence of process parameters on the uncut chip thickness.....	90
7.1.4	Determination of important parameters in laser-assisted micro-milling.	92
7.2	Laser structuring of Ti6Al4V and micro-milling of structured parts	95
7.2.1	Laser structuring of material workpiece	95
7.2.2	Cutting forces.....	98
7.2.3	Surface roughness.....	108
8	Summary and outlook.....	113
9	References	119

List of abbreviation

Abbreviation	Description
2D	Two-dimensional
3D	Three-dimensional
AE	Acoustic Emission
AISI	American Iron and Steel Institute
AlCrN	Aluminium Chromium Nitride
AM	Additive Manufacturing
ARPF	Ablation Rate Per Fluence
BUD	Built-up Direction
BUE	Built-up Edge
CAD	Computer Aided Design
CBN	Cubic Boron Nitride
CNC	Computer Numerical Control
Co	Cobalt
CO ₂	Carbon Oxide
CTR	Chip Thickness Reduction
DED	Directed Energy Deposition
DIN	Deutsches Institut für Normung
DMD	Direct Metal Deposition
EBM	Electron Beam Melting
EBSD	Electron Backscatter Diffraction
EDX	Energy Dispersive X-ray
FEM	Finite Element Method
FIB	Focused Ion Beam
FIPSS	Femtosecond-Induced Periodic Surface Structure
HAZ	Heat Affected Zone
HCP	Hexagonal Closed Packed
HIP	Hot Isostatic Pressing
HNO ₃	Nitride acid
IR	Infrared Radiation
LAMM	Laser Assisted Micro-Milling
LAM	Laser Assisted Machining
LIPSS	Laser-Induced Periodic Surface Structures
MD	Molecular Dynamic
MRR	Material Removal Rate
Nb	Niobium
NCD	Nano Crystalline Diamond
PBF	Powder Bed Fusion
PO	Pulse Overlap
PVD	Physical Vapor Deposition
SEM	Scanning Electron Microscopy
Si ₃ N ₄	Silicon Nitride
SLM	Selective Laser Melting
SPH	Smoothed Particle Hydrodynamic
TAM	Thermally Assisted Machining

Ti	Titan
Ti6Al4V	Titanium Aluminium Vanadium
TiAlN	Titanium Aluminium Nitride
TiAlSiN	Titanium Aluminium Silisium Nitride
TiN	Titanium Nitride
TTM	Two Temperature Model
USPL	Ultra Short Pulse Laser
UTS	Ultimate Tensile Strength
UV	Ultraviolet
WC	Tungsten carbide
WS ₂	Tungsten disulfide
Yb-YAG	Ytterbium-doped Yttrium Aluminium Garnet

List of formulas

Symbol	Unit	Description
Δx	μm	Shifting value
μ	-	Mean of Gaussian distribution
A	μm^2	Ablation area
a_e	mm	Radial depth of cut
a_p	mm	Axial depth of cut
ARPF	$\mu\text{m}^3.\text{pulse}^{-1}.\text{J}^{-1}.\text{cm}^2$	Ablation rate per pulse
ξ	-	Incubation factor
C	J/K	Heat capacity
C_y	mm	y center of tool position
D_L	μm	Laser beam diameter
dt	s	Time increment
dz	μm	Layer thickness
$d\phi$	$^\circ$	Angular shift
e_L	$\mu\text{J}/\mu\text{m}^3$	Specific ablation energy
E_{L_input}	J/cm^2	Laser input energy
E_p	J	Pulse energy
f_L	kHz	Laser repetition frequency
F_{res}	N	Resultant cutting force
F_x	N	Cutting force in x-direction
F_y	N	Cutting force in y-direction
f_z	$\mu\text{m}/\text{tooth}$	Feed per tooth
G	$\text{W}/\text{m}^3.\text{K}$	Electron phonon coupling factor
h	μm	Chip thickness
h_{cu}	μm	Maximum uncut chip thickness
h_{cu_crt}	μm	Critical uncut chip thickness
h_{min}	μm	Minimum uncut chip thickness
I_0	W/cm^2	Initial laser intensity
I_{L_peak}	W/cm^2	Laser peak intensity
K	$\text{W}/\text{m}.\text{K}$	Thermal conductivity
l_g	μm	Line gap
N	-	Total number of cutting teeth
n	rev/min	Rotational tool speed
N_{dis}	-	Number of discretization
N_p	-	Pulse number
N_s	-	Number of laser scan
P_i	-	Signal point
P_{L_ave}	W	Average laser power
P_{L_peak}	W	Peak laser power
PO	%	Pulse overlap
Q_w	mm^3	Material removal
r	μm	Spot radius
R	-	Surface reflectivity
Ra	μm	Average surface roughness
r_s	-	Spearman correlation

List of formulas

r_β	μm	Cutting edge radius
S	J	Energy source of laser pulse
S_a	μm	Arithmetical mean height of surface roughness
S_d	μm	Structure depth
S_{max}	-	Maximum value of signal
S_{mean}	-	Mean value of signal
S_z	μm	Maximum height of surface roughness
t	s	Modelling time
t_c	s	Cutting time
T_e	K	Electron Temperature
T_i	K	Lattice Temperature
t_p	ps	Irradiation time
u_c	J/mm^2	Specific cutting energy
v_c	m/min	Cutting speed
v_f	mm/min	Feed velocity
v_L	mm/s	Laser scan velocity
V_{rem}	mm^3	Removal chip volume
x_i	mm	Coordinate of cutting tooth in x-direction
y_i	mm	Coordinate of cutting tooth in y-direction
α	$^\circ$	Structure angle
α_{abs}	cm^{-1}	Absorption coefficient
β	$^\circ$	Helix angle
λ	-	Multiplier
σ	-	Standard deviation of Gaussian distribution
D	mm	Tool Diameter
ϕ	$^\circ$	Angular position of cutting tooth
φ_{L_peak}	J/cm^2	Laser peak fluence
$\varphi_{\text{th}}(1)$	J/cm^2	Ablation threshold for one pulse
ω	rad/s	Angular velocity

1 Introduction and motivation

Titanium alloys are widely used in aerospace, aeronautical, automobile, chemical, and medical industries due to their outstanding material properties. The manufacturing of different components made of titanium alloys faces several issues. Particularly regarding machining as one of the manufacturing processes, titanium alloys are well-known as difficult-to-cut materials. They have a high yield stress to tensile strength ratio (>0.9), and their flow stress increases at strain rates higher than 10^3 s^{-1} , which usually occurs in the machining process [1–3]. In addition, titanium alloys' low elastic modulus causes the material to spring back, followed by deflection, vibration, and chatter [4]. Moreover, two other highlighted machining issues of these materials are high cutting temperatures during machining due to their lower thermal conductivity and the capability to maintain high hardness at high temperatures. Furthermore, the chemical affinity of titanium alloys to the cutting tool materials causes extreme tool wear. Additionally, the phase transformation of titanium alloys may complicate the machining process.

As an alternative to machining for producing components made of titanium alloys, Additive Manufacturing AM technologies with the capability of manufacturing complex parts with high flexibility have gained more attention. AM technologies can produce near-net-shaped components. Therefore, a reduction in material waste and manufacturing cost can be achieved, which is highly important, particularly for titanium alloys, due to their high expense. Despite the remarkable benefits of the AM process, the poor surface quality and the limitation to reaching tight dimensional and geometrical tolerances cannot be overlooked. In this regard, applying different machining processes is required to finish AM parts. A wide range of AM process parameters, various methods for fabricating the parts using AM, and varied heating rates and complex thermal processes while printing the parts complicate the application of AM techniques, accompanied by a variation in additively induced mechanical, thermal, and microstructural properties of AM titanium alloys. This may also add more difficulty in their machining in addition to mentioned issues.

A growing demand for miniaturization in different fields led to the development of new methods or the adoption of the current processes on the micro-scale. Micro-machining as a micro-manufacturing process has been developed to produce small-sized features with great complexity. However, the micro-machining application encounters several challenges associated with the size effect, such as ploughing, considerable burr formation, surface deterioration, etc. Particularly in the micro-machining of titanium alloys as a difficult-to-cut material, the slender micro-cutting tools cannot withstand the great cutting forces during the process, followed by tool breakage or deflection. Moreover, reducing material removal for decreasing cutting forces may intensify the issue of size effect and, eventually, less process efficiency. Therefore, applying a laser beam as a heating source ahead of the cutting tool for reducing the material strength, and corresponding decreasing the cutting forces, has been introduced as Laser-Assisted Machining LAM to tackle this issue. The difficulty in controlling the temperature gradient and Heat Affected Zone HAZ, the limitation of the process to the dry condition, the probability of increasing tool wear due to the dominance of diffusion tool wear mechanism, and thermal expansion, particularly for micro-cutting tools are some drawbacks of the mentioned method [5–7]. As an

alternative to using a laser beam for reducing the material strength as a typical application of LAM, it can be utilized for the structuring of the workpiece through removing some parts of the material before cutting and inducing the controlled damage to weaken the material. Subsequently, the remained part of the material can be machined by less cutting forces under wet conditions, applying the oil or cutting lubricant, which may extend the tool life with less chatter and tool vibration.

The significance of the machinability of titanium, particularly for AM titanium alloys as a new generation of the material, and lack of knowledge, and limited scientific works for micro-machining of these parts have contributed to a comparative study in the micro-milling process between conventionally and additively manufactured Ti6Al4V, as a frequently used titanium alloy in the industry, in the current research work. Moreover, the capability of the novel introduced LAM method instead of the commonly used approach in machinability of Ti6Al4V is evaluated. Additionally, the influence of the material removal reduction using the laser pre-structuring of the workpiece on the subsequent micro-milling process is modelled in order to find the most influential parameters. The application of laser before machining in the introduced LAM method highlights the interaction between laser and material. Therefore, a comprehensive study is carried out to deeply understand this interaction for Ti6Al4V.

2 State of art

This chapter overviews the titanium material and additively manufactured titanium alloys. Moreover, different aspects of the micro-milling process have been introduced with emphasis on processing titanium alloys with respect to the tool, cutting force and specific cutting energy, surface roughness, burr formation, and tool wear. Further, the challenges of machining additively manufactured titanium alloys have been explained. The difficulty in machining titanium alloys as a difficult-to-cut material has led to the generation of new machining methods. In this regard, Laser Assisted Machining (LAM) as one of these techniques has been introduced. Different experimental and modelling investigations for improving machinability using LAM have been summarized, particularly for the micro-milling process. Furthermore, the interaction between laser and titanium material concerning ablation threshold and surface morphology has been discussed.

2.1 Titanium alloys

Titanium is available as commercial pure and as alloys. The alloying elements dissolved in titanium are classified as neutral, α -stabilizer, and β -stabilizer. The elements or additions that maintain or increase the temperature range of stability of the α phase are called α -stabilizer (see Figure 2.1b). In fact, they raise the α - β transient temperature. The most important of them are aluminum, tin, and zirconium. The elements that stabilize the β phase by lowering the α - β transient temperature are called β -stabilizer such as molybdenum, vanadium, and iron (see Figure 2.1c). The two most important impurities in titanium alloys are Oxygen as α -stabilizer and hydrogen as β -stabilizer. Titanium alloys are mainly divided into three categories of α -alloys, β -alloys, and α + β alloys. At low temperatures, pure titanium and titanium alloys with α -stabilizer have a hexagonal closed-packed structure (hcp) referred to as α -titanium. Body center cubic (bcc) is the stable structure at high temperatures, called β -titanium. Pure titanium undergoes an allotropic transformation from hcp(α) to bcc(β) by raising the temperature to 882 °C (Figure 2.1a).

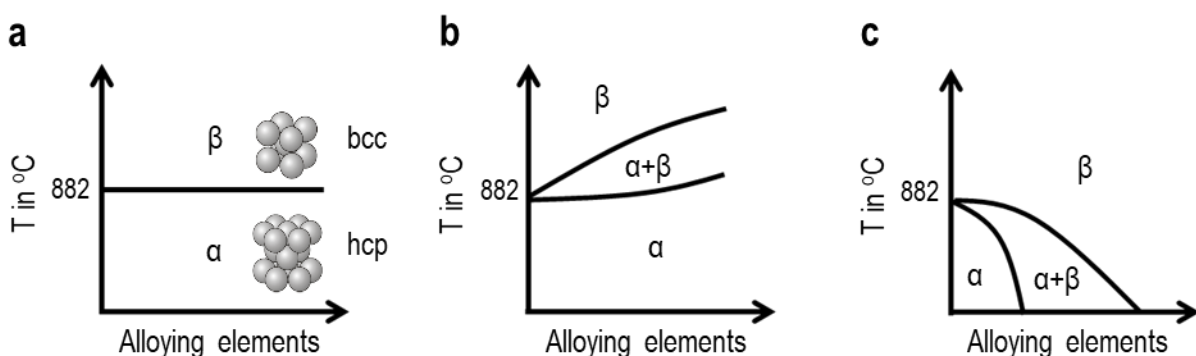


Figure 2.1: Influence of alloying elements on the extent of α and β phases: a) neutral, b) α -stabilizer, c) β -stabilizer [8].

The alloys containing one or more α and β stabilizing elements belong to α + β alloys. The mechanical properties of the titanium alloy are influenced by the individual properties of the α and β phases, their arrangement, and volume fraction [9]. For example, the α phase has a lower density than the β phase. The deformation mechanism of titanium alloys is highly dependent on the crystallographic structures of

the mentioned phases. In fact, the deformation is caused by the dislocation movement on the slip systems of these crystallographic structures.

Due to their outstanding properties, titanium alloys are widely used in different industrial sectors. One of the applications of titanium alloy is related to the aerospace industry, particularly in the engine, compressor discs, blades in jet engines and airframe systems, rockets, and satellites due to their high specific strength ratio. The primary reason for using titanium alloy in the aerospace industry is associated with decreasing weight, space limitation, high operating temperature, and corrosion resistance [10]. In the automobile industry, titanium alloys are used for intake and exhaust valves, connecting rods, retainers, and other parts to save weight as a significant benefit because of their high strength-to-weight ratio. Due to good biocompatibility, high corrosion resistance, and excellent strength-to-weight ratio, they have biomedical applications in which worn-out or broken body parts can be replaced with the titanium components such as knees, hip joints, and teeth. In chemical, petrochemical, and marine environments, titanium alloys indicate a high corrosion resistance. For example, they are used for tanks, heat exchangers, reactor vessels, etc., for chemical processing, desalination, and power generation plants [8].

2.2 Additively manufactured titanium alloys

Additive Manufacturing (AM), also known as 3D printing, is an innovative technology that can create complex geometries layer by layer. The capability of forming near-net-shaped components and, therefore, reducing machining time and cost, and low material waste make the AM technology an effective and economical manufacturing process, particularly for expensive and hard-to-machine materials such as titanium and super alloys [11]. Several conventional methods, such as powder processing, forging, casting, and powder metallurgy, can also produce Ti-based alloys [12–15]. However, the challenges of using these techniques lead to a rise in the production cost of titanium alloys and, consequently, their limited application. However, AM technology provides a broader range of applications for titanium alloys by reducing their production cost through shortened product development cycle, freedom in design as well as lower energy, material, and human resources.

The main AM technologies for metals can be classified into two categories, Powder Bed Fusion PBF and Directed Energy Deposition DED. PBF is based on scanning the bed of the powder, the metal powder laid down on the build platform, with the heat source, such as laser or electron beam, followed by either partial or completely melting the powders in the beam path, ultimately re-solidification and binding together. Layer by Layer formation according to the CAD model creates the final part. In DED technologies, the material injection into the melt pool instead of scanning on a powder bed fabricates the final component. PBF technologies offer better surface finish, and form and dimensional accuracy due to smaller utilized beam size and smaller layer thickness compared to DED technologies [16]. However, DED technologies have a higher deposition rate [16]. Therefore, PBF technologies can be applied to fabricate parts with more accuracy and complex small-size parts. For example, the Electron Beam Melting (EBM), as a PBF technology, has been successfully applied for manufacturing strong, void-free, and fully dense components with the high complexity in the automotive, aerospace, and medical implant industries [17–19]. Biamano et al. [20] indicated that EBM could ideally produce parts made of

titanium alloy-based material with little internal defect and homogeneously distributed alloying elements. Moreover, the Selective Laser Melting (SLM) technique, also as PBF technology, is suitable for fabricating aerospace components made of nickel-based superalloys, steels, and titanium-based alloy materials [21,22]. In contrast, DED technologies are suitable for relatively large components with high fabrication rates [16]. Moreover, they are appropriate for manufacturing metallic parts such as screws, valves, and mold tools [23,24].

In additive manufacturing of Ti6Al4V, thermal cycling and accumulation lead to different and complex microstructures. The formation of α' martensite at a high cooling rate, the formation of $\alpha+\beta$ phase at a low cooling rate [25], the decomposition of α' martensite into $\alpha+\beta$ phase, and large columnar grains formation [26] are some of the additively induced microstructures. The high temperature of substrate or powder in the PBF technique using the electron beam leads to cooling rate reduction and intrinsic heat treatment on the fabricating parts. Thus, the manufactured Ti6Al4V using mentioned technique indicates a fully lamellar ($\alpha + \beta$) microstructure [27]. The large columnar grains in the additively manufactured Ti6Al4V can result in considerably anisotropic microstructures and properties [28], as shown in Figure 2.2.



Figure 2.2: Anisotropic microstructure in a SLM part made of titanium [28].

Additively manufactured titanium alloys are subjected to different mechanical tests to evaluate the behavior of these materials at different conditions. They usually have outstanding mechanical properties compared to wrought/cast parts [11]. Murr et al. [29] studied the mechanical and microstructural properties of Ti6Al4V manufactured by the EBM process and compared them to wrought and cast Ti6Al4V parts. As concluded, AM techniques are more efficient for fabricating implant components with superior mechanical properties. Rafi et al. [25] compared Ti6Al4V parts manufactured by EBM and SLM. SLM parts indicated higher tensile strength due to their martensitic microstructure, while the EBM method enhanced the material's ductility by generating a lamellar phase. Moreover, SLM parts showed a higher fatigue limit (500 MPa) compared to 340 MPa for EMB parts, attributed to the presence of lamellar structures. Generally, laser-based technologies provide higher strength and lower ductility due to the formation of α' -martensite under rapid cooling condition [30]. The β to α' martensitic transformation occurs at a cooling rate above 410 K/s [31]. In [16], a comparison between additively manufactured and cast/wrought materials also indicated higher tensile strength and lower ductility for AM titanium parts. EBM parts showed higher ductility and lower tensile strength compared to SLM and Direct Metal

Deposition (DMD) parts due to the α - β microstructure of EBM parts through slow cooling in a vacuum atmosphere. Moreover, coarser grains were observed for cast and wrought material with equiaxed α - β microstructure. In [16], it was also mentioned that applying Hot Isostatic Pressing (HIP) and aging leads to a microstructure variation. As built DMD Ti6Al4V indicated the usual martensitic structure due to rapid cooling from the β phase, while the HIP'd and aged Ti6Al4V showed the grain boundary alpha and inter-granular coarse alpha plates. Moreover, the application of HIP in the case of DMD and SLM improved the material's ductility of Ti6Al4V. Additionally, a comparable fatigue resistance was reported for AM and conventionally manufactured Ti6Al4V. However, the limited fatigue property of AM-processed Ti6Al4V was reported in [28–30]. The irregular-shaped lack of fusion porosity is a typical defect in AM parts. Under cyclic loading, the large pores are the initiation site of fatigue cracks, followed by decreasing fatigue life. Applying HIP reduces the porosity size and leads to a relatively fully dense material. Another issue attributed to the AM-processed Ti6Al4V is the limited work hardening capacity [26,32] which is accompanied by an early necking of the material.

2.3 Micro-machining

Demands for the fabrication of Miniaturized components with high accuracies are considerably high. Several non-traditional methods can be introduced for this purpose, such as electro-discharge machining [33–35], laser micromanufacturing [36,37], lithography, electroplating and moulding [38,39], deep reactive ion etching [40,41], and deep UV lithography [42,43]. However, most of the mentioned methods face a limitation in producing complex components with three-dimensional geometries. Moreover, their working time and cost are considerably high. Alternatively, mechanical micro-machining is introduced as a promising method with a high level of flexibility and a relatively high Material Removal Rate (MRR).

Mechanical micro-machining is similar to the conventional machining process in a smaller size in the range of micrometers and can be categorized into different processes: micro-drilling, micro-turning, micro-milling, etc. One of the frequently used mechanical micro-machining processes is micro-milling. The kinematics of the micro-milling process is similar to the conventional milling. However, some issues in the micro-milling may complicate the machining process. The tool size can be extremely low, followed by a high length-to-diameter ratio [44,45]. This critical tool size (slender tool) results in a low stiffness of the micro-milling tool. Thus, the chatter may cause the tool breakage due to the low rigidity of the milling tool [46,47]. Furthermore, ploughing predominates in the material deformation mechanism that can deteriorate the surface quality. In addition, the size of the burr with respect to the size of the machined component in the micro-milling operation is much more pronounced compared to that for the conventional machining process. Therefore, the manufacturing cost is considerably influenced by the micro-deburring process that is time- and cost-consuming [48,49]. Furthermore, implementing the micro-milling process requires a machine tool with extremely high spindle speed. Moreover, the generated cutting temperature during machining influences tool wear, material removal mechanism, and surface quality. The detrimental effect of this factor is more considerable in the micro-machining process. According to the investigation of Mamedov and Lazoglu [50], 3D distortions and dimensional accuracy of the

machined micro-components are directly influenced by the cutting temperature. In [51], it was also reported that thermal expansion in the micro-scale range could not be underestimated.

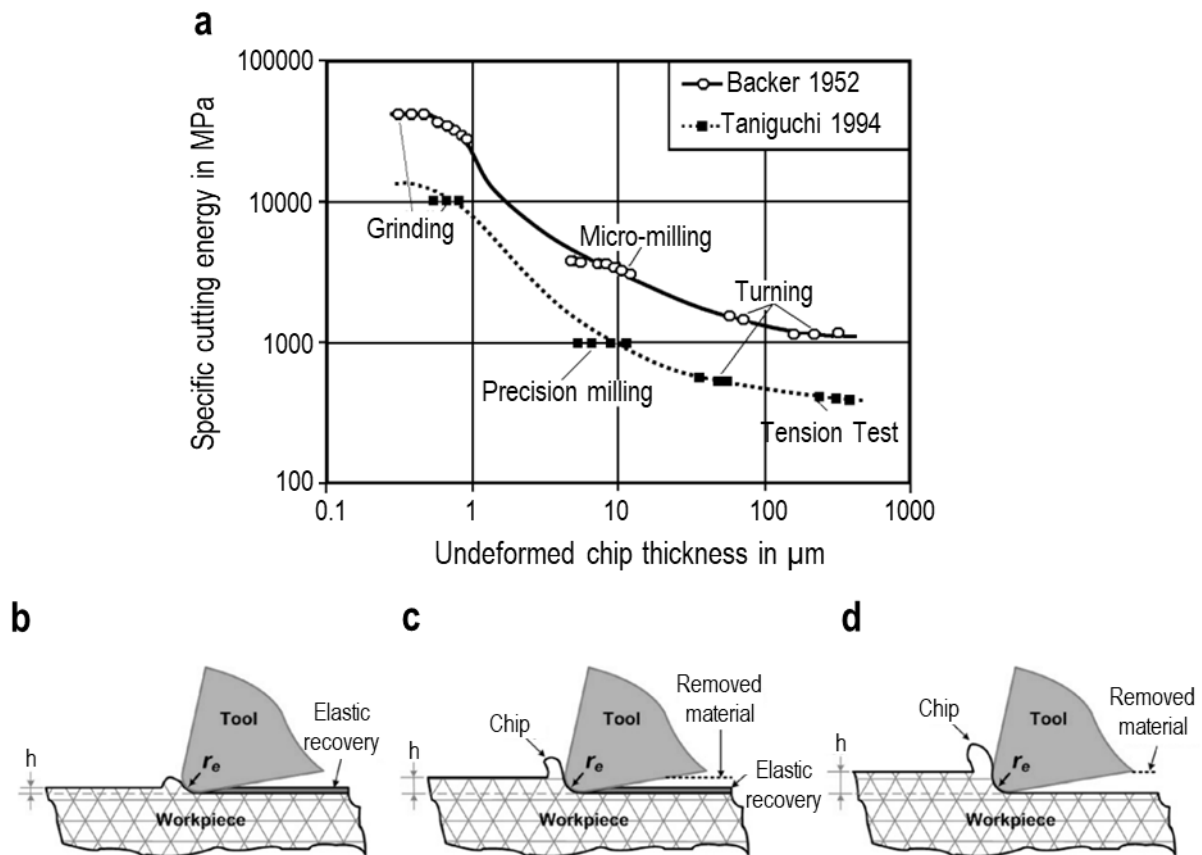


Figure 2.3: a) Influence of undeformed chip thickness on the specific cutting energy [52,53]. Chip formation with respect to the minimum chip thickness h_{\min} : b) $h \ll h_{\min}$, c) $h \approx h_{\min}$, d) $h \gg h_{\min}$ [54].

Generally, the material removal mechanism is influenced by material type, tool geometry, process parameters, and the machining scale. Regarding the scale of the machining, particularly for the micro-machining, the size effect is a frequent issue referred to as a non-linear increasing the specific cutting energy with decreasing the undeformed chip thickness. Backer et al. [52] indicated a difference in the shear energy in the unit volume for different machining processes: Turning, Micro-milling, and grinding. According to Figure 2.3a, a reducing trend in specific cutting energy from grinding to turning can be observed. Taniguchi [53] also confirmed the size effect in the range of different manufacturing processes (see Figure 2.3a).

The minimum chip thickness h_{\min} is determined in which the machining condition varies above and below this threshold. In this regard, three scenarios can be defined. If the undeformed chip thickness h is much lower than h_{\min} ($h \ll h_{\min}$), the material is compressed under the cutting tool instead of material removal (see Figure 2.3b). In this case, considerable elastic deformation of the material results in surface damage and, eventually, low surface quality. In the case of comparable sizes of h and h_{\min} shown in Figure 2.3c, the chip formation is expected in the primary shear zone. However, the specific cutting energy is significantly high due to the considerable proportion of ploughing effect. If h is greater than h_{\min} , the stable plastic deformation in the shearing zone results in chip formation (see Figure 2.3d). In this case, the

percentage of elastic recovery and ploughing effect is low. Generally, the chip thickness is not constant in the milling operation, like the orthogonal cutting. It changes with the tool rotation. Depending on the milling strategy, down or up milling, the chip thickness starts from zero to maximum value or vice versa. Therefore, all mentioned scenarios may occur that complicate the milling process, particularly on the micro-scale. Regarding the influence of different process parameters on the determined threshold h_{min} , the cutting edge radius r_β was reported as the most significant factor [55–58]. The cutting edge radius r_β depends on the manufacturing precision, tool material, particle size, coating, and the tool wear state [59]. The h/r_β ratio can significantly influence the machining accuracy, burr formation, and surface quality [60]. The size effect occurs when the ratio of undeformed chip thickness to cutting edge radius becomes critical. The importance of this ratio led to many investigations for several materials and different machining operations. Accordingly, this ratio changes from 0.14 to 0.48 [61]. The obtained ratio for different materials would be a good indicator for monitoring the process. If the ratio is smaller than the critical value, the machining parameters must be changed.

2.4 Micro-milling of titanium alloys

Based on the mentioned issues in the micro-machining process, the following aims to present in details different aspects of the micro-milling of the titanium alloys as difficult to cut material in terms of tool, cutting force and specific cutting energy, burr formation, surface roughness, and tool wear.

2.4.1 Tools

The suitable selection of the cutting tool is crucial in the micro-machining process of titanium alloys to decrease the overall machining time through reduction of cycle time. In this regard, tool material, coating, and geometry are significant for enhancing the tool life and improving the cutting process.

Regarding the tool material, some important characteristics can be mentioned. An appropriate cutting tool material used for machining titanium alloys should have good thermal conductivity for minimizing heat accumulation and preventing thermal shock, low chemical reactivity with titanium, high chemical stability to avoid a built-up edge formation, high resistance to abrasion, consistent cutting edge at elevated temperatures, good fatigue resistance against chip segmentation process, high compressive, tensile and shear strength, and high fracture toughness [62]. Titanium alloys are usually processed by carbide tools. Compared to carbide tools, ceramic tools are not appropriate due to their poor thermal conductivity, relatively low fracture toughness, and high reactivity with titanium alloys [63,64]. Moreover, a reduction in hot hardness at elevated temperatures is followed by weakening interparticle bond strength and considerable tool wear reported in [65] as another reason for the ineffectiveness of ceramic tools in machining titanium alloys. In the micro-milling process, fine-grain carbide micro-tools are used. They are mostly fabricated in tungsten carbide within a cobalt material matrix (WC/Co). The sharp cutting edge is not easily achievable for this type of micro-tools due to the limited edge strength. An edge roundness with a radius between 1 μm and 5 μm can be obtained [66]. In the machining of titanium alloy using the tungsten carbide (WC/Co) cutting tool, the cobalt diffusion [67] leads to a breakaway, pulling out and removing the WC particles. This can be followed by a detrimental effect on the hardness and wear resistance

[68], rapid cratering, plastic deformation of the cutting edge, and eventually catastrophic failure of the inserts [69]. The influence of carbide substrate on tool wear cannot be overlooked. Sadik et al. [70] enhanced the tool performance in the machining of Ti5553 through designing specific carbide substrates. One carbide substrate presents a reduced content of Co on the surface, followed by the decreasing melt formation of Ti with the binder phase. Moreover, the interaction of extra graphite, providing the source of carbon, with Ti Workpiece postpones attacking the carbon of the WC grains leading to chemical wear.

The application of the coating is extremely crucial for improving the machining of titanium alloys. Generally, an excellent thermal barrier and low friction coefficient leading to reducing the cutting forces are provided by the coating of the tools. However, a limitation regarding the application of the coating must be taken into account. The coating of the tool increases the cutting edge radius, which can be accompanied by more ploughing effect, greater cutting forces, and lower tool life. Özel et al. [66] investigated the influence of cubic boron nitride (cBN) coating in the micro-milling of Ti6Al4V alloy under dry condition using the tungsten carbide tool. The lowest tool wear was observed in the utilization of cBN coating. In [71], reducing friction and enhancing wear resistance in the machining of titanium alloys was also reported using the cBN coating. Thepsonthi and Özel [72] observed lower cutting temperature and wear rate for cBN-coated tools compared to an uncoated WC/Co tool. Schueler et al. [73] mentioned that friction at the tool/workpiece interface is the main cause of cutting edge deterioration, followed by accelerating tool wear, burr formation, and degrading the surface quality. In this regard, Mittal et al. [74] applied amorphous carbon-coated tools in high-speed micro-milling of Ti6Al4V and reported cutting force reduction associated with the low friction of coating. Moreover, applying Tungsten disulfide WS_2 coating over TiAlN also indicated a significant decrease in the cutting force. Aslantas et al. [75] evaluated the performance of the machining process considering tool wear, surface roughness, cutting force, and burr formation under the application of different material coatings. As reported, the values of cutting forces for uncoated and nanocrystalline diamond NCD-coated tools are greater than those for two other tools coated by TiN and AlCrN. Moreover, TiN- and AlCrN-coated tools indicated less wear with a minimum change in tool diameter compared to uncoated and NCD-coated tools. The minimum burr width was also observed for the TiN- and AlCrN-coated tools. In conclusion, the NCD-coated cutting tools indicated lower performance in comparison with TiN- and AlCrN-coated tools. Sui et al. [76] mentioned that the addition of Si to the coating of TiAlN changes the coating morphology from columnar to nanocrystal and simultaneously reduces the grain size. Therefore, the suppression of crack propagation is caused by this nanocrystal structure, and good fracture toughness is achievable. They reported that the TiAlSiN coating has the best cutting performance at various cutting speeds compared to two other utilized TiAlN and TiAlN/TiAlSiN composite coatings. Less area of built-up edge and chipping at the cutting edge in the case of TiAlSiN coating is due to its dense nanocrystal structure, high hardness, and good oxidation resistance. However, Sousa et al. [77] mentioned the importance of TiAlN coatings in today's industry due to their considerable wear resistance, high mechanical properties, high thermal stability, and high corrosion resistance at high machining temperature.

The micro-milling tools are geometrically similar to conventional milling tools. The micro-cutting tools are slender, which leads to less stability and more vibration in the process. Figure 2.4a-e provides the schematic of frequently used micro-milling geometries. Figure 2.4a and Figure 2.4b indicate micro-end mill tools with one and two flutes. An increase in the number of edges dramatically reduces the tool stiffness. These types of tools can be used for producing components with relatively sharp corners. However, the tool corner rapidly rounded, followed by less dimensionally and geometrical accuracy. To tackle this issue, the micro flat-end mill with a corner radius is presented in Figure 2.4c which increases the edge stability. Figure 2.4d shows the schematic of a ball-end micro mill used to produce the components with complex 3D geometries. The tapered micro-milling tool shown in Figure 2.4e is appropriate for the burr formation reduction. According to an investigation by Oliaei and Karpat, who focused on the predictable formation of Built-Up-Edge (BUE) in titanium alloy Ti6Al4V [78], the small clearance angle led to the most stable conditions of BUE formation. Figure 2.4f provides SEM images of some micro-mill tools.

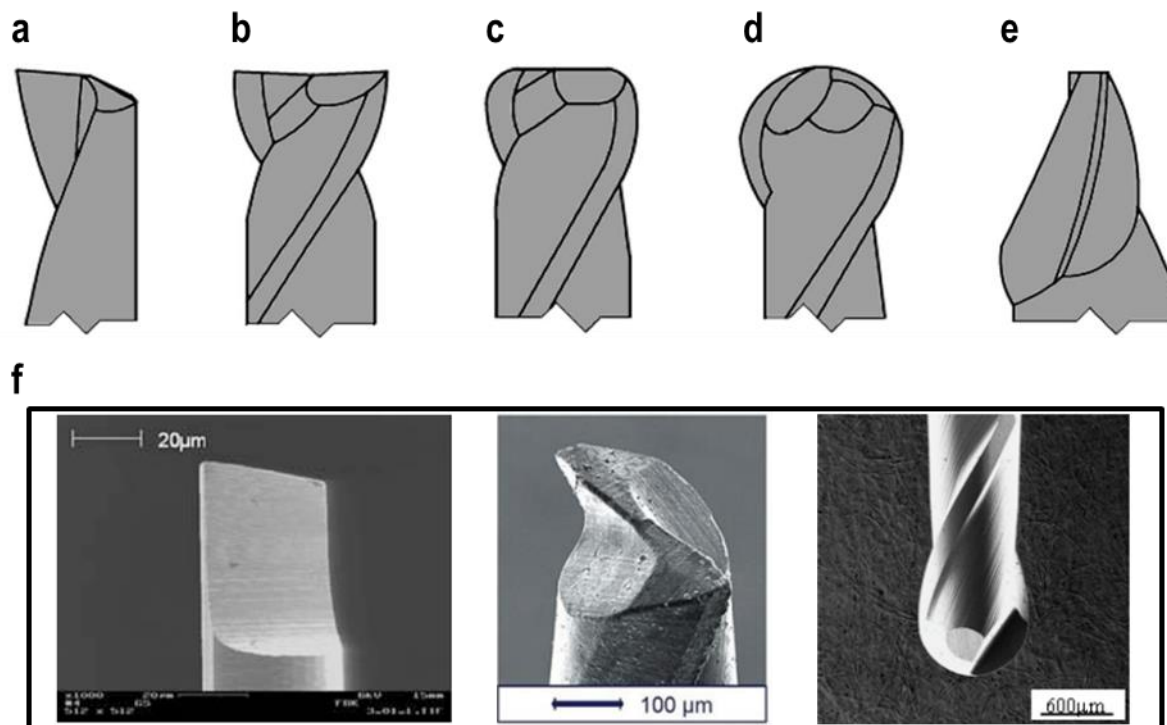


Figure 2.4: Different geometries of micro-milling tools: a) single-fluted flat end mill, b) two-fluted flat end mill, c) end mill with corner radius, d) ball-end mill, e) tapered micro mill [61], f) SEM images of micro-mill tools [73,79,80].

Apart from the macro-geometry of the tool, Aramcharoen and Mativenga [54] mentioned that cutting edge geometry, i.e. micro-geometry of the tool, influences machining outputs in terms of surface quality and burr formation in micro-milling. Wyen and Wegener [81] highlighted the role of cutting edge radius on cutting forces in orthogonal cutting of titanium alloy. Higher edge radius resulted in higher feed and cutting forces. In [82], it was reported that the cutting-edge radius plays an important role in increasing the compressive residual stress after up-milling of Ti6Al4V, which can enhance the fatigue life. In another study, Obikawa and Kani [83] modified the rake face of the micro-milling tool by generating microgrooves through the focused

ion beam (FIB). The cutting forces reduction of up to 27 % was reported. The tool fabrication process is also extremely crucial. In [84], internal micro-cracks in the cutting edge caused by improper grinding parameters and residual tensile stress in the cutting edges are determined as two main sources of high damage rate for tungsten carbide end mills for titanium alloy machining.

2.4.2 Cutting forces and specific cutting energy

Downscaling conventional milling to micro-milling results in lower magnitudes of the cutting force components. However, the comparable size of the chip thickness and edge radius enhances the ploughing effect, applied pressure to the tool's rake face due to the material's elastic recovery, and, consequently, the significant role of the size effect [85]. Therefore, a comparison between macro- and micro-machining can be provided by the specific cutting force defined as the magnitude of cutting force required for removing the chip area. Weber et al. [86] reported that the specific cutting force increases with reducing the depth of cut. Aramcharoen et al. [54] highlighted the importance of the size effect on the specific cutting force in the micro-milling process. A variation in the specific cutting force was observed by changing the ratio of undeformed chip thickness to the cutting edge radius. This ratio plays a significant role in the specific cutting force. When the undeformed chip thickness is less than the cutting edge radius, a dramatic increase in the specific cutting force is detectable. In simulating the micro-milling of Ti6Al4V, Pratap et al. [87] found that the maximum Von-Mises stress is higher than that of macro-milling. This can be associated with the low magnitude of the cutting edge radius and low uncut chip thickness in the micro-milling process. In fact, the size effect associated with ploughing and elastic recovery increases nonlinearly specific cutting forces at low feeds [88,89]. Like conventional milling, different parameters affect the cutting forces. In the machining of titanium alloy using a ball-end milling tool, the cutting forces were considerably influenced by the axial depth of cut and feed per tooth. However, the cutting speed indicated no remarkable effect [90].

The role of the micro/nanostructure is highlighted in the micro-machining process. Since the uncut chip thickness or feed per tooth in the micro-machining process is in the same order of magnitude of the grain sizes, the material grains may individually be deformed during the micro-cutting. Therefore, the deformation indicates considerable anisotropic features [91]. In addition to the grain size, titanium alloy's microstructure also remarkably influences the cutting forces. Depending on recrystallization, annealing time and temperature, different microstructures and mechanical properties can be achieved for titanium alloys. Attanasio et al. [92] investigated the influence of different microstructures of Ti6Al4V on the cutting forces in the micro-end milling process. Four different microstructures of titanium alloy (Milled annealed, bimodal, fully equiaxed, and fully lamellar) were compared. Fully lamellar microstructure indicated the lowest hardness value due to the element partitioning effect and coarse lamellar grains. This also resulted in lower cutting forces in the machining process. Moreover, the homogeneity in fully lamellar microstructure without hard equiaxed grains also reduced the cutting force fluctuations throughout the machining time. According to the nano-hardness measurement, bimodal exhibited more variation in hardness value between equiaxed α and lamellar ($\alpha+\beta$) grains, and more non-uniform microstructures. This caused

more cutting force fluctuations. As concluded, the microstructure plays an important role, particularly in micro-scale machining. In this case, the homogenous microstructure is extremely desirable to decrease the fluctuation in the machining process. In this regard, the lamellar structure is preferable. The interaction between feed per tooth and microstructure is also important. At higher feed per tooth, an increase in cutting forces among different microstructures can be justified by micro-hardness values. While no clear pattern was observed by reducing the feed, that may be associated with tool runout and ploughing effect.

2.4.3 Surface roughness

The surface quality and the topography of the generated surface using the micro-milling process significantly affect the performance and the functionality of the produced micro-components in terms of friction, lubrication, wear resistance, corrosion, withstanding stresses and temperature and fatigue conditions, etc. Therefore, surface quality is crucial in addition to the determined geometrical and dimensional tolerances for these micro-components. To achieve the desired surface quality, the selection of appropriate process parameters is extremely important. In this regard, many investigations have been carried out to study the influence of different process parameters on surface quality of titanium alloys that have been summarized in the following.

In [93], a considerable change in the surface roughness of the slot bottom was reported by increasing the feed from 0.084 $\mu\text{m}/\text{tooth}$ to 0.252 $\mu\text{m}/\text{tooth}$. However, the change in the cutting speed did not lead to different shaped regular scratches by the circular cutting edge motion. Thepsonthi et al. [94] found that feed per tooth or feed rate plays a significant role in the surface roughness compared to cutting speed and axial depth of cut at the slot milling of titanium alloy. Thepsonthi and Özel [95] also reported that feed per tooth is considered as the most important factor on the surface roughness in comparison with cutting speed, axial depth of cut, and the tool coating. Bandapalli et al. [96] also confirmed that the most influential factor on the surface roughness is the feed rate followed by the depth of cut and, finally, cutting speed, ranging from 30000 rpm to 90000 rpm, in the high-speed micro-milling of titanium alloy. However, an increase in the spindle speed could enhance the surface quality at a constant feed rate and depth of cut. Baldo et al. [97] suggested that increasing the cutting speed and reducing of feed rate may decrease the surface roughness. In [98], the role of cutting speed in changing the surface roughness is also highlighted through the development of a mathematical model. In high-speed micro-milling of the titanium alloy, the role of cutting speed is much more pronounced. As reported in [99], an increase in cutting speed from 10000 to 90000 rpm at a constant feed rate led to a significant reduction of surface roughness in the slot milling of Ti4Al4V. Generally, higher surface roughness is expected by increasing the feed rate in the conventional cutting. However, a 43 % reduction of surface roughness was reported by changing the feed rate from 1 to 5 mm/s at a relatively high cutting speed of 90000 rpm using a micro-mill tool with two flutes and a diameter of 500 μm . Bajpai et al. [99] explained that the irregular plastic flow of the material at lower feeds, correspondingly lower uncut chip thicknesses, negatively affects the surface quality. In details, the magnitude of the feed per tooth is comparable with the size of the cutting edge radius. As a result, the rubbing and ploughing process is much more

pronounced, which can deteriorate the surface quality [89]. However, the shearing mechanism can be dominant at higher feeds. K and Mathew [100] emphasized the importance of the ratio of feed per tooth to the cutting edge radius in the micro-milling of Ti6Al4V, using 3–3.5 μm cutting edge-rounding and a TiAlN coated cutting tool). As recommended, the feed per tooth would be better to be slightly higher than the cutting edge radius. At $f_z = 5 \mu\text{m}/\text{tooth}$, a reduction in surface roughness was observed with the machining length. However, the surface roughness increased with the machining progress at $f_z = 0.3 \mu\text{m}/\text{tooth}$. Apart from the cutting speed and feed, a considerable reduction in surface roughness by increasing the axial depth of cut from 10 μm to 50 μm was also reported by Bajpai et al. [99] in slot milling. Moreover, they observed that the tool diameter increase, from 300 μm to 500 μm , generated a rougher surface, approximately 15%. However, its influence was not as high as the effect of process parameters on surface roughness. In micro-milling of Ti6Al4V using a ball-end tool, an increase in axial depth of cut and feed per tooth also produced a smoother surface due to the low ploughing and rubbing effect [90]. The milling strategy is another factor that influences surface quality. Ahmadi et al. [101] reported the different surface textures based on the Electron Backscatter Diffraction (EBSD) analysis. Higher compressive deformation in down-milling was observed compared to the up-milling. In [93], it was also mentioned that the milling strategy could affect the surface quality. On the side walls, down milling indicated a smooth surface, whereas up milling generated a poor surface. However, Wang et al. [102] observed that the up-milling strategy produced better surface quality than the down-milling strategy. They also analyzed the effect of progressive tool wear on the machined surface in micro-milling of Ti6Al4V. Feed marks, material debris, plastic side flow, and material smears were detected as main surface defects. Material debris and plastic side flow mainly appeared by the progress of tool wear. Oliaei and Karpat [78] reported that the surface quality was also influenced by low tool stiffness. Therefore, the cutting forces during the micro-machining process affect the quality of the machined part [103,104].

Unlike conventional machining, surface roughness prediction in micro-machining is complicated due to the effects of minimum chip thickness, tool nose radius, and microstructures [105]. At the micro-scale, the material properties become inhomogeneous, affecting the process's stability and surface roughness [106]. In detail, the inhomogeneity of material properties and consequently variation in micro-hardness at micro-scale level cause the cutting tool vibration followed by irregular surface roughness. The finer grain sizes of the workpiece material led to slightly better surface quality for Ti6Al4V [101]. Zhao et al. [107] also reported that the enhancement of the surface roughness was caused by decreasing the grain size from 52 μm to 12 μm due to the restriction of the crack generation in ultra-precision of pure titanium. Different microstructures of titanium alloy can also affect the machined surface. Among equiaxial, bimodal, and martensitic microstructures, lower surface roughness for lamellar martensitic microstructure with the highest micro-hardness was reported [108]. Since the mechanical properties of Ti6Al4V are greatly influenced by different compositions of the phases, a change in the composition may be accompanied by variation in the machinability. In this regard, a dual-phase titanium alloy ($\alpha + \beta$) showed lower surface roughness than that for α titanium [109].

2.4.4 Burr formation

One of the critical machining challenges in the micro-milling is the burr formation. Generally, a relatively large cutting edge radius and ploughing effect, the significant tool run-out [110,111], chatter [46,112,113], and the unfavorable type and position of the micro-particles of the workpiece [114,115] may contribute to the burr formation.

According to [116], different types of burr are observable in the face milling process, such as the knife-type burr, the curl-type burr, the wave-type burr, the edge breakout, and the secondary burr. Particularly regarding the micro-milling process, the mechanism of the burr formation can be classified into Poisson, tear, and rollover. The compression of the material due to the ploughing effect followed by plastically bulging the material to the sides is the Poisson mechanism, as illustrated in Figure 2.5a. Figure 2.5b indicates the tearing of the uncut material rather than completely removing it from the workpiece. According to Figure 2.5c, the material was bent at the edges instead of removed from the workpiece, which is named as rollover mechanism.

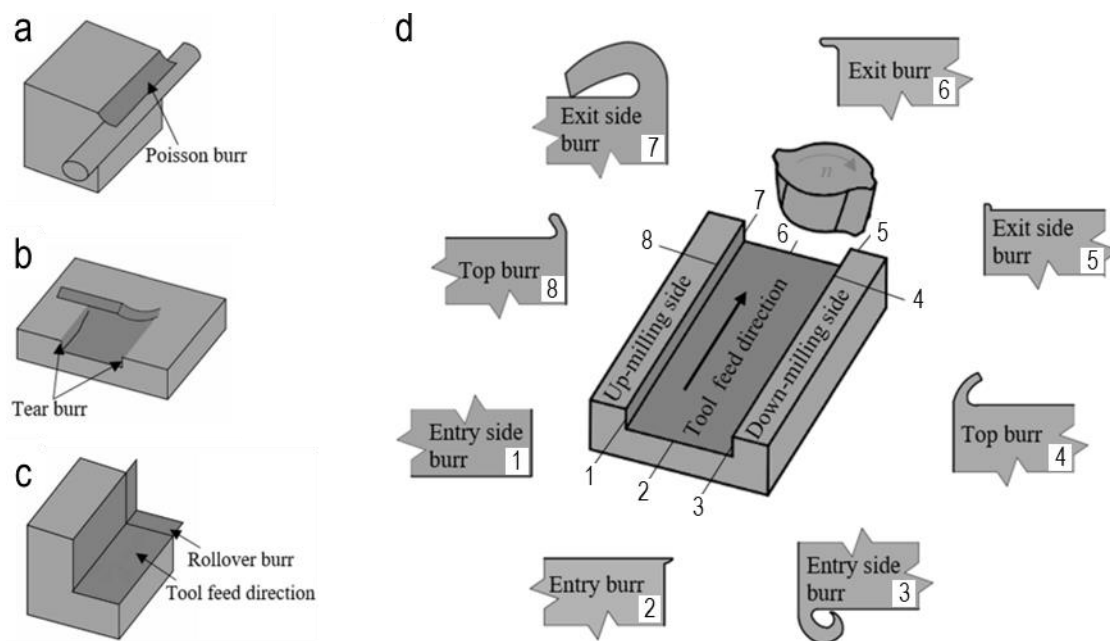


Figure 2.5: different burr formation mechanisms: a) Poisson, b) Tear, c) Rollover, d) different burr types in the slot-milling process [61].

Figure 2.5d indicates different types of burrs in the slot-milling process. Due to the process kinematic in slot milling, two types of the milling strategy, up- and -down milling, can be observed. Accordingly, a variation in the burr size for these two strategies can be detected. Moreover, the size and the form of the burr vary at different locations, Entry, middle, and Exit sides of the slot. Bissacco et al. [60] reported that exit side burrs were significantly larger than the entrance side burrs. They also explained that the top burr is generated by a very high biaxial compressive stress pushing the material toward the free surface. Bajpai et al. [99] detected a significant top burr, in height and width, at the down-milling side of the slot compared to the up-milling side in the case of 10000 rpm using a micro-mill tool with a diameter of 500 μm . At the down-milling side of the entry, the burr formation was also more pronounced due to the pile-up of the burrs generated at the multiple times of tool engagement. Additionally, the exiting the material may undergo plastic hinging at the

free surface, at the down-milling side of the entry, while entering the tool in every rotation get the burrs away from the edge, followed by little burr formation at the up-milling side of the entry. A very small burr was also observed at the slot bottom. The exit burr at the up-milling side was larger due to the plastic hinging of the free surface at the exit of the tool. In the study of the burr formation in the micro-ball end milling of Ti6Al4V, Chen et al. [117] also observed that the top burr height at down milling side was always higher than that for the up-milling side for axial depth of cut more than 15 μm . Schueler et al. [73] reported the wavy type of top burr in the slot-milling of Ti6Al4V (see Figure 2.6). Accordingly, the bottom side of the burr indicates a wavy form of plastically deformed material, and the top of the burr seems pretty similar to the adhesive particles. In the slot-milling of Ti-6Al-7Nb, a similar wave top burr formed on both sides of the slot, independent of the milling strategy ,up- and down milling.

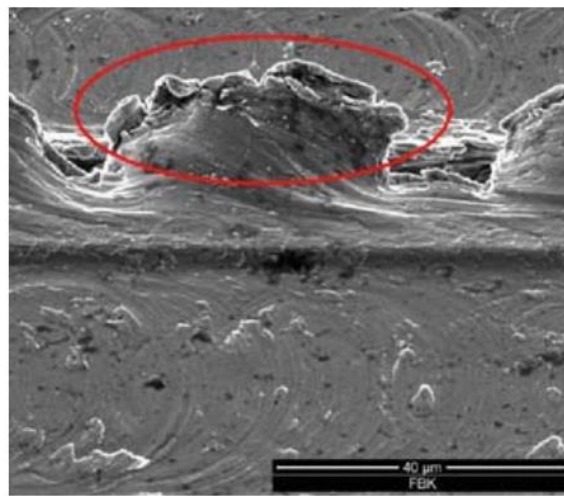


Figure 2.6: Wave-burr formation in the slot-milling of Ti6Al4V [73].

Several investigations have been devoted to studying the influence of different process parameters on the burr formation in the micro-milling of titanium alloys. In the study of Thepsonthi and Özel [72] regarding the multi-objective process optimization using a cBN coated micro-mill tool, the top burr width was highly influenced by feed per tooth compared to other process parameters of coating, spindle speed, and axial depth of cut. Higher feeds resulted in lower burr formation. Kim et al. [118] also found that the feed per tooth is a more dominant factor than spindle speed on the burr formation in the micro-end milling of titanium alloy. The largest top burr width was observed at 1 $\mu\text{m}/\text{tooth}$ at different spindle speeds. An increase in a feed from 1 $\mu\text{m}/\text{tooth}$ to 5 $\mu\text{m}/\text{tooth}$ led to decreasing the burr width. In [95], it was also mentioned that the feed significantly influenced burr formation. An increase in feed decreased the burr width for uncoated and cBN-coated micro-tools. Regarding the influence of cutting speed on the burr formation, Bajpai et al. [99] detected a different behavior in the top burr between two rotational speeds of 10000 rpm and 90000 rpm using a micro-mill tool with a diameter of 500 μm . At 90000 rpm, a smaller burr in the down-milling and a larger burr in the up-milling were detected, which is opposite to the observation for 10000 rpm. In detail, there were thin long top burrs in the up-milling region. A change in the burr formation mechanism may be associated with the low thermal conductivity of Ti6Al4V and, consequently, the formation of an adiabatic shear band caused by heat accumulation at high speeds. In fact, these burrs at high

speed are originated from segmented chips due to the adiabatic shear bands. Moreover, a smaller burr size, at the down-and-up milling side, was observed at 90000 rpm compared to that at 10000 rpm at the exit side of the slot. Kumar et al. [119] reported the influence of cutting speed on the burr height in the study of burr height prediction of Ti6Al4V in high-speed micro-milling. Higher cutting speeds resulted in lower burr heights. In detail, a 90 % reduction of the burr height was achieved by increasing the cutting speed from 79 m/min to 314 m/min. The sensitivity of the burr height to changing the process parameters was also observed by Bajpai et al. [99]. They also reported that tool diameter and the number of flutes did not influence the burr size. The burr width was not considerably influenced by changing the rotational cutting speed from 10000 rpm to 90000 rpm. Moreover, a change in feed rate from 1 mm/s to 5 mm/s did not influence the burr width. However, the burr height was considerably influenced by changing rotational speed and feed rate. An increase in depth of cut from 10 μm to 50 μm indicated a countable rise in height and width of the burr. The application of the coating resulted in an increasing the cutting edge radius that may negatively affect the cutting tool performance. In detail, a higher edge radius leads to more ratio of edge radius to the chip thickness followed by more ploughing effect and burr formation. Thepsonthi and Özel [72] reported that the application of coating slightly increased the top burr width. However, no presence of coating may lead to considerable tool wear and more rounding of the cutting edge, and ultimately higher edge radius to chip thickness ratio accompanied by the dominance of ploughing and more burr formation. Attanasio et al. [92] studied the influence of microstructure on burr formation. Among different microstructures, the smallest burr size, concerning width and height values, was reported for bimodal, which has the highest micro-hardness value compared to that for microstructures of Milled annealed, fully equiaxed, and fully lamellar.

2.4.5 Tool wear

Tool wear in the micro-machining of titanium alloys is a significant barrier. Several investigations have been carried out to study the different wear forms and wear mechanisms. Enlargement of the cutting-edge radius was reported by Vipidas and Mathew [100] as one of the wear modes in micro-milling Ti6Al4V, using TiAlN coated tungsten carbide micro-mill tool under dry machining conditions. Coating delamination and flaking of tool material from the flank surface at the beginning phase of the machining was detected as two other wear forms at 0.3 $\mu\text{m}/\text{tooth}$ where the ploughing phenomenon is dominant. The adhesive wear was reported as a significant wear mechanism. Ziberov et al. [79] detected that the tool wear was mainly concentrated on the tool tip, and the cutting edge rounding increased for the uncoated tungsten carbide micro mill tools in machining Ti6Al4V under dry conditions. Zheng et al. [120] classified wear modes into progressive normal wear failure and abnormal wear failure in micro-milling of Ti6Al4V with tungsten carbide tool. Abrasion marks, material adhesion, built-up edges (BUE), and micro-blade collapse were detected as progressive normal wear failure. In case of abnormal wear failure, severe plastic deformation, blade collapse, catastrophic fracture, and delamination of the cutting edge were reported. Regarding the wear mechanism, adhesive wear was observed in the whole cutting process and played a crucial role. Colpani et al. [121] conducted wear analysis in the micro-milling of titanium alloy for tools with two cutting edges made by coated tungsten carbide. According to the

results, the graphs describing the evolution of the flank wear in the micro-milling process include sections of decreasing, constant, and increasing slope of the tool wear curve, similar to macro-machining. Dadgari et al. [122] reported non-uniform flank wear as the dominant wear mode in the micro-milling of Ti6Al4V using an uncoated tungsten carbide tool. The initial rapid wear at the tool tip, non-uniform progress of wear on the cutting face, and eventually rapid abrasive wear followed by tool diameter reduction were categorized as three stages of the tool wear pattern. Kim et al. [118] conducted qualitative analysis on the tool wear using the optical microscope for Two flat carbide micro end-mills (tool diameter: 500 μm) at two different feeds and a constant rotational speed of 30000 rpm. After ten machining slots, in the case of feed (1 $\mu\text{m}/\text{tooth}$), blunt cutting edge and considerable tool wear were observed due to the ploughing. Slight wear was detected for higher feed (5 $\mu\text{m}/\text{tooth}$), and relatively sharp cutting remained.

2.5 Machining of additively manufactured parts

The inhomogeneous microstructures of AM parts and additively manufactured complex geometries complicate the processing of AM materials using different machining operations. Therefore, investigation regarding the machinability of AM parts is significantly crucial. Alexander et al. [123] reported a degree of anisotropy in terms of microstructure and material properties between the horizontal and vertical planes for Ti6Al4V alloy produced by EBM. The role of inhomogeneous microstructure and, consequently, variation in mechanical properties is much more pronounced in the case of micro-machining, where the process is significantly sensitive to the microstructure variations caused by different AM process parameters and varied thermal gradient and cooling rates at different positions of the fabricating parts. In the following, different studies regarding the machinability of AM titanium alloys as one of the frequently used working materials in AM technology have been summarized for milling and micro-milling processes.

In the milling process, Huang et al. [124] compared additively manufactured and wrought Ti6Al4V in the finish slot milling process. AM parts showed lower ductility and superior strength, resulting in a finer surface finish. This finding also agrees with the results of Polishetty et al. [125] concerning the lower surface roughness of SLM parts compared to the wrought material in the turning process. Bonaiti et al. [126] investigated the micro-machinability of Ti6Al4V produced by DED. A large burr formation was observed on the top of the down milling of AM parts, while less burr was generated for standard materials. Furthermore, the AM parts induced lower cutting forces than the standard materials despite their higher hardness. The lower surface roughness and cutting forces of AM parts compared to the conventionally produced samples were also reported by De Oliveira Campos et al. [127] who compared the machining of Ti6Al4V produced by SLM and casting. A finer acicular martensite structure of SLM parts led to higher hardness and strength, followed by more brittle behavior and lower stiffness. The SLM parts exhibited lower cutting forces (on average, 9.3% lower) and tool wear despite their higher hardness (16 % higher). Moreover, lower ductility and higher hardness leading to less plastic flow during the cutting generated lower surface roughness of SLM parts. Less tool wear and minimum change in the cutting edge radius during the machining of SLM parts led to lower burr formation than cast materials. The observation of De Oliveira

Campos et al. [127] and Bonaiti et al. [126] in the micro-milling of AM titanium alloys regarding the cutting forces oppose the reported results by other researchers in the macro-milling, macro-drilling, macro-and micro-turning operations [124,125,128–130]. The micro-machinability of the Ti6Al4V alloy produced by two AM processes, EBM and SLM, was analyzed by Rysava and Bruschi [131] concerning burr formation, surface integrity, and cutting tool condition. SLM parts exhibited lower surface roughness than that of EBM parts. Regardless of the manufacturing process, the adhered material to the tool was observed and no microstructural alternation was detected after machining. Regarding the burr formation for both AM parts, feed per tooth was found as a decisive factor compared to the cutting speed. Rysava et al. [132] investigated the influence of micro-tool geometries on the machinability of Ti6Al4V manufactured by SLM. Two uncoated tungsten carbide cutting tools were utilized with the same diameter of 300 μm : one with two flutes and another with four flutes. Using the tool with two flutes produced the best surface quality. It was mentioned that the probability of vibration increases with four fluted tools at the lowest value of cutting speed. The tool with four flutes generated less burr. The wear occurred for both tools through the adhesion of the material to the edges of the tools and the BUE formation. The metallic skeleton and many pores in the micro/meso/macro scale formed porous metallic material. Like the microstructure, different porous contributes to a variation in the material deformation and, finally, the generated surface. Oyelola et al. [133] also mentioned that the porosity and the irregular deposition caused by asymmetrical cooling in the AM process affect the machining behavior and surface integrity of the final machined surface. Varghese and Mujumdar [134] studied the influence of porous density on the surface roughness in the micro-end milling of Ti6Al4V. A reduction in surface roughness through increasing initial porosity from 30 % to 46 % at the larger depth of cut was observed. The closure of the pores after machining was mentioned as a reason for surface roughness reduction.

2.6 Laser-assisted machining

Laser Assisted Machining (LAM) is a promising method for enhancing the machinability of difficult-to-cut materials such as hardened steel, titanium alloys, and nickel-based superalloys. In this regard, the application of LAM can be divided into two main groups: material pre-heating and material removal before the cutting.

Figure 2.7a indicates how the material's strength changes with temperature. Accordingly, increasing temperature results in reducing the material strength. As illustrated in Figure 2.7b, the laser beam with the capability of guiding and focusing into a tiny spot generates intensive heat in a narrow region. Therefore, the workpiece is locally preheated using a focused laser beam ahead of the cutting zone that eases the cutting of the material due to the degradation of mechanical properties through material softening.

The contribution of laser to the total generated heat during the machining process is important and has been considered by several researchers [135–137]. In this regard, finding the optimum temperature for the material that must be cut is one of the challenges of this process. As reported in [138,139], the appropriate control of laser power, spot size, and scan speed leads to sufficient reduction of material strength, the resultant cutting forces, and less tool deflection.

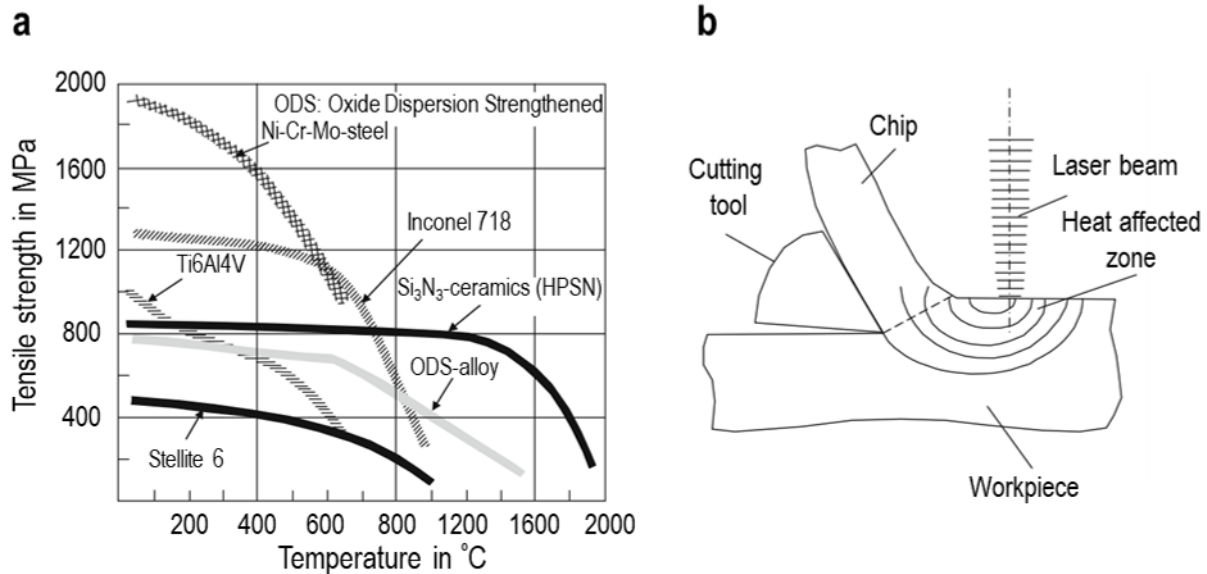


Figure 2.7: a) effect of temperature on tensile strength of different difficult-to-materials, b) illustration of laser-assisted machining [140].

Preheating the workpiece area in front of the tool, followed by decreasing the material strength and the material softening along the cutting path, is the common method in LAM. Despite the improving machinability through this method, the process control to prevent undesired alternation of material properties and HAZ for the machined surface is a challenging task that limits the application of common LAM [5]. Moreover, the application of LAM is only limited to dry conditions because of utilizing a focused laser beam ahead of the tool during the process [7]. In the investigation regarding evaluating the most common cutting tools with different coating types, Dargusch et al. [141] reported a higher tool wear rate for all cutting tools using LAM. Moreover, the dry machining process resulted in BUE that considerably increased in the case of LAM. Bermingham et al. [142] also reported that the dominant mechanism of tool wear is diffusion in Thermally Assisted Machining (TAM), which leads to the pulling out of a large section of tool material by removing BUE. Moreover, Xia et al. [143] explained that the short distance between the focused laser beam and the tool in the micro-milling process leads to tooling thermal expansion accompanied by changing the actual depth of cut and, consequently, a reduction of accuracy.

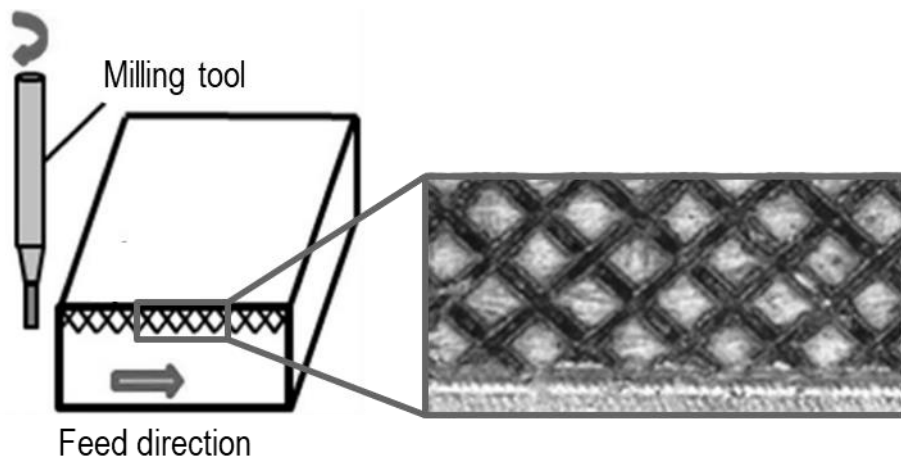


Figure 2.8: Structuring the workpiece before the micro-milling of austenitic stainless steel X5CrNi18-10 [144].

To tackle this issue, laser material removal is introduced as another LAM's application. The material is removed prior to machining by structuring the workpiece surface. Figure 2.8 indicates the structured workpiece before micro-milling austenitic stainless steel. As a result, subsequent machining requires less material to be removed. Furthermore, the laser-induced alteration of materials can potentially ease the material removal process during machining operations.

2.6.1 Laser-assisted micro-machining

In the micro-milling process, several issues may arise. The probability of tool deflection and the risk of tool breakage cannot be overestimated at higher uncut chip thicknesses. By reducing the uncut chip thicknesses to solve this issue, the considerable ploughing associated with the size effect can deteriorate the surface quality. LAM can be used as a promising method to tackle the mentioned issues in micro-machining difficult-to-cut materials. In the following, the investigations have been presented regarding applying LAM in the micro-machining process.

Several studies have been carried out to evaluate the application of laser pre-heating and, consequently, material softening in enhancing the machinability of difficult-to-cut material in the micro-machining process. Singh and Melkote [145] introduced the Laser-Assisted Micro-Machining (LAMM) method in the micro-grooving process of H-13 mold steel. LAMM exhibited a 17 % reduction in the thrust force due to thermal softening. However, a 36% increase in surface roughness was observed. A maximum reduction of 69 % for resultant peak forces was reported by Kumar and Melkote [146] using LAMM in micro-end milling of a hardened tool steel (A2 tool steel with 62 HRC). Furthermore, tool wear reduction and process efficiency enhancement by reducing specific cutting energy were obtained. The reduced average thrust and cutting forces by about 36 % and 39 %, respectively, for aluminum 6061-T6 ,and 56 % and 32 %, respectively, for steel 1018 were also observed by Jeon and Pfefferkorn [139] in the micro-end milling process. As reported, the reduction of specific cutting energy, 39 % and 32 % for Aluminum 6061-T6 and steel 1018, respectively, allows a significant increase in feed rate and enhances productivity. Applying LAMM by Shelton and Shin [147] in a long-time experiment for the slotting operation of AISI 316 indicated a 75 % reduction of the root mean square of Acoustic Emission AE. Moreover, the AE signal in LAMM increased approximately four times less than that for the conventional micro-milling, followed by less cutting forces, less tool wear, less tool deflection and vibration, and longer tool life. As a result, a finer surface, up to 37 % reduction of surface parameter Ra, using LAMM was observed. In the case of Ti6Al4V, a reduction in the AE signal was reported, while the surface roughness increased using LAMM. Shelton and Shin [147] highlighted the LAMM's great potential in reducing considerable burr formation in the side cutting of Inconel 718 and Ti6Al4V. Kim et al. [148] reported the fabrication of microchannel without cracks for borosilicate glass in the micro-milling process using CO₂ laser heating. The surface roughness and cutting forces were reduced by laser heating. An instantly heating of a local area with lower laser power, enhancement of MRR, any byproducts around the channel after the process, and consequently no post-processing were some of the mentioned advantages of using CO₂ laser heating. However, relatively high tool wear, an increase in flank wear, was reported. In micro-milling of A2 tool

steel (62 HRC), Kumar et al. [149] detected that the wear of tool coating in the conventional micro-machining was higher than that in LAMM.

The application of LAM for removing the material before machining through structuring the workpiece surface has also gained attention. Kadivar et al. [144] utilized an ultra-short pulse laser (USPL) to structure the workpiece surface, Austenitic stainless steel X5CrNi18-10, before the micro-milling process. The application of this method led to a reduction of the normal and tangential forces by 70 % and 50 %, respectively. Hao et al. [150] also applied the nanosecond laser micro-milling to fabricate an S-shaped high-aspect ratio micro-groove on copper. Subsequently, less excess material was removed by the micro-milling process, followed by improvement of surface roughness, low tool wear, and low burr formation. The application of laser structuring of the workpiece before the machining has not been limited to the micro-milling process. A reduction of normal and tangential grinding forces, 64 and 78 %, respectively, in grinding of silicon nitride (Si_3N_4) using structuring the workpiece by USPL was also reported by Azarhoushang et al. [151]. They have structured the workpiece with two patterns, parallel to the grinding direction and normal to the grinding direction. Besides considerable force reduction for both patterns, surface roughness has been slightly improved compared to conventional grinding. In addition to material removal before the grinding process, laser-induced damage was mentioned as another reason for force reduction. Figure 2.9 indicates the neighbor cracks around the generated laser cut line. An increase in laser input energy led to more material removal and crack propagation that eased the material removal in the grinding process.

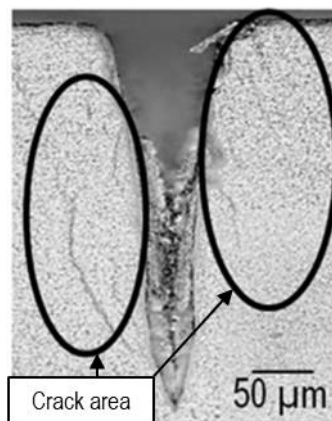


Figure 2.9: Induced laser cracks around the laser cut line for silicon nitride Si_3N_4 [151].

The application of laser pre-structuring the workpiece before the micro-grinding of Si_3N_4 was evaluated by Kadivar et al. [152]. The workpiece surface was structured using USPL. Structuring of the workpiece considerably reduced the grinding forces. 30 % structuring of the workpiece surface caused a 40 % reduction in grinding forces. Regarding part accuracy, the actual depth of cut equals the nominal depth of cut using the laser-assisted micro-grinding process, while the actual depth of cut for conventional micro-grinding was 30 % lower than the nominal depth of cut. Azarhoushang et al. [7] studied the influence of structuring on the grinding of the silicon nitride process. Accordingly, the part structuring using nano- and picosecond laser radiations before the grinding of silicon nitride reduced specific cutting energy up to 55 %. It was revealed in the single-grain test that the specific cutting energy

was mainly reduced by the lateral cracks induced by laser radiation. Additionally, the axial cracks' propagation can be minimized by the laser-assisted grinding process (see Figure 2.10a and Figure 2.10b). As reported, the grinding of silicon nitride could be carried out with the lowest specific cutting energy while the workpiece surface was 5 % laser structured. Paknejad et al. [153] studied the influence of laser structuring on single diamond grit scratching of silicon nitride. A significant reduction in normal, up to 89%, and tangential, up to 82%, scratching forces was reported. At different material removal volumes, the laser-structured surface exhibited constant specific cutting energy that was much lower than that of non-structured parts. Moreover, the depth ratio, as a degree of difference in maximum chip thickness between theoretical and experimental values, for the laser-structured surface was considerably lower than that for the non-structured part. Figure 2.10c indicates the effect of laser-induced wall through structuring on crack propagation. The presence of a structured surface led to intermittent cutting, followed by considerable structural damage and efficient chip formation (as an example, see the dashed green rectangle in Figure 2.10c).

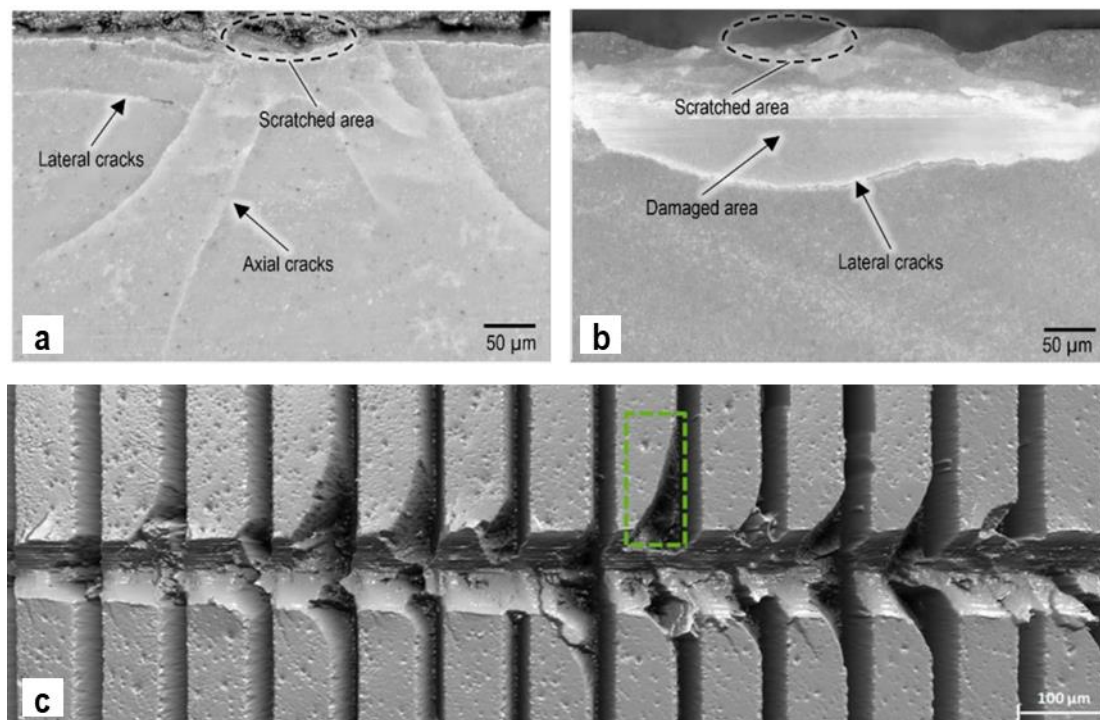


Figure 2.10: a) cross-section of non-structured workpiece, b) cross-section of structured workpiece after the single grain test, c) structural damage in single diamond grit scratching of silicon nitride [7,153].

2.7 Laser material processing

The laser-material interaction using USPL radiation is divided into several research areas, such as the mechanism of free carrier generation, the energy transfer from free carriers to the lattice, the ablation mechanisms for different materials, and the ablation quality. According to the application of USPL in pre-structuring the workpiece to assist the subsequent machining process, mentioned in the previous section, the fundamentals regarding the material removal in USPLs and the interaction between laser and matter in two main topics of ablation threshold and surface morphology for the titanium alloy have been presented in the following.

2.7.1 Ultra short pulse lasers and ablation

The interaction between laser and material shows a difference between USPLs and other laser types, continuous and short-pulsed lasers. The main reason for this difference is the laser irradiation time as a pulse duration, determining the dissipation of laser energy into the target material. There is a distinctive difference in laser absorption between different materials, e.g., Metals, Insulators and semiconductors, dielectric and ceramics, optically transparent materials, and polymers [154]. Metals have enough free electrons in the conduction band. In Metals, the absorption is dominated by free electrons. They are considerably heated to a high temperature due to their low heat capacity, whereas the lattice system is at ambient temperature. This results in a highly non-equilibrium condition between electron and lattice temperatures. After a pulse duration, the energy is transferred from high-temperature electrons to the lattice system. In detail, a photon is absorbed by the lattice's electrons, followed by a rise in their kinetic energy. Afterward, the electron-electron and electron-phonon interactions transform the kinetic energy into thermal energy. Moreover, the heated electrons explode away from the subsurface, and the parent ions are pulled out of the lattice system via electrostatic attraction [155], resulting in material removal.

For USPLs, two regimes of the ablation can be determined according to the investigation of Nolte et al. [156], who have worked on the ablation of a polycrystalline 1-mm thick copper foil using femto- and picosecond lasers. According to their investigation, the ablation depth per pulse, or ablation rate, is dominated by the optical laser penetration depth for low laser fluences. In contrast, thermal penetration depth plays a crucial role in high laser fluences. Moreover, it was reported that the ablation rate at high laser fluences is more significant than that at low laser fluences. Several investigations have been carried out to determine the ablation threshold. Mannion et al. [157] reported 0.1021 J/cm^2 as an ablation threshold with respect to the diameter of the ablated crater for titanium in multiple pulse ablation, pulse number $N_p = 100$, using an ultrafast laser with a pulse duration of 150 fs. The linear dependency between the crater's diameter and the laser fluence was observed. Based on the ablation per pulse, or ablation depth, two ablation regimes were detected. The corresponding ablation thresholds were 0.0723 J/cm^2 and 1.4082 J/cm^2 for low and high ablation regimes, respectively. Kumar et al. [155] also experimentally determined threshold ablation fluences of 0.19 J/cm^2 and 1.38 J/cm^2 for Ti6Al4V based on measured crater diameter and depth, respectively. Zheng et al. [158] determined the threshold value of 0.109 J/cm^2 based on the crater's diameter in multiple pulse micromachining of titanium alloy Ti6Al4V using a picosecond laser and $N_p = 2000$. The obtained value by Zheng et al. [158], equals 0.109 J/cm^2 , has a slight difference from 0.1021 J/cm^2 reported by Mannion et al. [157]. Cheng et al. [159] studied a single pulse ablation threshold for titanium alloy (Ti6Al4V) using a picosecond laser. They reported an ablation threshold value of 0.24 J/cm^2 that differs considerably from the reported one by Mannion et al. [157], who studied multiple pulse ablation. Mannion et al. [160] also reported $0.28 \pm 0.02 \text{ J/cm}^2$ as an ablation threshold for a single pulse that is approximately the same as the value reported by Cheng et al. [159]. Moreover, they studied the influence of damage accumulation on the ablation threshold by a laser with a pulse duration of 150 fs. They measured the ablation threshold for 5, 10, 15, and 20 laser pulses at

different laser fluences of 0.5, 1.53, and 4.32 J/cm². A reduction in the ablation threshold by increasing pulses was reported. Therefore, the ablation threshold depends on the pulse numbers. Kong and Wang [161] reported the ablation threshold of 0.27 J/cm², 0.18J/cm², and 0.21 J/cm² for Ti6Al4V in a single pulse, 50 pulses, and 75 pulses, respectively. For pulse numbers ranging from 100 to 5000, Yu et al. [162] also reported a threshold value range of 0.198-0.096 J/cm² for TC4 titanium alloy using a picosecond laser.

2.7.2 Surface morphology in laser-titanium alloys interaction

The laser incident on the material surface leads to different surface morphologies. Laser-Induced Periodic Surface Structures (LIPSS), or ripple pattern, is a frequent surface morphology among USPLs. Figure 2.11a indicates the ripple structure under laser irradiation. Many investigations have been carried out to study the interaction between USPL and the material concerning surface morphology. In this regard, Liu et al. [163] reported three types of structures, ripple, microgrooves, and rings, in studying Femtosecond-Induced Periodical Surface Structures (FIPSS) on titanium plates. They mentioned pulse number and laser fluence as two decisive factors leading to the generation of different surface morphologies. Based on the observation, the ripple structures were detected at all ranges of applied laser parameters. The ripple structure was also reported by Kong and Wang [161], who studied an ablated crater on Ti6Al4V with pulse numbers 50 using picosecond lasers. They reported the elimination of ripple structures by increasing laser fluences.

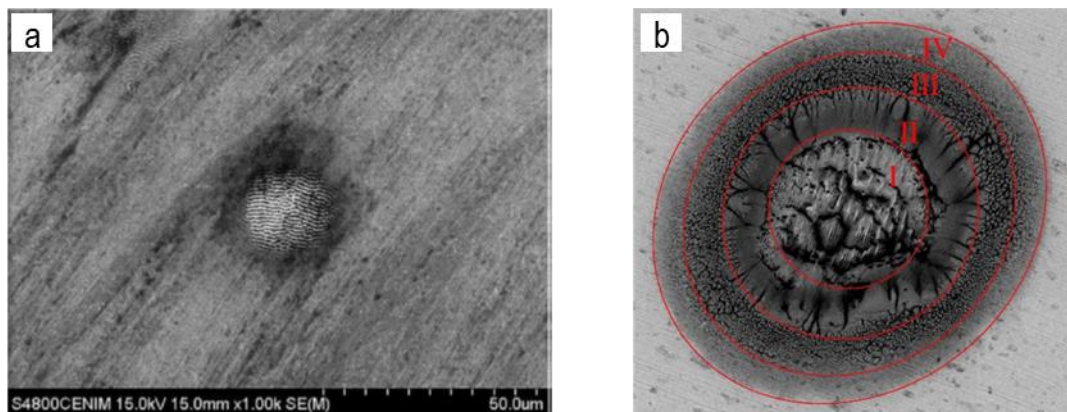


Figure 2.11: a) SEM image of ripple pattern at 1 μ J pulse energy and 10 pulses under picosecond laser irradiation for Ti6Al4V [164], b) Different surface morphologies throughout the laser beam at multiple-pulse picosecond laser drilling with laser fluence of 2.74 J/cm², 2000 pulses [162].

Kumar et al. [155] observed the ripple pattern structure without considerable surface damage at a low laser fluence of 0.84 J/cm² in single-pulse laser ablation of Ti6Al4V using a laser with a pulse duration of 100 fs. At a high laser fluence of 8.4 J/cm², significant surface damage occurred due to melting and vaporization. The energy distribution of the laser beam following the Gaussian distribution contributes to different ablation regions accompanied by various ablation morphologies. Yu et al. [162] reported four regions, as shown in Figure 2.11b, in the drilling of titanium alloy using a picosecond laser with 2000 pulses and a laser fluence of 2.74 J/cm². The huge amount of laser energy in the laser spot center (region 1) led to a considerable liquid phase and melt expulsion. Region 2 consists of the condensed and deposited

removed material, and region 3 is characterized by a well-distributed tiny microstructure. Slight heat-affected morphology was observed in region 4.

2.8 Modelling and simulation of laser-assisted machining

Many researchers have reported the improvement of machinability using LAM, as mentioned in section 2.6. However, the issues of controlling the process to prevent undesired material changes and HAZ after machining exhibit a significant challenge. Therefore, the role of simulating this process is highlighted to find the optimum process parameters. Most of the modellings regarding LAM have been primarily devoted to predicting the temperature distribution and HAZ in the workpiece during laser processing [165–169]. Figure 2.12 provides the temperature field using the Finite Element (FE) model at different laser scan speeds v_L and laser powers P_L . Accordingly, increasing v_L decreases the affected depth and maximum temperature due to the reduced laser-material interaction time. Furthermore, a rise in maximum temperature can be observed by increasing the laser power P_L at constant v_L . In addition, the developed models could predict the chip morphology, chip thickness, shear angle, stress level, strain rate, and cutting forces [170–172]. Using the mechanical and thermal model developed by Ding et al. [173] for the laser-assisted micro-milling of difficult-to-cut materials, Ti6Al4V, Inconel 718, and stainless steel AISI 422, it was shown that appropriate heating of the workpiece could reduce or eliminate BUE. Due to the limitations in simulating the chip formation using FE models, such as mesh tangling and distortion for large deformation, the smoothed particle hydrodynamics (SPH) can be utilized as a mesh-free Lagrangian numerical method. In [174,175], SPH was used for predicting temperature, cutting force, and modeling chip formation.

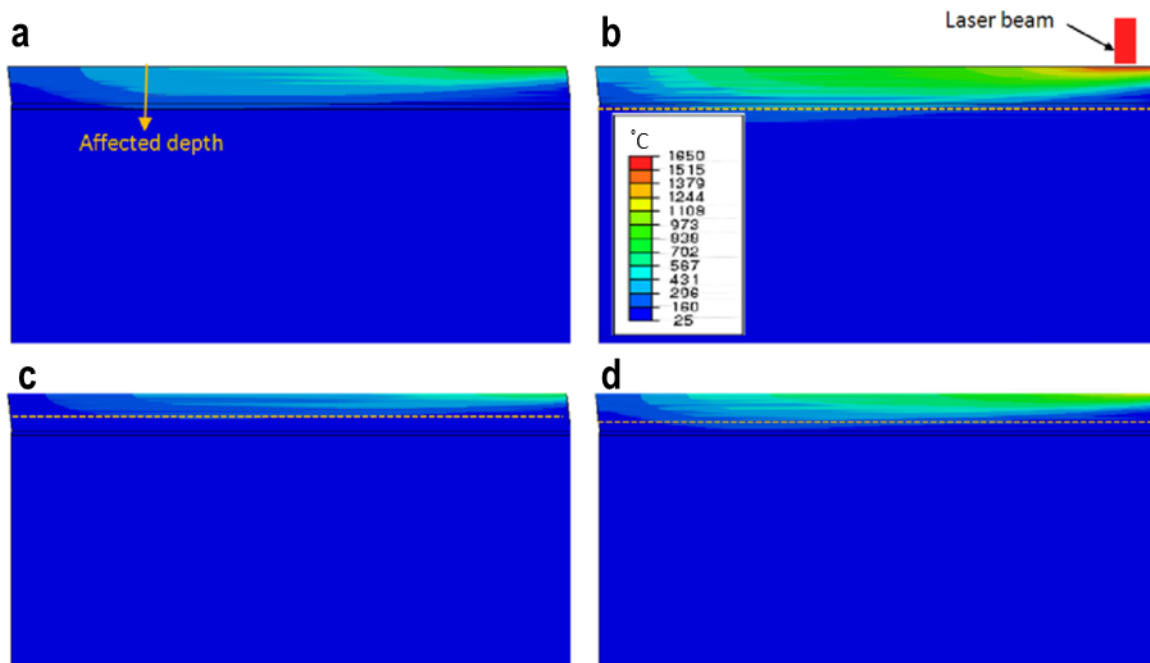


Figure 2.12: Simulation of temperature field induced by laser heating, a) $v_L=0.66$ m/s and $P_L=500$ W, b) $v_L=0.66$ m/s and $P_L=1000$ W, c) $v_L=1.33$ m/s and $P_L=500$ W, d) $v_L=1.33$ m/s and $P_L=1000$ W.

3 Objectives and approach

Additive Manufacturing (AM) technology applied to fabricate titanium alloys introduces novel microstructures, leading to alterations in their mechanical, material, and thermal characteristics compared to conventionally produced alloys. Achieving the desired surface quality, as well as precise dimensional and geometrical tolerances, in AM parts typically necessitates post-processing operations like machining. Machining titanium alloys presents several challenges. The distinctive properties of additively manufactured titanium parts introduce further complexities in their processing. Among the post-processing techniques, micro-milling emerges as a viable method for AM parts. Nevertheless, the inherent instability of micro-mill tools and the size effect phenomenon in micro-machining can pose significant complications, particularly in the context of AM titanium alloys. Hence, there is a demand for a comprehensive investigation into the micro-milling of AM titanium alloys.

Enhancing the machinability of titanium alloys can be accomplished through novel LAM as an alternative to the commonly used LAM approach due to several issues listed in Figure 3.1. By employing a laser to structure the components before machining, a reduction in the material volume that needs to be removed during the machining process is expected. This laser-based pre-structuring highlights a study concerning the interaction between the laser and the titanium alloy. Furthermore, a critical question emerges regarding the impact of laser structuring on the material removal process and its subsequent effect on uncut chip thicknesses. It is highly crucial to find out the key factors influencing the reduction in uncut chip thicknesses during machining. Additionally, a vital aspect to consider is the significance of pre-structuring titanium alloy as a difficult-to-cut material in improving machinability.

The presented study is structured around two primary research areas. Firstly, it deepens into understanding how the material properties of Additive Manufacturing (AM)-produced titanium alloys influence their machinability. Secondly, it investigates the impact of novel Laser-Assisted Machining (LAM) technique on the machining process of titanium alloys. Central to this study is the widely utilized titanium alloy, Ti6Al4V. According to the outlined objectives in Figure 3.1, this study determines its approaches across three distinct chapters.

Chapter 5 undertakes a comparative analysis between parts manufactured through Electron Beam Melting (EBM) - an AM method, and extrusion - a conventional manufacturing approach. The objective is to assess the machinability of AM-produced parts in micro-milling. Crucial machining outputs such as cutting force, specific cutting energy, surface roughness, and burr formation are analyzed.

Chapter 6 is dedicated to examining the interaction between Ultra-Short Pulsed Laser (USPL) and the material. This investigation encompasses multiple pulses, single linear laser scanning, and multiple linear laser scanning. The focal point lies in understanding the impact of laser structuring on material ablation and surface morphology.

In Chapter 7, the evaluation of a novel LAM method within the micro-milling process is under focus. The initial section 7.1 involves process modeling to understand the influence of an extensive range of process parameters on uncut chip thickness

reduction. Subsequently, Section 7.2 focuses on practical applications, encompassing the structuring of the workpiece and conducting micro-milling tests. These endeavors aim to ascertain the potential of the introduced method in improving the machinability of titanium.

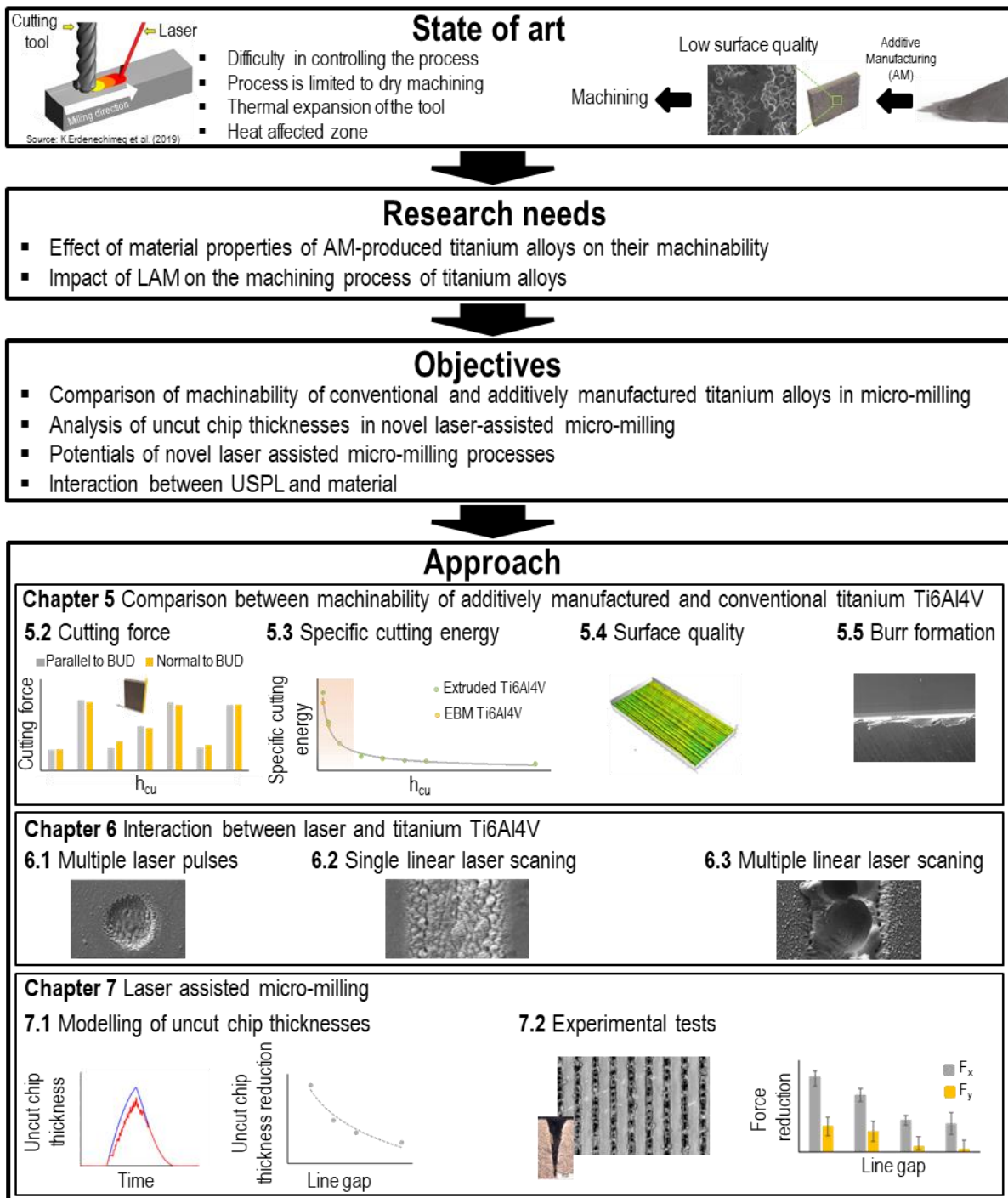


Figure 3.1: Research basis, objective, and approach of the work.

4 Experimental equipment and plan

In the following, the equipment, measurement, and analysis techniques used in this study to accomplish the mentioned goals are presented. Furthermore, the experimental design is discussed.

4.1 Experimental setup

4.1.1 Machine tool

The experimental tests in chapter 5, sections of 7.2.2 and 7.2.3, were carried out by a high-precision 5-axis CNC machining center (KERN Pyramid Nano). Hydrostatically driven X, Y, and Z axes enable the Kern Pyramid Nano to achieve the highest precision. Moreover, the hydrostatic bearing of the screw drives realizes high accelerations with excellent vibration damping. The smallest travel increments of 0.1 μm , wear-free guides and driver, friction-free movement, and high dynamic stiffness are other advantages of KERN Pyramid Nano, particularly for micro-machining. Furthermore, the axes, axes-drives, and machine frame are kept thermally stable by circulating and cooling hydraulic oil. Table 4.1 provides the specifications of the KERN Pyramid Nano.

Table 4.1: Specifications of KERN Pyramid Nano.

Linear axes	<ul style="list-style-type: none"> • Travel X/Y/Z: 500/500/400 mm • Feed rate: 25 m/min • Acceleration: up to 10 m/s²
Spindle	<ul style="list-style-type: none"> • HSK 40: 42.000 min⁻¹ 11 kW (S1) Roller bearing
Accuracies	<ul style="list-style-type: none"> • Positioning accuracy : $\leq 1,5 \mu\text{m}$ • Repeatability : $\leq 1 \mu\text{m}$
Technology	<ul style="list-style-type: none"> • Central cooling management with 5 circuits • Hydrostatic axes • 5-axis simultaneous machining • Heidenhain control TNC 640

Figure 4.1 indicates the experimental setup for the micro-milling process. The EBM and extruded Ti6Al4V samples were in a block form with a dimension of 30x20x2 mm and 30x20x10 mm, respectively, that could easily be fixed on dynamometer. In this study, the side wall of the samples was micro-milled through a down milling strategy under the wet condition, using a cutting oil (Oelheld Sinto-grind IGS 550), and the cutting forces, F_x and F_y , were measured.

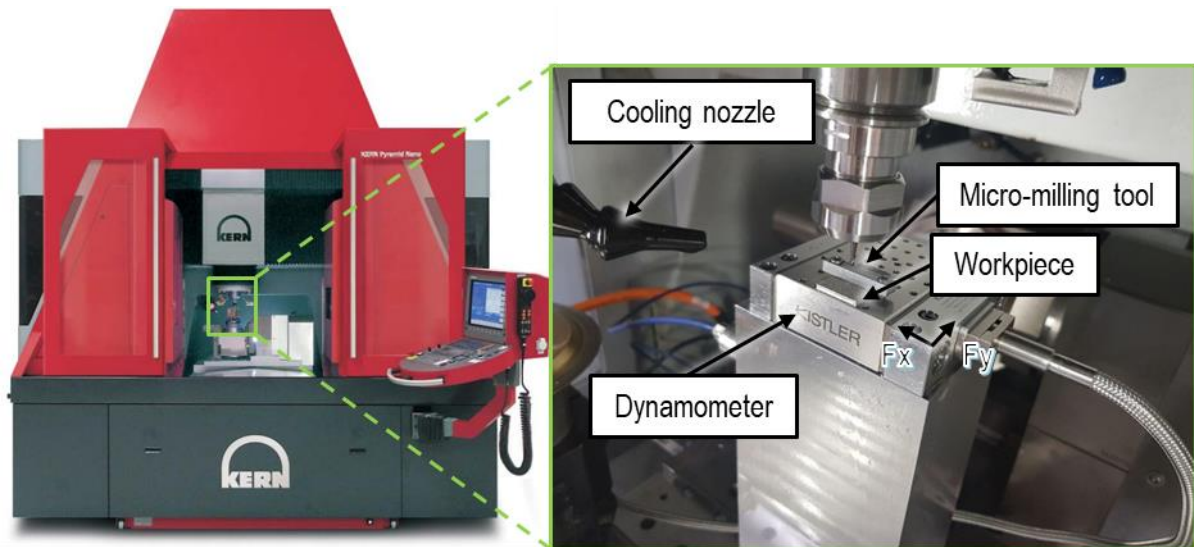


Figure 4.1: Experimental setup for the micro-milling test.

4.1.2 Laser device

The laser structuring of the parts in section 7.2.1 and the experimental tests regarding the interaction between Ultra-short pulse laser and material in chapter 6 was carried out by an ultrashort pulse Yb-YAG picosecond laser Trumf-TruMicro 5050 with the lens (LINOS F-Theta-Ronar). Table 4.2 provides the specifications of the laser device.

Table 4.2: Specifications of the picosecond pulsed laser device.

Wavelength in nm	1030
Maximum average power in W	50
Pulse width in ps	10
Maximum pulse energy in μJ	125
Repetition rate in kHz	400

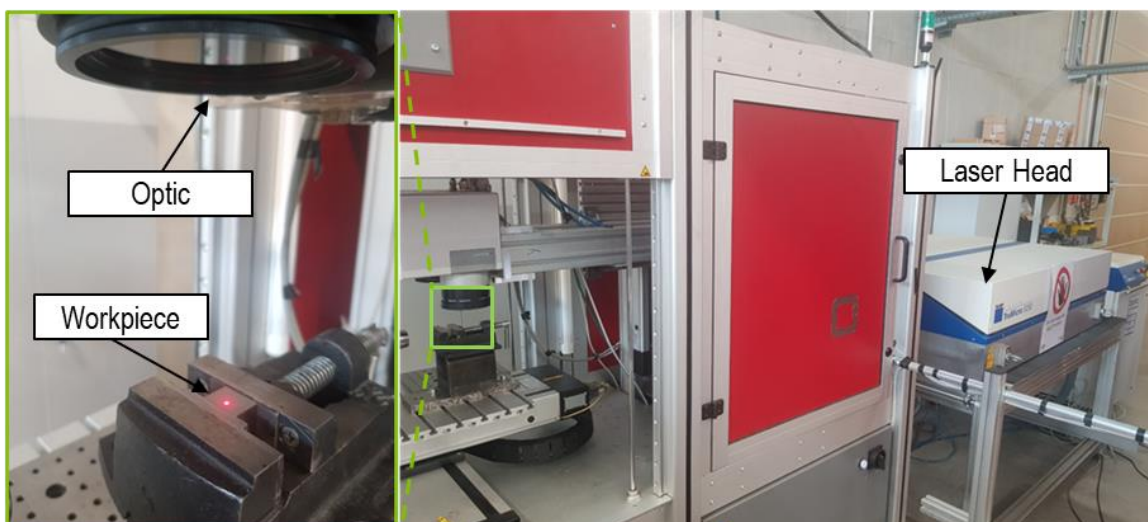


Figure 4.2: Setup for laser structuring of Ti6Al4V parts.

4.2 Workpiece materials and tool

4.2.1 Workpiece materials

The objective titanium alloy in this investigation is Ti6Al4V. The machinability of EBM made of Ti6Al4V is compared with Ti6Al4V manufactured by the extrusion process. The chemical composition and mechanical properties of Ti6Al4V for both methods, EBM and extruded ones, are provided in Table 4.3 and Table 4.4, respectively. The information was provided by manufacturers.

Table 4.3: Chemical composition of Ti6Al4V

Chemical composition (wt%) of Ti6Al4V								
	Al	V	C	Fe	O	N	H	Ti
EBM	6	4	0.03	0.1	0.15	0.01	0.003	Rest
Extrusion	5.5-6.75	3.5-4.5	≤ 0.08	≤ 0.4	≤ 0.2	≤ 0.05	≤ 0.015	Rest

According to Figure 4.3, the microstructure of the extruded Ti6Al4V is much coarser than EBM Ti6Al4V. This difference highlights the effect of the manufacturing method on the material microstructure. According to the obtained values from micro-hardness measurement, the EBM Ti6Al4V with 450 HV has a higher hardness than extruded Ti6Al4V with 350 HV.

Table 4.4: Mechanical properties of EBM and extruded Ti6Al4V.

Material	Yield strength in N/mm ²	Ultimate tensile strength in N/mm ²
EBM Ti6Al4V	950	1020
Extruded Ti6Al4V	830	895 ≤

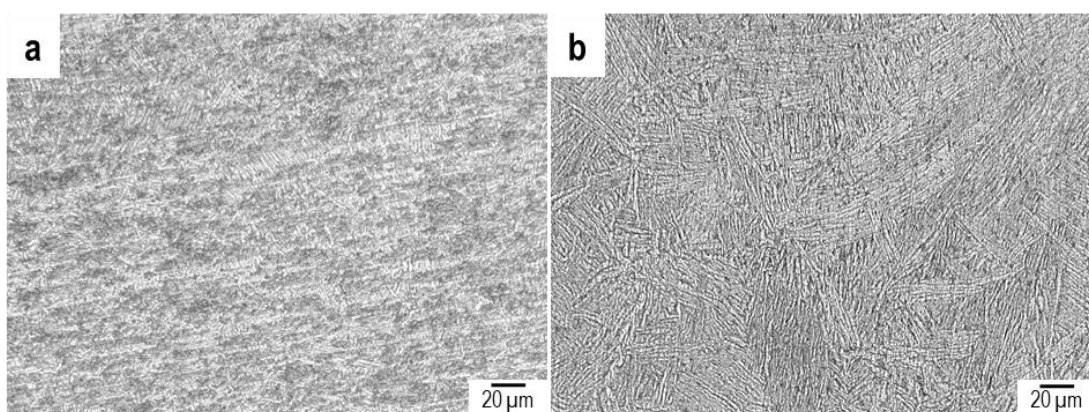


Figure 4.3: Microstructure of a) EBM Ti6Al4V, b) extruded Ti6Al4V.

4.2.2 Cutting tool

Three flutes micro-end milling tools with the same size and specification (WN 3142 R-N – made by company Gühring, with a PVD Coating (TiAlN), shaft DIN 6535-HA/HB) with 1.8 mm diameter were utilized for machining of Ti6Al4V alloy parts. Table 4.5 provides the geometrical features of the utilized cutting tools. Figure 4.4a

and Figure 4.4b indicate an SEM image of the cutting tool and the measured cutting-edge radius, respectively. The cutting-edge radius is measured from the contour obtained by averaging 20 distinct cutting-edge contours.

Table 4.5: Geometrical features of the cutting tool.

Tool diameter d_1 in mm	Shaft diameter d_2 in mm	Number of teeth	Total length l_1 in mm	Cutting edge length l_2 in mm
1.8	3	3	38	2

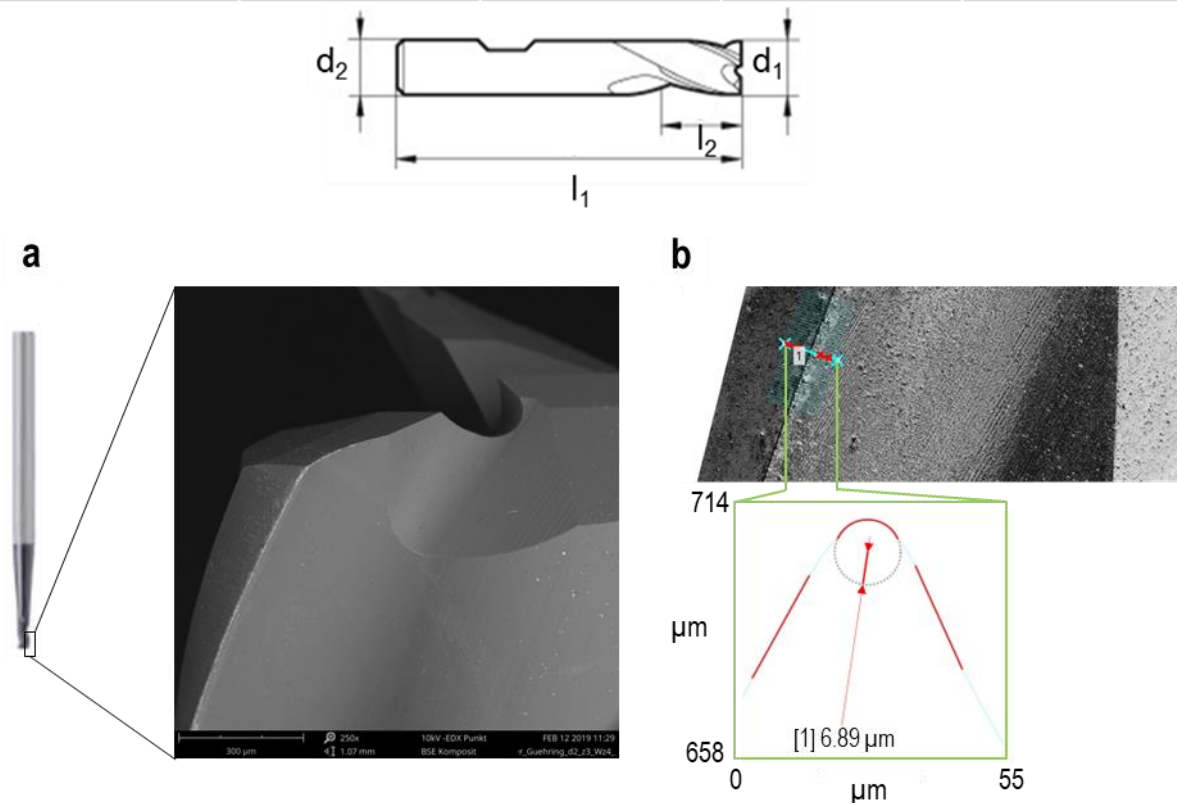


Figure 4.4: a) SEM image of cutting tool, b) cutting-edge radius.

4.3 Measurements and analysis

In the following, cutting forces measurement, surface roughness and topography analysis, tool wear and burr analysis, and material characterization techniques used in the current work are explained.

4.3.1 Cutting forces

The cutting forces were measured by a piezoelectric dynamometer (type 9256C2 from Kistler Company with Eigen frequencies 4 kHz, 4.8 kHz, and 4.6 kHz in x, y, and z directions, respectively, and the measuring area between -250 N and 250 N in all directions) with a sampling frequency of 300 kHz. Table 4.6 provides the dynamometer calibration parameters.

Table 4.6: Dynamometer calibration parameters.

Calibrated Range N	Sensitivity pC/N	Linearity $\leq \pm \%FSO$	Cross talk	
			%	%
F_x 0...250	-24.82	0.01	$F_x \rightarrow F_y$ 0.4	$F_x \rightarrow F_z$ -1.4
F_y 0...250	-12.79	0.05	$F_y \rightarrow F_x$ 0.3	$F_y \rightarrow F_z$ 0.3
F_z 0...250	-25.35	0.01	$F_z \rightarrow F_x$ 0.0	$F_z \rightarrow F_y$ 0.6

4.3.2 Surface roughness and topography

A confocal microscope (μ surf mobile plus - Nanofocus) was used in the qualitative and quantitative analysis of the machined surfaces in sections 5.4 and 7.2.3. In chapter 6, the laser ablation was also analyzed by the confocal microscope. Figure 4.5 indicates the confocal microscope and a table summarizing the information of the utilized objective.



Objective	Measuring area in $\mu\text{m} \times \mu\text{m}$	Working distance in mm	Verical resolution in nm	Lateral resolution in μm
50x	320x320	1	2	0.7

Figure 4.5: Confocal microscope.

4.3.3 Tool wear and burr analysis

In addition to the confocal microscope, an optical microscope (Keyence VHX 5000) (shown in Figure 4.6) and Scanning Electron Microscopy (SEM- XL30 ESEM Philips) were used for tool wear and burr formation analysis. Moreover, the surface morphology analysis in chapter 6 was carried out by SEM-XL30 ESEM Philips. For more investigating of the laser structured part, the corresponding Energy Dispersive X-ray Spectroscopy (EDX) was also used for elemental analysis.

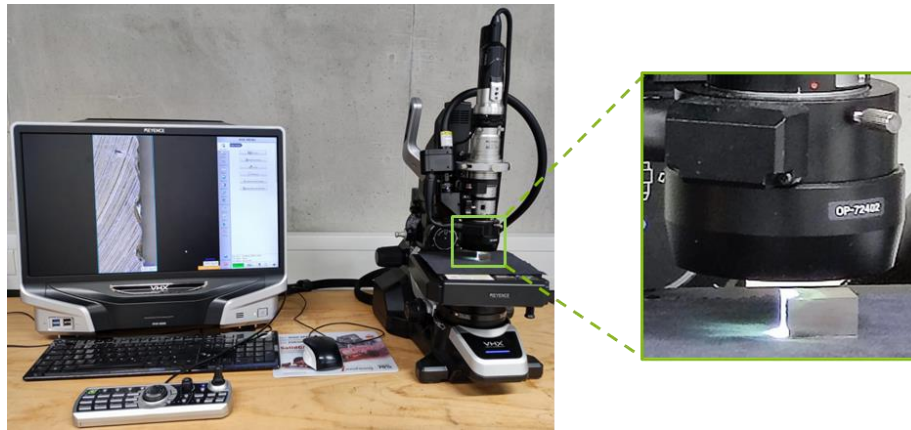


Figure 4.6: Optical microscope.

4.3.4 Material characterization

For studying the interaction between laser and Ti6Al4V in chapter 6 and investigation of the microstructure of samples (EBM and extruded Ti6Al4V), the polishing and etching were performed. Some workpieces were polished to obtain a mirror surface finish with a surface roughness of Ra below 20 nm. The procedure of the polishing is listed in Table 4.7. Figure 4.7 includes the polishing machine and a table summarizing its specifications. After polishing, samples were etched (Etchant Kroll's reagent, 1-3 ml HF, 2-6 ml HNO₃, 100 ml DI water, 30 seconds). Moreover, INNOVATEST FALCON 400 was used for the micro-hardness measurement (with HV0.05).

Table 4.7: Polishing steps.

Step	Medium	Lapping paste / Fluid	Rotational speed in rpm	Rotation	Single pressure in N	Time in min
Planar Grinding	SiC-paper/foil P320	Water	275	Synchronous	25	Until Plane
Grinding	SiC-paper/foil P600	Water	275	Synchronous	25	1:30
Pre-polishing	BETA	Dia-Complete Poly, 9 μm	135	Counter	30	5:00
Final polishing	OMEGA	Eposil F, 0.1 μm	135	Counter	40	10:00 (Water during the final 30 seconds)



Model	FORCIPOL 102
Number of wheels	1
Base motor power in HP	1
Wheel speed in RPM	50-600
Wheel rotation direction	CW/CCW

Figure 4.7: Polishing machine.

4.4 Experimental design

In the micro-milling tests in chapter 5, the radial depth of cut a_e and axial depth of cut a_p were kept constant and equal to 0.3 mm and 1 mm, after discussion with tool manufacturer, respectively. The cutting speed v_c and feed per tooth f_z were varying process parameters. By changing f_z at constant process parameters, the uncut chip thickness changes. The maximum uncut chip thickness h_{cu} is calculated as follows [176]:

$$h_{cu} = \frac{2f_z \sqrt{a_e D - a_e^2}}{D} \quad 4.1$$

where a_e , D , and f_z denote the radial depth of cut, tool diameter, and feed per tooth, respectively. Accordingly, higher feeds per tooth result in higher chip thicknesses. Table 4.8 provides the list of micro-milling process parameters. The cutting speed v_c was varied from 35 m/min to 80 m/min. To study different machining conditions and specific cutting energy for both EBM and extruded Ti6Al4V, the feed per tooth f_z ranging from 1.25 $\mu\text{m}/\text{tooth}$ to 50 $\mu\text{m}/\text{tooth}$ was selected. This range results in the uncut chip thicknesses h_{cu} from 0.9 μm to 37.3 μm . There was a limitation in increasing the cutting speed v_c for measuring the cutting forces. In fact, increasing the cutting speed at constant process parameters is followed by reducing the contact time between the tool and workpiece and increasing the contact frequency. An increase in contact frequency risks reaching the natural frequency of the dynamometer and, consequently, incorrect measurement of the cutting forces. Therefore, the working area for the cutting speed was selected according to the recommendation of the cutting tool manufacturer. The tests were randomly carried out to prevent the influence of tool wear on the experimental results. Moreover, each test was repeated at least two times, and the low variation between obtained results for each test confirms the good repeatability of the experiment. To consider the influence of tool deflection, particularly for calculating specific cutting energy u_c , the actual radial depth of cut was also measured by a measurement tactile probe.

According to the measurements, the difference between the theoretical and actual radial depth of cut was less than 10 μm , showing approximately a 3 % deviation.

Table 4.8: Micro-milling process parameters.

Cutting speed v_c in m/min	Feed per tooth f_z in $\mu\text{m}/\text{tooth}$	Uncut chip thickness h_{cu} in μm	Radial depth of cut a_e in mm	Axial depth of cut a_p in mm
35, 60 and 80	1.25	0.9	0.3	1
	2.5	1.8		
	5	3.7		
	10	7.4		
	15	11.2		
	20	14.9		
	25	18.6		
	50	37.3		

In the micro-milling of laser structured parts in section 7.2.2, the two feeds of 10 $\mu\text{m}/\text{tooth}$ and 50 $\mu\text{m}/\text{tooth}$ were selected at constant cutting speed $v_c = 35$ m/min to study the influence of structure density on the cutting forces at low and high feeds. For a better comparison between the micro-milling of laser structured and non-structured parts, half of the workpiece surfaces were laser structured. The cutting forces in the x and y directions for both, structured surfaces and non-structured surfaces, were measured at each test. The x and y directions denote the feed and normal directions, perpendicular to the feed direction, respectively (see Figure 4.1). The resultant cutting force is calculated as follow:

$$F_{res} = \sqrt{F_x^2 + F_y^2} \quad 4.2$$

In section 7.2.2, all generated laser structures were perpendicular to the milling direction. In fact, the structure angle α for these structured parts equals zero. In section 7.2.3, the influence of different structure angles on the surface roughness were analyzed in addition to $\alpha = 0^\circ$. Since the utilized tool in this study has a helix angle of 30° , the structure angles of $+30^\circ$, -30° and 90° have been selected to see the influence of the structure orientation with respect to the milling direction and helix angle on the generated surface after machining.

In the laser processing of the material in chapter 6, the experiments were carried out for multiple laser pulses, single linear laser scanning, and multiple linear laser scanning. Since it was impossible to incident only one pulse on the workpiece surface to study the interaction between Ultra-short pulse laser and Ti6Al4V without the cumulative effect of pulses, the experiments were conducted for multiple pulses. To determine the number of pulses N_p , a rotating disc made of aluminum with a diameter of 150 mm and rotational speed of 6369 rpm was subjected to the pico-second pulsed laser to separate the pulses. Using the Keyence microscope, the number of pulses was counted.

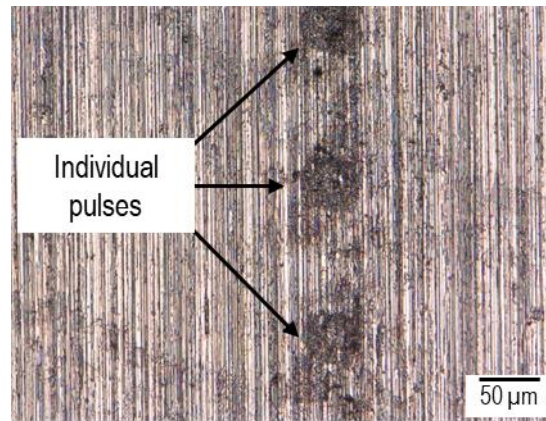


Figure 4.8: Separated pulses in pico-second pulsed laser irradiation on a rotating disc.

Figure 4.8 illustrates the separated pulses in a piece of the rotating disc. Based on the investigation, a possible minimum pulse number of 90 was found. For different laser irradiation times, the corresponding number of pulses N_p was determined.

Table 4.9: Ultra-short pulse laser process parameters.

Multiple pulses	P_L in W	5 - 50
	N_p	90 - 400
Single linear laser scanning	P_L in W	5 - 50
	v_L in mm/s	100 - 800
Multiple linear laser scanning	P_L in W	6.25 - 50
	v_L in mm/s	200 - 1600
	N_s	2 - 40

The Ultra-short pulse laser processing parameters are listed in Table 4.9. The experimental tests include a wide range of laser power P_{L_ave} to cover different laser fluences that may result in different ablation mechanisms. Accordingly, the multiple laser pulses were conducted at different pulse numbers N_p ranging from 90 to 400 and different average powers ($P_{L_ave} = 5-50$ W). In the case of single linear laser scanning, scan velocity v_L and average laser power P_{L_ave} were varying process parameters that ranged from 100 mm/s and 800 mm/s, and 5 W and 50 W, respectively. A high volume of melting for $v_L < 100$ mm/s and no considerable ablation at $v_L > 800$ mm/s led to the selection of the mentioned range of v_L . For multiple linear laser scanning, the number of laser scans N_s was also considered as an additional parameter that was selected from 2 and 40. Moreover, the range of v_L and P_{L_ave} equal 6.25-50 W and 200-1600 mm/s, respectively. The v_L and P_{L_ave} were selected in which to include a wide range of laser powers and scan velocities and investigating laser ablation and surface morphology at constant laser input energy E_{L_input} caused by their different combinations.

5 Comparison between machinability of additively manufactured and conventional titanium Ti6Al4V

As explained, different mechanical properties and microstructures were detected for EBM and extruded parts. This section aims to see how the differences influence the machinability of these parts with respect to the cutting force and specific cutting energy, surface quality, and burr formation.

5.1 Uncut chip thickness

The uncut chip thickness, a critical parameter in machining operations, is defined as the minimum radial distance between the current position of the cutting edge and its preceding location at the same angular position. This fundamental metric plays a pivotal role in determining the efficiency and precision of milling processes. The maximum uncut chip thickness, denoted as h_{cu} , represents a key factor in these operations and can be accurately calculated using the following equation:

$$h_{cu} = \frac{2f_z \sqrt{a_e D - a_e^2}}{D} \quad 5.1$$

Accordingly, h_{cu} is a function of the feed per tooth f_z , the radial depth of cut a_e , and the tool diameter D . Due to the importance of uncut chip thickness and its relationship to the cutting edge radius in micro-machining, the uncut chip thickness h_{cu} was used to present the results. Moreover, the relationship between the uncut chip thickness and the specific cutting energy is significant to find a safe cutting without the size effect and ploughing effect. In addition, the role of the uncut chip thickness in relation to the cutting-edge radius in the machined surface and burr formation should not be overlooked.

5.2 Cutting forces

Figure 5.1 indicates the influence of cutting speed on resultant cutting forces at different uncut chip thicknesses h_{cu} for both extruded and EBM Ti6Al4V. Minor differences were observed between cutting forces for EBM and extruded Ti6Al4V at uncut chip thicknesses between 7.4 μm and 37.3 μm despite the higher hardness and yield strength of EBM parts. Minor difference in cutting forces, despite the different strengths of the extruded and EBM material, were due to the fact that the total force results from the energy which is consumed for pure cutting, plastic deformation, and friction. On the one side, the higher strength of EBM Ti6Al4V, due to its fine microstructure followed by higher micro-hardness, in comparison with extruded Ti6Al4V can lead to higher energy consumption for pure cutting. On the other side, higher ductility and toughness of extruded parts, due to their coarser microstructure, increase the degree of plastic deformation in the chip formation process, followed by higher energy consumption. Higher cutting forces for coarser lamellar microstructures of Ti6Al4V despite their lower hardness and tensile strength were reported in [177,178]. Consequently, the higher strength of EBM parts and more ductile behavior of extruded Ti6Al4V have both led to the same resultant cutting forces.

No significant change in cutting forces could be observed by an increase in the cutting speed from $v_c = 35$ m/min to $v_c = 80$ m/min at chip thicknesses below 19 μm . However, at $h_{cu} = 37.3$ μm , force reduced with cutting speed, especially for the

extruded Ti6Al4V, which could be attributed to the thermal softening effect at higher chip thicknesses. An increase in cutting speed at higher chip thicknesses may generate more heat transferred into the material ahead of the cutting tool. This may ease removing the material by the subsequent cutting tooth and reducing the cutting force. Moreover, increasing cutting speed results in higher MRR that may be followed by less time for dissipation of generated heat in front of the tool and, finally, more heat accumulation. According to the constitutive law [179], the material yield point is influenced by temperature in addition to strain and strain rate. Therefore, more heat and temperature during the machining process may lead to decreasing yield point and eventually cutting force reduction.

Milling Tool	3 flutes; $\Phi = 1.8$ mm (WN 3142 R-N, PVD-TiAlN, Schaft DIN 6535-HA/HB), Gühring
Workpiece	Ti6Al4V; Extruded / EBM
Parameters	Down-milling; $v_c = 35 - 80$ m/min; $h_{cu} = 7.4 - 37.3$ μm ; $a_p = 1$ mm; $a_e = 0.3$ mm
Coolant	Oil

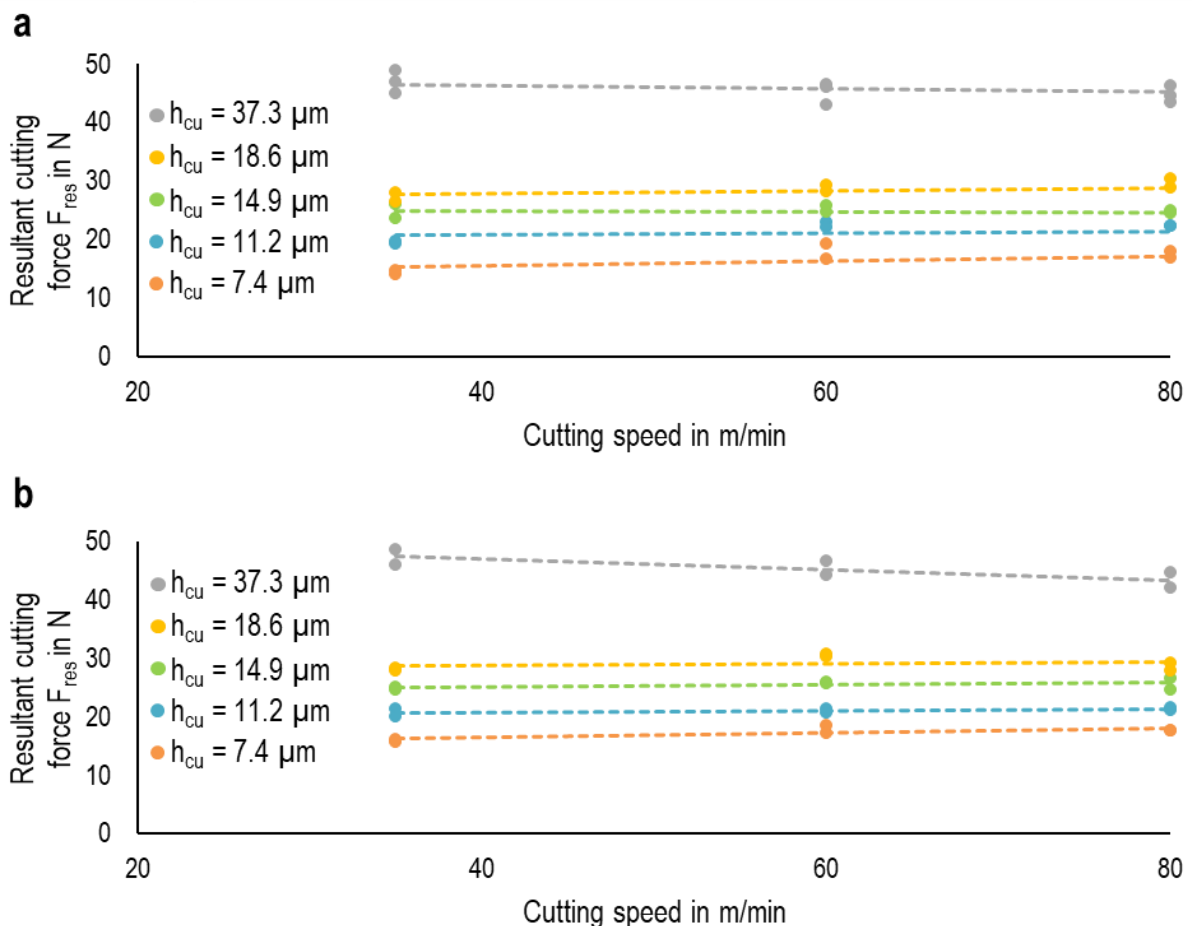


Figure 5.1: Influence of chip thickness and cutting speed for a) EBM and b) extruded Ti6Al4V at $h_{cu} > 7.4$ μm on resultant cutting force F_{res} .

According to Figure 5.1, an increase in uncut chip thickness h_{cu} from 7.4 μm to 37.3 μm led to increasing the resultant cutting force at different cutting speeds for both materials. In fact, more material removal results in more cutting forces. The influence of changing feed per tooth, resulting in different uncut chip thicknesses, on the cutting force is significant compared to that for cutting speed.

In additive manufacturing, each part is formed layer by layer in a direction, called Built-Up Direction (BUD). Therefore, differences between the material properties of manufactured parts in parallel and normal directions to the BUD may be expected due to the material anisotropy. In this regard, the micro-hardness measurement was carried out in two different directions, normal and parallel to the BUD, to evaluate the degree of anisotropy for EBM parts. The same micro-hardness values show that the EBM parts have isotropic mechanical properties. Additionally, in these two directions, milling experiments were conducted at different cutting speeds v_c and uncut chip thicknesses h_{cu} , and no remarkable differences between cutting forces were observed, as illustrated in Figure 5.2.

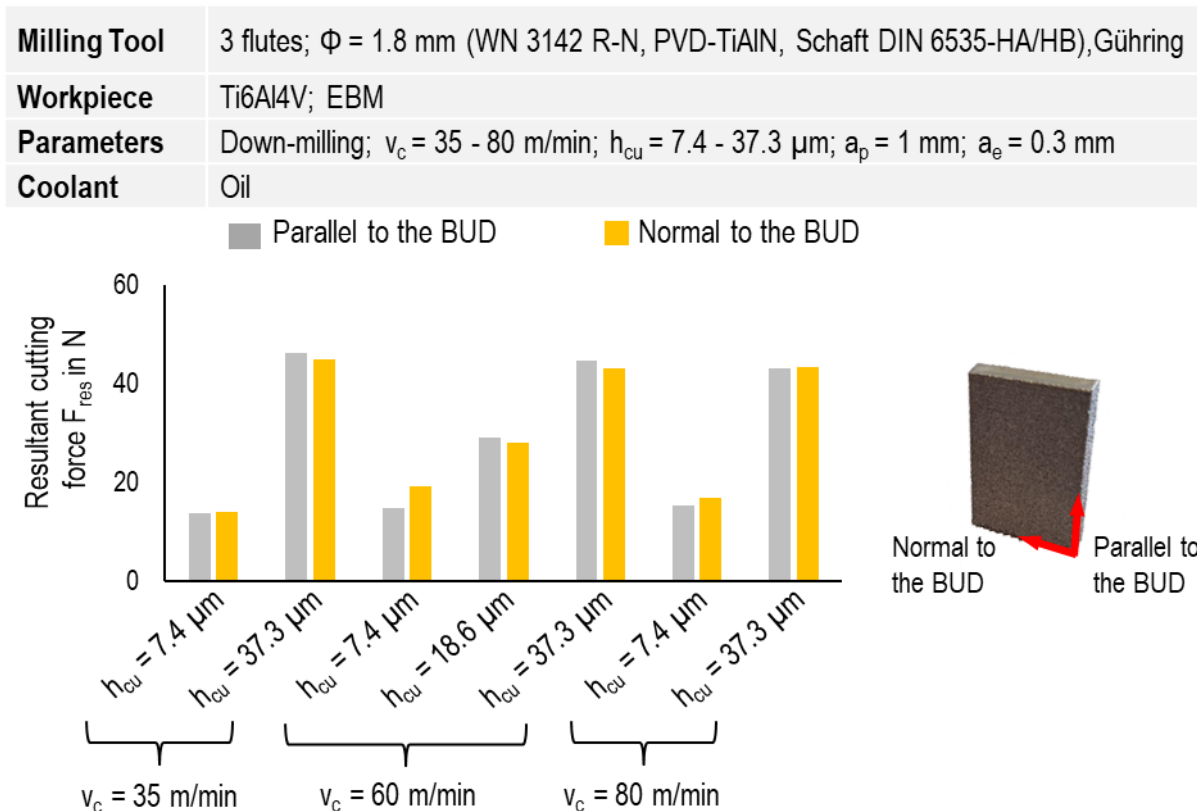


Figure 5.2: Comparison between the resultant forces when milling in normal and parallel to BUD.

5.3 Specific cutting energy

From the force components in x and y directions, F_x and F_y , the specific cutting energy u_c at different cutting parameters (chip thickness and cutting speed) was calculated as below [180]:

$$u_c = \frac{v_c}{V_{rem}} \int_0^{t_c} \sqrt{F_x^2 + F_y^2} dt \quad 5.2$$

Where v_c , V_{rem} , and t_c are, respectively, cutting speed, removal chip volume, and the cutting time. Figure 5.3 illustrates the relation between the uncut chip thickness and specific cutting energy for both EBM and extruded Ti6Al4V at different cutting speeds, $v_c = 35, 60,$ and 80 m/min. Accordingly, the influence of the size effect in the micro-milling process can be clearly observed. Once the uncut chip thickness decreases, the specific cutting energy non-linearly increases. For $h_{cu} < 7.4$ μm , the chip thickness is less than or comparable to the cutting edge radius of the utilized

milling tool. In this condition, the rake angle is negative, and the plastic deformation is considerable compared to the pure cutting in the chip formation process. As a result, the specific cutting energies increase. However, the proportion of the pure cutting in $h_{cu} > 7.4 \mu\text{m}$ is more significant than the plastic deformation, and therefore, lower specific cutting energies are expected. For $h_{cu} < 7.4 \mu\text{m}$, the specific cutting energies of extruded Ti6Al4V are 5-15% higher than those of the EBM parts.

Milling Tool	3 flutes; $\Phi = 1.8 \text{ mm}$ (WN 3142 R-N, PVD-TiAlN, Schaft DIN 6535-HA/HB), Gühring
Workpiece	Ti6Al4V; Extruded / EBM
Parameters	Down-milling; $v_c = 35 - 80 \text{ m/min}$; $h_{cu} = 0.9 - 37.3 \mu\text{m}$; $a_p = 1 \text{ mm}$; $a_e = 0.3 \text{ mm}$
Coolant	Oil

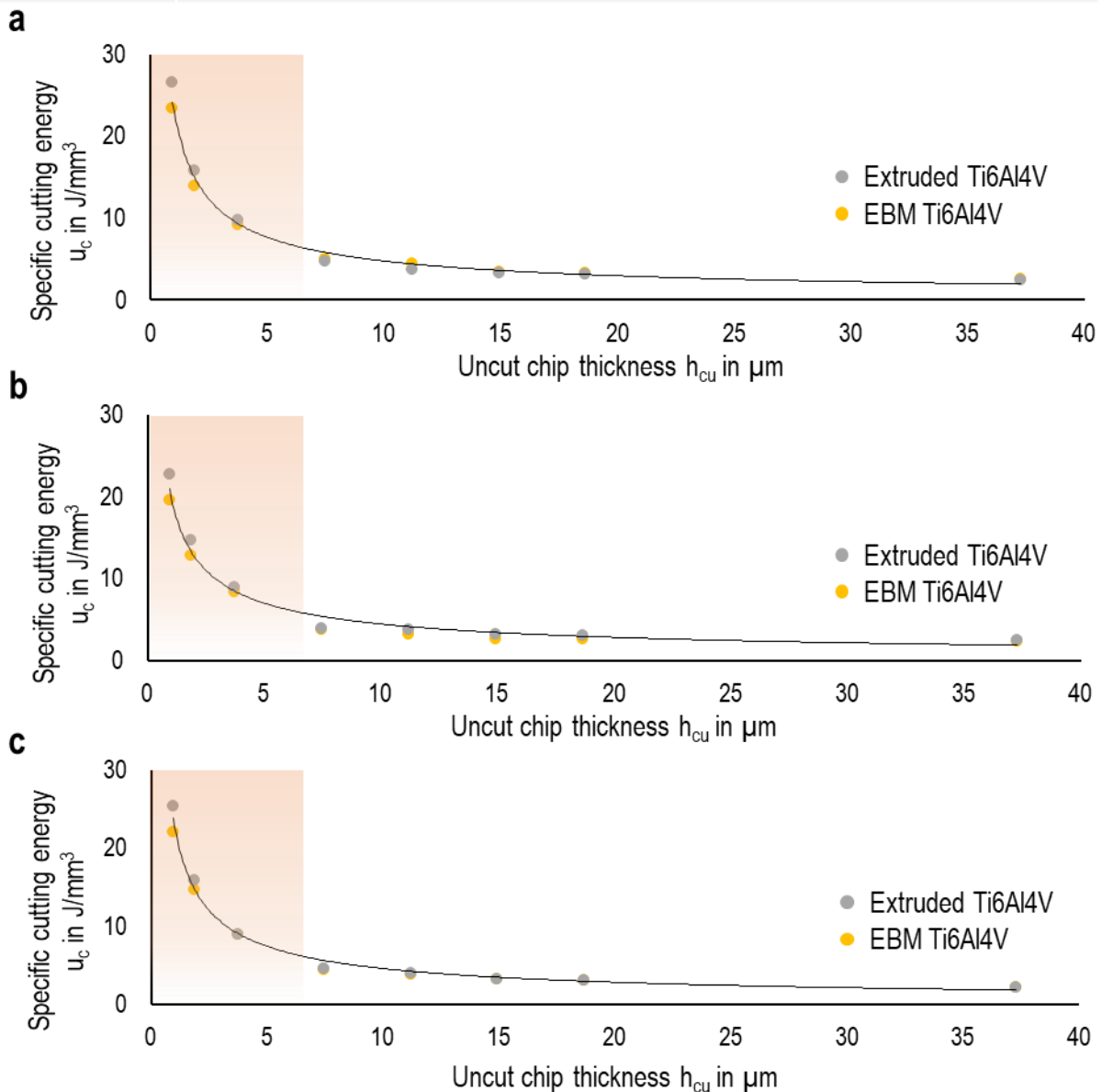


Figure 5.3: Influence of the chip thickness on the specific cutting energy u_c at a) $v_c = 35 \text{ m/min}$, b) $v_c = 60 \text{ m/min}$, and c) $v_c = 80 \text{ m/min}$.

As explained before, the ductile behavior of extruded parts with coarse lamellar microstructure is higher than that of EBM parts with fine microstructure. In the chip formation process, the material with high ductility requires more energy to reach the

fracture and be separated from the workpiece. So, more considerable plastic deformation of extruded parts is expected, particularly for $h_{cu} < 7.4 \mu\text{m}$, where the plastic deformation and ploughing are dominant and may intensify the influence of ductile behavior on energy consumption. As a consequence, higher specific cutting energies are expected for extruded Ti6Al4V. In the case of $h_{cu} > 7.4 \mu\text{m}$, where the pure cutting predominates over the plastic deformation and ploughing, the minimum specific energy of $u_c \approx 2.5 \text{ J/mm}^3$ was obtained, and it is nearly the same for both EBM and extruded Ti6Al4V. This indicates less effect of ductile behavior of extruded Ti6Al4V on chip formation when $h_{cu} > 7.4 \mu\text{m}$. In fact, the same specific cutting energies for these two materials resulted from the balance of higher strength of EBM Ti6Al4V and higher toughness of extruded Ti6Al4V.

5.4 Surface roughness

The EBM and extruded parts were machined, and produced surfaces were compared. As illustrated in Figure 5.4, the EBM parts show finer surfaces in most cases in comparison with extruded Ti6Al4V. The obtained results agree with those reported by Milton et al. [181] and Polishetty et al. [125]. This could be attributed to the higher brittle behavior of EBM parts with 450 HV Hardness compared to the extruded parts with 350 HV.

Milling Tool	3 flutes; $\Phi = 1.8$ mm (WN 3142 R-N, PVD-TiAlN, Schaft DIN 6535-HA/HB),Gühring
Workpiece	Ti6Al4V; Extruded / EBM
Parameters	Down-milling; $v_c = 35 - 80$ m/min; $h_{cu} = 0.9 - 37.3$ μm ; $a_p = 1$ mm; $a_e = 0.3$ mm
Coolant	Oil

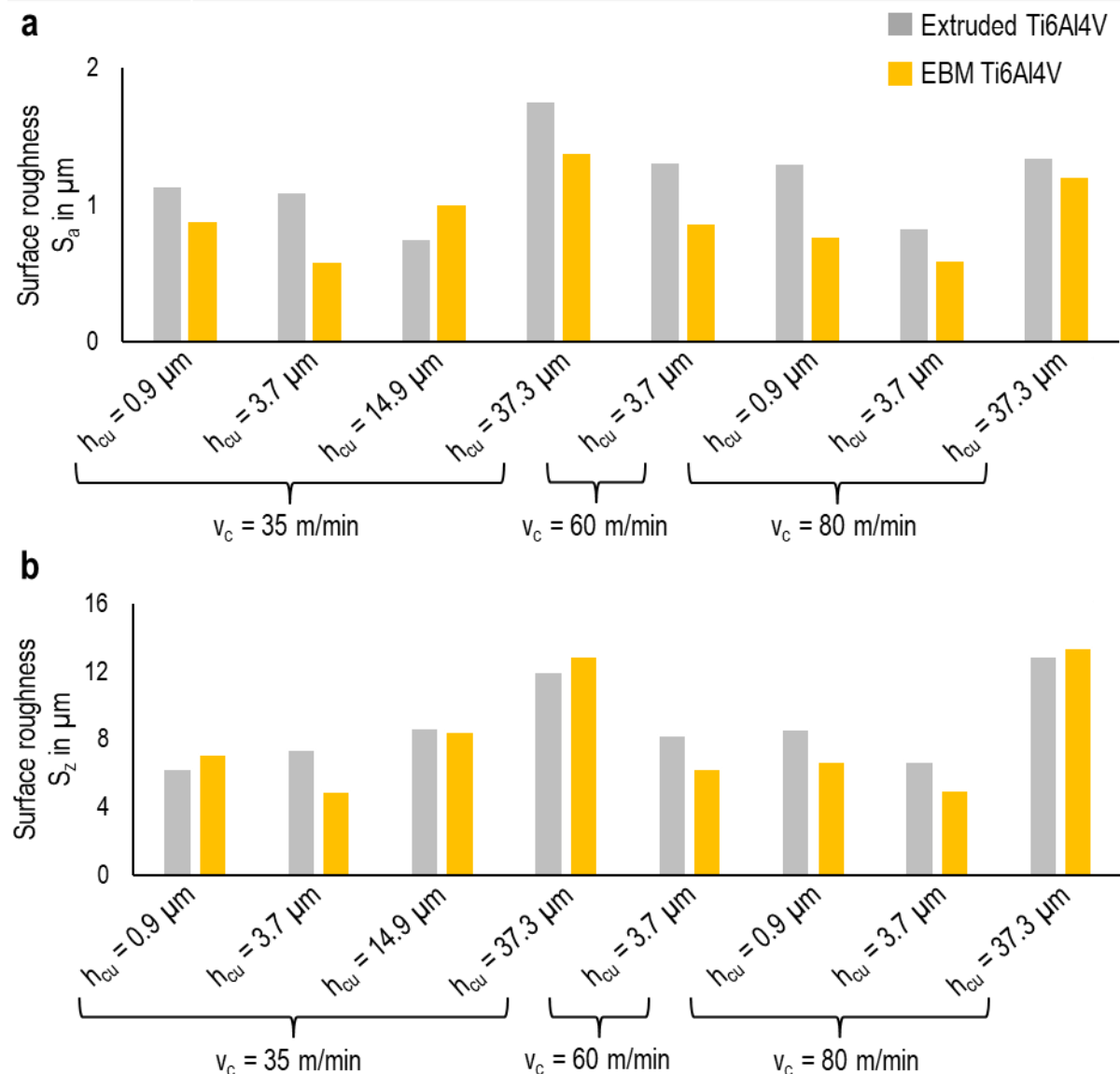


Figure 5.4: Surface roughness for EBM and extruded parts a) S_a , b) S_z .

More precisely, the material in front of the cutting edge either moves toward the rake face to form the chip or is squeezed under the flank face, which in turn results in the degradation of the machined surface. The material separation takes place at the stagnation point. In the case of extruded Ti6Al4V, the stagnation point stands at a

higher level compared to the EBM parts, which contributes to the conduction of more material under the tool and, eventually, more ploughing. Consequently, the more brittle characteristic of the EBM parts leads to the less pressed material through the ploughing on the machined surface leading to the finer surfaces.

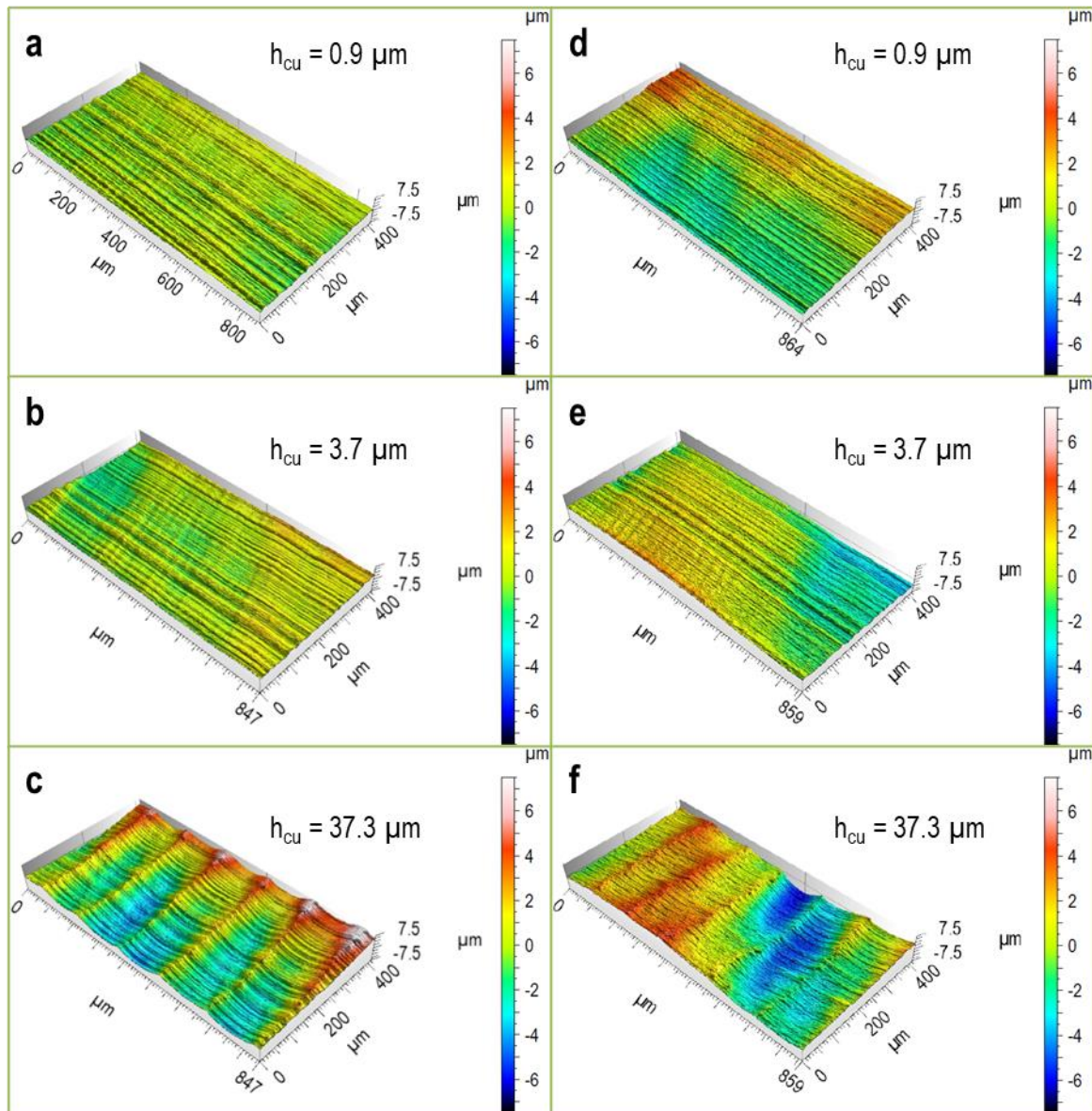


Figure 5.5: Confocal microscopy of the machined surface of EBM (a-c) and extruded (d-f) parts at a cutting speed of $v_c = 35\text{m/min}$.

At cutting speeds $v_c = 35\text{ m/min}$ and $v_c = 80\text{ m/min}$, the surface roughness parameters, S_a and S_z , decrease with increasing uncut chip thickness from $h_{cu} = 0.9\text{ }\mu\text{m}$ to $h_{cu} = 3.7\text{ }\mu\text{m}$ for EBM Ti6Al4V. Beyond $h_{cu} = 3.7\text{ }\mu\text{m}$, the surface roughness increases with chip thickness up to $h_{cu} = 37.3\text{ }\mu\text{m}$. The decrease in the surface roughness, from $h_{cu} = 0.9\text{ }\mu\text{m}$ to $h_{cu} = 3.7\text{ }\mu\text{m}$, is related to the reduction of the ploughing effect. Where the uncut chip thickness is higher than the cutting edge radius of the tool, the cutting behavior seems similar to macro-milling, and an increase in feed per tooth, or undeformed chip thickness, results in higher surface roughness, from $h_{cu} = 3.7\text{ }\mu\text{m}$ to $h_{cu} = 37.3\text{ }\mu\text{m}$, due to the generated feed marks caused by the process kinematic, combination of rotation of cutting edges and the linear feed motion. The influence of the size effect on the surface roughness can

also be seen for the extruded parts. This observation, influence of the size effect on the surface roughness, is also in good agreement with the founding of Chen et al. [111]. In micro milling and uncut chip thicknesses higher than the critical uncut chip thickness h_{cu-crt} , pure cutting is a dominant mechanism, while ploughing significantly takes place for the uncut chip thicknesses less than h_{cu-crt} , followed by surface degradation and more roughness.

Figure 5.5 provides a comparison between the micro-milled surface of EBM and extruded parts at the cutting speed of $v_c = 35$ m/min and chip thickness of $h_{cu} = 0.9$ μm , 3.7 μm , and 37.3 μm . The increase of chip thickness from 0.9 μm to 3.7 μm has not led to a remarkable change in the surface topography. However, the surface topography has been dramatically altered at $h_{cu} = 37.4$ μm . Feed marks on the machined surface with $h_{cu} = 37.3$ μm can be clearly observed. High surface roughness at $h_{cu} = 37.3$ μm is mainly associated with these feed marks. The waviness of extruded parts is observable also, particularly at $h_{cu} = 37.3$ μm .

Milling Tool	3 flutes; $\Phi = 1.8$ mm (WN 3142 R-N, PVD-TiAlN, Schaft DIN 6535-HA/HB),Gühring
Workpiece	Ti6Al4V; Extruded / EBM
Parameters	Down-milling; $v_c = 35 - 80$ m/min; $h_{cu} = 0.9 - 37.3$ μm ; $a_p = 1$ mm; $a_e = 0.3$ mm
Coolant	Oil

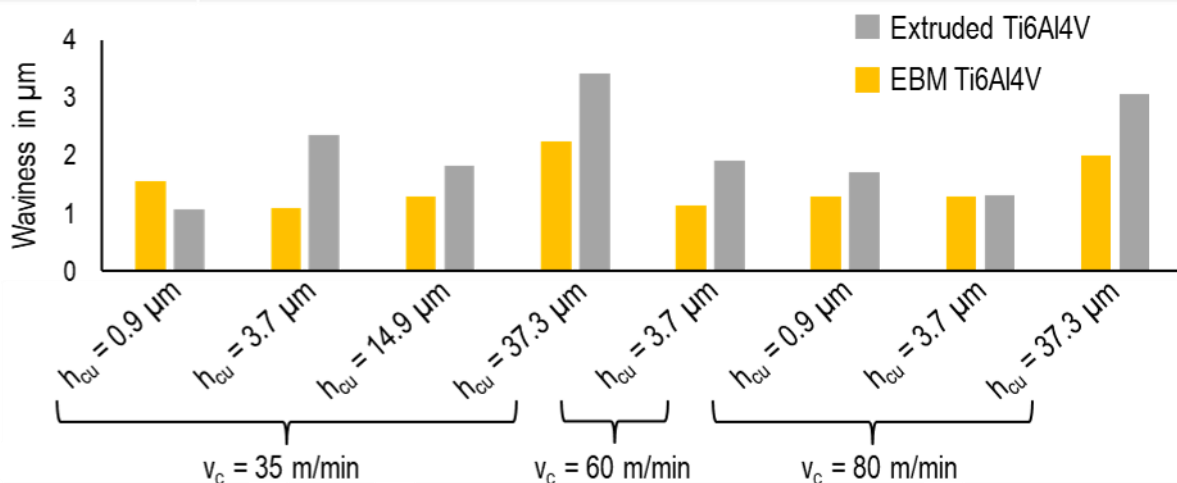


Figure 5.6: The waviness of EBM and extruded parts.

Figure 5.6 compares EBM and extruded parts with respect to the waviness. The waviness of the extruded parts was higher than the EBM parts in most cases. The high waviness of the extruded part at $h_{cu} = 37.3$ μm may be attributed to the lower hardness of the extruded part, and higher plastic deformation, compared to the EBM part.

5.5 Burr formation

Burr formation in machining processes can negatively impact the quality and precision of the finished product, causing dimensional inaccuracies and surface imperfections. Various factors, such as material, tool geometry, and machining parameters, affect the burr size and burr formation. In this section, the burr formation for two types of material, EBM and extruded Ti6Al4V, has been analyzed. The following images from burr formation were captured in two different views, as shown in Figure 5.7. The view direction perpendicular to the surface A indicates the burr width, and the view direction perpendicular to the surface B shows the burr height.

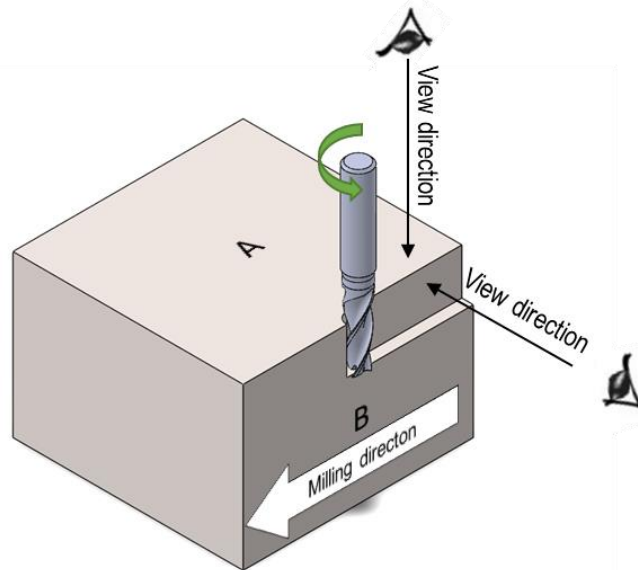


Figure 5.7: The direction views of the burr formation.

Milling Tool	3 flutes; $\Phi = 1.8$ mm (WN 3142 R-N, PVD-TiAlN, Schaft DIN 6535-HA/HB),Gühring
Workpiece	Ti6Al4V; Extruded
Parameters	Down-milling; $v_c = 35$ m/min; $h_{cu} = 0.9 - 37.3$ μm ; $a_p = 1$ mm; $a_e = 0.3$ mm
Coolant	Oil

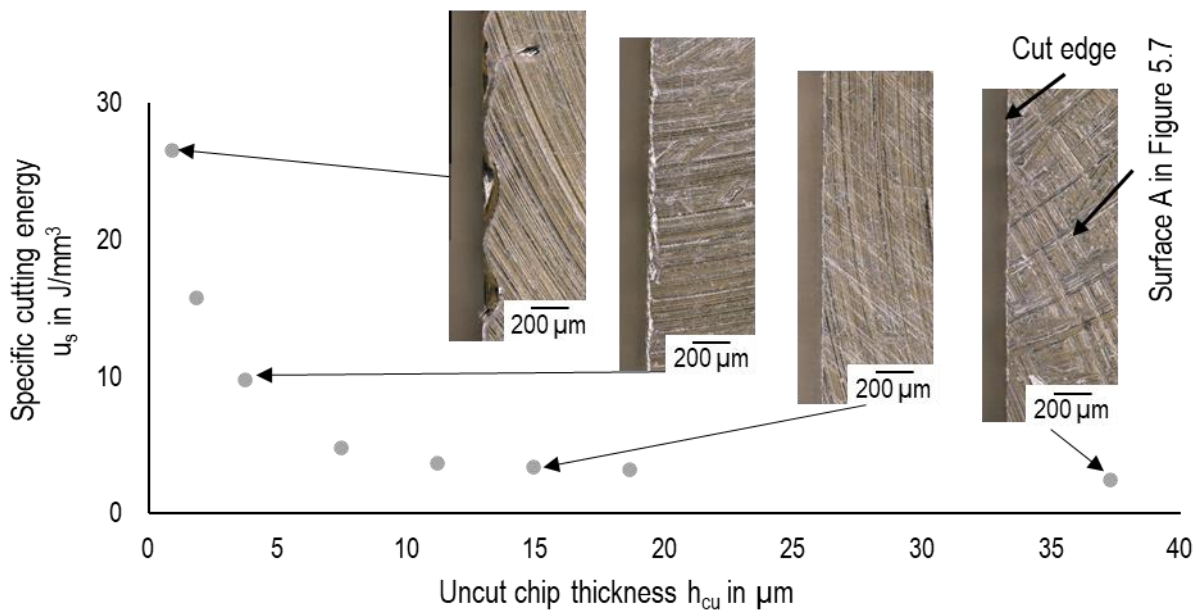
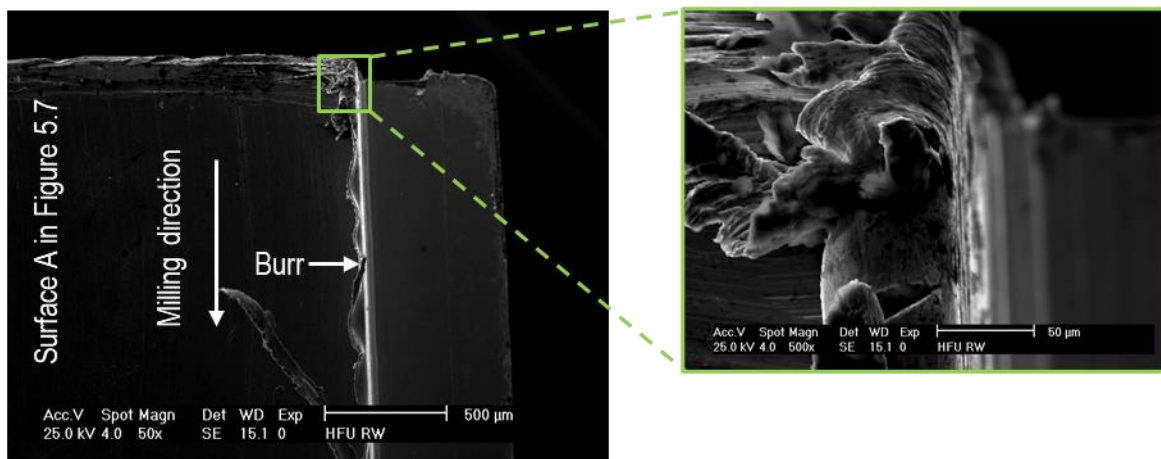


Figure 5.8: The correlation between specific cutting energy and burr formation for extruded Ti6Al4V.

Figure 5.8 indicates the correlation between the specific cutting energy, uncut chip thickness, and burr formation at constant cutting speed $v_c = 35$ m/min and feeds ranging from 1.25 $\mu\text{m}/\text{tooth}$ and 50 $\mu\text{m}/\text{tooth}$. The view direction in Figure 5.8 is perpendicular to surface A, which shows the top burr width. According to Bissacco et al. [60], a considerable biaxial compressive stress pushing the material toward the cut edge causes the top burr formation. At lower chip thicknesses where the ploughing could be dominant and specific cutting energy is larger, burrs were formed considerably. Whereas no burr could be observed at the higher chip thicknesses

possibly due to the reduced portion of ploughing. In detail, at the lower chip thicknesses, resulted from lower values of feed per tooth, where the ploughing is dominant, the material is compressed under the flank face, plastically bulging the material to the sides (Poisson mechanism) and forming the burr. Particularly in the down-milling strategy where the cutting tool moves from outside to the cut edge, the material is conducted to the cut edge, accompanied by significant burr formation. The significant burr formation on the down-milling side compared to the up-milling side was also confirmed by Bajpai et al. [99] and Chen et al. [117]. As illustrated in Figure 5.8, the role of feed per tooth leading to different chip thicknesses in the burr formation is significantly high. The influence of feed per tooth on the burr formation was also mentioned by several researchers [72,95,118].

a



b

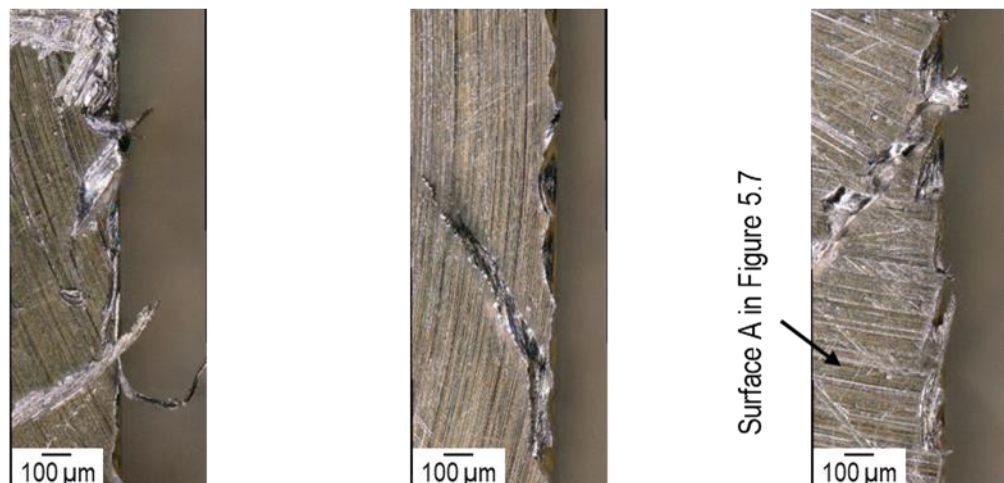


Figure 5.9: a) wavy type burr for extruded Ti6Al4V and burrs at the entry side, b) irregular burr formation at $v_c = 35$ m/min and $f_z = 1.25$ $\mu\text{m}/\text{tooth}$ (or $h_{cu} = 0.9$ μm) for extruded Ti6Al4V.

Figure 5.9a shows the burr formation for extruded Ti6Al4V at $h_{cu} = 0.9$ μm , and $f_z = 1.25$ $\mu\text{m}/\text{tooth}$, where the highest specific cutting energy was recorded. According to the classification by Chern [182], the generated burr in micro-milling of extruded Ti6Al4V is categorized as the wavy type. The continuous wavy type of burr can clearly be observed throughout the cut edge. This burr type was also reported by Schueler et al. [73] in the slot-milling of Ti6Al4V and Ti-6Al-7Nb, irrespective of the milling strategy, up-and down milling. Moreover, the burr formation is more considerable at the entry side. In fact, the cutting tooth in the down milling strategy conducts the material into the cut edge. Particularly at the entry side, the pile-up of

the burrs at multiple times of tool engagement and plastic hinging of the material at the free surface resulted in the generation of significant burr formation, as mentioned in the study of Bajpai et al. [99]. Apart from the wavy type of the burr formation, several long irregular burrs were also observed, as shown in Figure 5.9b.

In addition to the feed per tooth, or chip thickness, the effect of cutting speed on the burr formation was also analyzed. Figure 5.10 illustrates the top view burr formation of extruded Ti6Al4V at constant $f_z = 5 \mu\text{m}/\text{tooth}$ and different cutting speeds ranging from 35 m/min and 80 m/min. Accordingly, no significant change in the burr can be observed. Therefore, further study regarding the comparison between burr formation of EBM and extruded Ti6Al4V was only limited to the effect of feed per tooth.

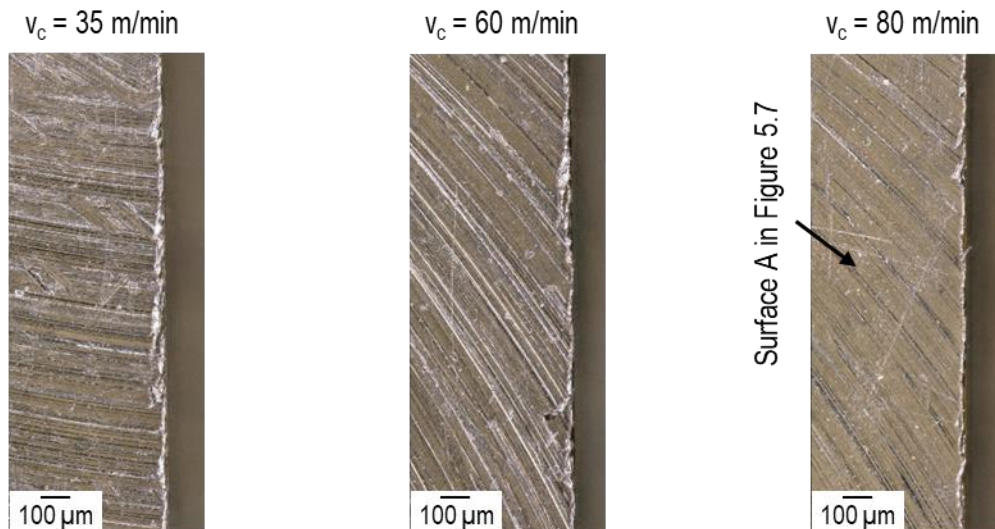


Figure 5.10: Burr formation for extruded Ti6Al4V at $f_z = 5 \mu\text{m}/\text{tooth}$ and different cutting speeds $v_c = 35, 60$ and 80 m/min .

According to Figure 5.11, no sign of burr formation can be seen for EBM and extruded Ti6Al4V at $f_z = 50 \mu\text{m}/\text{tooth}$ ($h_{cu} = 37.3 \mu\text{m}$). However, the burr is observable for both types of material at $f_z = 1.25 \mu\text{m}/\text{tooth}$ ($h_{cu} = 0.9 \mu\text{m}$) in the top view (surface A). The generated burr for extruded Ti6Al4V is the wavy type. In the case of EBM Ti6Al4V, the formed burr is discontinuous, and the burr width is smaller than that of the extruded parts. In the view direction of surface B, the discontinuity of the burr can also be detected for EBM Ti6Al4V. The burr height for extruded parts is more significant than that of EBM Ti6Al4V. The irregularities on the EBM part surface are present up to the depth of $70 \mu\text{m}$. These irregularities may interrupt the burr formation during the machining process, which results in discontinuous burrs. During the additive manufacturing process, the material powders are heated to partial melting, causing them to fuse together, eventually forming the part layer by layer. This process also results in sintering the powders in the workpiece sides. As a result, the surface of the workpiece may exhibit uneven texture and irregularities. To ensure the influence of irregularities on the burr formation, the irregularities from surface A were removed, and then surface B was micro-milled.

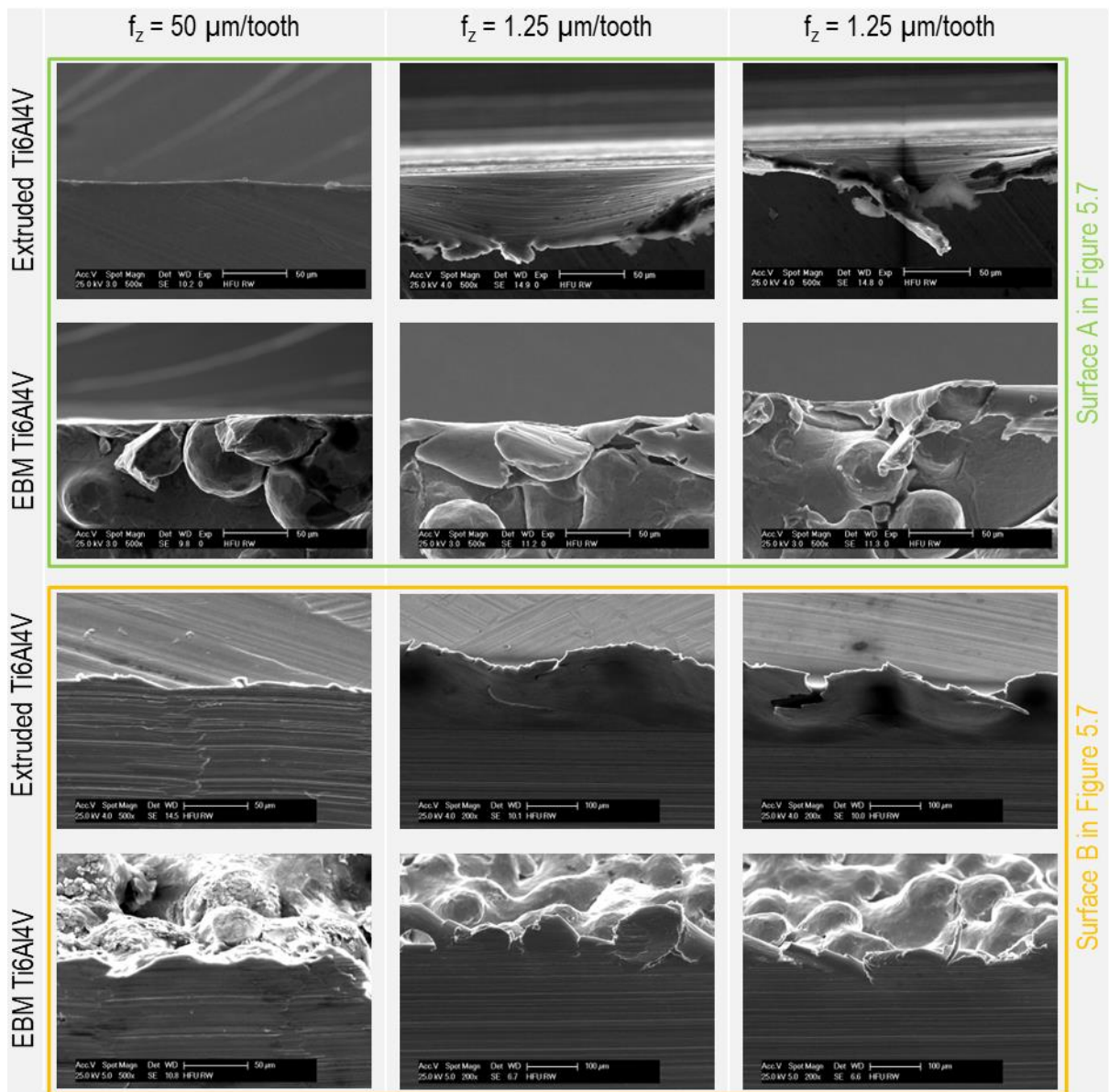


Figure 5.11: Burr formation for extruded and EBM Ti6Al4V at $f_z = 1.25 \mu\text{m/tooth}$ and $50 \mu\text{m/tooth}$ (correspondingly $h_{cu} = 0.9 \mu\text{m}$ and $37.7 \mu\text{m}$) at two different view directions.

After removing the irregularities from the surface of EBM parts (Surface A in Figure 5.7) through a preliminary milling pass, an additional test was carried out at $h_{cu} = 0.9 \mu\text{m}$ and $v_c = 35 \text{ m/min}$. Figure 5.12b indicates the burr formation of EBM parts without the presence of irregularities on the surface. The formed burr is significant and continuous and has a wavy shape. Moreover, the size of the burrs is more considerable for the EBM part after removing the irregularities on the surface compared to the EBM part with irregularities on the surface shown in Figure 5.12a. Thereby, it can be concluded that the irregularities on the surface of additive parts significantly influence the burr formation and size. Moreover, the hypothesis regarding the influence of micro-hardness on the burr formation would not be acceptable according to Figure 5.12b because the size of generated burr after removing the surface irregularities is comparable to that of the burr for the extruded part.

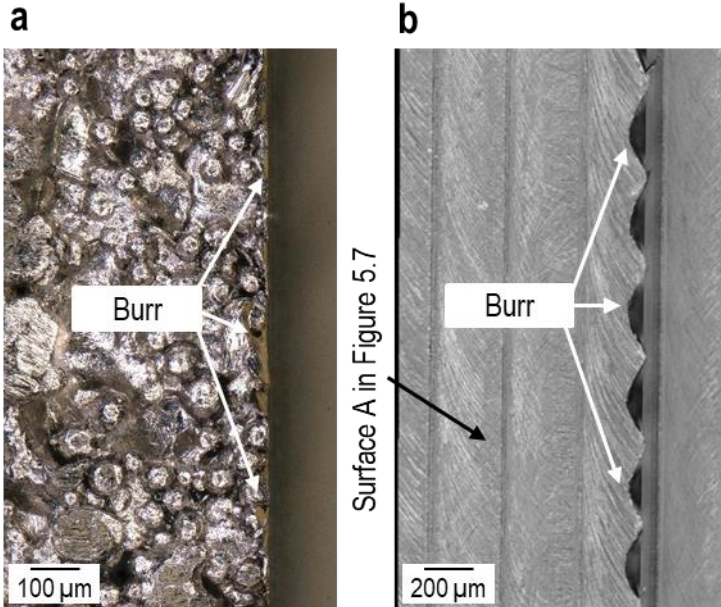


Figure 5.12: Burr formation in EBM parts: a) with irregularities on the surface and b) without irregularities on the surface.

5.6 Tool wear

The Sections 5.2, 5.3, 5.4, and 5.5 are allocated to the comparative study between Ti6Al4V titanium alloys manufactured by additive manufacturing, using EBM technique, and conventional method (extrusion) concerning cutting forces, specific cutting energy, surface roughness, and burr formation. However, the cutting tool condition has not been under the focus of the study through a long-term experiment.

Figure 5.13 provides the cutting tool condition, in two different views for three cutting edges, for machining these material types, EBM and extruded Ti6Al4V, after 150 mm machining for constant machining parameters $v_c = 35$ m/min and $f_z = 50$ μ m/tooth. Accordingly, no detectable tool wear can be observed for both materials. However, a deep investigation and extensive experimental tests regarding the tool wear analysis for both materials are required, which is outside the scope of the current study.

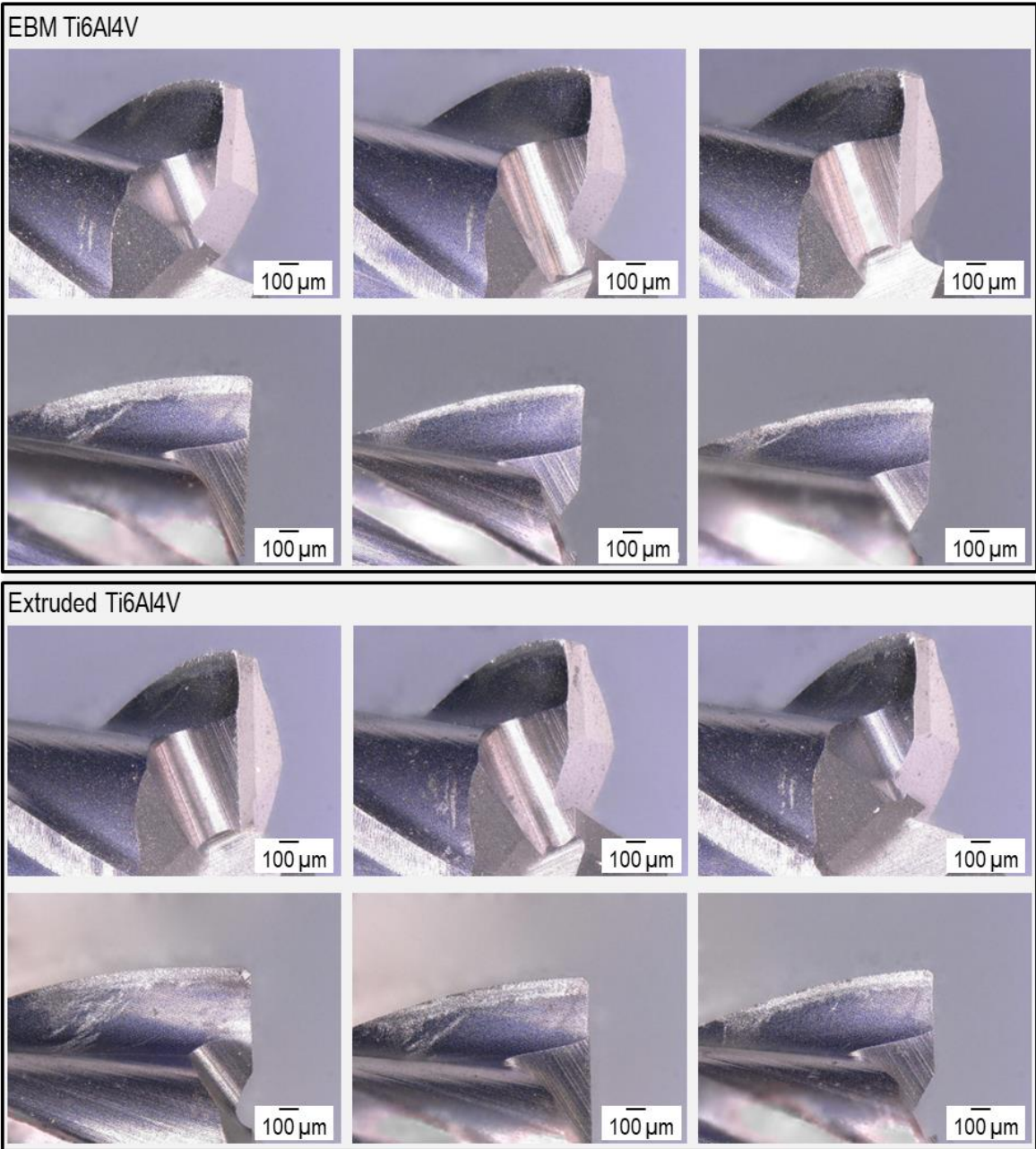


Figure 5.13: Comparison of cutting tool condition between EBM Ti6Al4V and extruded Ti6Al4V after 150 mm machining length at $v_c = 35$ m/min and $f_z = 50$ μ m/tooth.

6 Interaction between laser and titanium Ti6Al4V

The benefits of laser pre-structuring of the workpiece in improving the machinability have been mentioned in the state of the art. This process led to removing some parts of the material prior to machining, followed by reducing cutting forces. This highlights the importance of laser processing as an assisting approach in improving the machinability. To better understand the influence of laser on the material, this section has been devoted to investigating the interaction between laser and Ti6Al4V titanium alloy material with respect to surface morphology and geometrical features. The study has been conducted in three groups of multiple pulses, single linear laser scanning and multiple linear laser scanning. In the case of multiple pulses, the experiments were carried out at different average laser powers P_{L_ave} and the number of pulses N_p , and their influence on surface morphology and ablation depth were investigated. In the second section, single linear laser scanning was conducted at a wide range of laser input energies E_{L_input} caused by different combinations of average laser power P_{L_ave} and scan velocity v_L . In addition to studying surface morphology, several features of the ablation process in terms of ablation depth, ablation rate per pulse, ablation area, MRR, specific ablation energy and ablation rate per fluence were extracted from the generated lasered profiles. In the case of multiple laser scanning, the relation between laser constant laser input energy E_{L_input} caused by different combinations of P_{L_ave} and v_L and surface morphology and geometrical features of the generated profile has been studied. In the following, the investigation results have been summarized.

6.1 Multiple laser pulses

The laser parameters such as laser fluence, frequency, or repetition rate, wavelength and pulse duration are decisive parameters in the laser ablation process. Among them, laser fluence and pulse duration not only affect the ablation rate but also change the ablation mechanism. Pulse duration determines the physical coupling process between electrons and lattice system and energy dissipation into the target material. Shorter pulse duration results in shorter heat diffusion depth and less thermal damage, which plays an important role in the machining accuracy and ablation rate, as mentioned in [183–185]. In this study, pulse duration, in addition to laser frequency and wavelength, was kept constant, and laser fluence is a varying parameter. Moreover, the surface reflectivity and electron-phonon coupling factor are the variables that would change during the laser processing and influence the ablation process. The influence of mentioned variables will also be discussed in the following.

Since the average laser power P_{L_ave} could not be a good indicator to compare the results with other scientific studies, the laser peak fluence ϕ_{L_peak} and laser peak intensity I_{L_peak} were calculated. Since a pulsed laser was utilized in this study, the pulse energy E_p can be calculated as follow:

$$E_p = \frac{P_{L_ave}}{f_L} \quad \text{in } \mu\text{J} \quad 6.1$$

where f_L is laser frequency. Accordingly, the pulse energy varies from 12.5 μJ to 125 μJ for average laser powers ranging from 5 W to 50 W. Further, peak laser fluence ϕ_{L_peak} is calculated as below:

$$\varphi_{L_peak} = \frac{2E_p}{\pi r^2} \quad \text{in J/cm}^2 \quad 6.2$$

where r denotes the spot radius. The factor 2 in the above equation is related to the unevenly distributed energy of the Gaussian beam that led to more energy at the center of the beam than at the periphery. Peak laser power P_{L_peak} is obtained according to the following equation:

$$P_{L_peak} = \frac{E_p}{t_p} \quad \text{in W} \quad 6.3$$

Where t_p is the irradiation time at each pulse that equals to 12 ps. The product division of peak laser power and irradiation area results in peak laser intensity I_{L_peak} .

$$I_{L_peak} = \frac{P_{L_peak}}{\pi r^2} \quad \text{in W/cm}^2 \quad 6.4$$

The calculated mentioned parameters for a single pulse are summarized in Table 6.1. In the following, the influence of pulse energy E_p , peak laser fluence φ_{L_peak} and peak laser intensity I_{L_peak} on ablation depth and surface morphology are studied. According to the above equations, an increase in pulse energy E_p is followed by increasing peak laser fluence φ_{L_peak} and peak laser intensity I_{L_peak} . A linear relation between them can be found. However, these three calculated parameters are included in the following figures to illustrate the results comprehensively.

Table 6.1: Calculated laser parameters.

No	Average laser power P_{L_ave} in W	Pulse energy E_p in μJ	Peak laser fluence φ_{L_peak} in J/cm^2	Peak laser intensity I_{L_peak} in W/cm^2
1	5	12.5	0.498	2.49×10^{10}
2	10	25	0.995	4.98×10^{10}
3	15	37.5	1.49	7.46×10^{10}
4	20	50	1.99	9.95×10^{10}
5	25	62.5	2.49	12.4×10^{10}
6	30	75	2.99	14.9×10^{10}
7	35	87.5	3.48	17.4×10^{10}
8	40	100	3.98	19.9×10^{10}
9	45	112.5	4.48	22.4×10^{10}
10	50	125	4.98	24.9×10^{10}

Figure 6.1 provides the influence of pulse energy E_p , peak laser fluence φ_{L_peak} and peak laser intensity I_{L_peak} on ablation depth at constant pulse number of $N_p = 90$. A higher magnitude of pulse energies results in more ablation depth. More pulse energies E_p is followed by higher peak laser fluences φ_{L_peak} on the workpiece surface and eventually more material removal. High-temperature free electrons of titanium alloy material under laser processing transfer energy to the bound electrons of the lattice accompanied by high temperature and dense plasmas [162]. Eventually, the material removal occurs through plasma separation under coulomb repulsion.

Correspondingly, higher peak laser fluences ϕ_{L_peak} through increasing pulse energy E_p results in more high-temperature free electrons, accumulation of photon energy, and more generation of free-carrier plasmas. This leads to increasing ablation depth, particularly from $\phi_{L_peak} = 2.49 \text{ J/cm}^2$ to $\phi_{L_peak} = 2.99 \text{ J/cm}^2$ (Figure 6.1). Another reason for accelerating the ablation is the heat accumulation in the metal [186]. Heat accumulation considerably rises at higher laser fluences. Therefore, an increase in peak laser fluence ϕ_{L_peak} leading to a jump in ablation depth (as illustrated in Figure 6.1) can also be associated with a considerable rise in heat accumulation.

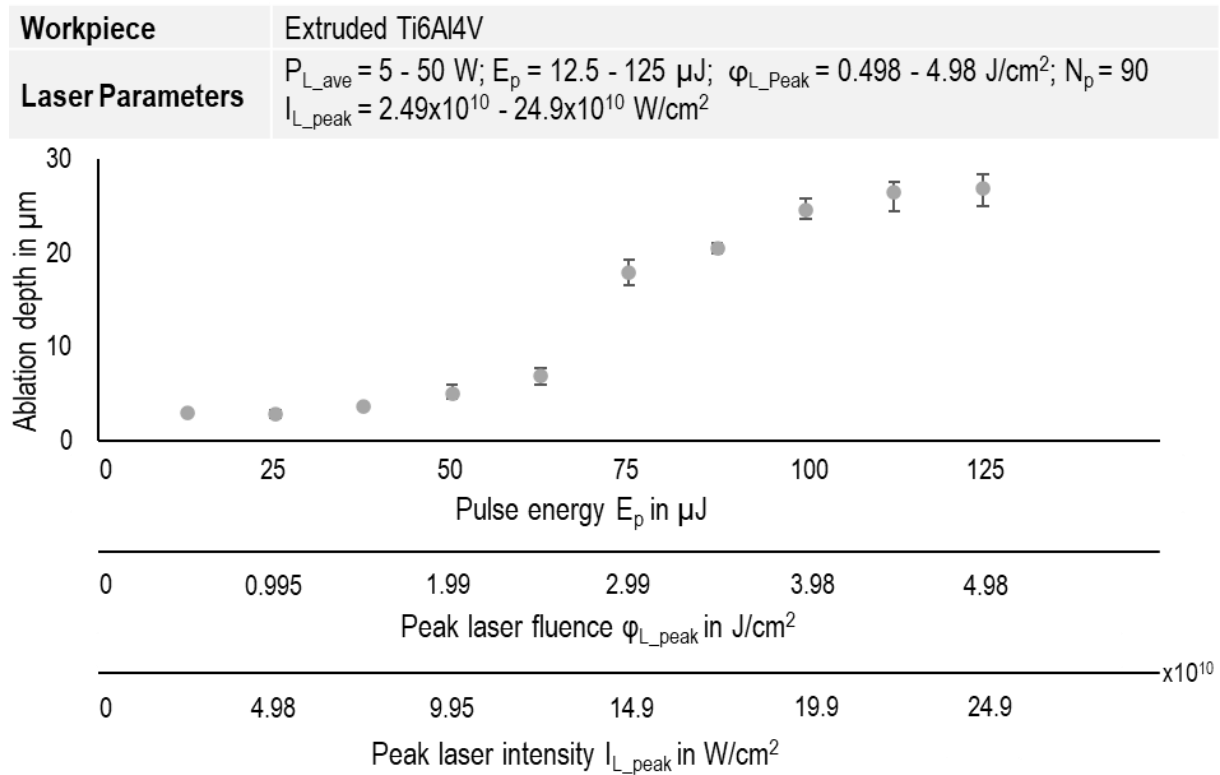


Figure 6.1: Influence of pulse energy E_p , peak laser fluence ϕ_{L_peak} and peak laser intensity I_{L_peak} on ablation depth at $N_p = 90$.

The reflection of the laser beam from the workpiece surface negatively affects the workpiece ablation volume. Generally, several factors influence surface reflectivity, such as polarization, laser intensity, sample surface roughness, phase transition and oxide films [187–190]. It is known that high laser intensities result in less surface reflectivity [191]. Therefore, increased peak laser intensity I_{L_peak} from 2.49 W/cm^2 to 14.9 W/cm^2 accompanied by more ablation depth can also be associated with reduced reflectivity and more laser absorption.

Equation 6.5 describes the Beer-Lambert law, which indicates that the laser intensity decays exponentially throughout the depth.

$$I(z) = (1 - R)I_0 e^{-\alpha_{abs}z} \quad 6.5$$

where R , α_{abs} and I_0 are surface reflectivity, absorption coefficient, and laser intensity, respectively. At constant surface reflectivity R and absorption coefficient α_{abs} , an increase in initial laser intensity I_0 results in more laser penetration. Additionally, an increase in initial laser intensity I_0 is accompanied by less reflectivity R that leads to

accelerating a rise in laser penetration depth according to equation 6.5 that is followed by more ablation depth.

For metals, the energy transfer between electron and lattice system has been studied by the Two Temperature Model (TTM) proposed by Anisimov et al. [192].

$$C_e(T_e) \frac{\partial T_e}{\partial t} = \nabla[K_e(T_e, T_i) \nabla T_e] - G(T_e)(T_e - T_i) + S(r, t_p) \quad 6.6$$

$$C_i(T_i) \frac{\partial T_i}{\partial t} = \nabla[K_i(T_i) \nabla T_i] + G(T_e)(T_e - T_i) \quad 6.7$$

where C and K are heat capacities, and thermal conductivities of the electron and lattice as denoted by subscript e and i , respectively, and $S(r, t_p)$ is the energy source of the laser pulse. T_e and T_i denote electron and lattice temperature, respectively. $G(T_e)$ is the electron-phonon coupling factor as a rate of energy exchange between electrons and lattice. A higher coupling factor results in more energy transfer from the electron to the lattice. This factor is a function of electron temperature, and this dependency has been investigated by Lin et al. [193]. As reported, an increase in electron temperature T_e leads to a non-monotonic change in electron-phonon coupling for titanium material. There is an increase in electron-phonon coupling factor with electron temperature. Afterwards, an electron-phonon coupling factor decreases. Therefore, increasing laser ablation with a rise in laser energy source could not be justified by changes in the electron-phonon coupling factor for the titanium material. The energy transfer from photon to electrons and then to the lattice is proved in [192]. The heat conduction between electron and lattice would continue while there is no thermal equilibrium between them. Under higher laser fluences, the electron temperature would be higher, which leads to a greater rate of electron heat conduction and a longer time for the electron subsystem to reach thermal equilibrium with the lattice. Therefore, more time for heat conduction from electron to lattice is followed by higher lattice temperature with more heat penetration depth. Thus, the ablation is not limited to the optical penetration depth. Consequently, the ablation would increase with increasing the share of other phenomena in the material removal, such as melting, vaporization and phase explosion. Further increase in pulse energy E_p from 75 μJ to 125 μJ , or ϕ_{L_peak} ranged from 2.99 J/cm^2 to 4.98 J/cm^2 and I_{L_peak} from 14.9 W/cm^2 to 24.9 W/cm^2 , led to a saturation state of ablation depth (see Figure 6.1).

Zheng et al. [158] explained that under high laser fluences, a considerably accumulated free-carrier plasma with a high density leads to difficulty in splashing the plasma under the coulomb repulsion and eventually, partial deposition of the plasma remains on the material's surface. Therefore, the deposited plasma causes a gradual saturation of the ablation feature size trend. In addition, the laser emission passes through the plasma, metal vapor, electrons, ions, and neutral particles, followed by absorbing some part of the laser energy. This shielding effect results in minimal energy radiation on the metal surface and eventually a decrease in material ablation rate.

As mentioned, the ablation threshold for titanium alloy was reported between 0.24 J/cm^2 and 0.28 J/cm^2 for a single pulse and accounted for a range between 0.08 J/cm^2 and 0.21 J/cm^2 for multiple pulses. This variation in the results can be associated with uncertainty in the measurement and applying varied laser process

parameters in different studies. The interaction between USPL and metallic material includes complicated processes such as melting, vaporization, spallation, phase explosion, etc., that are not easily differentiable [194,195]. In USPL, two ablation regimes can be determined. In a low ablation regime, the ablation is only limited to the laser optical penetration depth, while thermal penetration depth plays an important role in the high ablation regime. The mechanism of ablation differs in these two regimes. Spallation at low laser fluences and phase explosion at high laser fluences can be considered as the dominant material removal mechanism. According to Perez and Lewis [196], spallation occurs due to the expansion and remarkable change in the internal pressure of solid material where the stress goes above the material tensile strength limit. As a result, many pores near the surface initiate, grow and coalesce, that eventually leads to the ejection of the topmost layer of the surface layer. In the current study, the calculated peak laser fluences ϕ_{L_peak} ranging from 0.498 J/cm² to 4.98 J/cm² (see Table 6.1) indicate values much higher than the reported ablation threshold values. Since spallation occurs at laser fluences near the ablation threshold, it can be concluded that the dominance of phase explosion rather than spallation is more expected in the range of introduced process parameters.

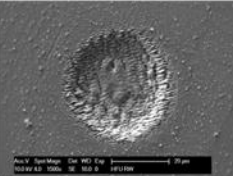
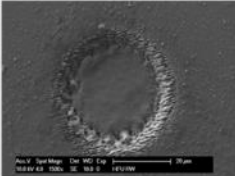
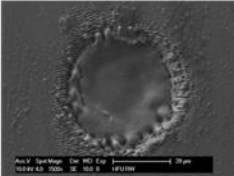
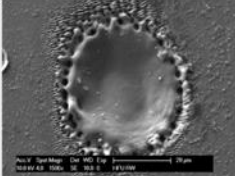
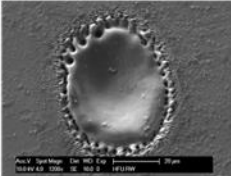
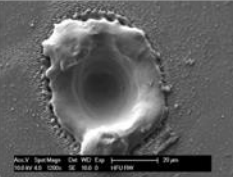
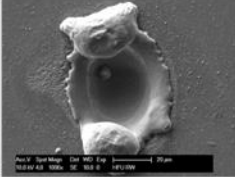
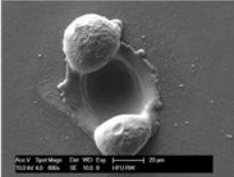
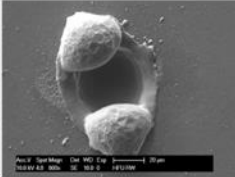
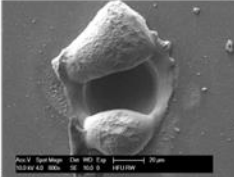
Workpiece	Extruded Ti6Al4V				
Laser Parameters	$P_{L_ave} = 5 - 50 \text{ W}$; $E_p = 12.5 - 125 \text{ }\mu\text{J}$; $\phi_{L_Peak} = 0.498 - 4.98 \text{ J/cm}^2$; $N_p = 90$ $I_{L_peak} = 2.49 \times 10^{10} - 24.9 \times 10^{10} \text{ W/cm}^2$				
$E_p = 12.5 \text{ }\mu\text{J}$ $\phi_{L_peak} = 0.498 \text{ J/cm}^2$ $I_{L_peak} = 2.49 \times 10^{10} \text{ W/cm}^2$	$E_p = 25 \text{ }\mu\text{J}$ $\phi_{L_peak} = 0.995 \text{ J/cm}^2$ $I_{L_peak} = 4.98 \times 10^{10} \text{ W/cm}^2$	$E_p = 37.5 \text{ }\mu\text{J}$ $\phi_{L_peak} = 1.49 \text{ J/cm}^2$ $I_{L_peak} = 7.46 \times 10^{10} \text{ W/cm}^2$	$E_p = 50 \text{ }\mu\text{J}$ $\phi_{L_peak} = 1.99 \text{ J/cm}^2$ $I_{L_peak} = 9.95 \times 10^{10} \text{ W/cm}^2$	$E_p = 62.5 \text{ }\mu\text{J}$ $\phi_{L_peak} = 2.49 \text{ J/cm}^2$ $I_{L_peak} = 12.4 \times 10^{10} \text{ W/cm}^2$	
					
$E_p = 75 \text{ }\mu\text{J}$ $\phi_{L_peak} = 2.99 \text{ J/cm}^2$ $I_{L_peak} = 14.9 \times 10^{10} \text{ W/cm}^2$	$E_p = 87.5 \text{ }\mu\text{J}$ $\phi_{L_peak} = 3.48 \text{ J/cm}^2$ $I_{L_peak} = 17.4 \times 10^{10} \text{ W/cm}^2$	$E_p = 100 \text{ }\mu\text{J}$ $\phi_{L_peak} = 3.98 \text{ J/cm}^2$ $I_{L_peak} = 19.9 \times 10^{10} \text{ W/cm}^2$	$E_p = 113 \text{ }\mu\text{J}$ $\phi_{L_peak} = 4.48 \text{ J/cm}^2$ $I_{L_peak} = 22.4 \times 10^{10} \text{ W/cm}^2$	$E_p = 125 \text{ }\mu\text{J}$ $\phi_{L_peak} = 4.98 \text{ J/cm}^2$ $I_{L_peak} = 24.9 \times 10^{10} \text{ W/cm}^2$	
					

Figure 6.2: Influence of pulse energy E_p , peak laser fluence ϕ_{L_peak} and peak laser intensity I_{L_peak} on surface morphology at $N_p = 90$.

The laser beam follows Gaussian distribution, resulting in more pulse energy E_p on the workpiece surface at the center than on the outer side. This leads to a different ablation regime and a variation in surface morphology throughout the laser spot radius. According to Figure 6.2, the Laser Induced Periodic Surface Structures (LIPSS) at the outer side of generated profile at $\phi_{L_peak} = 0.498 \text{ J/cm}^2$ can be seen. Several studies have investigated the formation of LIPSS and their different types. According to [197], they are formed by the interference of incident laser and surface plasmon polaritons caused by laser irradiation on the workpiece surface under certain conditions. As mentioned in the study of Bonse et al. [198], several factors influence the generation of LIPSS. Apart from the laser wavelength, the laser beam

polarization, the angle of incident and the local environment, the laser fluence and the number of laser pulses play a role in the generation of LIPSS. Since these two parameters vary in this study, their influence on LIPSS and surface morphology has been discussed in the following.

At the center of the profile at $\phi_{L_peak} = 0.498 \text{ J/cm}^2$, the initiation of melting and bridging between the ripple structures is detected. Increasing laser peak fluence ϕ_{L_peak} from 0.995 J/cm^2 to 2.49 J/cm^2 leads to the progress of melting, or liquid phase, and complete elimination of ripple structure at the center. Moreover, the micro-holes, in addition to the ripple structures at the outer side of generated profile for laser peak fluences ϕ_{L_peak} ranging from 0.995 J/cm^2 to 2.49 J/cm^2 can be observed. The affected area at $\phi_{L_peak} = 2.99 \text{ J/cm}^2$ shows a considerably deeper profile than that at $\phi_{L_peak} = 2.49 \text{ J/cm}^2$. This corresponds to a considerable rise in ablation depth illustrated in Figure 6.1. Additionally, melted material at $\phi_{L_peak} = 2.99 \text{ J/cm}^2$ was deposited on the outer side of the crater. By increasing peak laser fluence ϕ_{L_peak} through an increase in pulse energy E_p , the amount of the deposited molten material drastically increases outside the profile. Higher laser fluences lead to the formation of a considerable liquid phase, flowing the molten metal and formation of the bulges around the crater due to the combined phenomena of recoil pressure and surface tension [162].

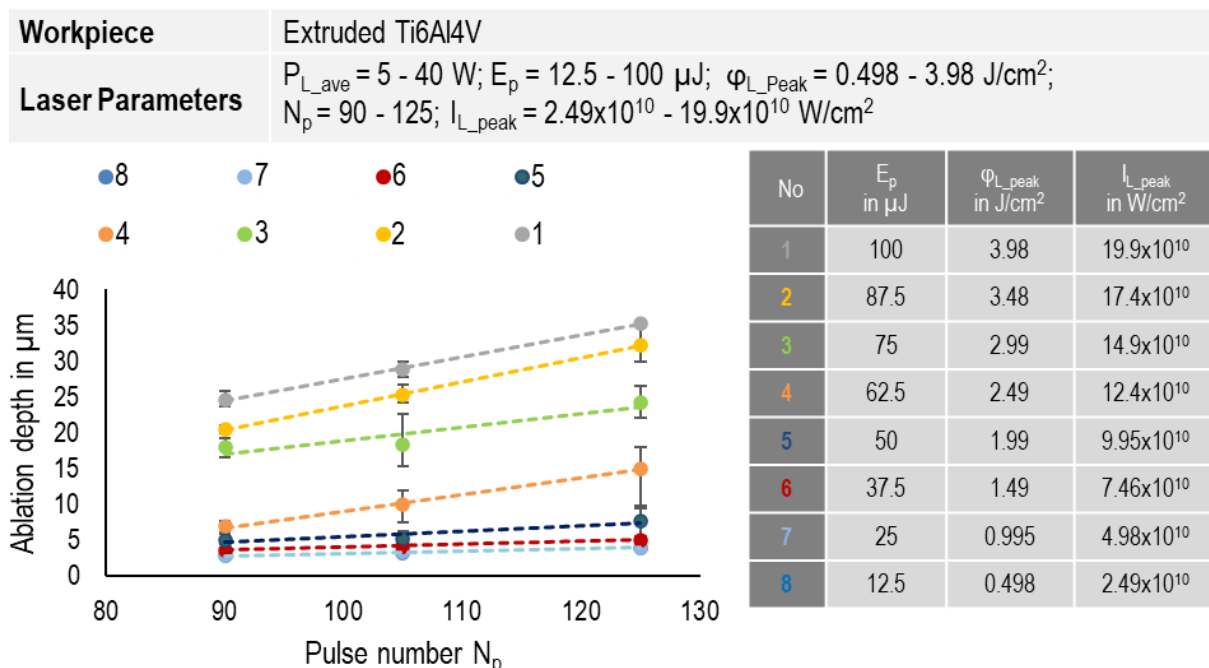


Figure 6.3: Influence of pulse number N_p , pulse energy E_p (corresponding to the peak laser fluence ϕ_{L_peak} and peak laser intensity I_{L_peak}) on ablation depth.

The influence of pulse number and pulse energy E_p , corresponding to the peak laser fluence ϕ_{L_peak} and peak laser intensity I_{L_peak} , on ablation depth is summarized in Figure 6.3. An increase in pulse number increases the ablation depth. Accordingly, the influence of pulse number on ablation depth is not as high as the effect of pulse energy E_p . As can be seen at pulse energies higher than $E_p = 50 \text{ } \mu\text{J}$, leading to greater peak laser fluences ϕ_{L_peak} as well as peak laser intensities I_{L_peak} , the influence of pulse number on the ablation depth is much more pronounced. More

heat and photon energy accumulation at higher laser fluences can lead to an acceleration in the ablation depth rise by introducing successive pulses [186].

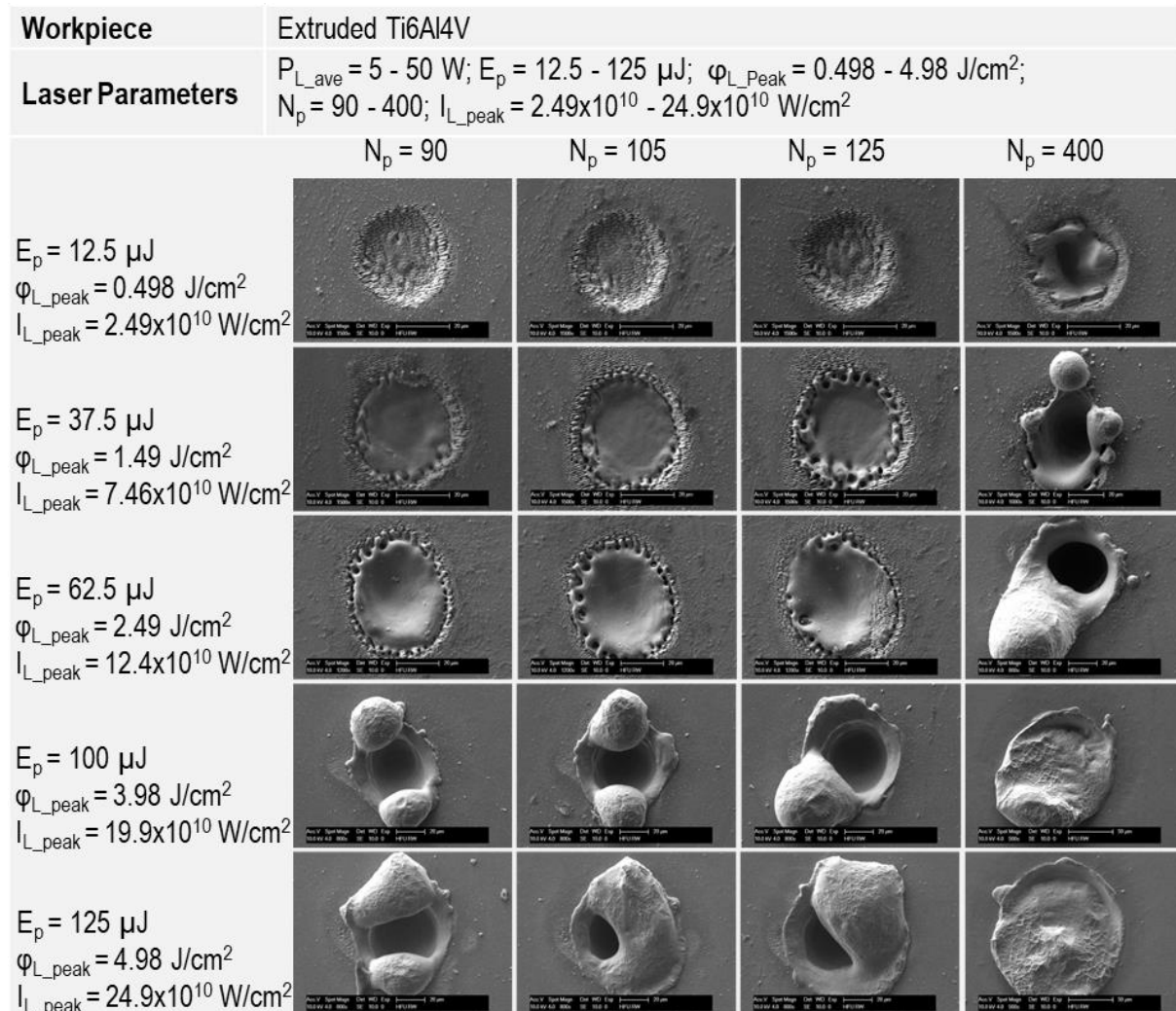


Figure 6.4: Influence of pulse energy E_p (corresponding to the peak laser fluence ϕ_{L_peak} and peak laser intensity I_{L_peak}) and pulse number N_p on the surface morphology.

Figure 6.4 provides the influence of pulse number on surface morphology at different pulse energies E_p , corresponding to different peak laser fluences ϕ_{L_peak} and peak laser intensities I_{L_peak} . At $\phi_{L_peak} = 0.498 \text{ J/cm}^2$, an increase in pulse number from 90 to 125 led to a slight increase in the liquid phase at the center of the crater with the presence of a ripple structure on the outside. More liquid phase formation with increasing pulse number can be related to heat accumulation. Further increasing the pulse number to 400 indicates a considerable deep crater and melted and recast surface. The influence of pulse numbers ranging from 90 to 125 at $\phi_{L_peak} = 1.49 \text{ J/cm}^2$ and 2.49 J/cm^2 led to a considerable volume of the liquid phase in the crater. However, micro-holes and ripple structures at the outside of the lasered profile can still be observed. At $N_p = 400$, a huge amount of condensed molten material outside the crater exists. At $\phi_{L_peak} = 3.98 \text{ J/cm}^2$, deeper craters were generated compared to those for lower magnitudes of peak laser fluences. The increase in pulse number led to increasing solidified molten material outside the crater. At $N_p = 400$, the molten material filled the crater. In fact, higher laser fluences result in increased accumulation of heat and photon energy, potentially leading to accelerated ablation

depth and the formation of a liquid phase with successive pulses. At $\phi_{L_peak} = 4.98 \text{ J/cm}^2$, the molten material is much more considerable than that at $\phi_{L_peak} = 3.98 \text{ J/cm}^2$. At $\phi_{L_peak} = 4.98 \text{ J/cm}^2$ and $N_p = 400$, the crater with the filled molten material can be again observed. The share of melting in the material removal at higher pulse energies E_p , or peak laser fluences ϕ_{L_peak} and intensities I_{L_peak} , is significant. It causes an acceleration in increasing ablation depth with the pulse number, as indicated in Figure 6.3.

According to Figure 6.4, at constant peak laser fluence, the number of pulses led to more melting formation, particularly at higher laser fluences. Deeper craters were formed at $N_p = 400$ up to $\phi_{L_peak} = 2.49 \text{ J/cm}^2$. It can be concluded that the role of peak laser fluence in melting formation and changing the surface morphology is considerable compared to the effect of pulse number.

6.2 Single linear laser scanning

For single linear laser scanning, laser scan velocity v_L and average laser power P_{L_ave} are determined as two main process parameters. Pulse energy E_p , peak laser fluence ϕ_{L_peak} , and peak laser intensity I_{L_peak} for a single pulse can be calculated based on P_{L_ave} as explained in the section of "Multiple laser pulses".

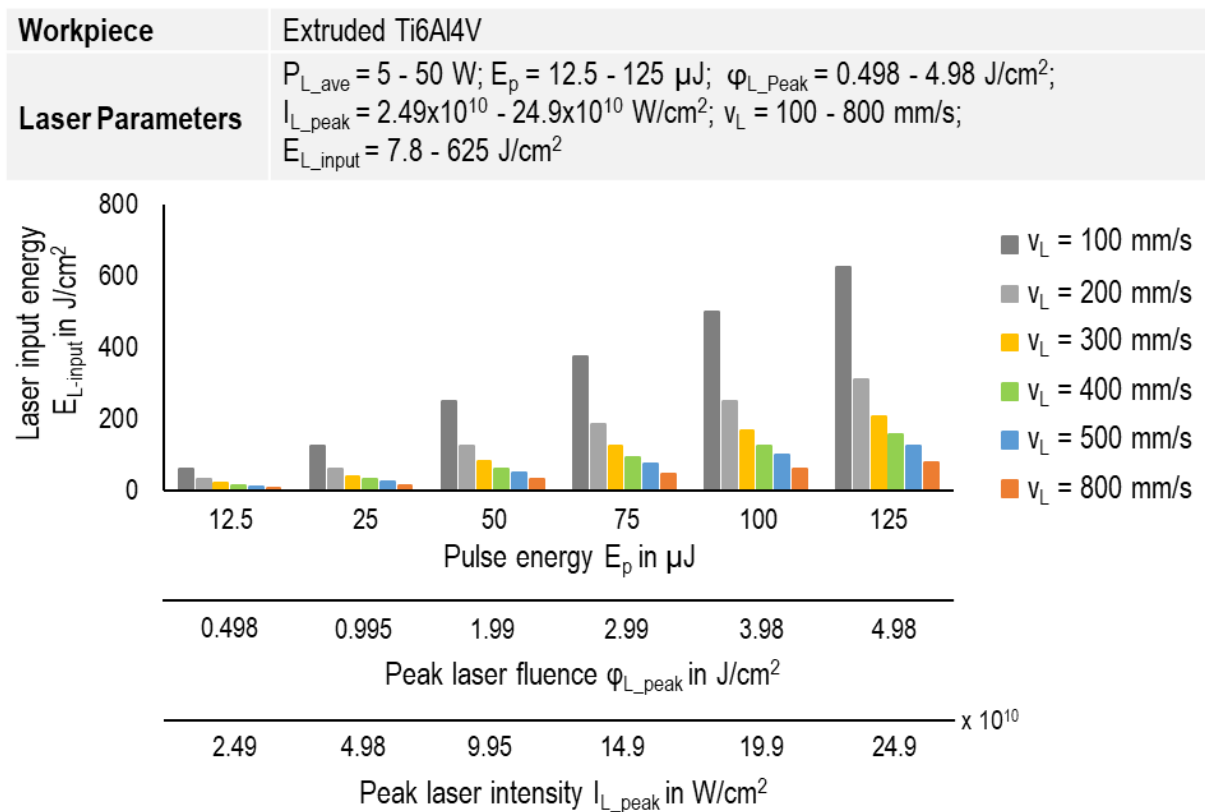


Figure 6.5: Correlation between pulse energy E_p (corresponding to peak laser fluence ϕ_{L_peak} and peak laser intensity I_{L_peak}) and calculated laser input energies E_{L_input} at different average laser powers P_{L_ave} and scan velocities v_L .

To consider the amount of energy transferred to the surface at different combinations of v_L and P_{L_ave} , the laser input energy E_{L_input} as an additional parameter is introduced as follows:

$$E_{L_input} = \frac{P_{L_ave}}{v_L \times D_L} \quad \text{in J/cm}^2 \quad 6.8$$

where D_L is the laser beam diameter. Accordingly, the laser input energy E_{L_input} is a function of v_L and P_{L_ave} .

Figure 6.5 illustrates the calculated E_{L_input} at different P_{L_ave} and v_L . Instead of P_{L_ave} ranging from 5 W to 50 W, the calculated parameters in terms of pulse energy E_p , peak laser fluence ϕ_{L_peak} and peak laser intensity I_{L_peak} are provided in the horizontal axis. Accordingly, a logarithmic increase in E_{L_input} can be seen by reducing v_L at constant E_p , or correspondingly constant ϕ_{L_peak} and I_{L_peak} . This logarithmic trend accelerates at higher magnitudes of E_p . In other words, the influence of v_L on E_{L_input} at higher magnitudes of E_p is much more considerable. Additionally, an increase in E_p results in an exponentially increasing E_{L_input} , and this trend speeds up at lower values of v_L . The following explains how the variation in E_{L_input} caused by different combinations of P_{L_ave} and v_L affect the surface morphology and the ablation process.

Figure 6.6 summarized top-view SEM images of lasered profiles created at different values of laser input energies, E_{L_input} . At constant scan speed, v_L , an increase in E_{L_input} is followed by changing the surface morphology. A rise in E_{L_input} at constant v_L corresponds to more pulse energy transferred to the workpiece surface and deeper laser penetration. This can be accompanied by more creation of melting. Particularly at scan velocities, v_L lower than 400 mm/s, a massive amount of melting could be observed by increasing E_{L_input} .

Moreover, the changing rate in surface morphology with E_{L_input} speeds up at lower laser scan velocities v_L . This is in accordance with the considerable rate of increase in E_{L_input} with pulse energy, E_p , or peak laser fluence, ϕ_{L_peak} , and peak laser intensity, I_{L_peak} , at lower values of v_L (see Figure 6.5). In fact, the number of pulse incidents on the workpiece surface increases at lower scan velocities and consequently, more damage accumulation is expected. This may lead to a dramatic change in the material removal mechanism, dominance of melting and vaporization rather than the material ionization, and rapid alternation in the surface morphology. At $v_L = 500$ and 800 mm/s, an increase in E_{L_input} only led to creating a liquid phase and joining the ripple structure in some areas of the lasered profile.

No sign of melting on the generated profiles could be observed at pulse energies, E_p , of 12.5 μJ and 25 μJ , even at low scanning speed, v_L , of 100 mm/s. The ripple microstructure is detectable, which highlights the dominance of direct solid-vapor transition as the material removal mechanism. A reduction in E_{L_input} through increasing v_L from 100 mm/s to 800 mm/s at $E_p = 12.5 \mu\text{J}$ and 25 μJ led to a slight variation in surface morphology. The rate of this change in the surface morphology with v_L is much more considerable for higher values of E_p , corresponding to higher ϕ_{L_peak} and I_{L_peak} . This also corresponds to a tremendous variation in E_{L_input} with changing v_L at higher values of E_p , as illustrated in Figure 6.5. At constant pulse energy E_p , an increase in v_L is followed by a reduction in the number of pulse incidents. Therefore, a change in surface morphology due to less damage accumulation is expected. Since heat accumulation at higher pulse energies E_p is considerable, a reduction in pulse incidents remarkably influences decreasing melting formation and even changing the dominant material removal mechanism.

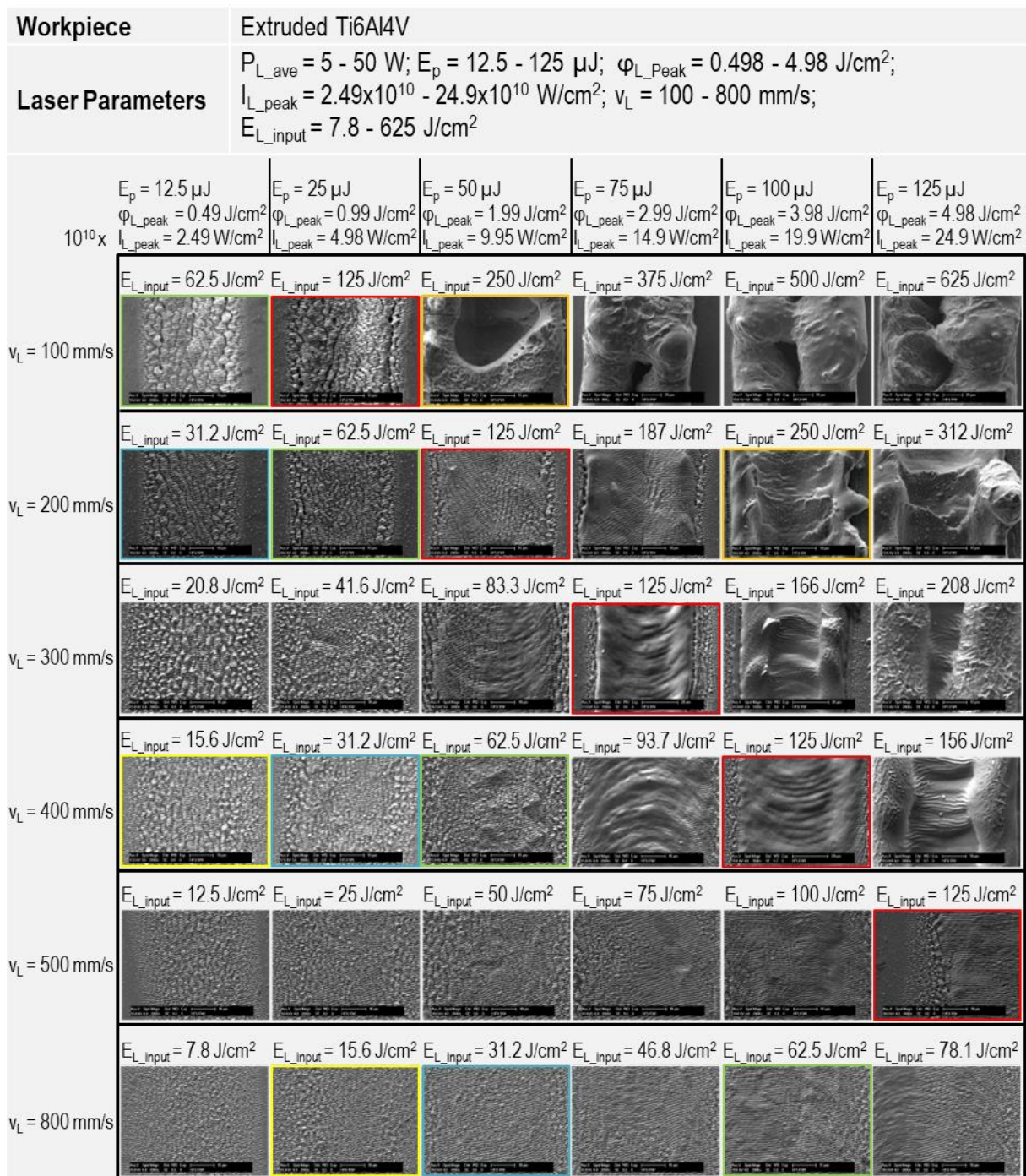


Figure 6.6: SEM images of lasered profiles at different laser input energies E_{L_input} .

According to Figure 6.6, a variation in surface morphology could be observed by changing the values of v_L and E_p , corresponding to ϕ_{L_peak} and I_{L_peak} , at constant laser input energies, E_{L_input} . For instance, at $E_{L_input} = 125 \text{ J/cm}^2$ (red color), a variation in surface morphology from ripple microstructure to considerable melting could be detected. This wide range of changes in surface morphology indicates that the constant E_{L_input} cannot guarantee the same effects on the workpiece surface. This issue will be discussed in detail in the next section of "Multiple linear laser scanning".

For analyzing the geometrical features, confocal microscopy was used to measure lasered profiles. Further, TXT files, exported from measurement software, were

imported into MATLAB. Using a written script, mean profiles could be obtained from the measured 3D profiles. To calculate the mean profile, the lasered profile should be horizontally aligned. In this regard, the given 3D profile shown in Figure 6.7a is subjected to the rotational matrix with a determined rotational angle. Next, the area of the rotated profile, which is highlighted by gray color in Figure 6.7b, is filled and the rotated 3D profile in Figure 6.7c can be obtained. The average calculation through the whole of the 3D profile (in Figure 6.7c) results in the 2D profile shown in Figure 6.7d. This procedure was carried out for all experimental tests.

Figure 6.8 provides ablation depth, ablation rate, ablation area and MRR calculated from obtained 2D profiles at different scanning speeds, v_L , and average laser powers, P_{L_ave} , that leads to different pulse energies E_p , peak laser fluences ϕ_{L_peak} , and peak laser intensities I_{L_peak} . These four parameters (P_{L_ave} , E_p , ϕ_{L_peak} and I_{L_peak}) are summarized in a table in Figure 6.8. Since a massive melting occurred for most of the lasered profiles at $v_L = 100$ mm/s, it was impossible to measure the geometrical features. Therefore, the results for this scan velocity have been excluded from Figure 6.8.

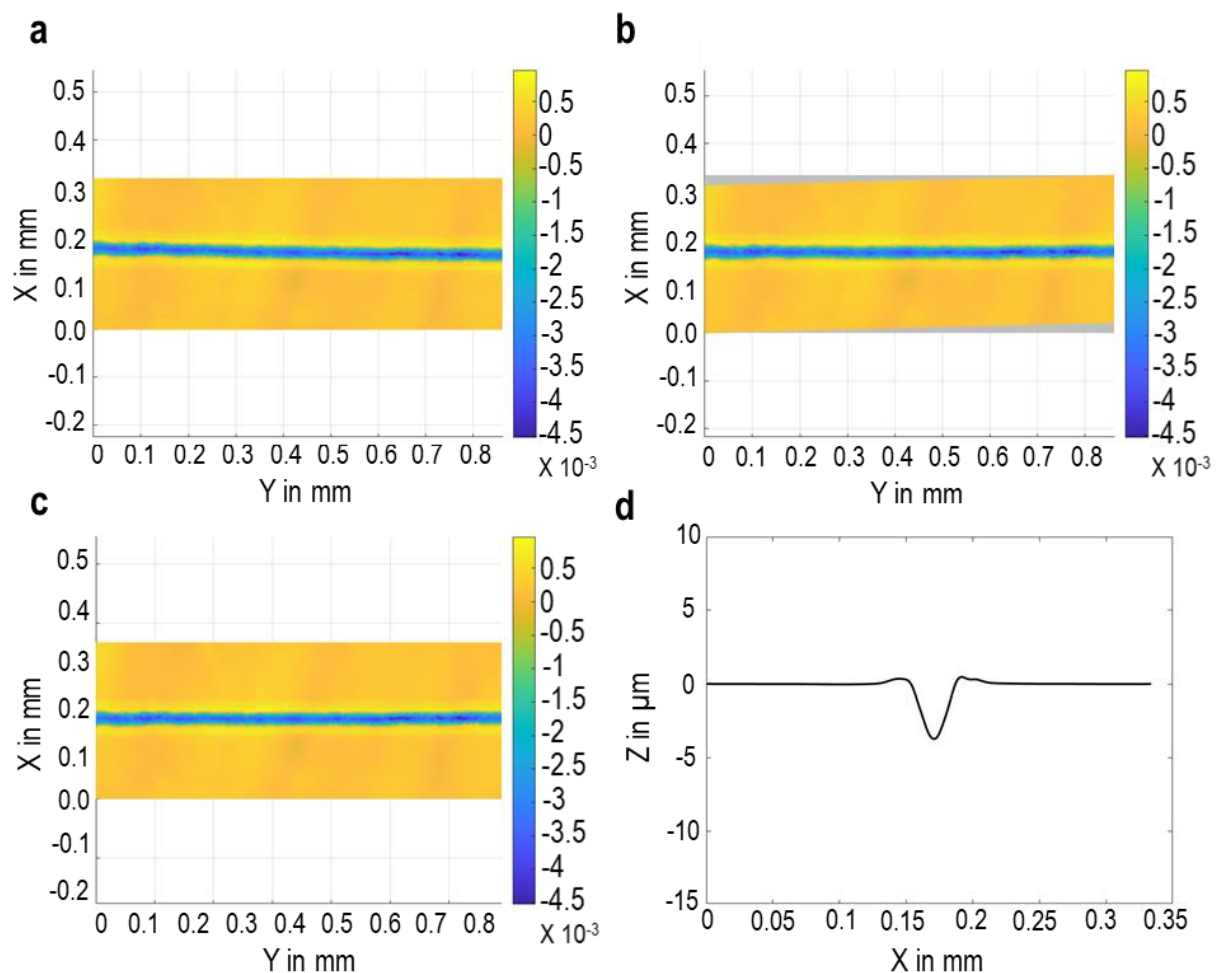


Figure 6.7: The procedure of calculating the mean profile: a) given Profile, b) rotated profile, c) filled profile, d) mean 2D Profile.

According to Figure 6.8a, an increase in pulse energy E_p , resulting in higher ϕ_{L_peak} and I_{L_peak} , is followed by more ablation depth at all scan velocities. In detail, the rate of increasing ablation depth with E_p is higher at lower scan velocities, particularly for $v_L = 200, 300$ and 400 mm/s. The considerable rise in E_{L_input} with pulse energy E_p at

lower values of v_L shown in Figure 6.5 leads to more heat accumulation, changing the dominance of the material removal mechanism to significant melting and vaporization, instead of direct solid-vapor transition, and eventually a dramatic rise in the ablation depth.

No	Average laser power P_{L_ave} in W	Pulse energy E_p in μJ	Peak laser fluence ϕ_{L_peak} in J/cm^2	Peak laser intensity I_{L_peak} in W/cm^2
1	5	12.5	0.498	2.49×10^{10}
2	10	25	0.995	4.98×10^{10}
3	20	50	1.99	9.95×10^{10}
4	30	75	2.99	14.9×10^{10}
5	40	100	3.98	19.9×10^{10}
6	50	125	4.98	24.9×10^{10}

■ $v_L = 200$ mm/s ■ $v_L = 300$ mm/s ■ $v_L = 400$ mm/s ■ $v_L = 500$ mm/s ■ $v_L = 800$ mm/s

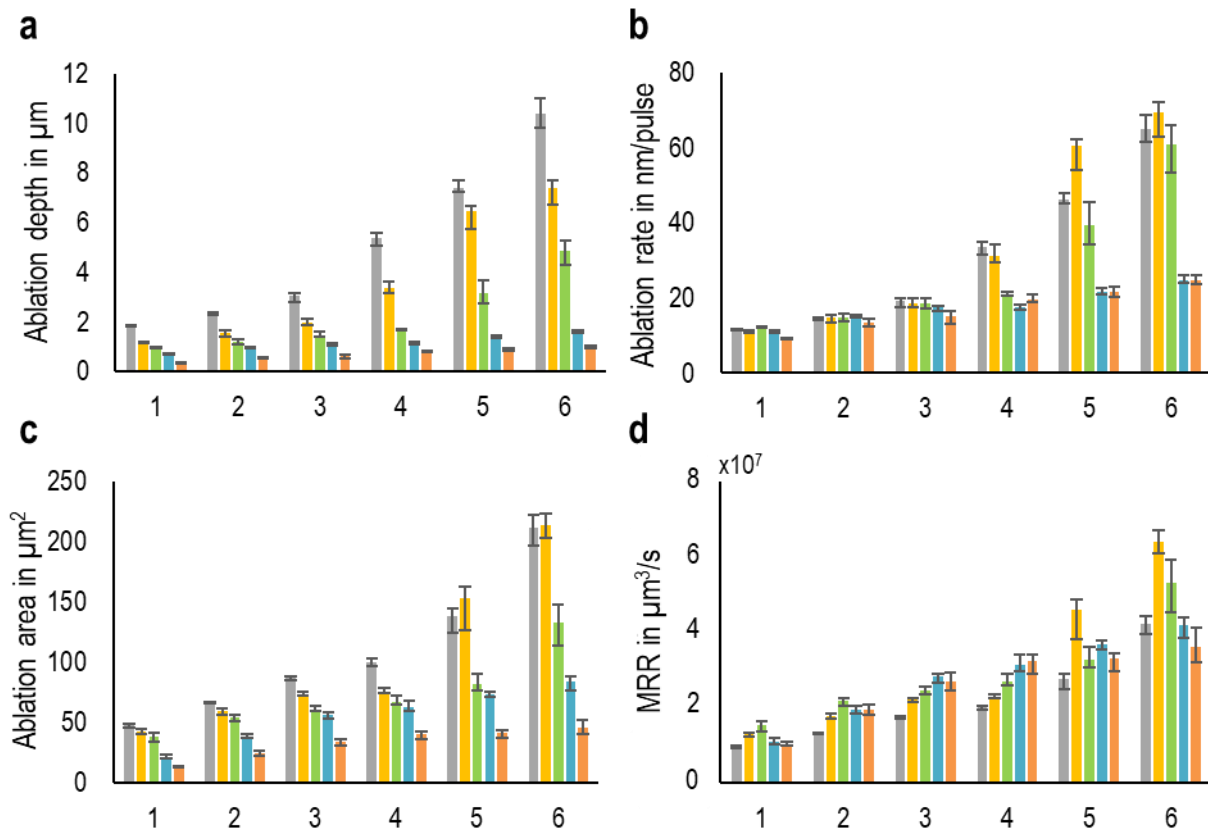


Figure 6.8: Influence of pulse energy E_p (corresponding to peak laser fluence ϕ_{L_peak} and peak laser intensity I_{L_peak}) and velocity v_L on: a) ablation depth, b) ablation rate, c) ablation area, d) MRR.

According to Figure 6.6, a considerable melted material can be seen for scan velocities, $v_L = 200, 300$ and 400 mm/s, after $E_p = 50 \mu\text{J}$, confirming a rapid increase in ablation depth due to more melting and vaporization. Moreover, a dramatic rise in laser input energy introduced on the workpiece surface leads to more laser penetration depth accompanied by more ablation depth. As illustrated in Figure 6.8a,

an increase in ablation depth with E_p , correspondingly ϕ_{L_peak} and I_{L_peak} , at $v_L = 500$ and 800 mm/s is not as significant as that at lower scan velocities. No dramatic change in surface morphology and mainly creation of ripple structure at all values of E_p , or ϕ_{L_peak} and I_{L_peak} , for $v_L = 500$ and 800 mm/s shown in Figure 6.6 highlights the dominance of material ionization and, consequently, no dramatic change in ablation depth.

As shown in Figure 6.8a, a reduction in v_L at constant E_p , or ϕ_{L_peak} and I_{L_peak} , led to a rise in ablation depth. According to Figure 6.5, a logarithmic increase in E_{L_input} through reduction of v_L with the same trend could be detected. This highlights how considerable is the influence of a rise in E_{L_input} on the progress of ablation depth. At higher magnitudes of P_{L_ave} , corresponding to E_p , ϕ_{L_peak} and I_{L_peak} , the rate of logarithmic increase in ablation depth with reduction of v_L is much more considerable. According to Figure 6.6, the surface morphology at higher magnitudes of E_p has rapidly changed by a decrease in the scan velocity accompanied by significant melting. This confirms the dramatic changing in the material removal mechanism, more laser heat penetration and the dominance of melting and vaporization. As a result, a significant rise in ablation depth at higher pulse energies with reducing v_L is expectable.

For calculation of ablation rate, since the ablation width was almost constant for all experiments, the ablation depth is divided by the number of pulses N_p on the material surface in one beam diameter of laser movement. N_p is calculated as follows:

$$N_p = \frac{D_L}{v_L} \times f_L \quad 6.9$$

Accordingly, the number of pulses varied from 160 to 40 for scan velocities ranging from 200 mm/s to 800 mm/s. Figure 6.8b provides the ablation per pulse at different process parameters. Accordingly, the ablation per pulse at different scan velocities has slight variation at lower magnitudes of pulse energies, particularly $E_p = 12.5$ and 25 and 50 μJ . At linear laser scanning with constant E_p , a reduction in scan velocity increases the number of pulses on the material surface, followed by higher ablation depth. However, the ablation rate has not the same trend. Ablation per pulse for lower pulse energies, $E_p = 12.5$, 25 and 50 μJ , shows no considerable variation at different scan velocities. This indicates that during the material ablation, the successive pulses did not considerably influence the induced ablation in the case of lower pulse energies. No remarkable change in surface morphologies with changing scan velocity (shown in Figure 6.6) also confirms this issue. On the contrary, at higher pulse energies, specifically for $E_p = 75$, 100 and 125 μJ , a high degree of variation in ablation per pulse could be seen. According to Figure 6.6, decreasing v_L at mentioned pulse energies dramatically changed surface morphology and led to a massive formation of melted material. This highlighted the considerable influence of the number of pulses with high energy on surface morphology and a remarkable variation in ablation per pulse.

The calculated ablation area at different process parameters is summarized in Figure 6.8c. An increase in pulse energy E_p leads to removing more material at different scan velocities. As can be seen, the rate of increase in ablation area with E_p is much higher at $v_L = 200$, 300 and 400 mm/s compared with $v_L = 500$ and 800 mm/s. This trend is the same for the ablation depth. At $E_p = 12.5$, 25 , 50 and 75 μJ , a reduced v_L

followed by increasing E_{L_input} resulted in more ablation area. However, the ablation area does not follow this trend when scan velocity is reduced at $E_p = 100$ and $125 \mu\text{J}$. This can be related to a considerable amount of melting at higher pulse energies and lower scan velocities that leads to re-solidification of melted material rather than its removal from the crater and eventually irregular trend of ablation area with v_L . This may also affect ablation per pulse at $E_p = 100$ and $125 \mu\text{J}$ where its value at $v_L = 300$ mm/s is higher than that at $v_L = 200$ mm/s.

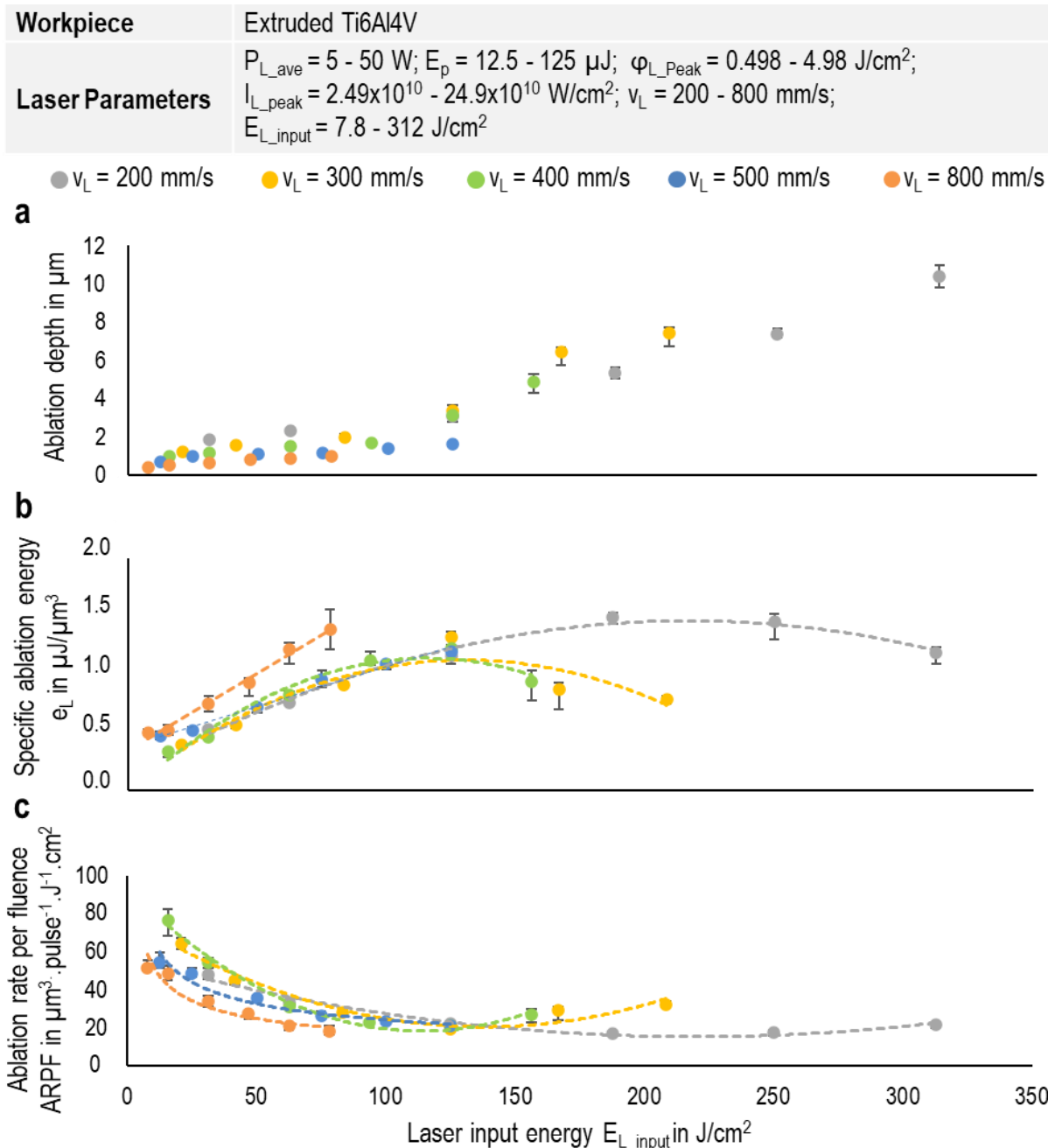


Figure 6.9: Correlation between laser input energy E_{L_input} and: a) and ablation depth, b) specific ablation energy e_L , c) ablation rate per fluence ARPF.

As shown previously, increasing E_p , correspondingly ϕ_{L_peak} and I_{L_peak} , and reducing v_L followed by higher magnitudes of E_{L_input} led to more ablation depth and area. However, this does not guarantee more MRR, according to Figure 6.8d. Apart from $E_p = 100$ and $125 \mu\text{J}$ that resolidified melted material affected the material removal,

increasing v_L at constant pulse energies always did not result in more MRR. Accordingly, there is an optimum v_L for the maximum MRR, and this optimum value varies at different pulse energies.

Figure 6.9a provides a correlation between laser input energy E_{L_input} and ablation depth. Accordingly, an increase in ablation depth with E_{L_input} can be seen at different scan velocities. Increasing the E_{L_input} from 125 J/cm^2 caused a dramatic rise in ablation depth, even at various scan speeds, i.e., $v_L = 200, 300$ and 400 mm/s . This is mainly related to more melting and vaporization in the ablation process (see Figure 6.6). For $v_L = 500$ and 800 mm/s , ablation depth with E_{L_input} ranged from 7.8 J/cm^2 to 125 J/cm^2 shows a slight linear increase. The surface morphologies at $E_{L_input} < 125 \text{ J/cm}^2$ showed limited or no melting and, therefore, the dominance of material ionization. A comparison between measured ablation depth at different v_L indicates that an increase in E_{L_input} always does not guarantee higher ablation depth in single linear laser scanning. In addition to a variation in surface morphology, a different ablation depth can be seen at various constant laser input energies, $E_{L_input} = 15.625 \text{ J/cm}^2, 31.25 \text{ J/cm}^2, 62.5 \text{ J/cm}^2$ and 125 J/cm^2 . This issue will be discussed in the next section.

Figure 6.9b and c indicate specific ablation energy e_L and Ablation Rate Per Fluence ARPF versus laser input energy E_{L_input} , respectively. The specific ablation energy is considered as a good indicator for evaluating the ablation efficiency. In detail, lower specific energy means better ablation efficiency. To make the measured material removal independent of the number of pulses, varied at different scan velocities, and laser energy, corresponding to peak laser fluence ϕ_{L_peak} , ARPF is introduced and calculated as follows:

$$\text{ARPF} = \frac{A \times v_L}{f_L \times \phi_{L_peak}} \quad \text{in } \mu\text{m}^3 \cdot \text{pulse}^{-1} \cdot \text{J}^{-1} \cdot \text{cm}^2 \quad 6.10$$

where A is the ablation area. According to Figure 6.9b, the specific ablation energy increases linearly with E_{L_input} at scan velocities $v_L = 500$ and 800 mm/s . It indicates that the rate of increase in energy transferred on the workpiece surface is higher than the rate of increasing material removal. According to Figure 6.6, an increase in E_{L_input} at $v_L = 500$ and 800 mm/s led to the local formation of melting on the workpiece surface. In fact, at higher magnitudes of E_{L_input} , the share of transferred energy on the workpiece surface causing material removal decreases and is consumed in locally melting formation. This also led to an exponentially decreasing trend for ARPF with E_{L_input} , as indicated in Figure 6.9c. At $v_L = 800 \text{ mm/s}$, the specific ablation energy is higher than that at $v_L = 500 \text{ mm/s}$. The number of pulse incidents on the material surface in one laser beam diameter movement at $v_L = 500 \text{ mm/s}$ accounts for 64, which is higher than that for $v_L = 800 \text{ mm/s}$ (with 40 pulses). Increasing the number of pulses could ease the material removal for subsequent pulses. Thus, less specific ablation energy at $v_L = 500 \text{ mm/s}$ is expected, leading to more ARPF (Figure 6.9c). At $v_L = 200, 300$ and 400 mm/s , a non-monotonic change in specific ablation energy with E_{L_input} can be observed. The specific ablation energy increases with E_{L_input} . Afterwards, a reduction in e_L can be seen. In the case of ARPF, initially a decreasing and further an increasing trend with increasing E_{L_input} is observable. This turning point varies and equals to $E_{L_input} = 187.5 \text{ J/cm}^2$ for scan velocity $v_L = 200 \text{ mm/s}$, and $E_{L_input} = 125 \text{ J/cm}^2$ for scan velocities $v_L = 300$ and 400

mm/s, respectively. A considerable amount of heat accumulation at higher laser input energies, corresponding to higher pulse energies, accelerates the material removal. This was followed by the reducing trend in the specific ablation energy and an increase in ARPF. Considerable melting confirms remarkable heat accumulation for scan velocities $v_L = 200, 300$ and 400 mm/s at higher magnitudes of E_{L_input} as indicated in Figure 6.6.

6.3 Multiple linear laser scanning

According to equation 6.8, laser input energy E_{L_input} is a function of two variables, average laser power P_{L_ave} and scan velocity v_L . Based on this formula, power and scan velocity can be changed to lead to a constant E_{L_input} . The following aims to answer the question of whether constant E_{L_input} obtained from different combinations of P_{L_ave} and v_L has the same effect on surface morphology and the ablation process. In this regard, four sets of laser parameters were selected to obtain a constant E_{L_input} of 3.9 J/cm². Table 6.2 summarizes applied laser parameters.

Table 6.2: Laser parameters.

No	P_{L_ave} in W	v_L in mm/s
1	6.25	200
2	12.5	400
3	25	800
4	50	1600

Figure 6.10 provides SEM images from the top view of lasered profiles at different scanning numbers N_s for different sets of P_{L_ave} and v_L . An increase in N_s led to a degradation of lasered profile for each set of laser parameters. Moreover, a remarkable difference between surface morphologies among different sets of laser parameters can be seen. This change is considerably faster and remarkable at lower average laser powers and scan velocity values, particularly for $P_{L_ave} = 6.25$ W and $v_L = 200$ mm/s. The calculation of pulse overlap (PO) according to equation 6.11 for scan velocities ranging from 200 mm/s to 1600 mm/s indicates no notable change (the value varied from 99.3 % to 95 %).

$$PO = \frac{D_L - \frac{v_L}{f}}{D_L} \times 100 \quad 6.11$$

Therefore, it can be concluded that the pulse overlap (PO) has no remarkable influence on the variation of surface morphologies in this case, because there is only a difference of around 4%.

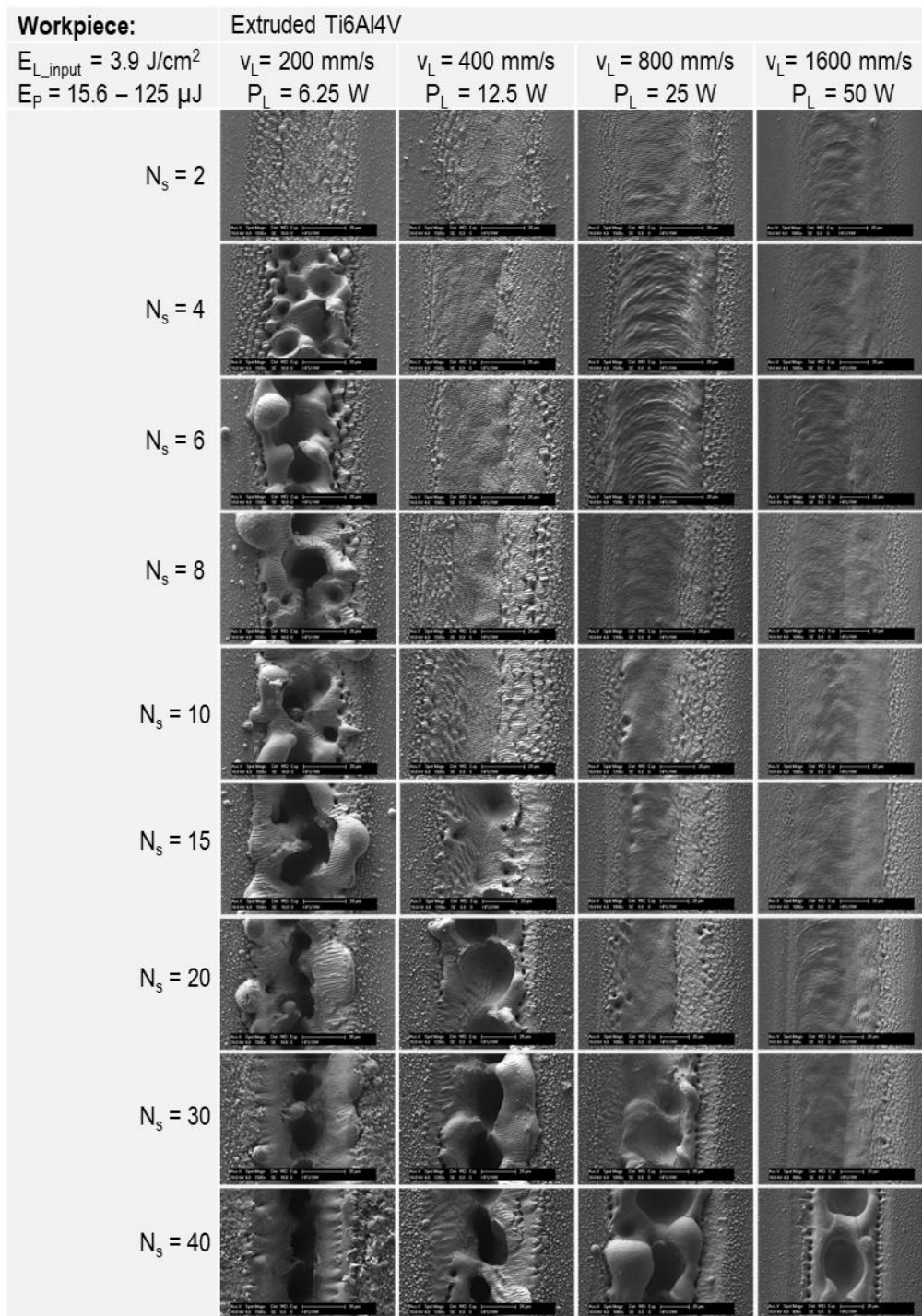


Figure 6.10: SEM images of lasered profiles with varying average laser powers P_{L_ave} and scan velocities v_L at the different number of laser scanning N_s and constant laser input energy $E_{L_input} = 3.9 \text{ J/cm}^2$.

As indicated in Figure 6.11a, an increase in v_L results in a dramatic decreasing number of pulses N_p introduced on the material surface in one beam diameter of laser movement. Moreover, an increase in P_{L_ave} corresponds to more pulse energy, according to Figure 6.11b. The multiple products of pulse number N_p and pulse energy E_p at each combination of laser parameters, provided in Table 6.2, result in constant laser energy of $2500 \text{ } \mu\text{J}$ introduced on the material surface. However, the generated surface caused by different combinations of laser parameters indicates a variation in surface morphology. Accordingly, it can be concluded that the incident of

total constant energy on the material surface through lower pulse energy with a higher number of repetitions leads to more surface degradation than that by higher pulse energy with a lower number of incidents. This can be related to more pulse incidents at lower values of v_L followed by more damage accumulation and eventually accelerating surface degradation.

According to Figure 6.12a, at lower laser powers and scan velocities, that corresponds to lower E_p and higher N_p , an increase in ablation depth with N_s is considerably more significant than that at higher scan velocities and laser powers, denoting higher E_p and lower N_p . The ablation area for $N_s = 2-15$ provided in Figure 6.12b also shows a higher value and more significant increasing trend at lower magnitudes of P_{L_ave} and v_L . In multiple laser scanning, an increase in N_s results in higher N_p . A difference between the number of pulses N_p at different scan velocities is going to be higher with the progress of N_s . Lower values of v_L result in a higher rate of increase in N_p with increasing N_s . A factor that should be taken into account is the influence of the number of pulses N_p on the ablation.

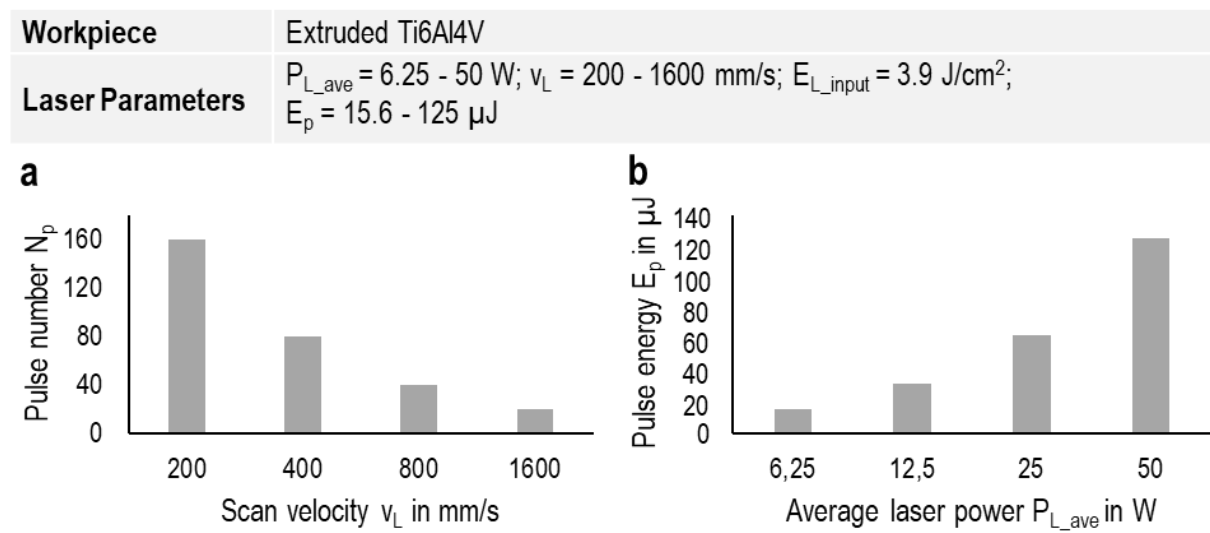


Figure 6.11: a) Influence of laser scan velocity v_L on pulse number N_p , b) Pulse energy E_p at different laser powers.

The dependence of the ablation threshold on N_p is summarized in the following equation and is considered as an incubation effect.

$$\varphi_{th}(N) = \varphi_{th}(1)N_p^{\xi-1} \quad 6.12$$

where ξ and $\varphi_{th}(1)$ are the incubation factor and ablation threshold for one pulse, respectively. Accordingly, a degree of incubation in the material is characterized by this factor ξ in which at $\xi = 1$, the number of pulses does not influence the ablation threshold, while lower values of ξ highlight more effect of pulse number on the ablation threshold. A higher number of pulses leads to less ablation threshold and consequently eases the material removal for subsequent pulses. Accordingly, the ablation threshold is caused by a higher number of pulses that leads to easing the material removal for further pulses. In several literatures [199–202], the formation of micro- and nano-structures at the hole bottom, multiple reflections of the incoming radiation from the hole walls and plasma absorption and scattering are reasons for this phenomenon. According to Figure 6.10, the workpiece surface has remarkably

degraded and is much rougher at lower magnitudes of P_{L_ave} and v_L . The reflectivity of the material is highly influenced by surface roughness. The workpiece surface with more roughness becomes more diffusive. According to [203,204], the absorption can be enhanced not only by macro and micro-structures but also by nano-structures, followed by reducing the reflectivity. It can be concluded that less ablation threshold, caused by a higher pulse number, and more laser absorption, due to more laser induced-degraded surface, were followed by an acceleration in the material ablation at lower scan velocities and powers.

Workpiece	Extruded Ti6Al4V
Laser Parameters	$P_{L_ave} = 12.5, 25$ and 50 W; $v_L = 400, 800$ and 1600 mm/s; $E_{L_input} = 3.9$ J/cm ² ; $E_p = 31.3, 62.5$ and 125 μ J; $N_s = 2 - 40$

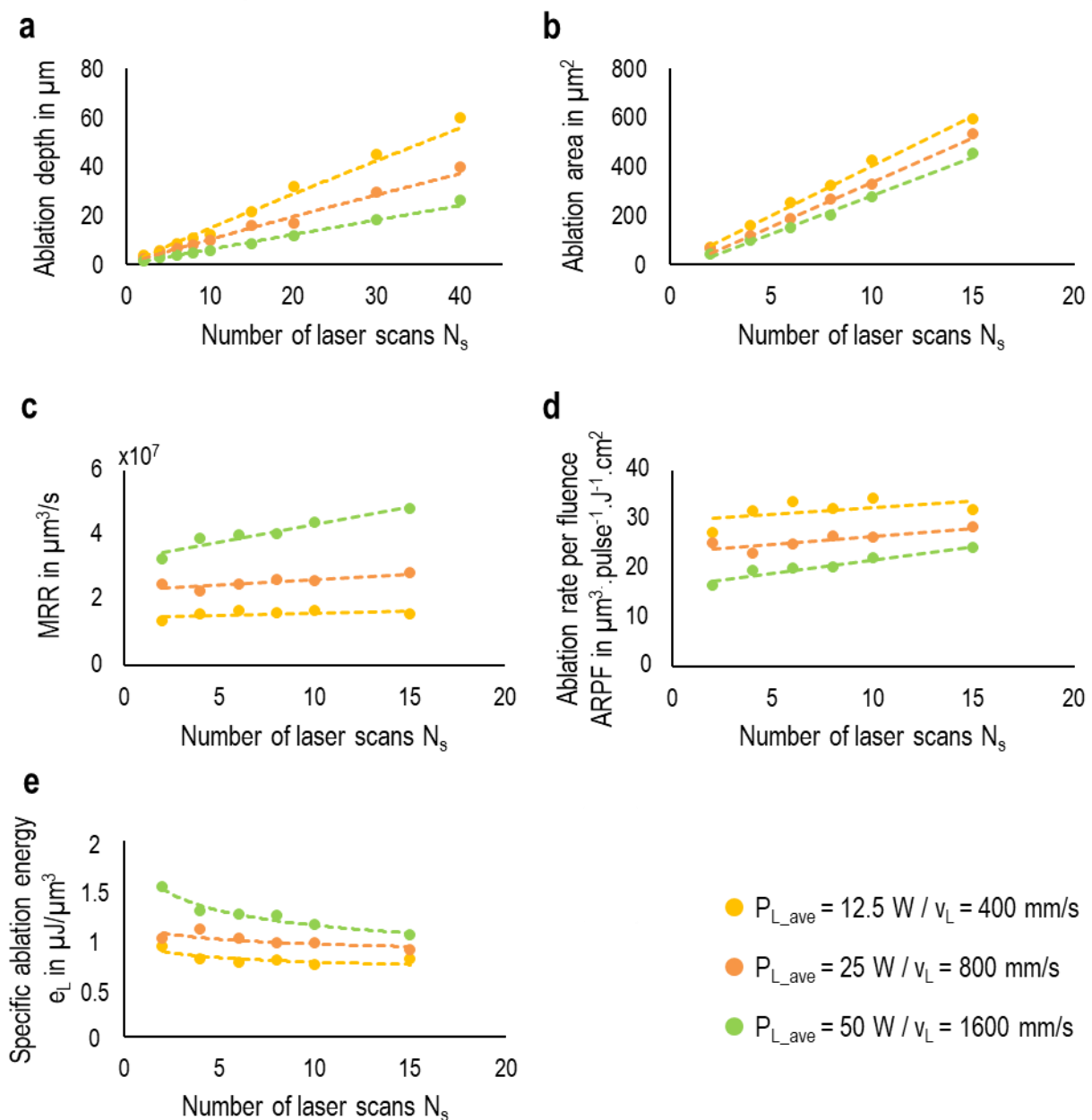


Figure 6.12: Influence of number of laser scans N_s on: a) ablation depth, b) ablation area, c) MRR, d) Ablation rate per fluence, e) specific ablation energy.

As indicated in Figure 6.12c, higher MRR can be found at higher values of P_{L_ave} and v_L at different N_s . It can be concluded that greater pulse energies and a lower number of pulses would increase MRR, which is in agreement with the founding of Yu et al. [162] who worked on multiple-pulse drilling of titanium alloy. At $P_{L_ave} = 25$ W and $v_L = 800$ mm/s as well as $P_{L_ave} = 12.5$ W and $v_L = 400$ mm/s, MRR stays constant with increasing N_s . A slight increase in MRR can be detected at N_s ranged from 2 to 15 for $P_{L_ave} = 50$ W and $v_L = 1600$ mm/s.

As illustrated in Figure 6.12d, Ablation Rate Per Fluence (ARPF) indicates higher values for $P_{L_ave} = 12.5$ W and $v_L = 400$ mm/s at different N_s compared to those for two other sets of laser parameters, $P_{L_ave} = 25$ W and $v_L = 800$ mm/s / $P_{L_ave} = 50$ W and $v_L = 1600$ mm/s. According to Figure 6.12e, lower values of specific ablation energy can be seen at $P_{L_ave} = 12.5$ W and $v_L = 400$ mm/s. Lower values of e_L and higher values of ARPF at lower magnitudes of laser powers and scan velocities again highlight the incubation effect's role in multiple linear laser scanning.

An increase in the number of pulses through decreasing v_L is followed by more laser induced-damage accumulation, a reduction of ablation threshold and consequently lower specific ablation energy accompanied by higher ARPF. An increasing number of laser scans N_s led to a slight rise in ARPF at all sets of laser parameters, particularly at $P_{L_ave} = 50$ W and $v_L = 1600$ mm/s, which is associated with a greater reducing trend of corresponding specific ablation energy (see green line in Figure 6.12e). At two other sets of laser parameters, specific ablation energy indicates no remarkable change, only a slight reduction, with N_s .

Figure 6.13 provides the influence of N_s ranging from 2 to 130 on ablation depth for two sets of laser parameters at a constant E_{L_input} of 3.9 J/cm². One set includes lowest average laser power and scan velocity, $P_{L_ave} = 6.25$ W and $v_L = 200$ mm/s, and another one contains highest values of average laser power and scan velocity, $P_{L_ave} = 50$ W and $v_L = 1600$ mm/s. For two sets of laser parameters, an increase in N_s led to increasing ablation depth. This trend is much more considerable at $P_{L_ave} = 6.25$ W and $v_L = 200$ mm/s till $N_s = 20$ due to the incubation effect as explained before. Afterwards, an increase in ablation depth slowed down with N_s for $v_L = 200$ mm/s and $P_{L_ave} = 6.25$ W. In multiple laser scanning, it is difficult for ablated material to splash outward the lasered profile due to increasing lasered profile depth and pressure gradient inside the profile. This leads to the formation of a recast layer inside the lasered profile. In fact, the recast layers result from the ablation and solidification of materials falling back on the side-wall surface of the lasered profile. This recast layer can prevent the propagation of laser energy to the deeper position and, finally, a gradual decrease in the rate of increase in the ablation depth. Zhao et al. [205] reported self-cleaning for a gradual decrease in the ablation rate. The laser beam may be reflected multiple times on the side-wall surface of the lasered profile, thereby refining the side-wall morphology, and the recast layer inside the lasered profile would be cleaned. Furthermore, there is a particle mass inside the cavity containing the plasma and the vaporized material gas, which would absorb part of the laser energy and release energy into the surrounding area. So, the recast layer would be swept away. Consequently, the amount of energy is consumed for cleaning the lasered profile instead of ablation and eventually, a decrease in the ablation rate is expected.

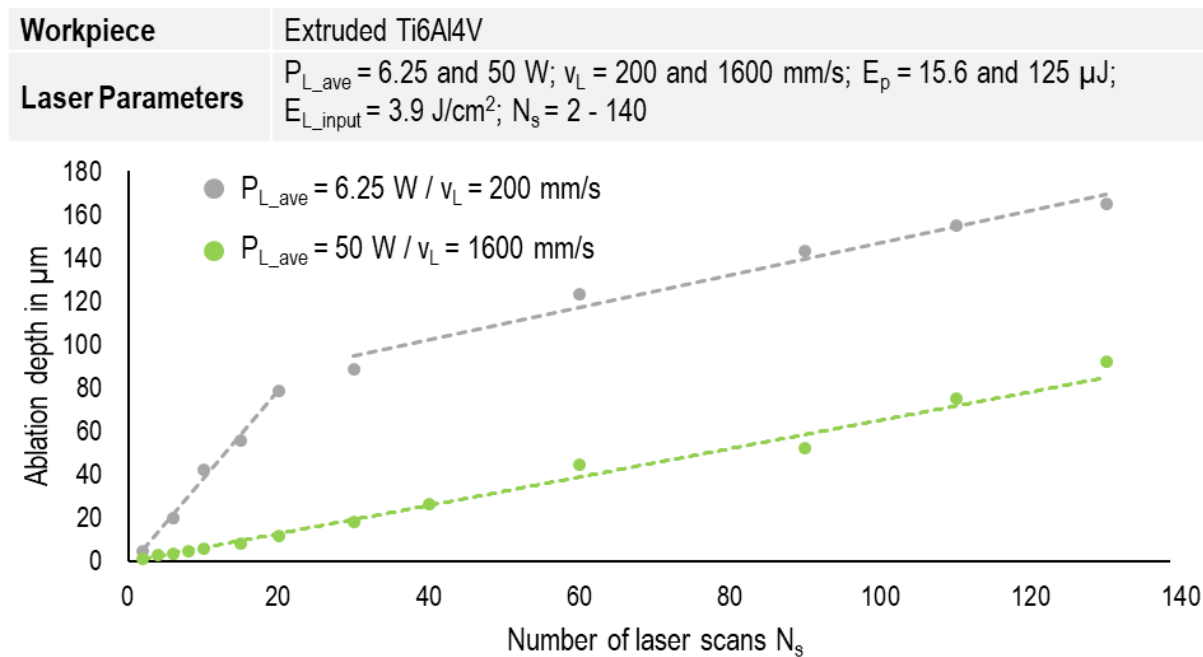
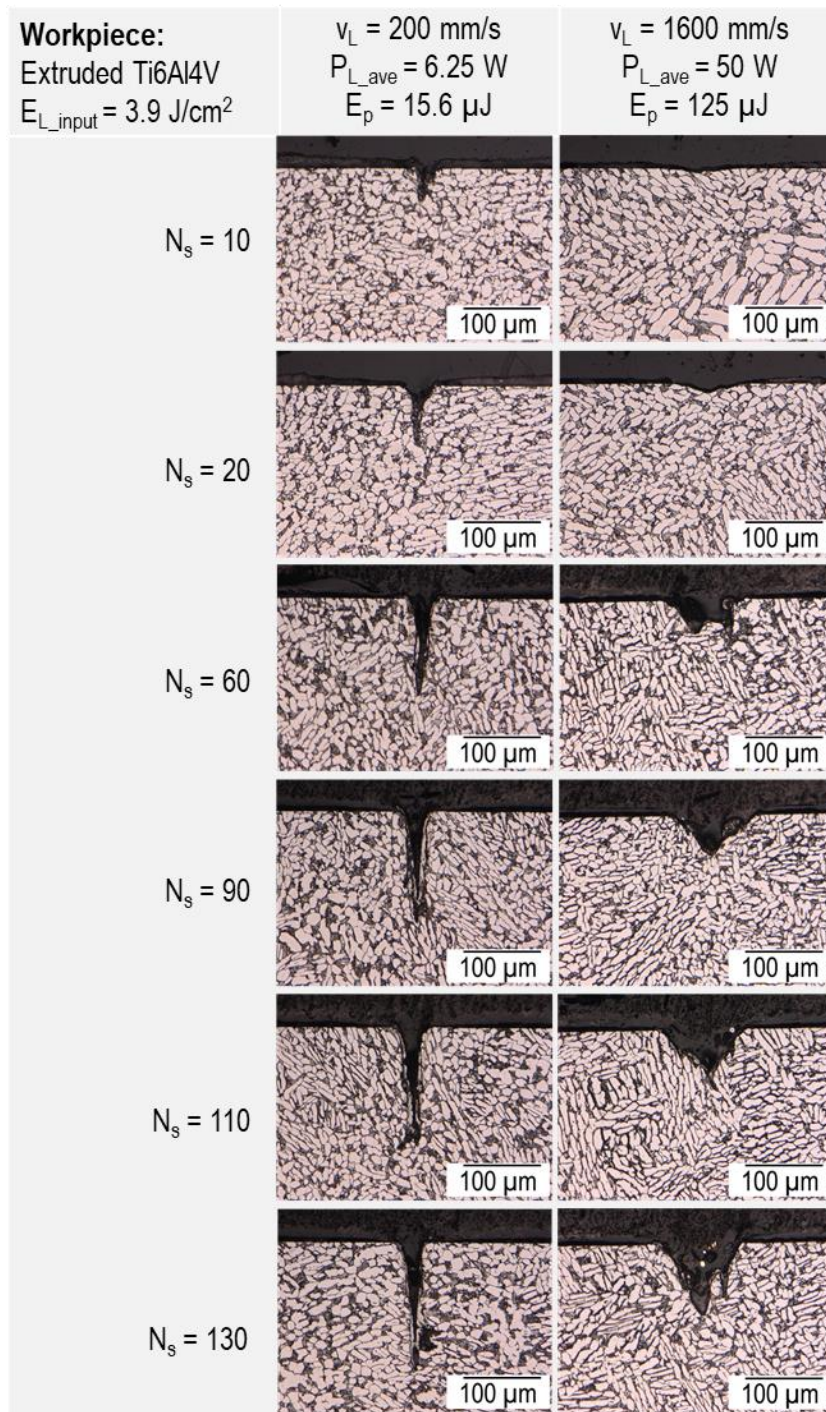


Figure 6.13: Influence of the number of laser scans on ablation depth.

In the case of $v_L = 1600$ mm/s and $P_{L_ave} = 50$ W, a linear trend in increasing ablation depth is still observable up to $N_s = 140$; however, at different N_s , the ablation depth at $v_L = 200$ mm/s and $P_{L_ave} = 6.25$ W is tremendously higher than that at $v_L = 1600$ mm/s and $P_{L_ave} = 50$ W. It can be concluded that introducing a certain amount of energy on the surface through lower pulse energy with higher repetition results in a deeper profile.

Figure 6.14 provides the cross-section of corresponding lasered profiles for these two sets of laser parameters. At different numbers of laser scans, the lasered profiles at $P_{L_ave} = 6.25$ W and $v_L = 200$ mm/s have narrower width and higher depth in comparison with those at $P_{L_ave} = 50$ W and $v_L = 1600$ mm/s. At constant laser input energy E_{L_input} , lower laser powers and scan velocities, corresponding to lower pulse energy with a higher number of repetitions, result in higher depth and lower width profiles. While greater laser power and higher scan velocities, denoting higher pulse energy with a lower number of repetitions, provide a wider profile with lower depth. Since the laser beam has a Gaussian shape, an increase in P_{L_ave} results in a greater laser intensity curve throughout the laser beam. Thus, more area of laser beam affects the material ablation that causes a wider profile. The wider lasered profile eases the plasma splashing from the crater, while the narrower crater would not let the generated plasma move out. Therefore, the accumulation of high-temperature plasma may also be considered as a factor in the acceleration of rising ablation depth till $N_s = 20$ at $P_{L_ave} = 6.25$ W and $v_L = 200$ mm/s (see Figure 6.13). However, further plasma accumulation prevents transferring laser pulse energy to the material. Moreover, difficulty in removing the molten material from the narrower crater with high depth eventually leads to slowing down the progress of ablation depth with the laser scanning number.

Figure 6.14: Lasered profiles at different number of laser scans N_s .

7 Laser assisted micro-milling

In the introduced LAM in the current investigation, the ultra-short pulse laser structuring removes some parts of the material before the machining process. Indeed, the material removal through laser structuring contributes to the reduction of uncut chip thicknesses during the process. For a better understanding of the presented LAM approach, a kinematic model has been developed and introduced in section 7.1. Since the experimental investigation has been allocated to the milling process, the model considers the kinematic of the milling process and aims to study how the structuring affects the uncut chip thickness. In sections 7.1.1, 7.1.2, and 7.1.3, the modelling results have been introduced, and eventually, the potential factors in the reduction of uncut chip thicknesses have been determined in section 7.1.4. Based on finding the most influential parameters according to the modelling results, the experimental tests have been conducted to see how considerable the role of the introduced LAM approach is on the machinability of Ti6Al4V material. The details of structuring the workpiece and experimental results have been provided in section 7.2.

7.1 Modelling of the uncut chip thickness

For the development of the model, the potential factors in laser-assisted machining should be determined. According to Figure 7.1, the input parameters of the developed model can be mainly categorized into the structure, tool geometry, and process parameters. Compared to the conventional milling process, additional parameters are associated with the structure.

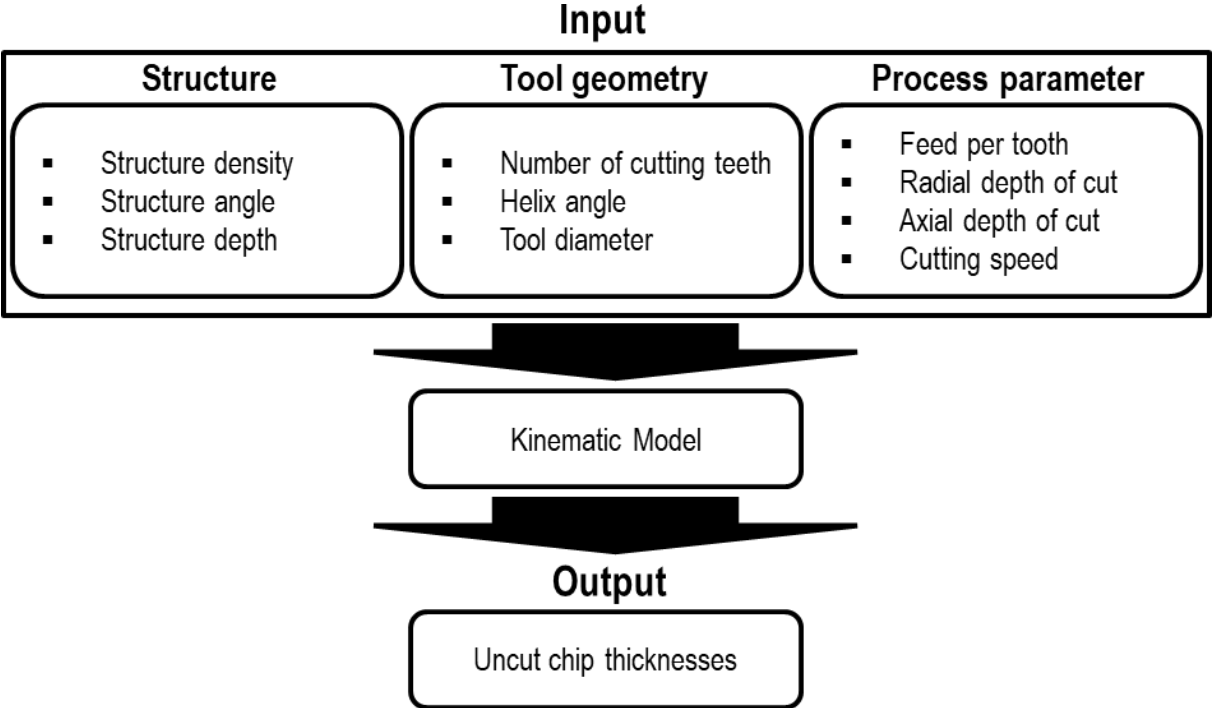


Figure 7.1: Input and output parameters in modelling of laser-assisted micro-milling.

According to Figure 7.1, structure density, or line gap l_g , structure angle α , and structure depth s_d are considered as structuring parameters. The number of cutting teeth N , helix angle β , and tool diameter D characterize tool geometry in the model. The feed per tooth f_z , radial depth of cut a_e , axial depth of cut a_p , and cutting

speed v_c are included in the process parameters. The model output is calculated uncut chip thickness with the given input parameters. In the following, the details of the kinematic model development have been discussed. Moreover, the calculation of uncut chip thickness and uncut chip thickness reduction have been provided.

According to Figure 7.2b, the milling tool moves throughout the x-direction, and material removal occurs due to contact between the tool and the workpiece. The modelling is conducted in two dimensions. For converting the 3D model to a 2D model, the workpiece and cutting tool were discretized in 20 layers throughout the z-direction (see Figure 7.2b and c). The axial depth of cut was kept constant and equals 1 mm. Therefore, each layer's thickness would be 50 μm . The modelling can be carried out at each discretized layer as a 2D task. The top view in Figure 7.2a indicates the 2D geometry of the workpiece at each layer. In fact, the workpiece is assumed to be a planar surface.

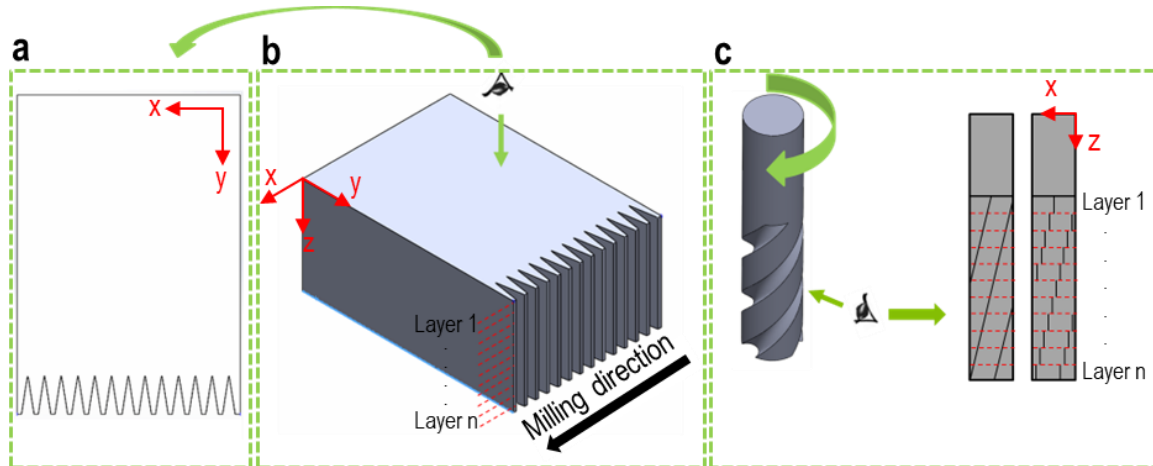


Figure 7.2: The process of converting a 3D model to a 2D model. a) 2D geometry of the workpiece from a top view, b) workpiece discretization, c) cutting tool discretization.

After discretization of the cutting tool, it is assumed for each layer that the cutting tooth is vertical rather than having a helix shape (see Figure 7.2c). In other words, the cutting tooth at each layer has a helix angle of $\beta = 0^\circ$ and is entirely vertically straight. For considering the helix angle of the cutting tooth, the angular shift, which will be further explained and calculated according to equation 7.9, is applied between vertically cutting teeth at every two successive layers. Therefore, the movement of each tooth can easily be calculated and detected in a 2D plane, and the modelling can be performed separately for different layers.

Each structured workpiece includes several structure elements. Therefore, the structure element should be developed before creating a structured workpiece in a 2D plane. Since the structuring of the part is carried out by a laser beam with a Gaussian shape, the generated structure element is assumed to follow the Gaussian form. Figure 7.3a provides the Gaussian curve, highlighted with red color, that is in good agreement with the experimentally generated lasered profile. The depth and width of the Gaussian curve as a structure element are 200 μm and 80 μm , respectively (see Figure 7.3b). The structured workpiece at each layer can be generated by putting the structure elements next to each other, as shown in Figure 7.3c.

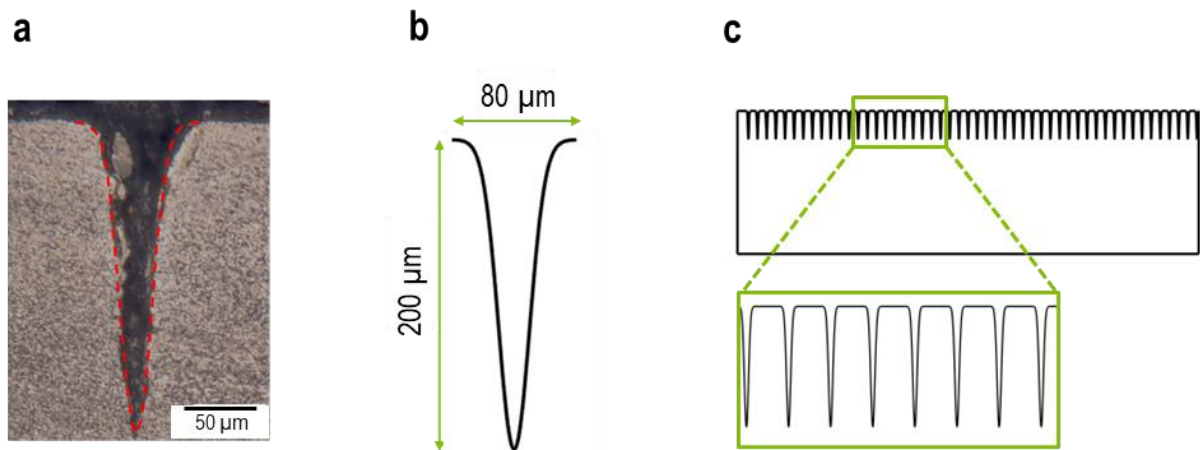


Figure 7.3: a) the fitted Gaussian curve on the lasered profile, b) the structure element and c) the structured workpiece for one layer.

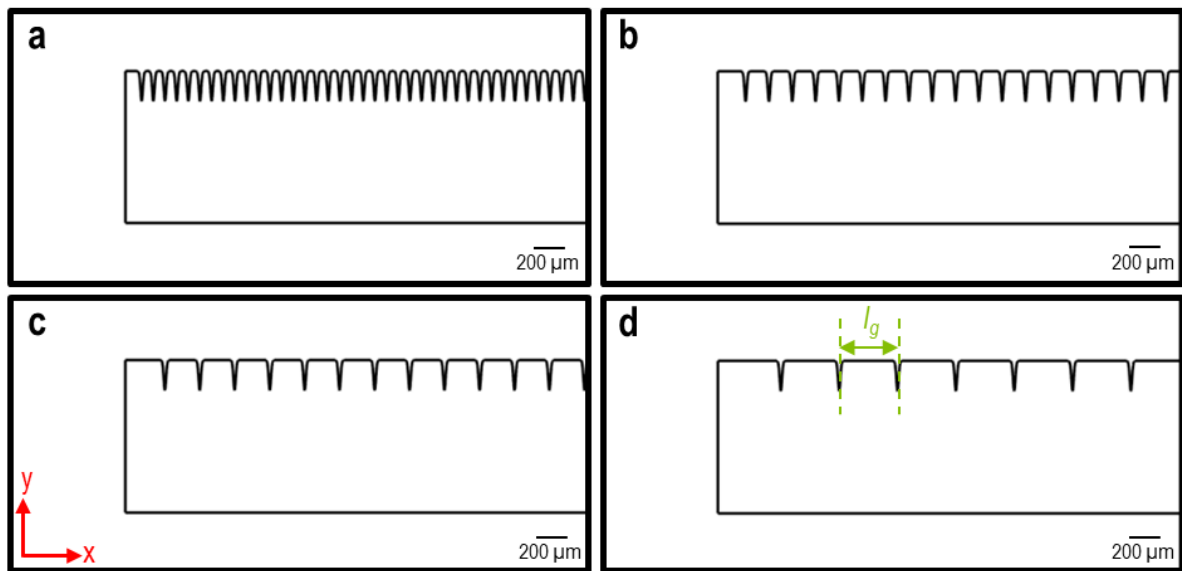


Figure 7.4: Structured workpiece at different line gaps: a) $l_g = 100 \mu\text{m}$, b) $l_g = 200 \mu\text{m}$, c) $l_g = 300 \mu\text{m}$, d) $l_g = 500 \mu\text{m}$.

As mentioned, the structure parameters can be categorized in depth, angle, and density. The structure depth can be adjusted by applying the multiplier λ to the Gaussian formulation, used for creating each structure element.

$$f(x) = \frac{\lambda}{\sigma\sqrt{2\pi}} e^{-\frac{1}{2}\left(\frac{x-\mu}{\sigma}\right)^2} \quad 7.1$$

Where λ , μ , and σ are the multiplier, mean, and standard deviation of the Gaussian distribution. The $f(x)$ denotes the Gaussian curve. To obtain a curve as close as possible with an experimentally lasered profile, the standard deviation was set to 10 after several trials. The structure density can be set by changing the distance between structure elements, line gap l_g , at each layer. As shown in Figure 7.4, the structured parts with different structure densities can be obtained by changing l_g from $100 \mu\text{m}$ to $500 \mu\text{m}$. Increasing structure density, or decreasing the line gap, indicates more material removal before machining.

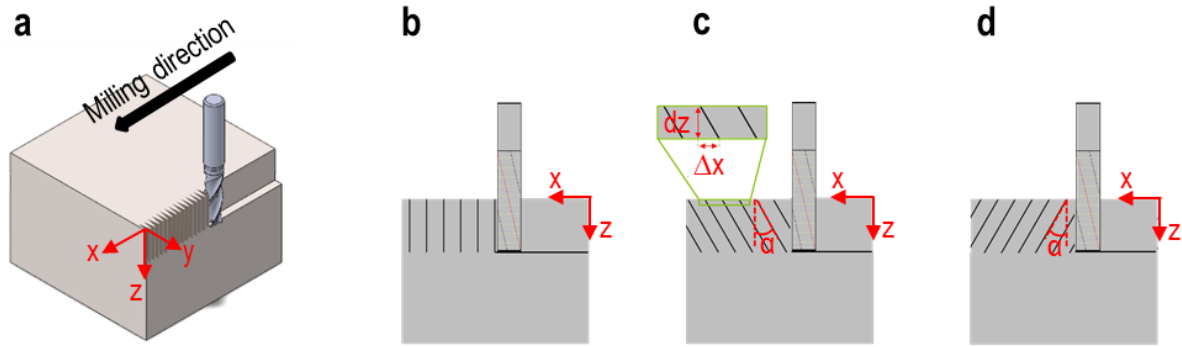


Figure 7.5. Structured workpieces with different structure angles: a) $\alpha = 0^\circ$, b) $\alpha > 0^\circ$, c) $\alpha < 0^\circ$.

Figure 7.5a indicates the schematic of the milling structured parts. The cutting tool moves from the right side to the left side throughout the x direction. According to the milling directions, three different structures can be defined. The structure with the angle $\alpha = 0^\circ$ shown in Figure 7.5b includes the vertical linear pattern perpendicular to the milling direction. In this case, the structured part at different layers is similar, and shifting the structured part at other layers is not required. Figure 7.5c and Figure 7.5d show the workpieces with the aligned structures, the structure angle α is not equal to zero. Concerning the milling direction, the structure angle can be either positive or negative. In these two cases, the structured part should be shifted either to the right or left direction, depending on the sign of the structure angle, in the successive layers. The shifting value Δx can be calculated based on equation 7.2.

$$\Delta x = dz \times \tan(\alpha) \quad 7.2$$

$$dz = \frac{a_p}{N_{dis}} \quad 7.3$$

where dz is the layer thickness which is calculated according to equation 7.3 with respect to N_{dis} and a_p denoting the number of discretization, the number of layers, and axial depth of cut, respectively. The coordinate of each cutting tooth, x_i and y_i , at each layer can be described as follow:

$$x_i = \frac{v_f \times t}{60} + \left(\frac{D}{2}\right) \times \sin(\phi) \quad 7.4$$

$$y_i = \left(\frac{D}{2}\right) \times \cos(\phi) + C_y \quad 7.5$$

where t , v_f , D , ϕ and C_y denote modelling time, feed velocity, tool diameter, the angular position of each cutting tooth and y center of tool position, respectively. A change in C_y can change the position of the cutting tool with respect to the workpiece in y direction, followed by changing the radial depth of cut a_e . The feed velocity v_f is calculated as below:

$$v_f = n \times N \times f_z \quad 7.6$$

where n , N , and f_z are rotational tool speed, the number of cutting teeth, and feed per tooth, respectively. The modelling time t is increased by the time increment dt . Due to the contact between the cutting tool and the workpiece, material removal would occur. In the case of the structured workpiece, the importance of time increment is much more highlighted because at each contact between the workpiece and the

cutting tooth, the cutting procedure is interrupted, due to the structure elements, and the time increment should be small enough so that the contact between the cutting tooth and each tiny structure element is detected. Therefore, the time increment was set to 20 μs after several trials, observing the cutting path in the case of the structured workpiece, particularly with the high structure density.

To calculate the mentioned coordinates, x_i and y_i , at each time increment according to equations 7.4 and 7.5, the angular position of each cutting tooth at each discretized layer should be calculated as below:

$$\phi = \omega t - \left(\frac{2\pi j}{N}\right) + (k-1) \times d\phi \quad j=1,\dots,N / k=1,\dots,N_{\text{dis}} \quad 7.7$$

where N is the total number of cutting teeth. In this study, the number of teeth N is equal to 3. Moreover, tooth number and layer number are described in the above equation with j and k , respectively. Accordingly, the angular position ϕ of 120° , 240° , and 360° for tooth 1, tooth 2, and tooth 3 can be determined at the first layer $k = 1$ and modelling time $t = 0$ s. An increase in layer number from $k = 1$ to $k = 2$ results in adding the term of the angular shift $d\phi$ for calculating the angular position ϕ . Obviously, higher layer number k leads to more value of angular shift according to $(k-1) \times d\phi$. At the modelling time $t \neq 0$, the angular velocity ω also has an influence on determining the angular position ϕ of each cutting tooth. By increasing the modelling time t , the angular position of each cutting tooth would also change, leading to the rotation of the cutting tool. The higher value of ω results in more cutting tool rotation, or correspondingly more change in the angular position ϕ . ω as the angular velocity can be calculated as a function of the rotational speed n as follow:

$$\omega = n \times \left(\frac{2\pi}{60}\right) \quad 7.8$$

Also, the calculation of angular shift $d\phi$ is provided in the following equation:

$$d\phi = \arctan\left(\frac{dz \times \tan(\beta)}{\left(\frac{D}{2}\right)}\right) \quad 7.9$$

Where β is the helix angle. The angular shift $d\phi$ can be determined by calculating dz according to equation 7.3. Using the above equations, each layer's coordinate of the cutting tooth tip, x_i and y_i , can be calculated at each modelling time. The coordinate x_i denotes the milling direction and describes the position of the cutting tooth tip in this direction. The coordinate y_i denotes the position of the cutting tooth tip with respect to the workpiece. According to the obtained coordinate of the cutting tooth tip and the predetermined coordinate of the workpiece, the contact between each cutting tooth and the workpiece is checked at each time increment and layer to remove the material and calculate the uncut chip thickness. In the case of contact, the material removal takes place, and the uncut chip thickness is calculated. The contact between the tool and workpiece includes several time increments, and at each, the calculated chip thickness is saved in a matrix, and in the case of no contact between the tool and workpiece, the chip thickness is set to zero. Equation 7.10 provides the corresponding matrix, including the values of uncut chip thicknesses at all layers and time increments. Accordingly, the number of rows n and columns m denotes the number of layers and increments in the modelling, respectively.

$$\begin{bmatrix}
 h_{11} & h_{12} & h_{13} & \dots & h_{1(m-2)} & h_{1(m-1)} & h_{1(m)} \\
 h_{21} & h_{22} & h_{23} & \dots & h_{2(m-2)} & h_{2(m-1)} & h_{2(m)} \\
 h_{31} & h_{32} & h_{33} & \dots & h_{3(m-2)} & h_{3(m-1)} & h_{3(m)} \\
 \vdots & \vdots & \vdots & \ddots & \vdots & \vdots & \vdots \\
 h_{(n-2)1} & h_{(n-2)2} & h_{(n-2)3} & \dots & h_{(n-2)(m-2)} & h_{(n-2)(m-1)} & h_{(n-2)(m)} \\
 h_{(n-1)1} & h_{(n-1)2} & h_{(n-1)3} & \dots & h_{(n-1)(m-2)} & h_{(n-1)(m-1)} & h_{(n-1)(m)} \\
 h_{(n)1} & h_{(n)2} & h_{(n)3} & \dots & h_{(n)(m-2)} & h_{(n)(m-1)} & h_{(n)(m)}
 \end{bmatrix}_{n \times m} \quad 7.10$$

In fact, n in equation 7.10 corresponds to N_{dis} , as mentioned before. Also, m results from the division product of total modelling time and time increment dt . For layer one, the modelling is conducted at different time increments that lead to creating the first row in the introduced matrix. Then the modelling is also applied to other layers, followed by creating other rows of the matrix. Eventually, the created matrix includes comprehensive information regarding the chip thickness values at different layers and time increments. It is noted to mention that an individual matrix is created for each cutting tooth.

$$\left[\sum_{i=1}^n h_{i1} \quad \sum_{i=1}^n h_{i2} \quad \sum_{i=1}^n h_{i3} \quad \dots \quad \sum_{i=1}^n h_{i(m-2)} \quad \sum_{i=1}^n h_{i(m-1)} \quad \sum_{i=1}^n h_{im} \right]_{1 \times m} \quad 7.11$$

According to equation 7.11, at each time increment, the chip thickness values are summed up throughout the layers, which result in an individual value for each time increment. The obtained vector in equation 7.11 provides the total uncut chip thickness.

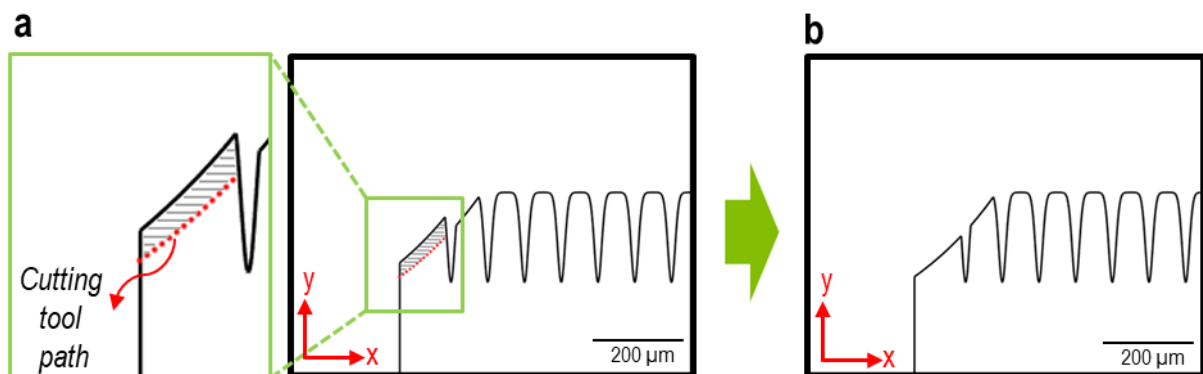


Figure 7.6: Material removal in modelling of milling the structured part: a) removal procedure, b) the workpiece after material removal.

The dotted red line in Figure 7.6a shows the path of the cutting tooth determined according to the above equations for directions x and y . Moreover, the shaded area is part of the material which should be removed from the workpiece. Figure 7.6b indicates the workpiece after removing the shaded area. Indeed, the geometry of the workpiece has been updated in the case of material removal. In detail, the cutting tool path, highlighted by the dotted red line, inside the workpiece geometry is considered as a new workpiece surface, and all surfaces above the tool path should

be removed to form the new workpiece geometry. During the contact between the cutting tooth and the workpiece, the workpiece geometry is not updated, and only the uncut chip thickness is calculated. Once the cutting tooth exits the predetermined geometry of the workpiece, the geometry is updated. Updating the workpiece geometry must be done to correctly detect the contact between the upcoming cutting tooth and the workpiece. The two successive cutting teeth would not simultaneously come into contact with the workpiece because of the applied radial depth of cut as well as the utilized tool with three teeth having an equal angular distance. Therefore, the applied method for updating the workpiece geometry is appropriate. Figure 7.7 also provides an overview of removing the structured parts at some modelling steps for one exemplary layer. Accordingly, the movement of the cutting tool throughout the x-direction and the contact between the structure elements and the cutting tool at different time increments led to the material removal and eventually completely removing the structures from the workpiece, as shown in Figure 7.7e.

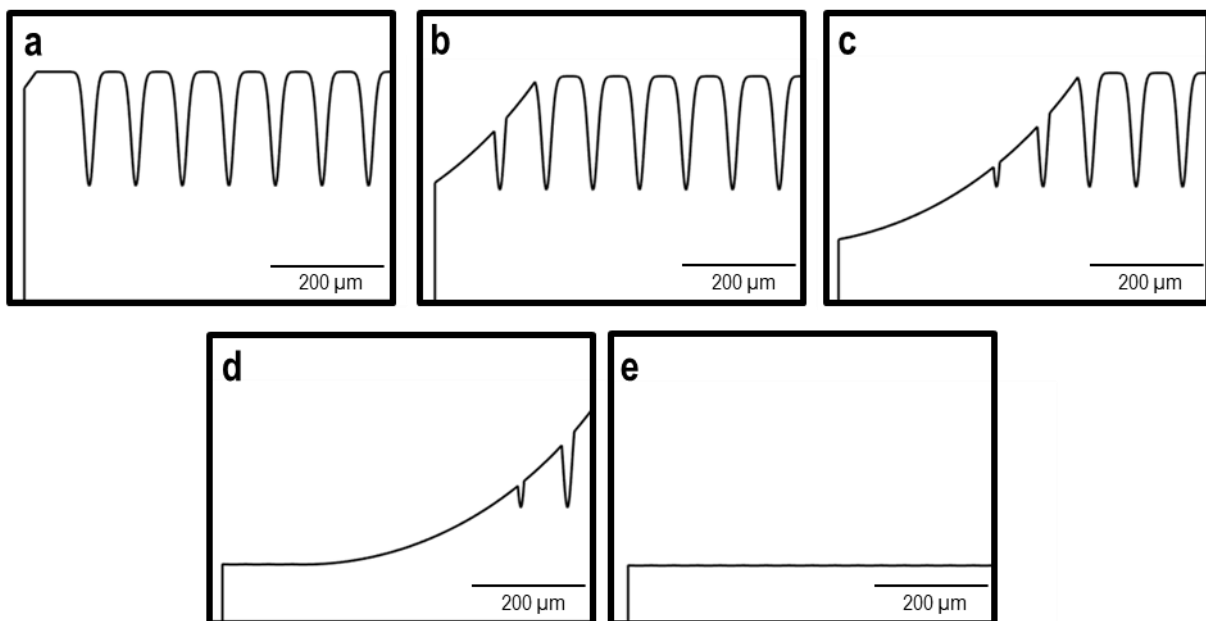


Figure 7.7: Material removal at different modelling time : a) $t = 0.0230$ s, b) $t = 0.0379$ s, c) $t = 0.0570$ s, d) $t = 0.0778$ s, e) $t = 0.1201$ s at $f_z = 10$ $\mu\text{m}/\text{tooth}$ (feed velocity $v_f = 185$ mm/min).

Figure 7.8 indicates how uncut chip thickness changes in one layer for non-structured and structured parts at one revolution of the cutting tool. As mentioned before, the uncut chip thickness is recorded for each layer at each time increment. Since the modelling was conducted for a tool with three teeth, the uncut chip thickness is calculated and recorded for these three teeth, indicated with red, black, and blue colors for tooth 1, tooth 2, and tooth 3, respectively. The maximum uncut chip thickness obtained for the given process parameters and each cutting tooth accounted for 7.5 μm for the non-structured part (see Figure 7.8), which is the same as the calculated maximum uncut chip thickness using the equation 4.1.

According to Figure 7.8a, the uncut chip thickness increases abruptly to the maximum value at the beginning of contact between the tool and workpiece due to the down milling strategy. Afterward, the uncut chip thickness decreases slightly to zero. This trend can also be observed for structured parts, but rapid drops and rises in the uncut chip thickness can be seen according to Figure 7.8b. The reason for that

is associated with the structured workpiece that interrupts the cutting process, followed by the remarkable fluctuation in the uncut chip thickness.

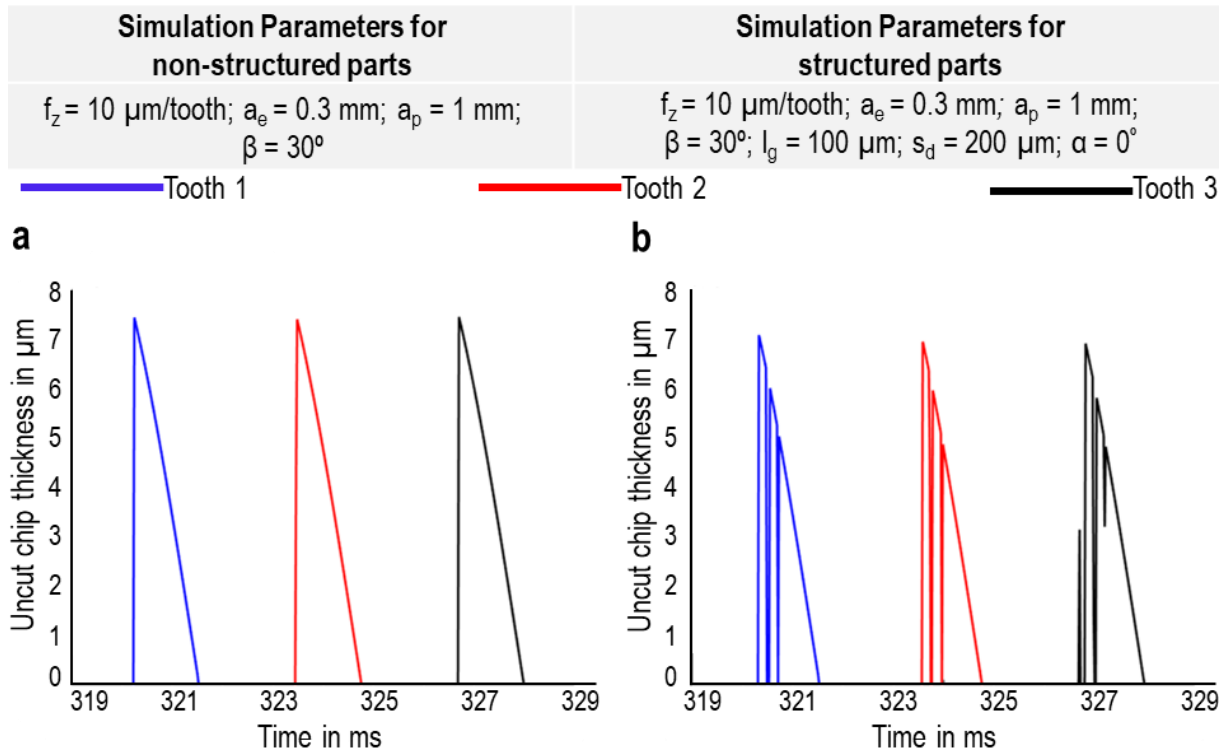


Figure 7.8: Calculated uncut chip thickness in one layer for: a) non-structured part, b) structured part at $f_z = 10 \mu\text{m/tooth}$, $a_e = 0.3 \text{ mm}$ for cutting tool diameter 1.8 mm with three cutting teeth.

As indicated in Figure 7.8, the maximum uncut chip thickness for the structured part has been reduced through the structuring. Figure 7.9 gathers the uncut chip thickness curves for structured and non-structured parts in one diagram for one tool revolution to better analyze changing the uncut chip thicknesses in machining the structured parts. Accordingly, the interruption of uncut chip thickness resulting from structuring the parts in the contact between the tool and workpiece can be seen. Consequently, a remarkable reduction of uncut chip volume is observable in the contact period between the tool and workpiece, in addition to decreasing the maximum uncut chip thickness. As seen in the structured workpiece case, the chip thickness diagram for different teeth is not similar. Once the cutting tooth approaches the structured workpiece, the cutting tooth would come into contact with different areas of the structure elements, and the intersection between the cutting tooth path and the structure elements may vary. This leads to a variation in maximum uncut chip thickness and the volume of the uncut chip, or uncut chip thickness diagram. Additionally, this variation exists not only between the different cutting teeth but also for one tooth in the next contact.

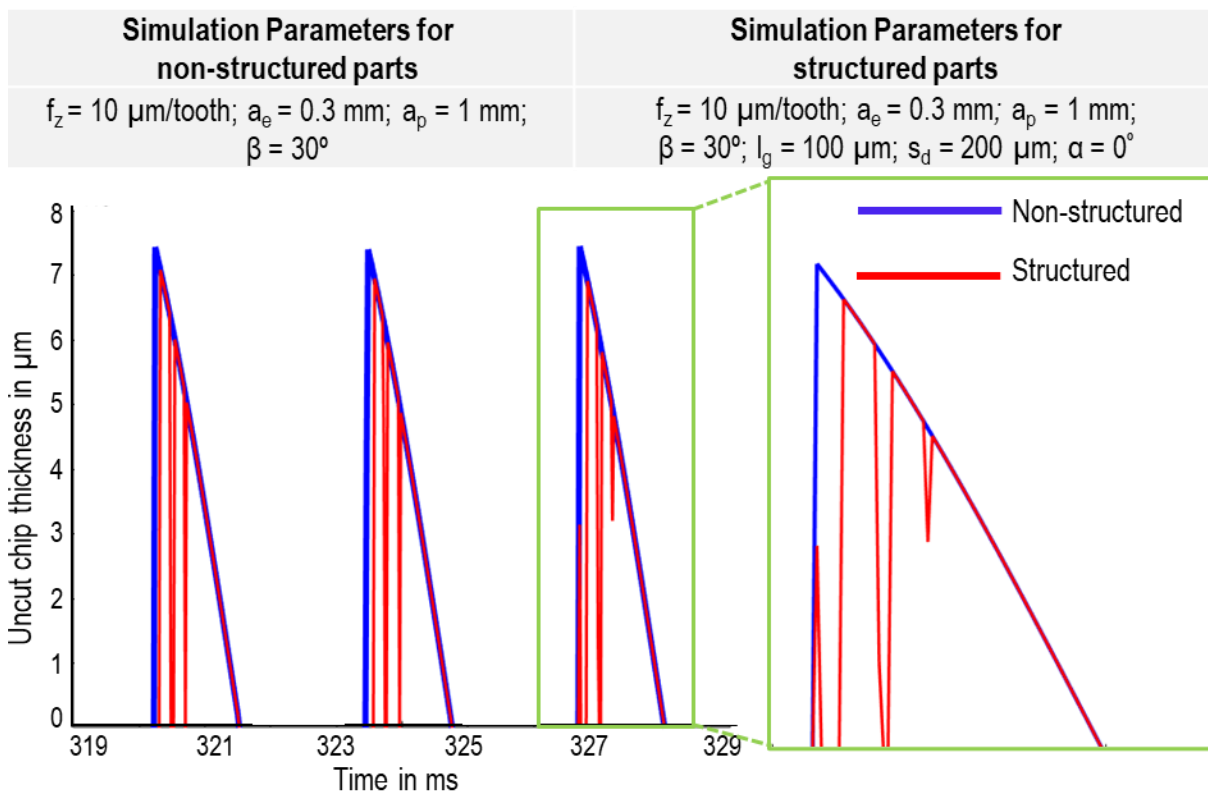


Figure 7.9: Comparison between structured and non-structured parts in one revolution of cutting tool for one layer.

After calculating and recording the uncut chip thicknesses, the modelling is repeated for the next layer. At each layer, the initial position of three cutting teeth is changed with respect to the calculated angular shift $d\phi$. The angular shift considers the helix shape of the cutting tool. In the case of an aligned structure, the structure elements should also be shifted by Δx . Moreover, the modelling time t is reset to 0 for each layer. Figure 7.10a and b provide the uncut chip thickness curves at different layers for one cutting tooth at machining non-structured and structured parts, respectively. As can be seen, the uncut chip thickness curve is shifted to the left side at successive layers. Additionally, the reduction of maximum uncut chip thickness in some layers can clearly be observed. This is associated with the position of entry contact between the cutting tooth and the structured workpiece in the corresponding layers that does not lead to removing the material where there is a maximum uncut chip thickness. Instead, the cutting tooth moves in the air. However, some layers indicate no remarkable change in maximum uncut chip thickness. To comprehensively analyze the influence of structuring on the chip thickness reduction, the total uncut chip thickness curve is calculated. This can be obtained for each tooth by summing uncut chip thickness curves at different layers (see equation 7.11). Figure 7.10c compares the total uncut chip thickness curves for the structured and non-structured parts highlighted by red and blue colors, respectively. Accordingly, the structuring of the part reduces the uncut chip volume and maximum uncut chip thickness. Furthermore, a fluctuation in the uncut chip thickness curve associated with the structured workpiece can be observed. This is initiated from the dramatic drop and rise in the uncut chip thickness at different layers, followed by a fluctuation in the total uncut chip thickness diagram.

The percentage of uncut chip thickness reduction is calculated to quantify the influence of structuring on changing the uncut chip thicknesses. In this regard, the area under the blue curve, as the unstructured part, and the red curve, as the structured part, are calculated, and finally, the uncut chip thickness reduction CTR is obtained as follows:

$$\text{CTR} = \frac{\text{Area}_{\text{blue}} - \text{Area}_{\text{red}}}{\text{Area}_{\text{blue}}} \times 100 \quad 7.12$$

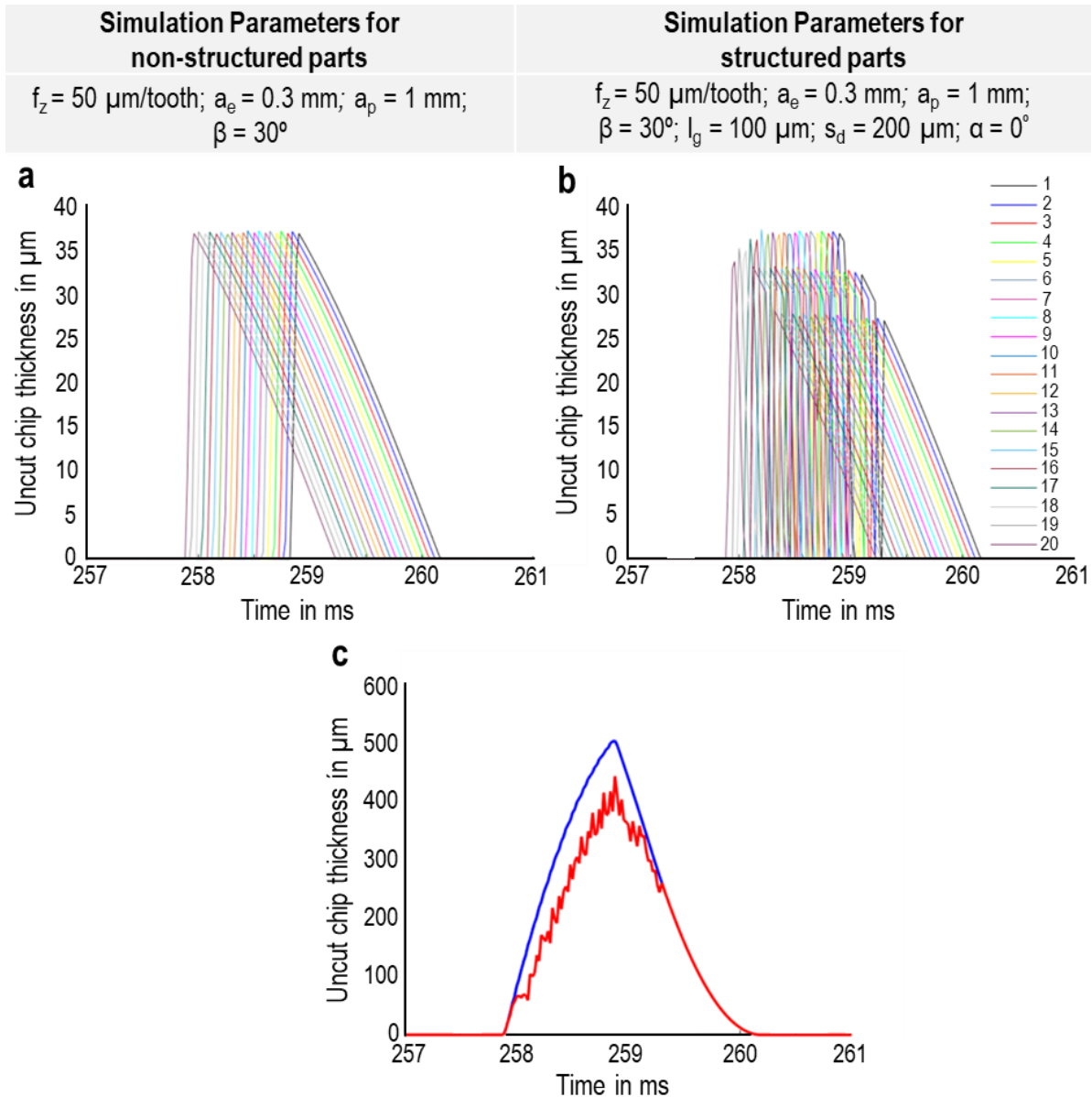
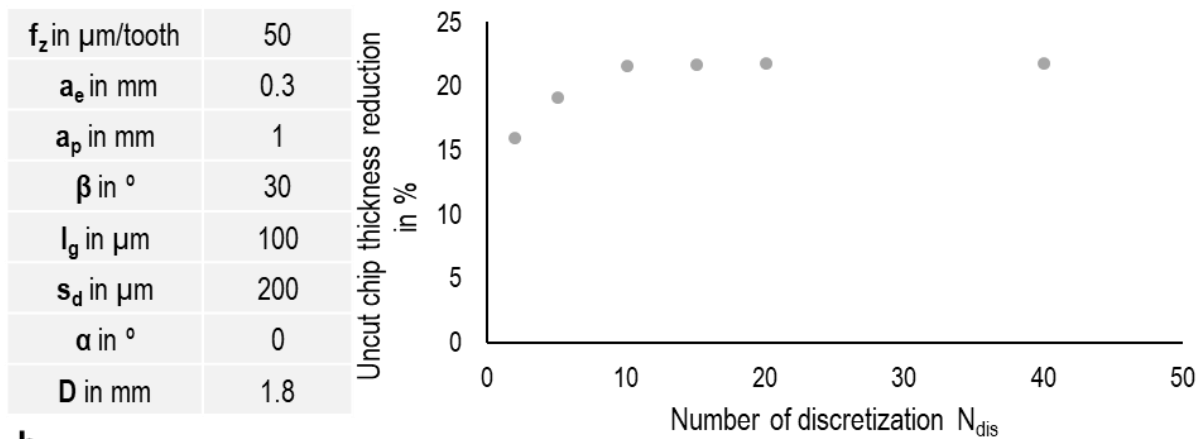


Figure 7.10: a) uncut chip thickness curves at different layers for non-structured part, b) uncut chip thickness curves at different layers for structured part, c) comparison between total uncut chip thickness curves for structured and non-structured parts for one tooth in one revolution of the cutting tool.

For implementing the modelling, time and space should be discretized. As mentioned, the time increment in the modelling was set to $20 \mu\text{s}$ to have smooth enough cutting tooth movement at each time increment that does not lead to skipping the structure elements. With respect to the space, the number of discretization in the modelling was set to 20. The reason is associated with the uncut chip thickness

diagram. In the case of the non-structured part, the uncut chip thickness increases to the maximum once the contact between the tool and the workpiece takes place. Afterward, a reduction in the uncut chip thickness would be observed. The number of discretization should be enough to guarantee a smooth increase and reduction, with no fluctuation, in the uncut chip thickness diagram of non-structured part (see the blue diagram shown in Figure 7.10c). Obviously, a fluctuation in the uncut chip thickness diagram, for non-structured part, would affect the calculation of CTR and lead to inaccurate results. To find enough number of discretization N_{dis} , some modelling with different values of N_{dis} have been conducted, and CTR has been calculated and summarized in Figure 7.11a. Moreover, the normalized uncut chip thickness diagram for the non-structured part was provided at different values of N_{dis} .

a



b

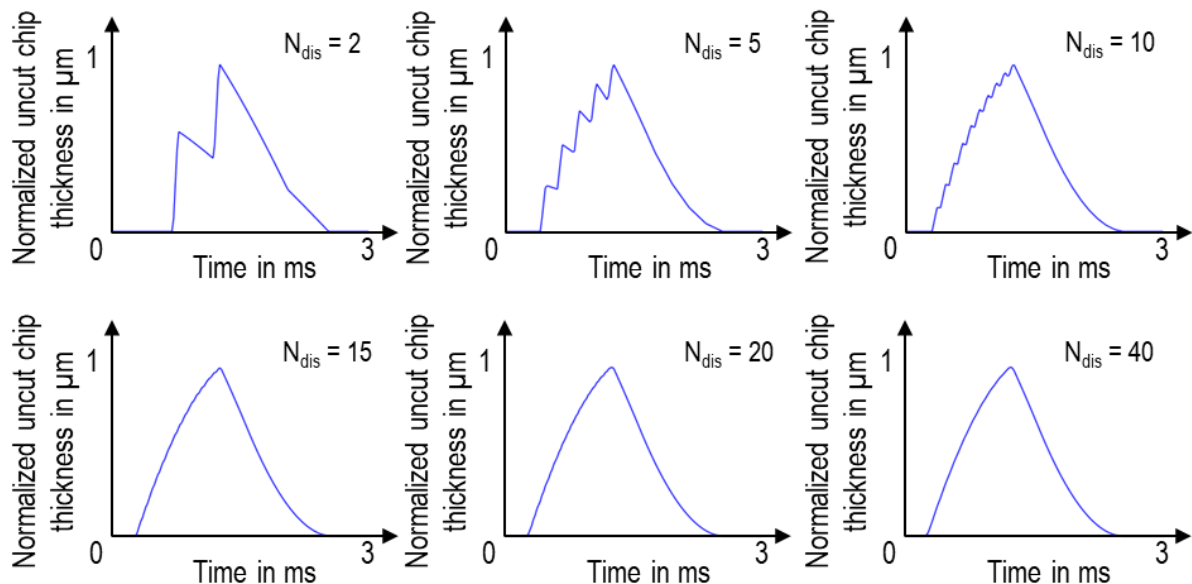


Figure 7.11: a) influence of the number of discretization N_{dis} on CTR, b) normalized chip thickness diagrams at different numbers of discretization N_{dis} for non-structured parts.

According to Figure 7.11a, an increase in CTR can be seen from $N_{dis} = 2$ to $N_{dis} = 10$. As indicated in Figure 7.11b, the chip thickness diagram is dramatically changed at mentioned range. At $N_{dis} = 2$, a remarkable decrease in chip thickness value can be observed before reaching the peak value. Moreover, this irregular fluctuation in the chip thickness diagram can also be observed at $N_{dis} = 5$ and 10. This highlights

insufficient discretization in the modelling, leading to the results' unreliability. However, an increase in N_{dis} ranging from 2 and 10 leads to smoothing the chip thickness diagram. At $N_{dis} > 10$, the chip thickness diagrams are entirely smooth with no irregular fluctuations. Moreover, no change in CTR at $N_{dis} > 10$ can also be observed. To guarantee the reliability of the result, the number of discretization is set to 20 to be far enough away from the determined threshold ($N_{dis} = 10$) and prevent increasing the modelling time by selecting higher values of N_{dis} .

In the following sections, the influence of structure, tool, and process parameters on CTR have been discussed, and the most crucial parameters have been identified.

7.1.1 Influence of structure parameters on the uncut chip thickness

As discussed, the structure parameters are categorized into density, depth, and angle. Figure 7.12 indicates the influence of mentioned parameters on CTR. The structure density can be adjusted by the structure line gap l_g . A higher structure density can be obtained by the lower structure line gap l_g . According to Figure 7.12a, the increase in structure density by reducing structure line gap l_g contributes to a tremendous increase in CTR. In fact, reducing structure line gap l_g leads to more material removal before the process and eventually a higher decrease in the uncut chip thickness. A non-linear relation between structure density, or line gap l_g , and CTR could be observed. A change in line gap l_g from 500 μm to 300 μm , at given cutting parameters in Figure 7.12, slightly increased CTR from 5.9 % to 8.6 %. A further decreasing line gap l_g to 200 μm led to an increasing CTR of 12.1 %. Although the change in line gap from $l_g = 300 \mu\text{m}$ to $l_g = 200 \mu\text{m}$ is lower than that from $l_g = 500 \mu\text{m}$ to $l_g = 300 \mu\text{m}$, the corresponding changing CTR in this range, $l_g = 200\text{-}300 \mu\text{m}$, shows a slightly higher value. A further reduction in l_g from 200 μm to 100 μm leads to a considerable rise in CTR from 12.1 % to 21.9 %. It can be concluded that the increase in structure density through reducing line gap l_g leads to more CTR. In detail, each cutting tooth comes into contact with more structure elements once the line gap decreases. As a result, more reduction in chip volume is expected, which would speed up increasing CTR.

Figure 7.12b shows the influence of structure depth s_d on CTR. An increase in s_d is followed by increasing CTR at different structure densities, and a linear relation between structure depth s_d and CTR can be found while the structure depths are less than the radial depth of cut, in this case, $a_e < 300 \mu\text{m}$. As explained, the material removal through structuring the workpiece results in uncut chip thickness reduction and a decrease in chip volume. Increasing removed material volume through laser structuring the workpiece surface can be carried out by reducing the line gaps l_g , or increasing structure density, or increasing structure depth s_d . Therefore, increasing structure depth leads to more CTR. Although a further increase in structure depth s_d more than the radial depth of cut increases CTR, the rising trend with structure depth s_d gradually decreases at different structure densities. In fact, at the radial depth of cut less than the structure depth s_d , all removed material through pre-structuring the workpiece would not affect the uncut chip thickness reduction. Thus, CTR increases by structure depth s_d with a slower trend. In this case, an increase in CTR is associated with the wider lasered profile at the range of radial depth of cut, followed by more removed material and, finally, higher CTR.

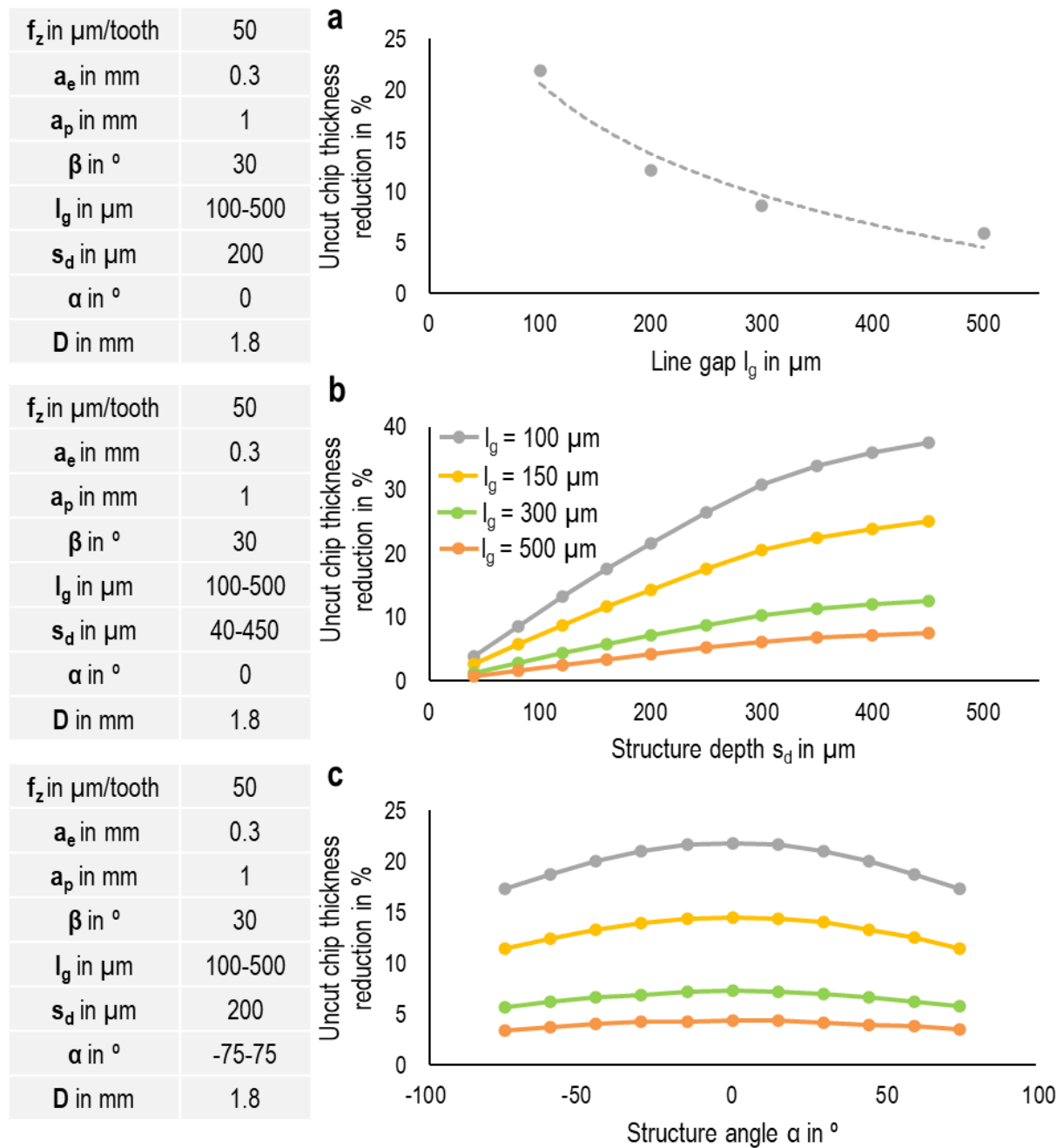


Figure 7.12: a) Influence of line gap l_g (or structure density) on CTR, b) Influence of structure depth s_d on CTR, c) Influence of structure angle α on CTR.

At higher structure densities, or lower line gaps, an increase in CTR with structure depth s_d accelerates. As an example, by increasing structure depth s_d from 40 μm to 300 μm at $l_g = 100 \mu\text{m}$, CTR increases from 3.9 % to 30.85 %. In the case of $l_g = 500 \mu\text{m}$, CTR enhances from 0.75 % to 6.21 %. This tremendous change at higher structure densities is associated with the considerable rise in volume of the removed material before the machining process caused by higher structure densities and structure depths. Moreover, at higher structure depths, a change in CTR through changing the structure density, or line gap l_g , is much more considerable. This highlights the role of both factors, line gap l_g and structure depth s_d , in reducing the uncut chip thicknesses and, finally, enhancing CTR.

A change in structure angle α does not influence the volume of removed material before the milling process. Therefore, a tremendous effect on CTR would not be expected. As illustrated in Figure 7.12c, CTR has no countable change at $l_g = 300 \mu\text{m}$ and $500 \mu\text{m}$. A non-linear change in CTR, at $l_g = 100 \mu\text{m}$ and $l_g = 150 \mu\text{m}$, is detectable by changing the structure angle α . Moreover, no difference in CTR can be observed between negative and positive structure angles at different structure densities. At $l_g = 100 \mu\text{m}$, CTR decreases from 21.81 % to 17.26 % once the structure angle α changes from 0 to +75 (or -75). This change in CTR through changing the structure angle α at $l_g = 100 \mu\text{m}$, that is higher than other line gaps, is neglectable compared to the influence of two other structure parameters, structure density and structure depth, on CTR. The interaction between the parameters as well as the determination of influential parameters, are the topics that will be extensively discussed in section 7.1.4.

7.1.2 Influence of tool geometry on the uncut chip thickness

In the developed model, the tool parameters in terms of helix angle β , tool diameter D , and the number of cutting teeth N are considered. Since the modelling aims to investigate the influence of varied process parameters on CTR, the number of cutting teeth plays no crucial role because the movement of the cutting tool in the modelling is adjusted based on the feed per tooth, and each tooth removes the same amount of the material. Therefore, the change in the number of cutting teeth N would not influence CTR. Regarding the helix angle β , this question arises whether increasing the helix angle leading to more intersection with structure elements can enhance CTR. By changing the tool diameter D at the same process parameters, the cutting tooth path would change, affecting the uncut chip geometry. Therefore, the influence of structuring on the reduction of chip thicknesses at varied uncut chip geometries caused by different tool diameters is another question that must be answered.

According to Figure 7.13a, a change in helix angle β from 0° to 45° does not influence CTR at varied structure densities. Thus, more intersection between cutting tool and structure elements through increasing helix angle does not affect CTR. As illustrated in Figure 7.13b, a change in tool diameter can affect CTR. Particularly at $l_g = 100 \mu\text{m}$, a reduction in tool diameter leads to an enhancement of CTR from 19 % to 27 %. Therefore, the lower tool diameters result in higher values of CTR.

According to Figure 7.14, a change in tool diameter D leads to a variation in uncut chip geometry. At $D = 0.9 \text{ mm}$, the cutting tooth with higher attacking angles comes into contact with the workpiece, followed by a thicker uncut chip geometry. An increasing tool diameter D from 0.9 mm to 3.6 mm results in a longer contact length (shown with the red line color in Figure 7.14) and narrower uncut chip geometry. Therefore, laser structuring the workpiece leads to higher CTR at thicker uncut chip geometry.

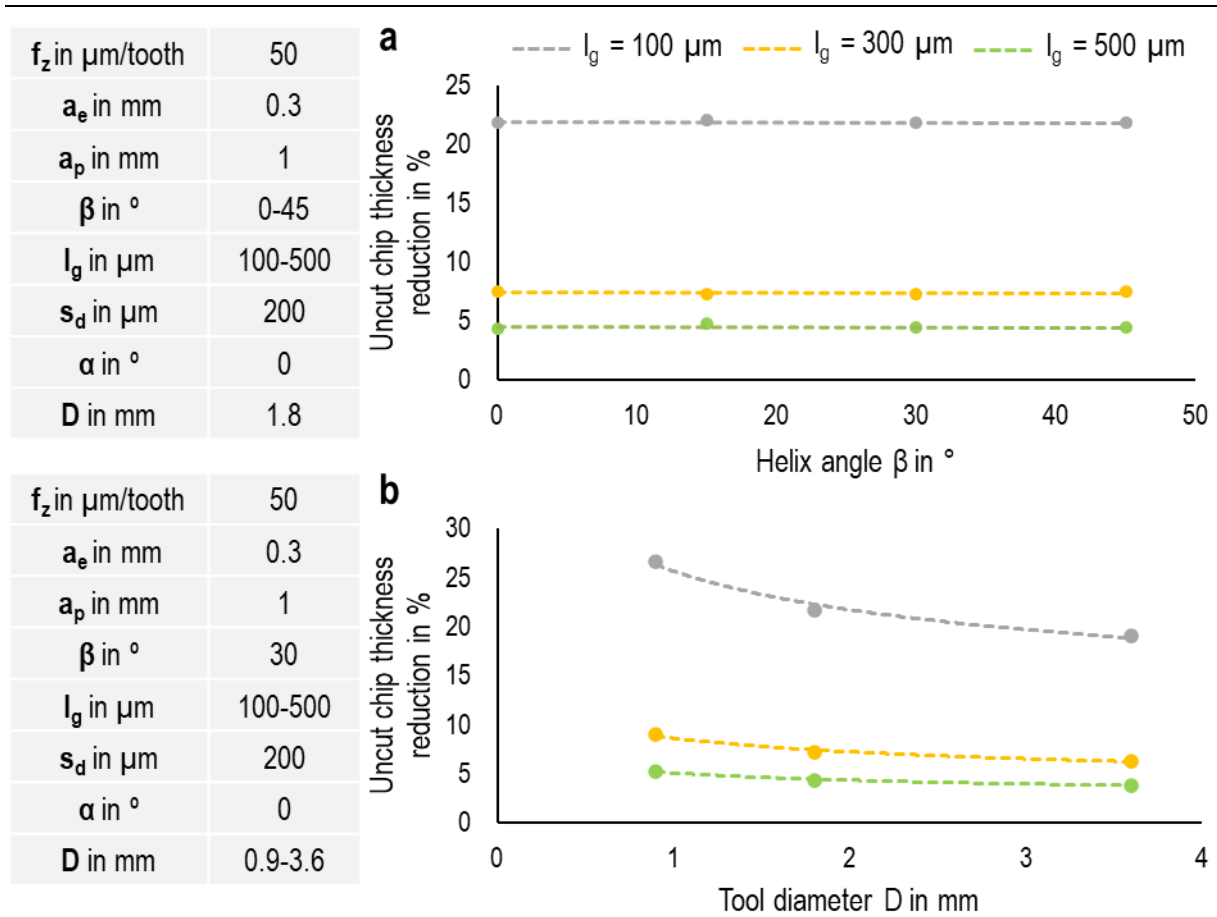


Figure 7.13: a) influence of helix angle β on CTR, b) influence of tool diameter D on CTR.

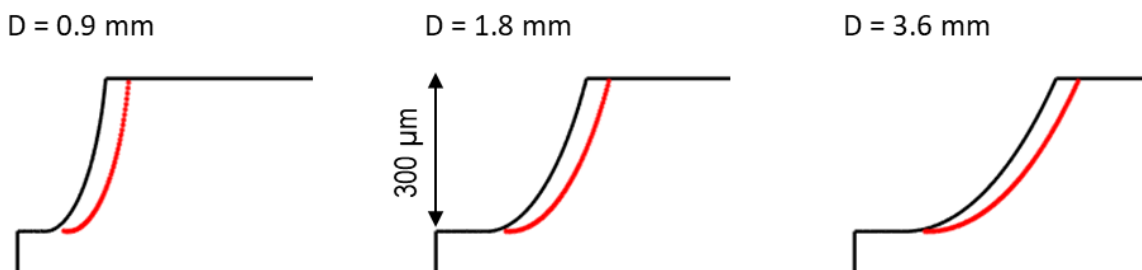


Figure 7.14: Influence of tool diameter D on uncut chip geometry.

7.1.3 Influence of process parameters on the uncut chip thickness

The influence of process parameters in terms of axial depth of cut a_p , feed per tooth f_z , and radial depth of cut a_e on CTR is summarized in Figure 7.15. By changing the axial depth a_p , CTR remains constant at different structure densities (see Figure 7.15a). On one side, a higher axial depth of cut a_p results in more intersection between the cutting tool and structure elements. On the other side, more material would be removed by increasing the axial depth of cut a_p . Eventually, this leads to no change in CTR by changing a_p . According to Figure 7.15b, CTR increases from 19.16 % to 23.9 % by increasing feed from 25 $\mu\text{m}/\text{tooth}$ to 70 $\mu\text{m}/\text{tooth}$ at $l_g = 100 \mu\text{m}$. A slight increase in CTR with feed can also be observed at other structure densities. More chip volume is expected by increasing feed. Thus, structuring the workpiece is more highlighted in reducing chip thicknesses at larger chip volume followed by a slight enhancement of CTR with feed f_z . Moreover, the structure density has no countable influence on the rate of increasing CTR with feed f_z . As illustrated in Figure

7.15c, a reduction in the radial depth of cut a_e is accompanied by increasing CTR. A decrease in the radial depth of cut a_e limits a higher proportion of uncut chip volume in the range of the structure depth. Consequently, more intersection between uncut chip volume and structure elements leads to higher CTR. This trend considerably accelerates at the structure density with $l_g = 100 \mu\text{m}$. The reduction in the radial depth of cut a_e at higher structure densities results in a tremendous decrease in uncut chip thicknesses due to a more significant intersection between structure elements and uncut chip volume limited at the range of structure depth. This is followed by an acceleration in increasing CTR.

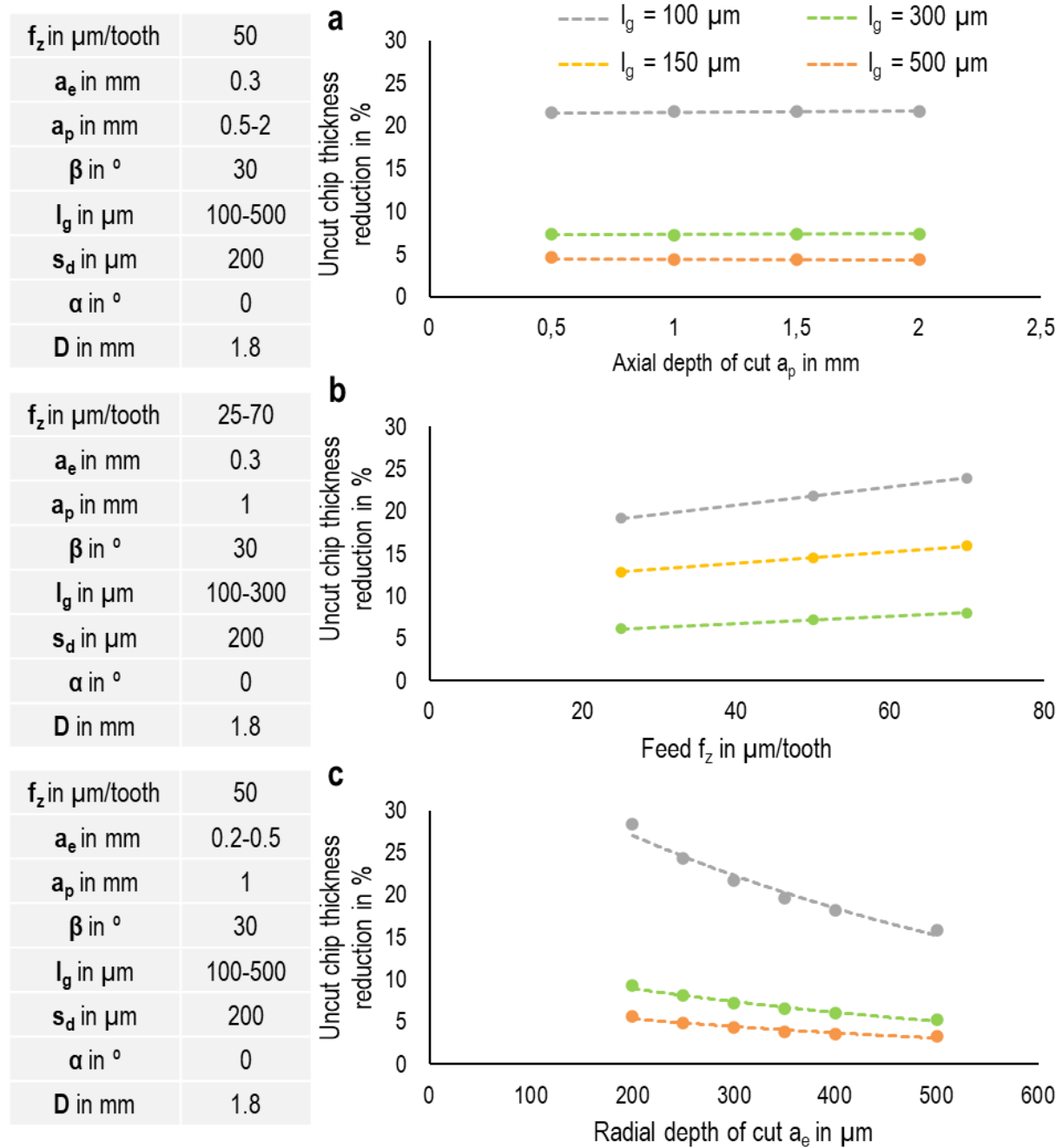


Figure 7.15: Influence of process parameters on CTR: a) axial depth of cut a_p , b) feed f_z , c) radial depth of cut a_e .

7.1.4 Determination of important parameters in laser-assisted micro-milling

In previous sections, the influence of different parameters in three categories of structure, process, and tool on CTR has been discussed. The current section aims to find the influential parameters.

Figure 7.16 compares the combined influence between structure density l_g and various LAM parameters on CTR. According to Figure 7.16a, no change in CTR at different values of helix angle β is detectable. However, reducing l_g from 500 μm to 100 μm indicates a considerable increase in CTR. Figure 7.16b also highlights the remarkable influence of l_g on CTR again. In the case of f_z , a slight increase in CTR with f_z is detectable, particularly at lower values of l_g . Figure 7.16c also shows that the lower values of l_g led to increasing the influence of radial depth of cut a_e on CTR. Regarding the influence of structure angle α on CTR illustrated in Figure 7.16d, a slight change in CTR with α is again observable at lower values of l_g . The influence of tool diameter on CTR is only indicated at lower values of l_g (see Figure 7.16e). Like β , a_p did not affect CTR, as represented in Figure 7.16f. According to Figure 7.16g, the influence of structure depth s_d on CTR considerably increases with reducing the l_g . Moreover, the influence of l_g on CTR is affected by changing s_d . In detail, l_g is more effective at higher values of s_d (deeper structures). In fact, l_g and s_d directly influence reducing the volume of removed material by laser structuring prior to machining. Therefore, they have a decisive role in CTR. Apart from s_d , other parameters such as f_z , a_e , d , and α influence the effectiveness of l_g on CTR but are not as high as the effect of s_d .

To quantify the influence of different parameters on CTR, the Spearman correlation coefficient is calculated for each individual dataset associated with Figure 7.16(a-g). This coefficient is a non-parametric measure of the correlation between two variables. In fact, it measures the strength and direction of the monotonic relationship between two variables. A monotonic relationship is a type of relationship where, as one variable increases, the other variable also tends to increase or decrease. The Spearman correlation coefficient ranges from -1 to 1, where -1 indicates a perfect negative correlation, 1 indicates a perfect positive correlation, and 0 indicates no correlation. It is calculated by ranking the values of each variable and then calculating the correlation between their ranks. In the case of repetitive values, the rank of each value is determined by averaging the ranks that would be assigned to each occurrence of that value. The following equation provides the calculation of Spearman rank coefficient r_s .

$$r_s = 1 - \frac{6}{n(n^2 - 1)} \left(\sum_{i=1}^n d_i^2 + \frac{1}{12} \sum_{j=1}^l m_j(m_j^2 - 1) \right) \quad 7.13$$

where n , d , m , and l are the number of variable pairs, the difference in the ranks of the two coordinates for each data pair, the multiplicities of ranks, and its number.

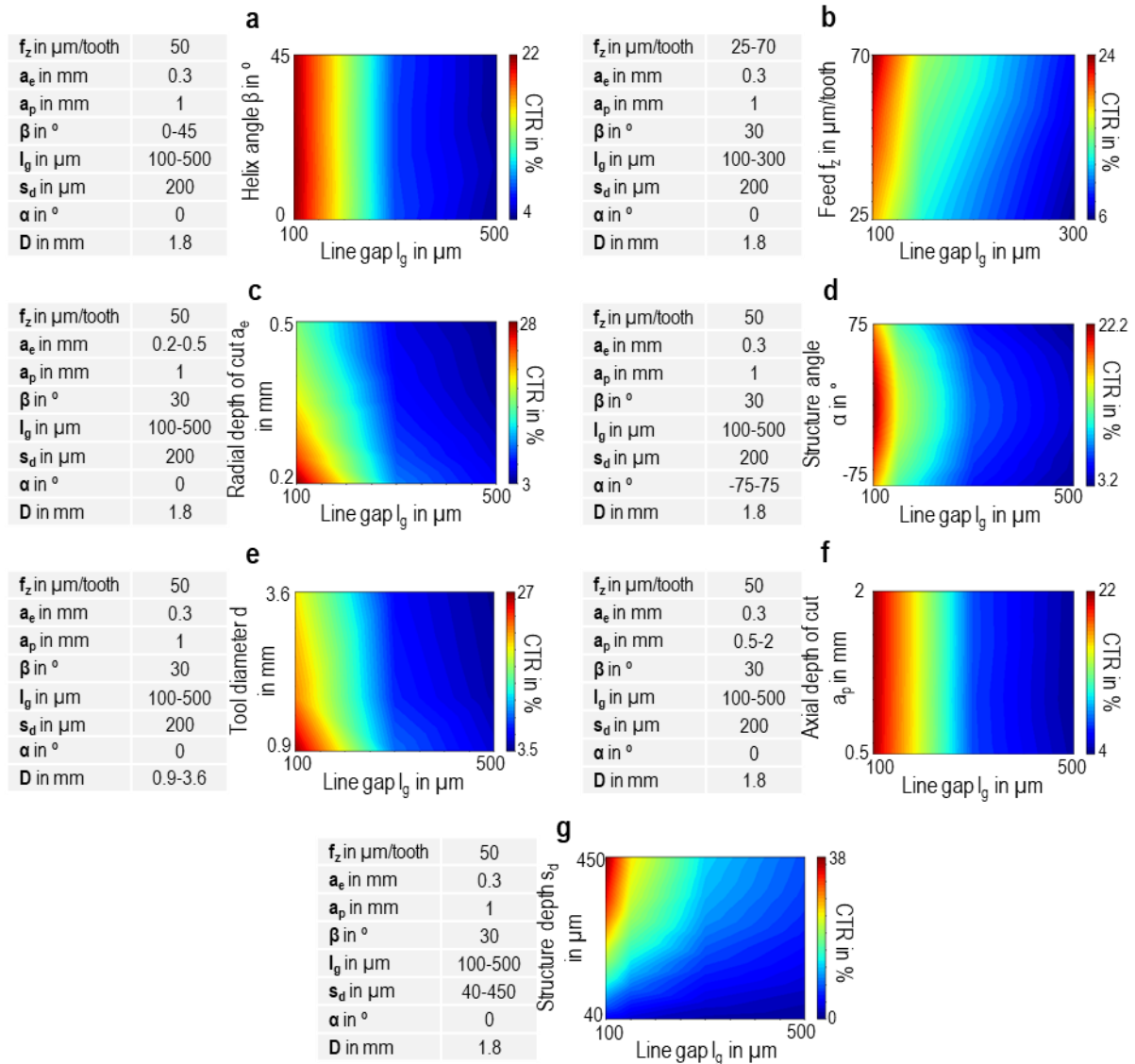


Figure 7.16: A comparative illustration between the combined influence of the line gap l_g and various LAM process parameters on CTR: a) helix angle β , b) feed f_z , c) radial depth of cut a_e , d) structure angle α , e) tool diameter D, f) axial depth of cut a_p , g) structure depth s_d .

Table 7.1 provides the calculated Spearman correlation coefficient of parameters for the dataset associated with Figure 7.16(a-g). Accordingly, r_s equals zero for parameters β and a_p . Therefore, no correlation between CTR and mentioned parameters exists. The r_s values for f_z , a_e , d, and α account for 0.31, -0.36, -0.31, and -0.24, respectively. The corresponding value of r_s for l_g stands for -0.95, -0.93, -0.95, and -0.97, which show a significantly higher correlation with CTR. The value of r_s for s_d and l_g related to Figure 7.16g stand for 0.67 and -0.68, respectively. The reason for the reduction of r_s for l_g is the influence of s_d on the effectiveness of l_g on CTR, where no remarkable change of CTR is observable with changing l_g at lower values of s_d . Therefore, both factors are considered as the most influential parameters on CTR. Among them, structure density l_g is used as a varying structure parameter for the experimental test.

Table 7.1: Spearman correlation coefficient.

Image No		r_s
a	β	0
	l_g	-1
b	f_z	0.31
	l_g	-0.95
c	a_e	-0.36
	l_g	-0.93
d	α	-0.24
	l_g	-0.97
e	d	-0.31
	l_g	-0.95
f	a_p	0
	l_g	-1
g	s_d	0.67
	l_g	-0.68

7.2 Laser structuring of Ti6Al4V and micro-milling of structured parts

In the previous section, the influence of laser structuring the workpiece on chip thickness reduction through the developed model has extensively been discussed, and the influential parameters on chip thickness reduction have been found. Based on the findings, it can be expected that structuring the workpiece leading to chip thickness reduction can affect cutting forces in the micro-milling of Ti6Al4V material. According to the modelling results, a fluctuation in the chip thickness diagram in the case of structured parts was observed. This fluctuation in chip thicknesses may be a source of instability in the process that can negatively affect the surface quality. Therefore, an investigation regarding the influence of structuring on surface roughness has been also under focus in the current section. In the following, the laser structuring of the Ti6Al4V material has been discussed in section 7.2.1. Among different variables in the presented laser-assisted machining process, the structure density in the experiment was under concentration, and the structuring of the parts was performed at different structure densities. The influence of laser structuring on cutting forces and surface roughness has been discussed in sections 7.2.2 and 7.2.3, respectively.

7.2.1 Laser structuring of material workpiece

Some tests were performed with different laser scan speeds at single linear laser scanning. The laser power was set to 100% ($P_{L_ave} = 50 \text{ W}$) in all tests to achieve a maximum MRR. Increasing the laser scan speed v_L obviously results in a smaller heat-affected zone. High heat-affected zones and melting were evident at laser scanning speeds below $v_L = 200 \text{ mm/s}$. However, at laser scanning speeds above $v_L = 200 \text{ mm/s}$, the sign of heat affected zone was limited. Since structuring the workpiece is performed at multiple scanning to achieve a deeper structure depth and remove more material before the machining process, the selection of appropriate laser scan velocity is important to prevent as possible as melting with preserving high material removal. Further, one preliminary test was carried out with a laser power $P_{L_ave} = 50 \text{ W}$, a laser repetition frequency $f_L = 400 \text{ kHz}$, and a laser scan velocity $v_L = 200 \text{ mm/s}$ with $N_s = 80$ as the number of laser scanning.

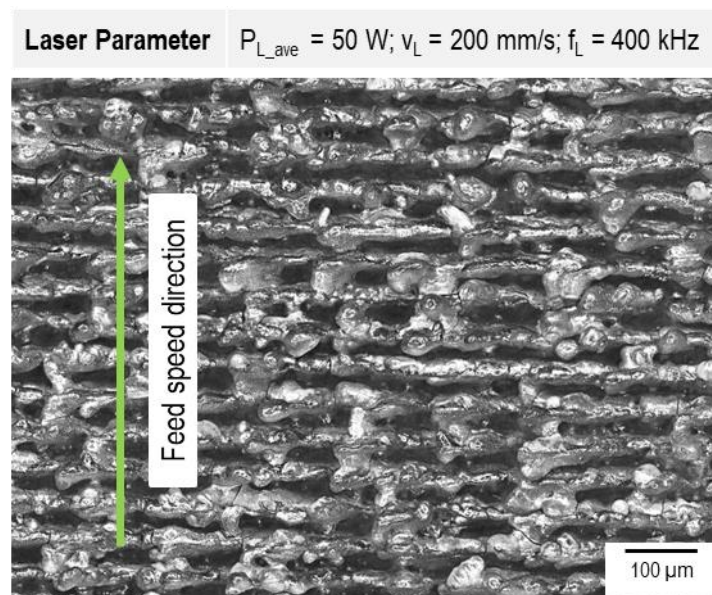


Figure 7.17: Laser structured part with line gap 100 μm .

The linear pattern with a line gap of $100\ \mu\text{m}$ was selected to structure the part, as shown in Figure 7.17. The milling direction with respect to the pattern orientation can also be observed. After machining the structured part, considerable tool wear was observed after a material removal of $Q_w = 18\ \text{mm}^3$, as shown in Figure 7.18. The significant tool wear may be mainly associated with the massive amount of melted material in structuring the parts. To tackle this issue, the laser scan velocity v_L was changed from $200\ \text{mm/s}$ to $600\ \text{mm/s}$. No remarkable tool wear was detected for milling the structured surface. The laser parameters were set to a laser power of $P_{L:\text{ave}} = 50\ \text{W}$, a laser repetition frequency of $f_L = 400\ \text{kHz}$, and a laser scan velocity of $v_L = 600\ \text{mm/s}$. The focal length and the nominal laser diameter were $100\ \text{mm}$ and $80\ \mu\text{m}$, respectively.

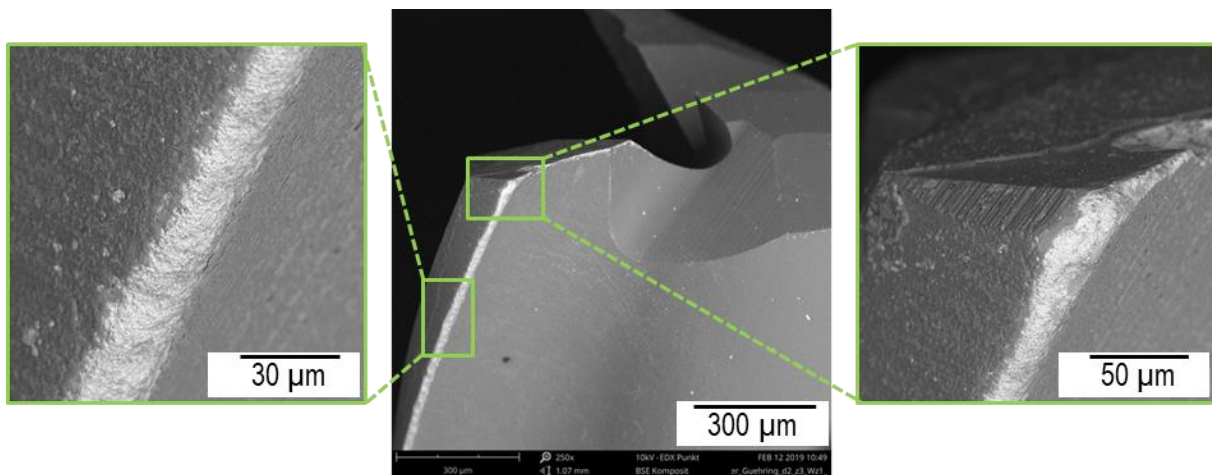


Figure 7.18: Tool wear after a material removal of $Q_w = 18\ \text{mm}^3$ at $v_c = 35\ \text{m/min}$, $a_p = 1\ \text{mm}$, $a_e = 0.3\ \text{mm}$, and $f_z = 20\ \mu\text{m/tooth}$.

A simple linear pattern was selected for the structuring of the workpiece. Then, the structure density was adjusted by changing the distance between two successive structure lines. Ti6Al4V parts were structured at different structure densities, as indicated in Figure 7.20(a-d). Accordingly, 100 , 200 , 300 , and $500\ \mu\text{m}$ were selected for the line gap l_g between structure lines. Moreover, Figure 7.20(e-h) provides 3D images of structured parts at different line gaps. After $N_s = 80$, the structured profile with approximately $200\ \mu\text{m}$ structure depth s_d and structure width s_w of $80\ \mu\text{m}$ was obtained. The generated profile is illustrated in Figure 7.19.



Figure 7.19: Laser structured profile.

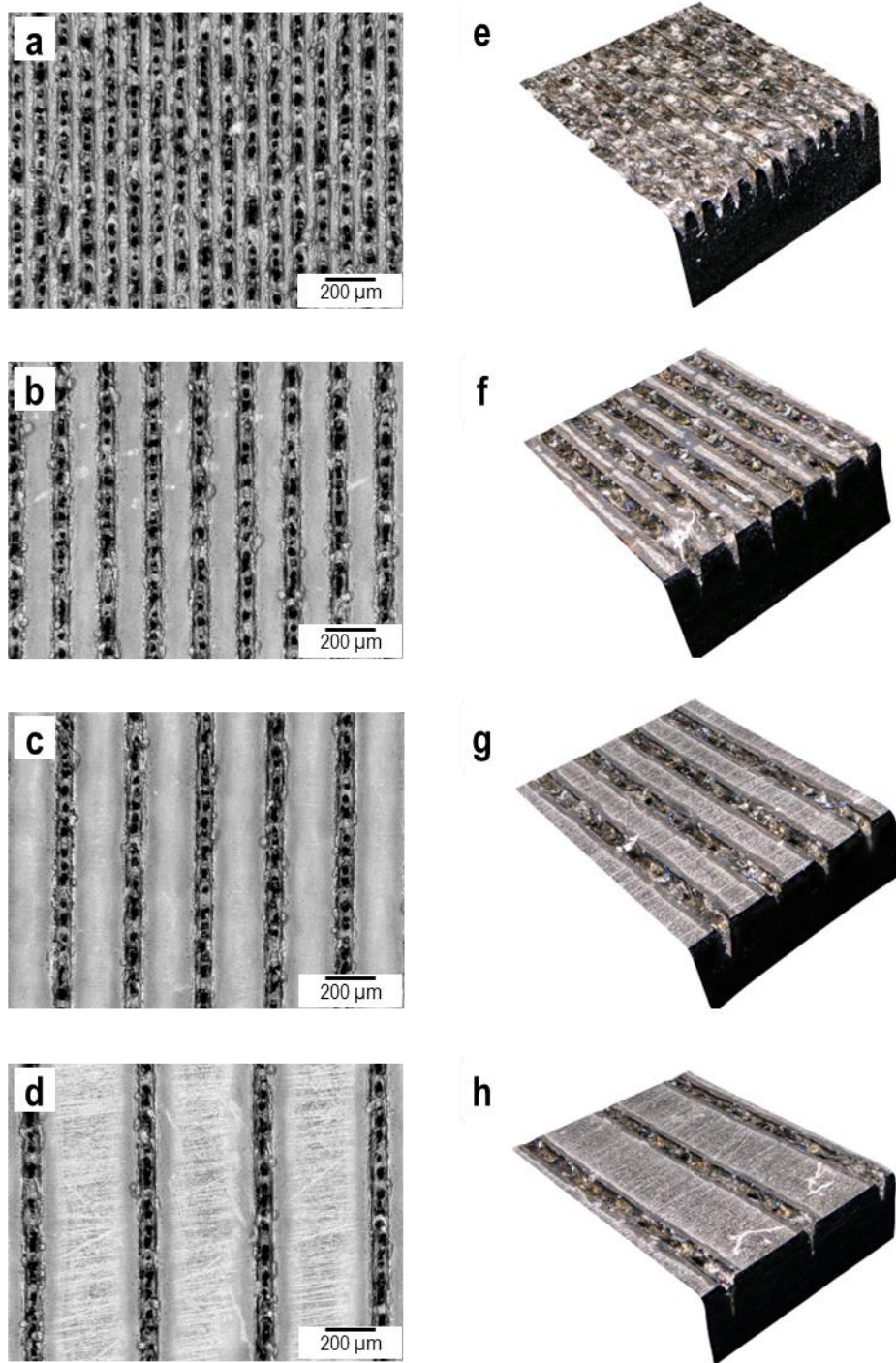


Figure 7.20: Structured parts at different structure densities with different line gaps: a) $l_g = 100 \mu\text{m}$, b) $l_g = 200 \mu\text{m}$, c) $l_g = 300 \mu\text{m}$, d) $l_g = 500 \mu\text{m}$. 3D images of structured parts at different structure densities with different line gaps: e) $l_g = 100 \mu\text{m}$, f) $l_g = 200 \mu\text{m}$, g) $l_g = 300 \mu\text{m}$, h) $l_g = 500 \mu\text{m}$.

Since the laser beam energy follows the Gaussian distribution, a variation in ablation regions can be expected. According to Figure 7.21a, a considerable ablation occurred at the center of the structure line (region 1). In this region, a significant amount of laser energy is absorbed by the material, followed by melting and vaporization, and explosive boiling (phase explosion) as a frequent mechanism of material removal at USPL. In region 2, the removed material through melting is condensed and deposited. In region 3, the melt sputter particles are deposited on the outer area of the structure line. An EDX analysis of the structured line was carried out

at three different regions (button, side, and out of the structure), and the results are summarized in Figure 7.21b. Accordingly, a dramatic increase in the percentage of oxygen can be seen from region 1 to region 3. This shows that the deposited material, particularly in region 3, is considerably oxidized. Moreover, a reduction in the percentage of pure titanium is observed from region 1 to region 3. In region 3, no Nitrogen was quantified. For other material elements, no remarkable change is detected.

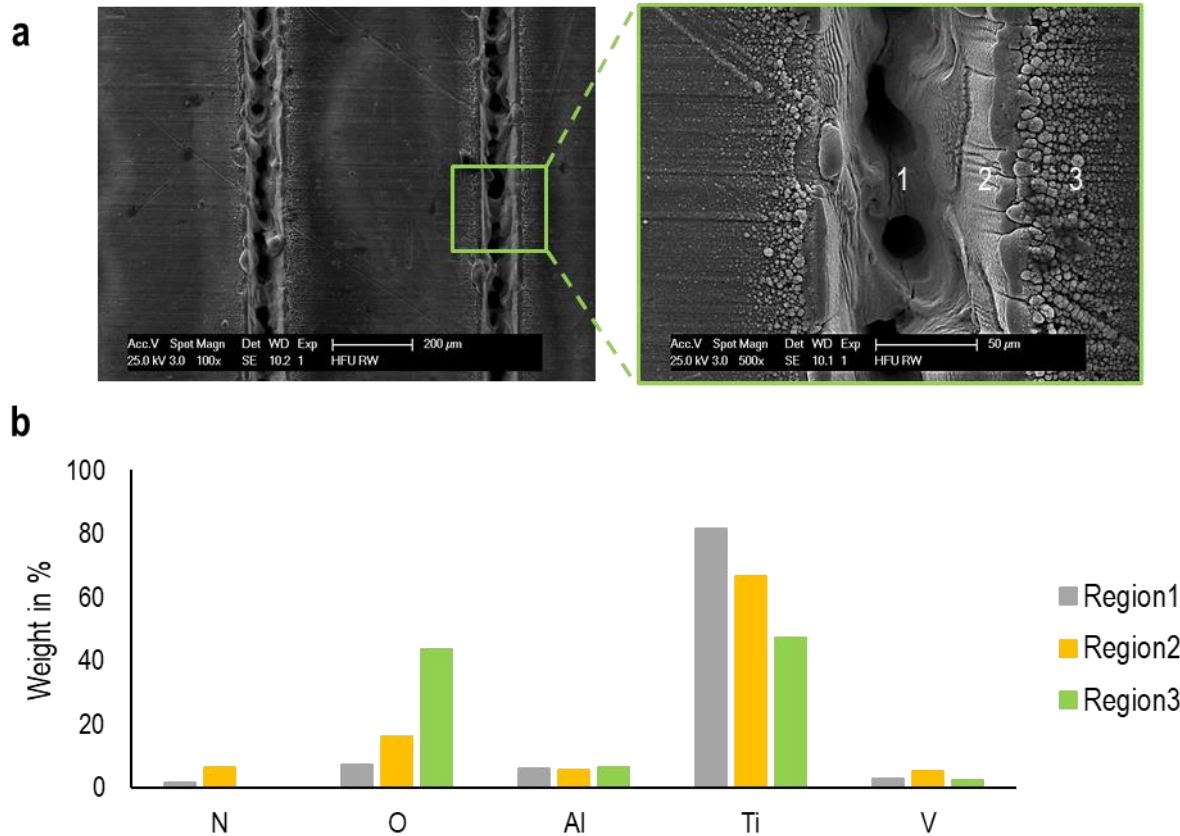


Figure 7.21: a) SEM image from the top view of the structured part, b) weight percentage of various material elements at different regions.

7.2.2 Cutting forces

According to the modelling results and comparing the chip thickness diagram between structured and non-structured parts, a reduction in maximum uncut chip thickness and chip volume through structuring the part was observable. This may also affect the cutting forces. In this regard, for comparing the structured and non-structured parts, the maximum and mean values of the cutting forces signal as the main two features are extracted as explained in the following.

Figure 7.22a indicates a schematic of the cutting force signal. Once a cutting tooth comes into contact with the workpiece, the cutting force signal increases to the maximum value corresponding to the maximum chip thickness. Afterwards, the cutting force drops to the zero value. Then, the subsequent cutting tooth approaches the workpiece, and this procedure is repeated. The maximum values, corresponding to the signal peaks, are detected throughout the signal. They are shown by the red point in Figure 7.22b. Further, the average value from collected peaks is calculated as follows and is considered as the maximum value of the signal s_{max} :

$$s_{\max} = \frac{1}{n} \sum_{i=1}^n p_i \quad 7.14$$

where p_i and n denote the values of peak points and the number of peak points, respectively. According to Figure 7.22c, the ranges of the signal highlighted with red color indicate the contact time between the tool and workpiece. Therefore, the corresponding signal points are subjected to the average calculation and considered as a mean value of the signal s_{mean} (see equation 7.15 and 7.16).

$$s_{\text{mean}} = \frac{1}{n_1} \sum_{i=1}^{n_1} r_i \quad 7.15$$

where n_1 corresponds to the number of detected ranges and r_i is considered as an average signal value at each range and calculated as below:

$$r_i = \frac{1}{n_{2,i}} \sum_{j=1}^{n_{2,i}} p_{i,j} \quad 7.16$$

where $n_{2,i}$ and $p_{i,j}$ denote the number of signal points at each range and the value of the signal points, respectively.

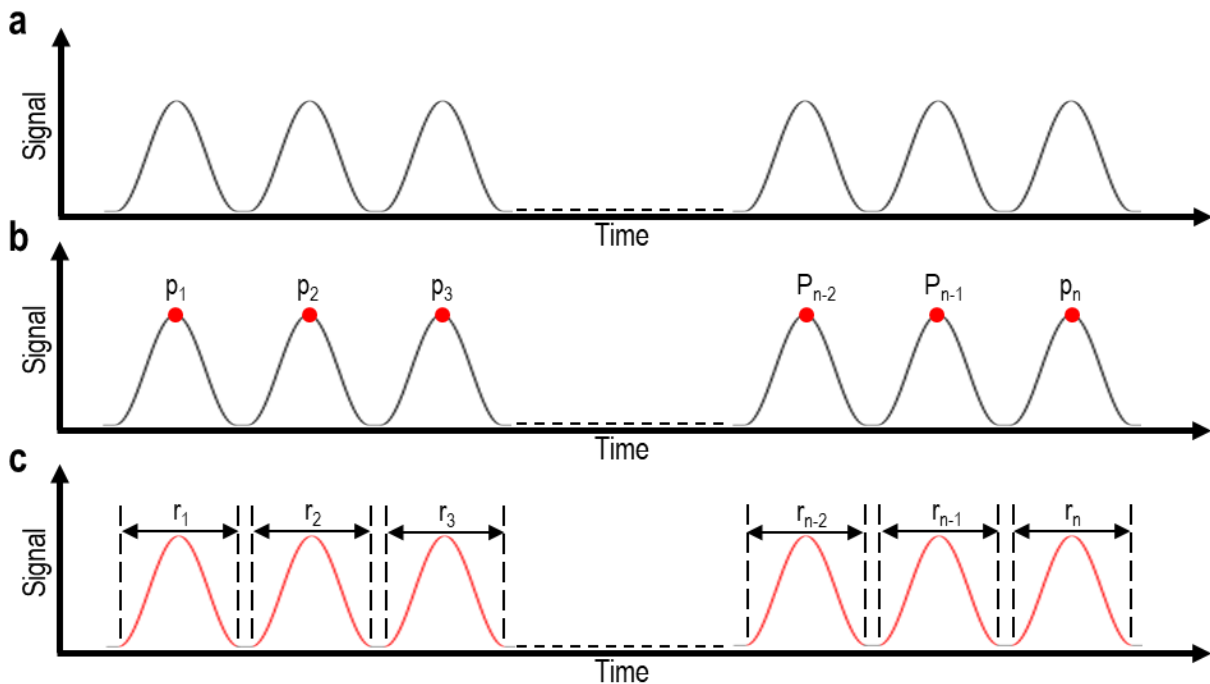


Figure 7.22: a) the schematic of the signal, b) extraction of maximum value s_{\max} , c) extraction of mean value s_{mean} .

The cutting forces were measured in two directions of x and y , denoting feed direction and normal to the feed direction, respectively. Also, the resultant cutting force F_{res} can be calculated with respect to F_x and F_y , according to equation 4.2.

The feature extraction, mean and maximum values, is carried out for both cutting forces, F_x and F_y , and the resultant cutting force for structured and non-structured parts. These extracted features are used to calculate cutting force reduction in the machining of structured parts.

As explained, this section has been allocated to study how considerable is the influence of laser structuring on the machinability of titanium alloy materials with respect to cutting forces. Figure 7.23 summarizes the experimental results for micro-milling laser-structured parts with line gaps of 100, 200, 300, and 500 μm at two different feeds of 10 and 50 $\mu\text{m}/\text{tooth}$. The orange and red dash lines denote the average values from the peak and entire force signal, respectively, for the micro-milling of non-structured parts. The grey and green points indicate the average values from the peak and entire force signal, respectively, at the micro-milling of structured parts. The average from peak forces is obviously higher than the average from entire force signals at both structured and non-structured parts. Accordingly, the reduction in both force values at the x and y directions can clearly be observed in the case of milling of structured parts for both $f_z = 10 \mu\text{m}/\text{tooth}$ and $f_z = 50 \mu\text{m}/\text{tooth}$. This highlights the effectiveness of laser structuring in reducing cutting forces in micro-milling Ti6Al4V as a hard-to-cut material. With respect to the reduction in the peak of the force signal, it can be concluded that the laser-structuring, which removes some amount of the material prior to machining, has led to the reduction in maximum chip thicknesses during the micro-milling process. Eventually, this contributed to less peak forces. A decrease in the entire force signal highlights that in addition to maximum chip thicknesses, the chip volume in the contact time between the tool and workpiece was also influenced by the structuring of the part. Due to an increase in the structure density through the reduction of the line gap l_g from 500 μm to 100 μm , a decrease in cutting forces, in x and y directions and for peak and entire of the force signal, is observed at both feeds. The higher the structure density, the more material would be removed from the workpiece surface through laser-structuring before machining. Therefore, this leads to a higher reduction in maximum chip thicknesses as well as chip volumes in the contact time between the tool and the workpiece. Therefore, a higher force reduction with respect to the peak and entire of signal is expected.

The trend lines highlighted by grey and green colors indicate a logarithmic relation between line gaps l_g and cutting forces, F_x and F_y . An increase in the line gap l_g , or decreasing structure density, resulted in a logarithmic rise in cutting forces, F_x and F_y . This logarithmic relation between line gap l_g and cutting forces in the x and y direction and for the entire and peak of the cutting force signals at $f_z = 10 \mu\text{m}/\text{tooth}$ and $f_z = 50 \mu\text{m}/\text{tooth}$ are summarized in equation 7.17 and equation 7.18, respectively.

$$\begin{bmatrix} F_{x_peak} \\ F_{y_peak} \\ F_{x_entire} \\ F_{y_entire} \end{bmatrix} = \begin{bmatrix} 4.7 \\ 0.5 \\ 2.7 \\ 0.5 \end{bmatrix} \times \ln(l_g) + \begin{bmatrix} -6.4 \\ 8.3 \\ -5.6 \\ 1.8 \end{bmatrix} \quad 7.17$$

$$\begin{bmatrix} F_{x_peak} \\ F_{y_peak} \\ F_{x_entire} \\ F_{y_entire} \end{bmatrix} = \begin{bmatrix} 6.5 \\ 4.2 \\ 3.3 \\ 2.1 \end{bmatrix} \times \ln(l_g) + \begin{bmatrix} -4.0 \\ 12.2 \\ -3.6 \\ 2.8 \end{bmatrix} \quad 7.18$$

Milling Tool	3 flutes; $\Phi = 1.8$ mm (WN 3142 R-N, PVD-TiAlN, Schaft DIN 6535-HA/HB), Gühring
Workpiece	Extruded Ti6Al4V
Parameters	Down-milling; $v_c = 35$ m/min; $f_z = 10$ and 50 $\mu\text{m}/\text{tooth}$; $a_p = 1$ mm; $a_e = 0.3$ mm
Coolant	Oil
Laser	$P_{L_ave} = 50$ W; $v_L = 600$ mm/s; $f_L = 400$ kHz
Structure	$l_g = 100, 200, 300$ and 500 μm ; $s_d \approx 200$ μm ; $s_w = 80$ μm

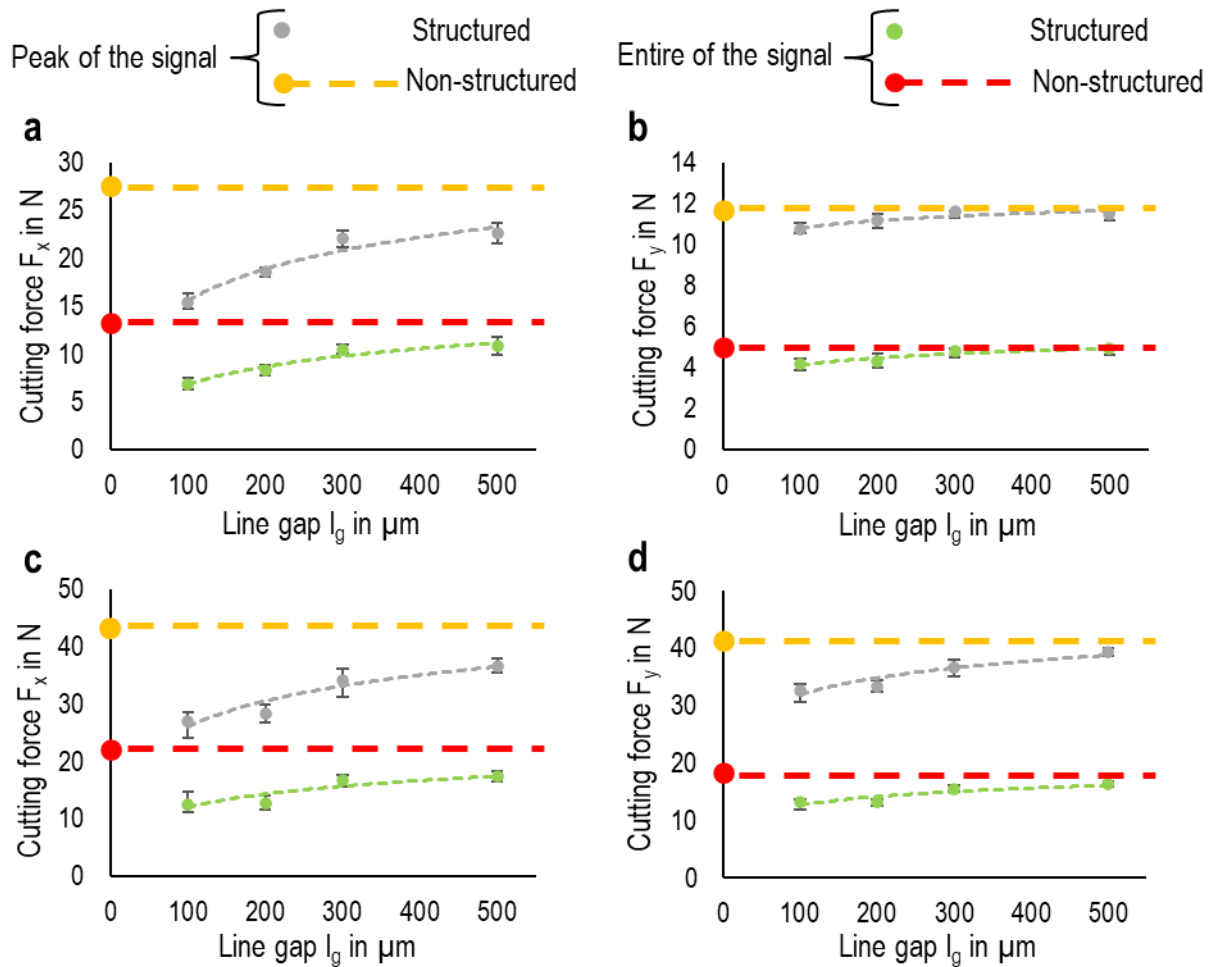


Figure 7.23: Influence of structure density on reduction of cutting forces in x and y directions: a) F_x at $f_z = 10$ $\mu\text{m}/\text{tooth}$, b) F_y at $f_z = 10$ $\mu\text{m}/\text{tooth}$, c) F_x at $f_z = 50$ $\mu\text{m}/\text{tooth}$, d) F_y at $f_z = 50$ $\mu\text{m}/\text{tooth}$.

The equations 7.17 and 7.18 can be summarized in a simple linear equation provided as follow:

$$Y = m \times X + b \tag{7.19}$$

Where Y contains the vector of cutting forces and m is the slope of the linear graph. Moreover, X equals $\ln(l_g)$, and b is the linear graph intercept. Obviously, higher values of the m indicate more influence of X on Y. In other words, the cutting force is more influenced by changing the line gap l_g if the slope of the linear diagram is greater. Therefore, the line gap l_g has more influence on cutting forces, peak and entire of the signals, in the x-direction according to equations 7.17 and 7.18.

Moreover, a comparison with respect to the slope of the diagrams between the peak and entire signals indicates that the signal peaks are more influenced by changing l_g for both F_x and F_y . Comparing $f_z = 10 \mu\text{m/tooth}$ and $f_z = 50 \mu\text{m/tooth}$, it can be concluded that the peak and entire cutting force signals at higher feeds are more affected by changing l_g .

Milling Tool	3 flutes; $\Phi = 1.8 \text{ mm}$ (WN 3142 R-N, PVD-TiAlN, Schaft DIN 6535-HA/HB), Gühring
Workpiece	Extruded Ti6Al4V
Parameters	Down-milling; $v_c = 35 \text{ m/min}$; $f_z = 10$ and $50 \mu\text{m/tooth}$; $a_p = 1 \text{ mm}$; $a_e = 0.3 \text{ mm}$
Coolant	Oil
Laser	$P_{L_ave} = 50 \text{ W}$; $v_L = 600 \text{ mm/s}$; $f_L = 400 \text{ kHz}$
Structure	$l_g = 100, 200, 300$ and $500 \mu\text{m}$; $s_d \approx 200 \mu\text{m}$; $s_w = 80 \mu\text{m}$

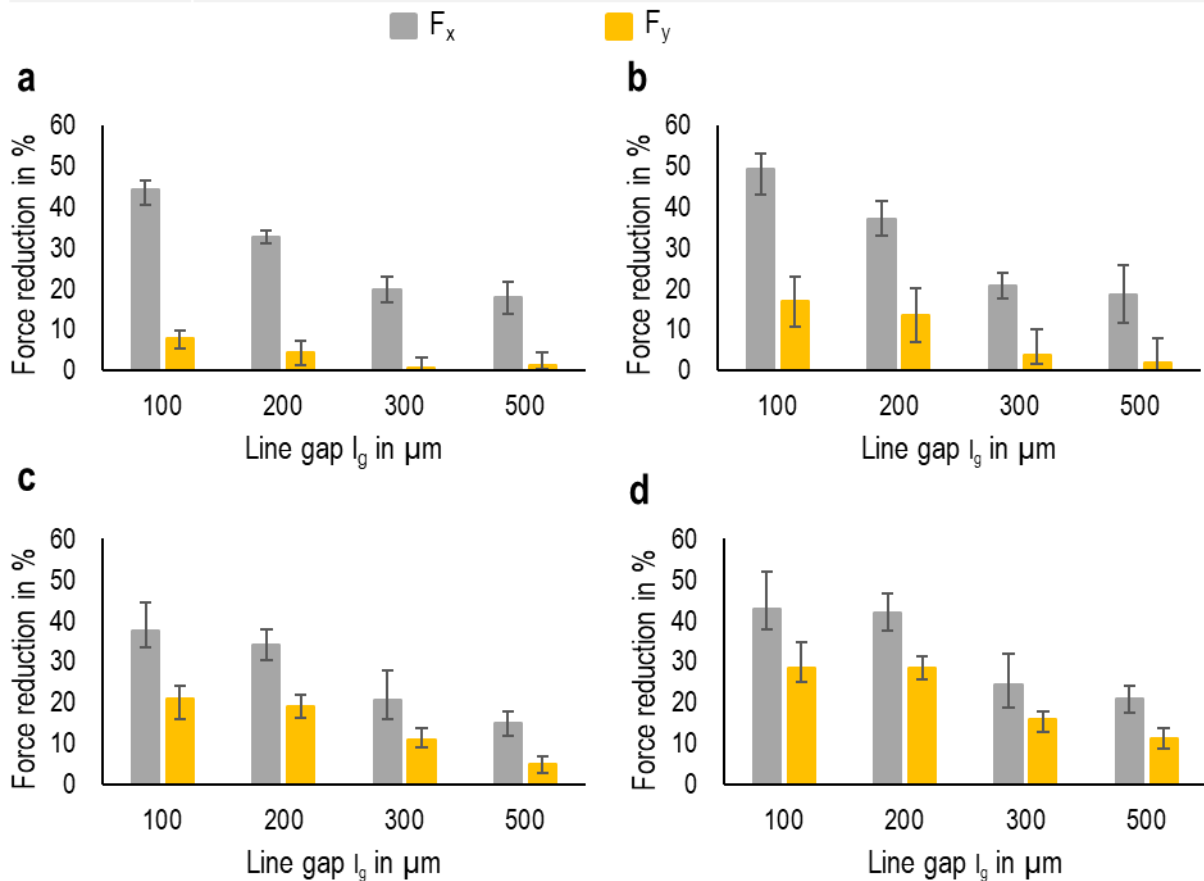


Figure 7.24: Percentage of force reduction for: a) peak of the signal at $f_z = 10 \mu\text{m/tooth}$, b) entire of the signal at $f_z = 10 \mu\text{m/tooth}$, c) peak of the signal at $f_z = 50 \mu\text{m/tooth}$, d) entire of the signal at $f_z = 50 \mu\text{m/tooth}$.

As mentioned, the cutting forces in two directions, x, and y, were measured. The directions x and y denote the milling direction and normal direction, perpendicular to the milling direction, respectively. To compare the amount of force reduction in these two directions, the percentage of force reduction for the peak and entire force signal, in both directions, was calculated. According to Figure 7.24, grey and orange colors denote the percentage of force reduction for F_x and F_y , respectively. Obviously, increasing the structure density through the decrease line gap l_g has led to an

increase in the percentage of force reduction for all force components, F_x and F_y , at both feeds.

As shown in Figure 7.24a and Figure 7.24b, the percentage of force reduction at $f_z = 10 \mu\text{m/tooth}$ in the x-direction is considerable compared to that in the y-direction for both the peak and entire signal at all structure densities. The cutting tool impacts the laser-induced walls or structures in the x-direction. These walls have significantly lower stiffness compared to the non-structured bulk material since there is no material behind them (the bulk material barely supports these structured filigree features). Therefore, the structure strength against removing in the x-direction is expected to be lower than that in the y-direction. Additionally, because of the domino effect of the structures in the x-direction, occurring during cutting and particularly at high structure densities, removing one structured feature eases removing of the other features. Hence, the cutting force in the x-direction is significantly reduced. At $f_z = 10 \mu\text{m/tooth}$, the entire signals show a higher percentage of force reduction than that for the peak of the signals, particularly at line gaps of 100 and 200 μm . This indicates that the structuring of the part not only led to the reduction of maximum chip thicknesses followed by decreasing peak signals but also tremendously reduced the material volume that should be removed in the machining process. This is followed by less chip thicknesses and, consequently, less forces in the contact time between the tool and workpiece. In the case of $f_z = 50 \mu\text{m/tooth}$, as shown in Figure 7.24c and Figure 7.24d, higher force reduction for F_x compared to that for F_y can also be observed for both peak and entire force signals. Again, the reduction of force with respect to the entire signal is higher than that for the signal's peak. Compared to $f_z = 10 \mu\text{m/tooth}$, force reduction for F_y is more pronounced. The decrease in cutting force in the y-direction highlights the probability of less tool deflection. Therefore, the laser-structuring of the parts provides the possibility of using higher feeds with less tool deflections. For $f_z = 50 \mu\text{m/tooth}$, the percentage of force reduction is approximately as high as that for $f_z = 10 \mu\text{m/tooth}$. This indicates the applicability of laser-structuring for machining with higher MRR.

In previous experiments, the radial depth of cut a_e is set to 300 μm , which is higher than the structure depth. Moreover, some experiments with multiple passes and $a_e = 50 \mu\text{m}$ were conducted to investigate the influence of removed material using laser-structuring throughout the structure depth on cutting forces. At each pass, the cutting forces in the x and y directions were measured. Figure 7.25a provides the schematic of the process, which is conducted for 5 passes. Therefore, the structure depth is reduced around 50 μm after each pass. Figure 7.25c and Figure 7.25d show how the cutting forces, F_x and F_y , change after each pass. The grey and orange colors denote the non-structured and structured conditions, respectively. Accordingly, a non-linear relation between structure depth and cutting forces can clearly be seen. A change in cutting force F_x with the structure depth is greater than that for F_y . According to Figure 7.25b, a reduction in uncut chip thickness and, consequently, the percentage of reducing cutting forces, F_x and F_y , is much more pronounced at the first pass compared to other passes. For the subsequent passes, a decrease in the percentage of cutting force reduction can be observed mainly due to the decreasing percentage of uncut chip thickness reduction.

Milling Tool	3 flutes; $\Phi = 1.8$ mm (WN 3142 R-N, PVD-TiAlN, Schaft DIN 6535-HA/HB), Gühring
Workpiece	Extruded Ti6Al4V
Parameters	Down-milling; $v_c = 35$ m/min; $f_z = 10$ $\mu\text{m}/\text{tooth}$; $a_p = 1$ mm; $a_e = 5 \times 0.5$ mm
Coolant	Oil
Laser	$P_{L_{ave}} = 50$ W; $v_L = 600$ mm/s; $f_L = 400$ kHz
Structure	$l_g = 100$ μm ; $s_d \approx 200$ μm ; $s_w = 80$ μm

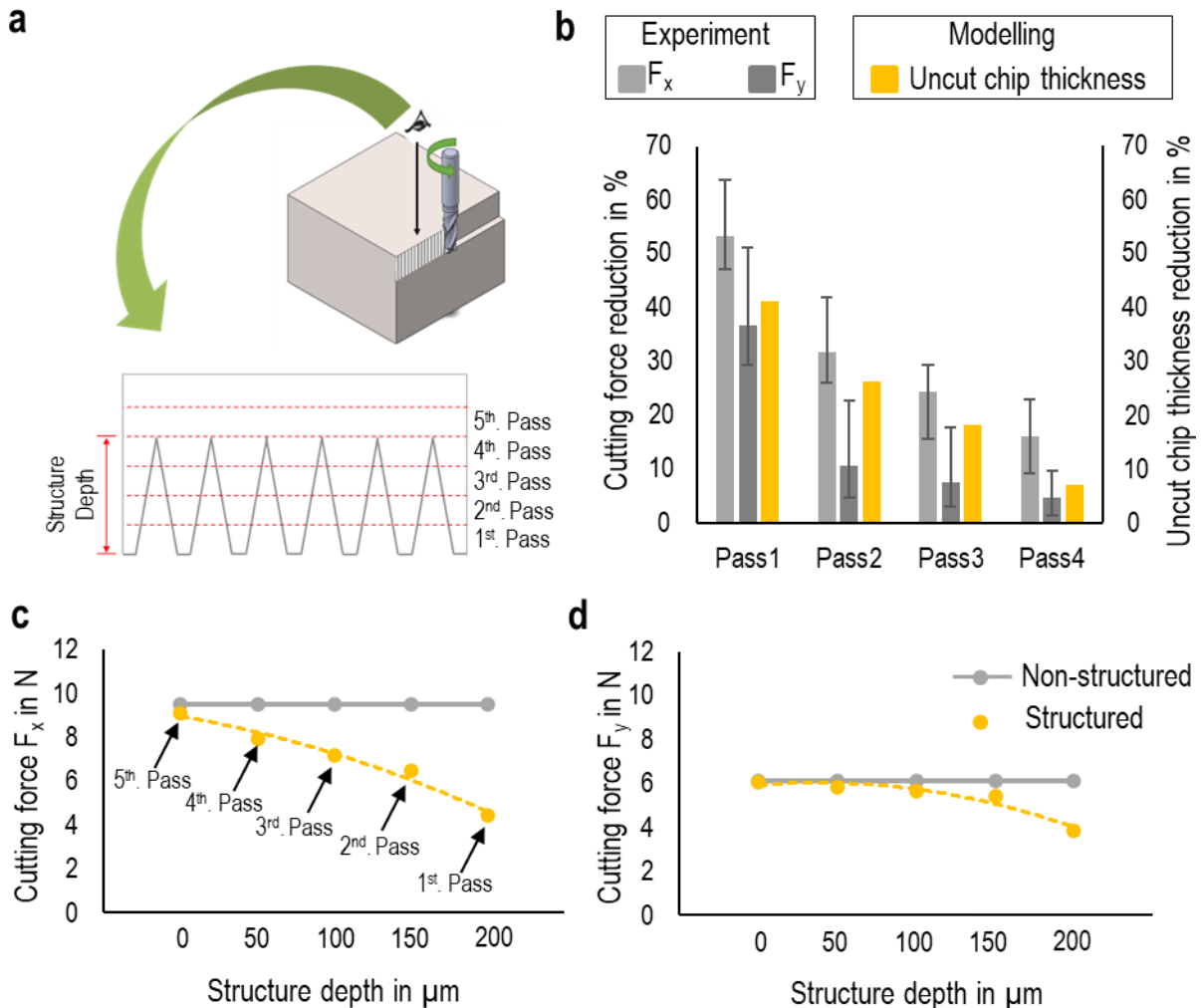


Figure 7.25: Influence of laser structuring on cutting forces in multiple passes at $f_z = 10$ $\mu\text{m}/\text{tooth}$: a) schematic of the process, b) the percentage of cutting force and chip thickness reduction, c) cutting force F_x , d) cutting force F_y .

Figure 7.26 provides the micro-milled surfaces for different passes. Accordingly, the structured area after each pass was reduced, and the line gap between structures is constant and equals 100 μm . The chip thicknesses during machining would be reduced through the structuring of the part, accompanied by a reduction in cutting forces. Therefore, a more structured area results in more chip thickness reduction and, consequently, less cutting forces. Thus, a reduction in the structured area after each pass led to an increasing the chip thicknesses at the micro-milling of the next pass, followed by decreasing the percentage of force reduction. After five passes, no sign of structuring on the surface is detectable. As shown in Figure 7.25b, the

percentage of force reduction for F_x is higher than that for F_y at all passes. For all force components, the percentage of force reduction decreases after each pass. This demonstrates the influence of removed material volume by laser structuring on reducing cutting forces.

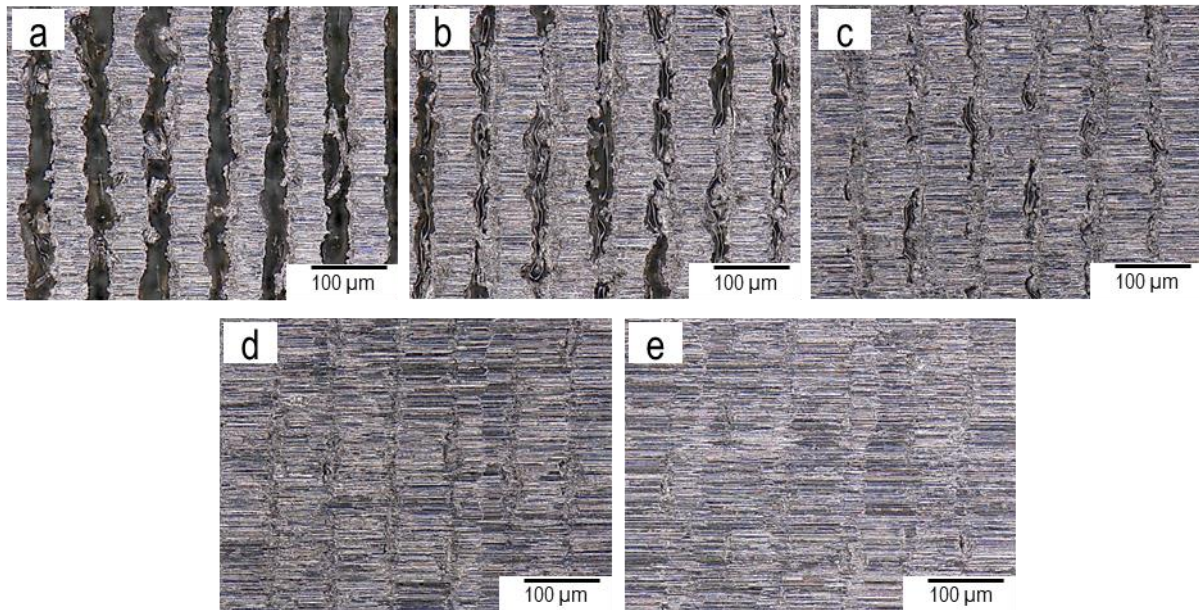


Figure 7.26: Machined surface after: a) Pass 1, b) Pass 2, c) Pass 3, d) Pass 4, e) Pass 5 at $v_c = 35$ and $f_z = 10$ $\mu\text{m}/\text{tooth}$.

Figure 7.27 summarizes the influence of structure density, or line gap l_g , on the resultant cutting force, based on the entire of signal, and uncut chip thickness reduction for two feeds of 10 $\mu\text{m}/\text{tooth}$ and 50 $\mu\text{m}/\text{tooth}$. According to the modelling results, highlighted by orange color, increasing structure density by reducing the line gap l_g leads to an increase in uncut chip thickness reduction for both feeds. At each structure density, a slightly higher value of uncut chip thickness reduction for $f_z = 50$ $\mu\text{m}/\text{tooth}$ is detectable compared to that for $f_z = 10$ $\mu\text{m}/\text{tooth}$. Higher uncut chip thickness reduction through decreasing line gap l_g would be accompanied by higher cutting force reduction, highlighted by the gray color in Figure 7.27.

As shown in Figure 7.27, the reduction in cutting force is much more pronounced compared to the uncut chip thickness reduction at each arbitrary line gap l_g , or structure density. This difference highlights that other factors, in addition to uncut chip thickness reduction, play an important role in reducing the cutting force in the novel LAM process. In this regard, the laser-structured part was cross-sectioned, and the micro-hardness test was carried out. Figure 7.28a indicates the cross-sectioned structured profile and the micro-hardness values. Figure 7.28b also provides a diagram concerning the hardness values versus distance to the lasered profile. The average hardness for HAZ and the base material were around 230 HV, average value from No: 1,6, and 11, and 322HV, average value from No: 2-5, 7-10, and 12-15, respectively. Accordingly, the material hardness in the vicinity of the lasered profile was reduced by approximately 30 percent. The reduction of micro-hardness of Ti6Al4V in HAZ through a thermally based process was also observed by Campo et al. [206]. They reported that the equiaxed primary α in a matrix of transformed β in HAZ was followed by a significant reduction of micro-hardness due to a higher volume fraction of β compared to that in the base material. Therefore, the laser-

induced material alteration in HAZ through the laser structuring can be considered as another influencing factor in reducing cutting forces.

Milling Tool	3 flutes; $\Phi = 1.8$ mm (WN 3142 R-N, PVD-TiAlN, Schaft DIN 6535-HA/HB), Gühring
Workpiece	Extruded Ti6Al4V
Parameters	Down-milling; $v_c = 35$ m/min; $f_z = 10$ and 50 $\mu\text{m}/\text{tooth}$; $a_p = 1$ mm; $a_e = 0.3$ mm
Coolant	Oil
Laser	$P_{L_ave} = 50$ W; $v_L = 600$ mm/s; $f_L = 400$ kHz
Structure	$l_g = 100, 300$ and 500 μm ; $s_d \approx 200$ μm ; $s_w = 80$ μm

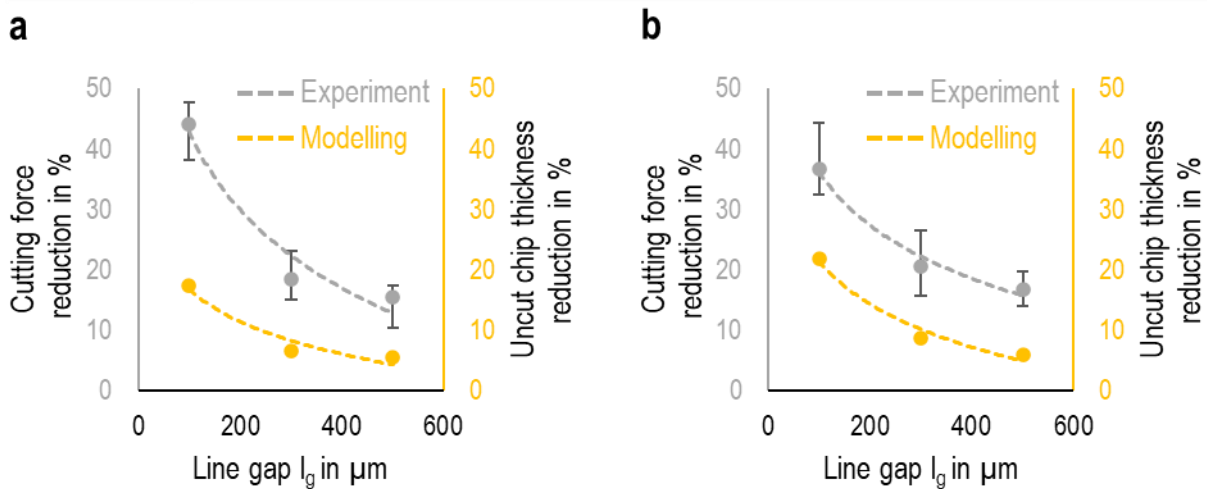


Figure 7.27: Influence of line gap l_g on cutting force and chip thickness reduction at: a) $f_z = 10$ $\mu\text{m}/\text{tooth}$, b) $f_z = 50$ $\mu\text{m}/\text{tooth}$.

According to the investigation carried out by Lokesh et al. [207], regarding the influence of process parameters on frictional forces, it was reported that a change in the depth of cut results in a considerable changing of frictional forces compared to that for cutting speed and feed rate. An increase in the depth of cut leads to a higher area of contact at the interfaces of the tool-workpiece and tool-chip accompanied by rising frictional forces. Accordingly, structuring the parts before machining leads to removing some part of the material and consequently less contact between tool and workpiece during machining, leading to less frictional forces and eventually lower cutting force components. At each arbitrary line gap, the difference between the gray and orange curves, that indicates the cutting force and uncut chip thickness reduction, respectively, denotes the contribution of a laser-induced material alteration and reduction of frictional forces in reducing cutting force.

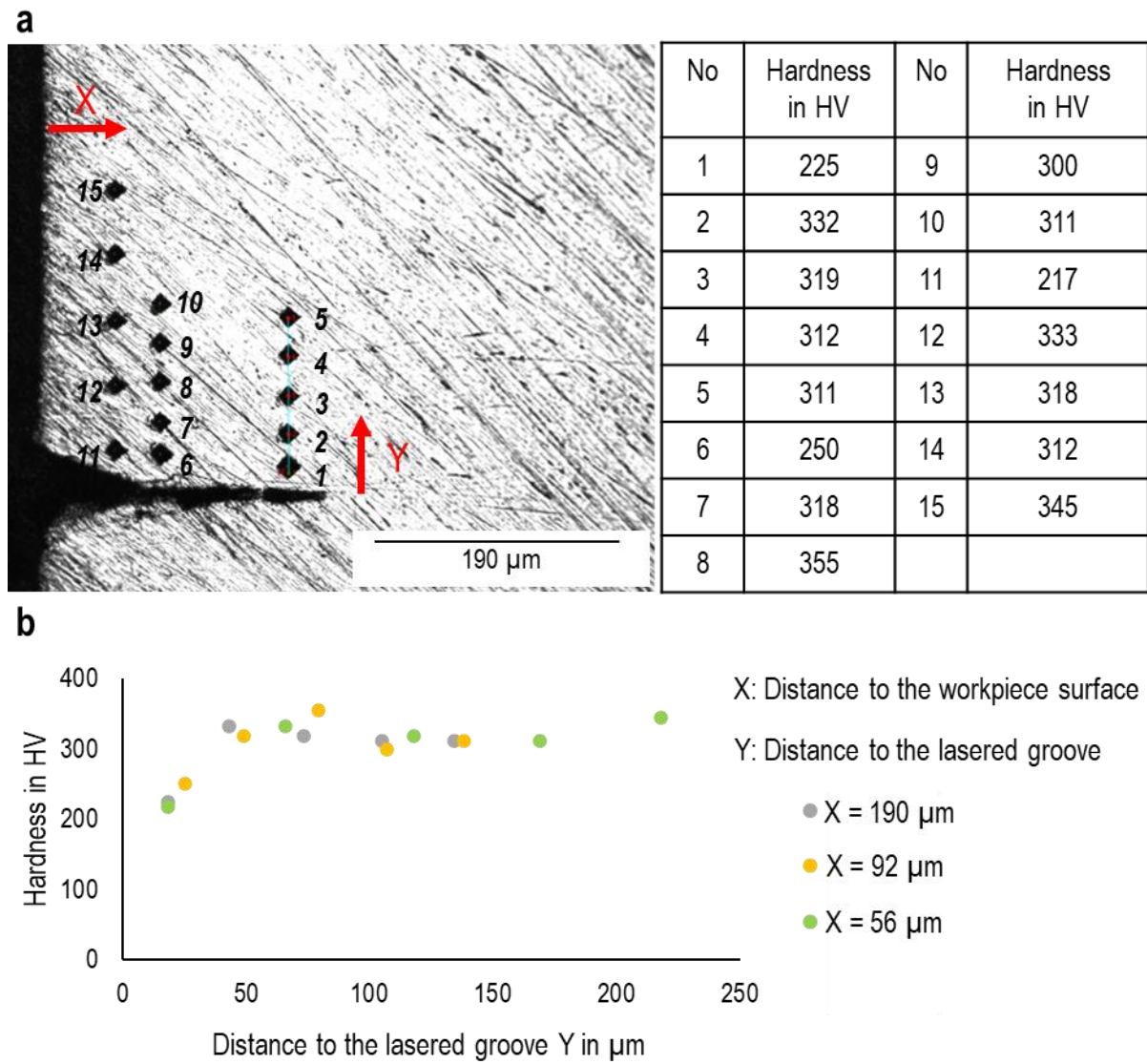


Figure 7.28: a) micro-hardness indentations and measurements in the vicinity of the lasered groove, b) micro-hardness values versus distance to the lasered groove and distance to the workpiece surface.

7.2.3 Surface roughness

In the previous section, the influence of structuring on the reduction of cutting forces has extensively been discussed. This section aims to see how structuring the workpiece may affect the generated surface after the laser-assisted micro-milling process.

Figure 7.29 provides the surface roughness values, S_a and S_z , for structured and non-structured parts at two different feeds, $f_z = 10$ and $25 \mu\text{m}/\text{tooth}$. According to Figure 7.29a, no detectable difference in the average value of S_a between structured and non-structured parts can be seen. However, a variation of S_a values in the case of structured parts indicates a wider range. In the case of S_z , shown in Figure 7.29b, a slightly lower value of S_z can be detected for the structured part. Again, more variation for the S_z values of the structured part is observable. Regarding $f_z = 25 \mu\text{m}/\text{tooth}$, a slight increase in the values of S_a and S_z can be seen for the structured part.

Milling Tool	3 flutes; $\Phi = 1.8 \text{ mm}$ (WN 3142 R-N, PVD-TiAlN, Schaft DIN 6535-HA/HB), Gühring
Workpiece	Extruded Ti6Al4V
Parameters	Down-milling; $v_c = 60 \text{ m/min}$; $f_z = 10$ and $25 \mu\text{m}/\text{tooth}$; $a_p = 1 \text{ mm}$; $a_e = 0.3 \text{ mm}$
Coolant	Oil
Laser	$P_{L_ave} = 50 \text{ W}$; $v_L = 600 \text{ mm/s}$; $f_L = 400 \text{ kHz}$
Structure	$l_g = 100 \mu\text{m}$; $s_d \approx 200 \mu\text{m}$; $s_w = 80 \mu\text{m}$

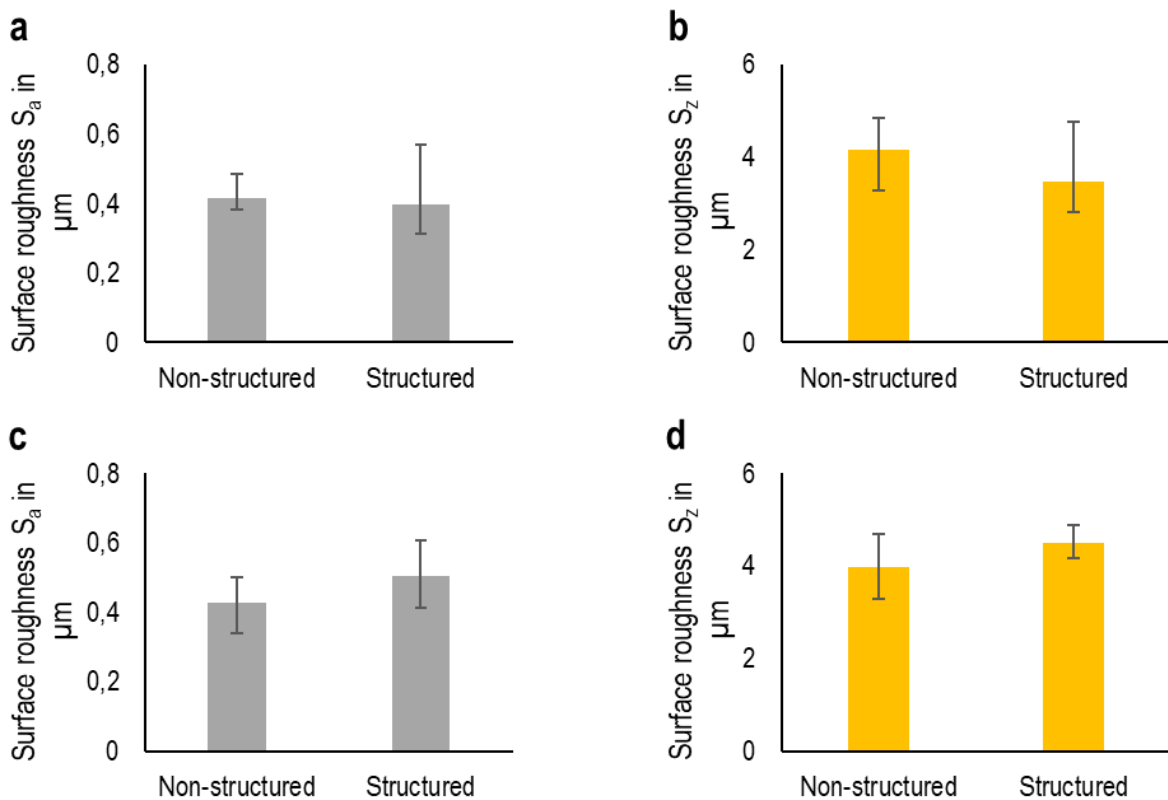


Figure 7.29: Influence of structuring on the generated machined surface: a) S_a , b) S_z at $f_z = 10 \mu\text{m}/\text{tooth}$, and c) S_a , d) S_z at $f_z = 25 \mu\text{m}/\text{tooth}$.

According to the modelling results in section 7.1, structuring the workpiece leads to the fluctuation in chip thicknesses during the contact between the tool and the workpiece. This fluctuation may be a source of instability during the process that can be followed by degradation of the machined surface. According to the summarized results in Figure 7.29, it can be concluded that the workpiece's structuring did not considerably affect the roughness of the machined surface.

Milling Tool	3 flutes; $\Phi = 1.8$ mm (WN 3142 R-N, PVD-TiAlN, Schaft DIN 6535-HA/HB), Gühring
Workpiece	Extruded Ti6Al4V
Parameters	Down-milling; $v_c = 35$ m/min; $f_z = 10$ $\mu\text{m}/\text{tooth}$; $a_p = 1$ mm; $a_e = 0.3$ mm
Coolant	Oil
Laser	$P_{L_ave} = 50$ W; $v_L = 600$ mm/s; $f_L = 400$ kHz
Structure	$l_g = 200$ μm ; $s_d \approx 200$ μm ; $s_w = 80$ μm ; $\alpha = +30, -30, 90$

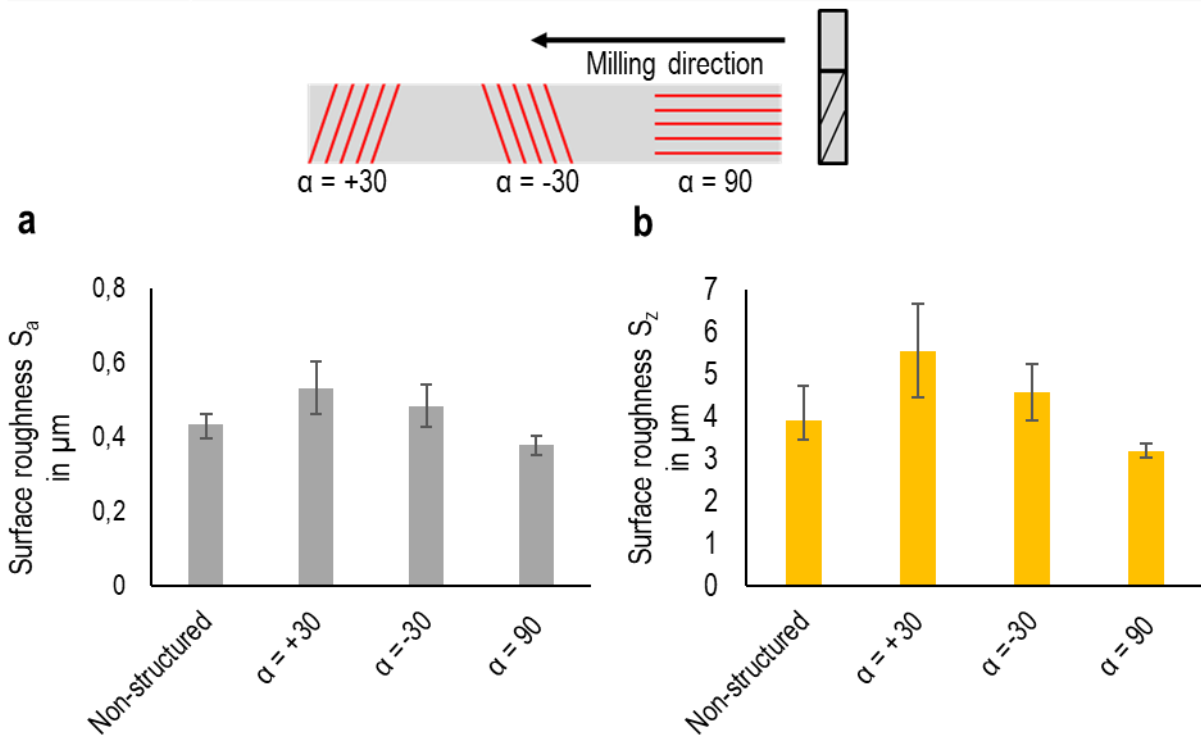


Figure 7.30: Influence of different structure angles on surface roughness: a) S_a , b) S_z .

In previous experiments, the structure lines were perpendicular to the milling direction, the structure angle $\alpha = 0^\circ$. Additional experiments were carried out at different structure angles, $\alpha = +30^\circ$, $\alpha = 90^\circ$, and $\alpha = -30^\circ$, to see the influence of this parameter on the surface roughness. According to Figure 7.30, a variation between surface roughness at different structure angles can be observed. In fact, a change in structure angle α changes the tool's approach to the structure elements. In the case of $\alpha = -30^\circ$, each cutting tooth comes into contact with the entire structure line or the bulk material. Therefore, the cutting condition would differ from one cutting tooth to the subsequent one. In fact, the material removal by the next cutting tooth would either increase or decrease depending on the area where the cutting approaches the workpiece. The cutting condition changes throughout the contact time between each

cutting tooth and structured workpiece with $\alpha = +30^\circ$. In detail, the cutting tooth comes into contact with multiple structure lines instead of one structure line, and some sections of the cutting tooth remove less material. Removing less material is not limited to the specific sections of each cutting tooth, and it varies from contact to contact. However, the particular sections of each cutting tooth contact with the structure lines, accompanied by less material, for structured workpiece with $\alpha = 90^\circ$.

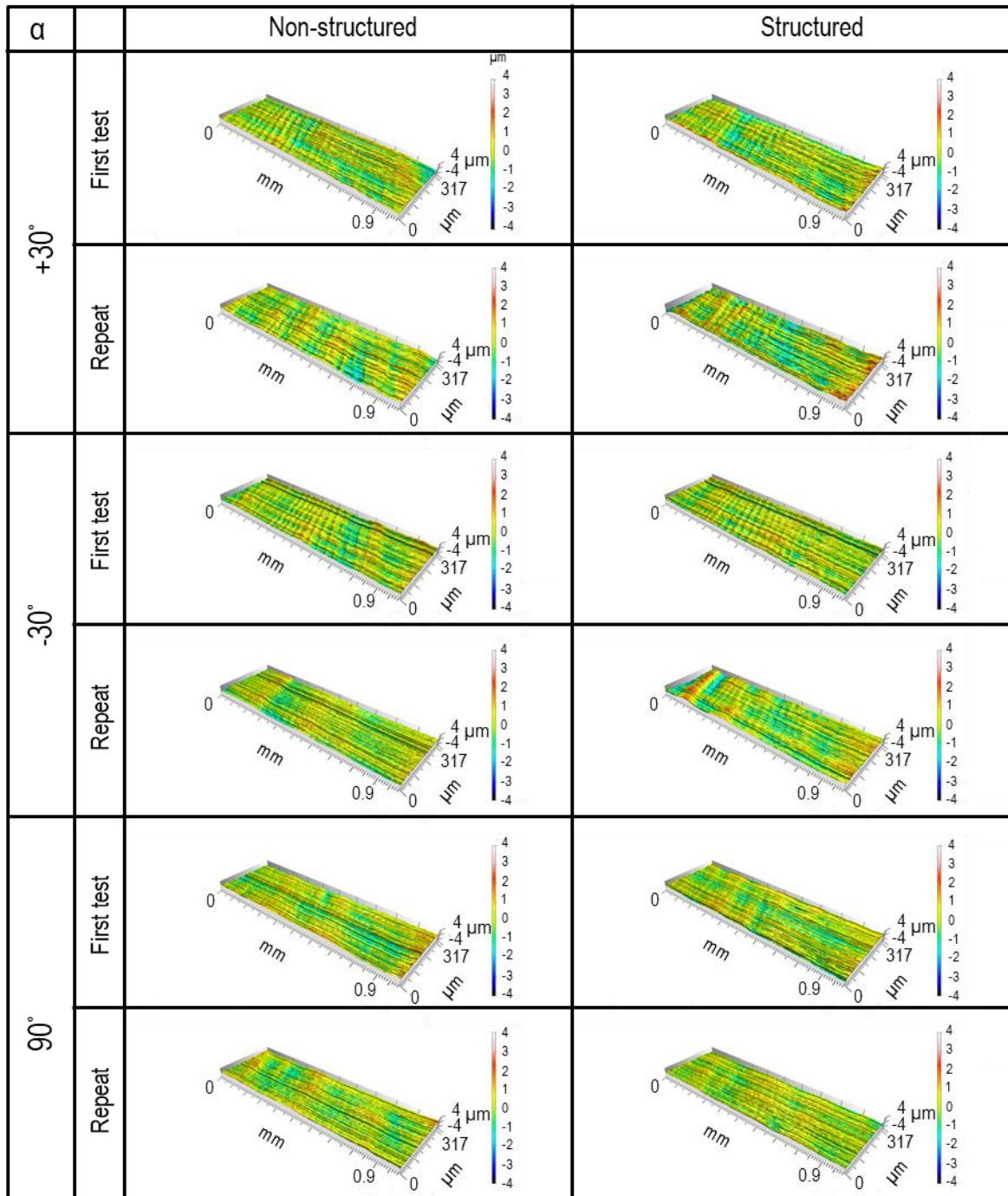


Figure 7.31: Machined surfaces for structured and non-structured parts at $f_z = 10 \mu\text{m/tooth}$.

As illustrated in Figure 7.30, a decrease in surface roughness values, S_a and S_z , can be observed by changing the structure angle α from $+30^\circ$ to -30° . According to the above explanation, a variation in cutting condition in the contact time between each tooth and multiple structure lines of the workpiece (with $\alpha = +30^\circ$) may lead to

instability (vibration) in the process, followed by increasing the surface roughness. On the other hand, when the cutting tooth removes either the bulk material or the remaining material in the structure line (at $\alpha = -30^\circ$), it may not cause as significant of a change in the cutting conditions, and consequently, it is less likely to lead to instability compared to when $\alpha = +30^\circ$. Changing the structure angle α from -30° to 90° also results in further decreasing the surface roughness. In the case of the structured workpiece with $\alpha = 90^\circ$, not only no variation in the cutting condition from one cutting tooth to the next one but also no change in material removal at different sections of each cutting tooth during the process takes place. This would help the process stability and eventually less roughness of the machined surface.

The surface roughness values, S_a and S_z , for $\alpha = +30^\circ$ and $\alpha = -30^\circ$ exhibited higher magnitude compared to those for the non-structured part. In the case of structure lines parallel to the milling direction, the surface roughness values, S_a and S_z , are lower than those for non-structured parts. Figure 7.31 provides a qualitative comparison between machined surfaces with different structure angles. Moreover, the corresponding machined surfaces of non-structured parts have also been included in Figure 7.31. Compared to $\alpha = +30^\circ$ and $\alpha = -30^\circ$, the surface improvement can be seen for the structured workpiece with $\alpha = 90^\circ$. This highlights the role of structure orientations with respect to the helix angle of the cutting tool.

8 Summery and outlook

The current investigation has been allocated to studying the application of a novel laser-assisted machining in improving the machinability of Ti6Al4V as one of the frequently used titanium alloys and difficult-to-cut materials. Moreover, the study regarding the influence of additively manufactured titanium alloys on their machinability has been under concentration. In this regard, the study was mainly divided into three sections. In the following, the results of each section have been summarized.

In the first section, the machinability of Ti6Al4V was evaluated. Due to the generation of new material properties induced by additive manufacturing, a comparative study was conducted between EBM Ti6Al4V parts and conventional parts produced by the extrusion process based on cutting forces, specific cutting energy, surface quality, and burr formation. The results of this comparison have been presented as follows:

- The same cutting forces at chip thicknesses between 7.4 μm and 37.3 μm were obtained for both EBM and extruded Ti6Al4V. The cutting force was remarkably influenced by the chip thickness. Higher chip thicknesses resulted in higher cutting forces. Moreover, the cutting forces were not influenced by a high deformation rate, or strain rate, through increasing the cutting speed, ranging from 35 m/min to 80 m/min, at constant chip thickness for both EBM and extruded Ti6Al4V. Therefore, this indicates the same material response for both materials at different strain rates. A slight reduction in force by increasing cutting speed could be only observed at $h_{\text{cu}} = 37.3 \mu\text{m}$ for both materials, which could be attributed to a dominating thermal softening effect at higher uncut chip thicknesses.
- Regarding the study of the size effect through the specific cutting energy for both materials, a non-linear correlation between the uncut chip thickness and the specific cutting energy was found. A considerable increase in the specific cutting energy could be associated with a high ploughing effect. At $h_{\text{cu}} < 7.4 \mu\text{m}$, the extruded parts exhibited higher specific cutting energies than the EBM parts due to more effect of ductile behavior (plastic deformation) of extruded parts on the energy of chip formation that is associated with the coarser microstructure of extruded parts. At $h_{\text{cu}} > 7.4 \mu\text{m}$, the pure cutting regime predominates over the plastic deformation, and the minimum specific energy of $u_c \approx 2.5 \text{ J/mm}^3$ was obtained for both materials.
- According to the analysis of machined surfaces, S_a and S_z values of extruded parts were, in most cases, higher than those in EBM parts. However, EBM parts indicated, in some cases, higher surface roughness. But in general, it can be concluded that the surface quality of EBM parts exhibited better condition compared to that for the extruded parts. Due to the higher hardness of EBM parts and, consequently, their higher brittle characteristic, less plastic flow on the machined surface of the EBM parts produced a finer surface, lower roughness and waviness values compared to the extruded parts.
- A high portion of the ploughing regime at low uncut chip thicknesses led to considerable burr formation and high specific cutting energy. An increase in the uncut chip thickness was followed by the dominance of pure cutting as a material removal mechanism and, consequently, less burr formation. A discontinuity in the burr formation was observed at EBM parts due to the irregularities on the surface. After removing the irregularity, the continuous and wavy-type burr was observed for EBM parts. This type of burr was also

observable for extruded parts. The size of the burr for both material types was relatively comparable.

Since the structuring of the part before machining in the novel LAM is carried out by laser, the second section has been allocated to study the interaction between laser and Ti6Al4V in multiple pulses, single linear and multiple linear laser scanning. The results of this section were indicated as follows:

- At multiple pulses, deeper ablation depth was obtained with increasing pulse energy E_p , resulting in higher peak laser fluence ϕ_{L_peak} and peak laser intensity I_{L_peak} . More generation of high-temperature free electrons, considerable high-temperature free carrier plasmas, heat accumulation, higher conduction time between electron and lattice, and reduction of surface reflectivity were probable reasons for the dramatic rise in ablation depth with increasing E_p . Difficulty in splashing the plasma under the coulomb repulsion and shielding effect may lead to the saturation state of the ablation process at higher laser fluences. The pulse energy E_p had more influence on ablation depth in comparison with the pulse number N_p . Moreover, a higher effect of pulse number N_p on ablation depth was observed at greater pulse energies due to the significant heat accumulation at higher laser fluences. By increasing the pulse number at $E_p = 12.5 \mu\text{J}$, the liquid phase was formed at the center of the lasered profile, and bridging ripple structures occurred. At greater pulse energies, melted material considerably formed, and the surface morphology was not highly influenced by a change in pulse number N_p . Only increasing feature size and more melt formation were observed.
- In the case of single linear laser scanning, Laser input energy E_{L_input} as an additional parameter was determined. E_{L_input} is a function of average laser power P_{L_ave} and laser scan velocity v_L . Different combinations of these two parameters result in different values of E_{L_input} , followed by a variation in surface morphology and ablation features. In detail, E_{L_input} logarithmically increases by reducing v_L at constant pulse energy E_p , denoting constant P_{L_ave} , followed by a logarithmic rise in the ablation depth. At constant v_L , greater E_{L_input} and deeper ablation depth were caused by increasing E_p , corresponding to higher P_{L_ave} , ϕ_{L_peak} , and I_{L_peak} . A rising trend in E_{L_input} and ablation depth as well as the surface degradation with increasing E_p was more considerable at lower scan velocities. These can be associated with more heat accumulation at higher pulse energies as well as a higher number of pulse incidents N_p at lower scan velocities. An increasing trend in the ablation area with E_{L_input} was also observed. The almost constant same value for ablation rate per pulse at different scan velocities and constant E_p , at laser pulse energies $E_p < 75 \mu\text{J}$, was detected. Therefore, the successive pulses had no outstanding influence on the ablation process of subsequent pulses. Furthermore, LIPSS, instead of considerable melting, was observed as the surface morphology at corresponding parameters, $v_L = 200\text{-}800 \text{ mm/s}$ and $E_p < 75 \mu\text{J}$. No remarkable surface morphology variation was detected by changing v_L at constant pulse energy for $E_p < 75 \mu\text{J}$. While surface morphology exhibited a dramatic change, ranging from a huge melting to LIPSS with increasing scan velocities at $E_p > 75 \mu\text{J}$, accompanied by a variation in ablation rate per pulse. In the case of MRR, no clear trend can be

found. In detail, an optimum v_L led to a maximum MRR that differs at different pulse energies. At laser input energies $E_{L_input} > 125 \text{ J/cm}^2$, a dramatic rise in ablation depth can be observed. The laser-induced surface morphology at this range indicated considerable melting on the workpiece surface. At $E_{L_input} < 125 \text{ J/cm}^2$, the ablation depth slightly linearly increased with E_{L_input} at scan velocities $v_L = 500$ and 800 mm/s , and the ripple structures and no sign of melting were observed. Higher specific ablation energies and a lower values of ablation rate per fluence at all scan velocities were caused by increasing E_{L_input} . In fact, a proportion of transferred energy on the workpiece surface leading to the melting formation instead of material removal could be increased. This resulted in higher specific ablation energy and a lower ablation rate per fluence. However, a further rise in E_{L_input} changed this trend and led to decreasing specific ablation energy and increasing ablation rate per fluence due to the considerable heat accumulation accelerating the ablation process.

- Concerning the multiple laser scanning, the constant laser input energy E_{L_input} obtained by different combinations of scan velocity v_L and average laser power P_{L_ave} caused a variation in surface morphology and feature size of the lasered profile. As observed, lower scan velocities and average laser powers led to a considerable rise in the ablation depth and ablation area. In detail, surface morphology alternation and a rise in ablation depth and area can be accelerated by a constant amount of energy introduced by lower laser pulse energy with a higher number of repetitions. One reason can be associated with less ablation threshold and surface reflectivity for subsequent pulses because of the incubation factor and more surface degradation. Plasma accumulation due to the difficulty in splashing the plasma from the deeper and narrower lasered profile caused by lower values of P_{L_ave} and v_L can be considered as another reason. The plasma shielding and self-cleaning of the lasered profile after $N_s = 20$ may lead to slowing the rising trend in the ablation with N_s . Less specific ablation energy and a higher ablation rate per fluence were reported for lower laser powers and scan velocities at different N_s . However, higher P_{L_ave} and v_L can enhance MRR.
- According to the obtained results, introducing the same amount of energy on the material through higher laser powers and scan velocities led to more MRR and, therefore, lower laser processing time. However, another crucial factor regarding the processing cost must also be considered that is associated with the amount of removed material per applied energy indicated by the specific ablation energy e_L . Based on the results for multiple laser processing, lower values of P_L and v_L led to lower specific ablation energies. It should be mentioned that the processing time also has an influence on the cost. Therefore, it is important to find the trade-off between time and cost depending on the application.

In the third section, the application of novel-introduced LAM in the micro-milling of Ti6Al4V has been studied. Since the workpiece surface is structured before machining in this process, the amount of the material to be removed would decrease. In this regard, a kinematic model was developed to study the effect of different process parameters on the chip thickness. The modelling results indicated that structuring the parts before the machining reduces uncut chip thicknesses. As

mentioned, the modelling parameters are categorized into structure, tool, and process parameters. Among them, the line gap between structure lines, or structure densities, l_g and structure depth s_d played an important role in CTR. Moreover, the interaction between l_g and s_d was also considerable. In detail, at lower values of s_d , the influence of l_g on CTR was not as significant as its influence on CTR at higher values of s_d . Changing the value of l_g also remarkably affected the influence of s_d on CTR. The helix angle β and axial depth of cut a_p showed no influence on CTR. Additionally, the influence of other parameters (f_z , a_e , α , Φ) on CTR was not as high as the effect of l_g and s_d , and their influence was much more pronounced at higher structure densities, lower values of l_g . For the experimental investigation, the structure density, or structure line gap l_g , as a varying process parameter was selected. The effect of laser structuring prior to the micro-milling on the machinability of Ti6Al4V with respect to cutting forces and surface roughness was investigated, and the following results have been obtained.

- The laser structuring of the workpiece significantly reduced the cutting forces for both F_x and F_y . The cutting force reduction in the x-direction based on the entire of the signal in all experimental tests exhibited higher percentage values, 18.5-49 % and 21-43 % for feeds of 10 and 50 $\mu\text{m}/\text{tooth}$, respectively, compared to that in the y-direction, 5-17 % and 11-28 % for feeds of 10 and 50 $\mu\text{m}/\text{tooth}$, respectively. This can be associated with the domino effect as well as the less structure strength against removing in the x-direction. With respect to the signal's peak, higher cutting force reduction in the x-direction compared to that for the y-direction was also detected.
- The experimental tests with different structure densities highlighted the importance of this parameter in decreasing the cutting forces. The structure density was adjusted by changing the line gap l_g between two structure lines. Increasing structure density, or reducing the line gap l_g , resulted in higher cutting force reduction. The relation between the line gap l_g and cutting forces indicated a logarithmic trend.
- A force reduction for F_y at $f_z = 50 \mu\text{m}/\text{tooth}$, 5-21 % and 11-28 % for peak and entire of the signal, respectively, was higher than that at $f_z = 10 \mu\text{m}/\text{tooth}$, 1-8 % and 3.5-17 % for peak and entire of the signal, respectively. This signifies reducing the probability of tool deflection by means of laser-structuring, particularly for higher feeds. The relatively same percentage of force reduction at $f_z = 10 \mu\text{m}/\text{tooth}$ and 50 $\mu\text{m}/\text{tooth}$ with respect to F_x , highlights the feasibility of this novel LAM for using in higher feeds and consequently enhancing MRR.
- Removing material prior to the machining process led to a decrease in the uncut chip thicknesses, accompanied by cutting force reduction. At each arbitrary structure density, a higher percentage of cutting force reduction, obtained from the experimental investigation, compared to the percentage of uncut chip thickness reduction, CTR calculated from modelling, indicated the influence of other factors in addition to the uncut chip thickness on cutting forces. A 30 % reduction of micro-hardness in the vicinity of lasered structures was reported, followed by decreasing material strength. Therefore, laser-induced material alternation also played an important role in reducing the cutting forces at the LAM process. Moreover, less frictional forces due to the less contact between the tool and workpiece probably caused by structuring the workpiece surfaces was considered as another factor in reducing the cutting force components.

- The structuring of the workpiece did not considerably affect the surface roughness of the machined surface in the case of structured workpieces with $\alpha = 0^\circ$. However, it was found that the orientation of structure lines, or structure angle α , in relation with the helix angle β of the tool can influence the machined surface.

In this investigation, the application of novel LAM has been studied for improving the machineability of Ti6Al4V as one of the difficult-to-cut materials. However, several aspects for future works are needed to be investigated, which have been mentioned as follows:

- In this process, the structuring of the workpiece is carried out by laser. As a result, the laser-induced material alternation occurs, which eases further machining remained material. Therefore, the modelling HAZ's progress with the number of laser scanning N_s would be beneficial for finding optimum laser parameters with respect to the radial depth of cut in the machining. Therefore, as large as possible area of HAZ can be obtained without remaining laser-induced HAZ after machining. HAZ in the laser structuring of Ti6Al4V leads to reducing the material hardness, followed by decreasing the machining forces. In the case of other materials, the effect of laser on HAZ and material ablation may vary. Therefore, the applicability of the introduced LAM to other materials can be another future research topic.
- Among different parameters of LAM, line gap l_g and structure depth s_d remarkably influenced chip thickness reduction. This study has experimentally investigated the influence of line gap l_g , or structure density, on cutting forces. Hence, the effect of structure depth s_d on the cutting forces can also be an opening topic for future work. Moreover, increasing cutting speed v_c in the range of high-speed machining may strongly impact the structure elements. Therefore, the influence of cutting speed v_c in this range can be researched. Furthermore, extensive research is highly demanded to evaluate the dynamics of the process to see the effect of structure angle α in relation with helix angle β on the process stability for slender cutting tools.
- As mentioned in this study, one of the drawbacks of AM parts is the low surface quality that should be subjected to further machining processes. AM technology provides high flexibility for producing parts with different shapes. Therefore, it is possible to form the structure elements on the workpiece manufactured by AM rather than structuring it by laser through removing the material. In this case, the finishing of AM parts can be carried out by less cutting forces due to the formation of structures on their surface during AM. In this regard, the interaction between AM and machining is challenging. In detail, finding the optimum parameters in the AM process is crucial to produce the additively induced microstructures in the outer layers of AM parts, removed by machining, to enhance machinability. Additionally, the high flexibility of AM can provide different structure patterns and a variation in the shapes of structure profiles (or grooves). Therefore, an investigation through experimental and modeling approaches to find the best structure patterns and groove shapes is another challenging task.
- In current investigation, the laser incidents perpendicularly the workpiece surface. In the case of applying the presented LAM method for free formed

surface, the angle of incident would change that affect the surface reflectivity, the laser input energy and laser-material interaction mechanism. Therefore, this affects the efficiency of the laser ablation. In this regard, applying laser-structuring for workpieces with complex geometries is another demanding potential research.

9 References

- [1] Chichili DR, Ramesh KT, Hemker KJ. The high-strain-rate response of alpha-titanium: experiments, deformation mechanisms and modeling. *Acta Materialia* 1998;46(3):1025–43. [https://doi.org/10.1016/S1359-6454\(97\)00287-5](https://doi.org/10.1016/S1359-6454(97)00287-5).
- [2] Ramesh KT. Effects of high rates of loading on the deformation behavior and failure mechanisms of hexagonal close-packed metals and alloys. *Metallurgical and Materials Transactions A* 2002;33(13):927–35. <https://doi.org/10.1007/s11661-002-1025-1>.
- [3] Follansbee PS, Gray GT. An analysis of the low temperature, low and high strain-rate deformation of Ti–6Al–4V. *Metallurgical and Materials Transactions A* 1989;20(5):863–74. <https://doi.org/10.1007/BF02651653>.
- [4] Pramanik A. Problems and solutions in machining of titanium alloys. *Int J Adv Manuf Technol* 2014;70(5-8):919–28. <https://doi.org/10.1007/s00170-013-5326-x>.
- [5] Chryssolouris G, Anifantis N, Karagiannis S. Laser Assisted Machining: An Overview. *Journal of Manufacturing Science and Engineering* 1997;119(4B):766–9. <https://doi.org/10.1115/1.2836822>.
- [6] Rozzi JC, Pfefferkorn FE, Shin YC, Incropera FP. Experimental Evaluation of the Laser Assisted Machining of Silicon Nitride Ceramics. *Journal of Manufacturing Science and Engineering* 2000;122(4):666–70. <https://doi.org/10.1115/1.1286556>.
- [7] Azarhoushang B, Soltani B, Daneshi A. Study of the effects of laser micro structuring on grinding of silicon nitride ceramics. *CIRP Annals* 2018;67(1):329–32. <https://doi.org/10.1016/j.cirp.2018.04.084>.
- [8] Veiga C, Davim J, Loureiro A. Properties and applications of titanium alloys: A brief review. *Reviews on Advanced Materials Science* 2012;32:133–48.
- [9] Leyens C, Peters M (eds.). *Titanium and titanium alloys: Fundamentals and applications*. 1st ed. Weinheim, Chichester: Wiley-VCH; 2010.
- [10] Boyer RR. An overview on the use of titanium in the aerospace industry. *Materials Science and Engineering: A* 1996;213(1-2):103–14. [https://doi.org/10.1016/0921-5093\(96\)10233-1](https://doi.org/10.1016/0921-5093(96)10233-1).
- [11] Herzog D, Seyda V, Wycisk E, Emmelmann C. Additive manufacturing of metals. *Acta Materialia* 2016;117:371–92. <https://doi.org/10.1016/j.actamat.2016.07.019>.
- [12] Sherif E-SM, Abdo HS, Latief FH, Alharthi NH, Abedin SZE. Fabrication of Ti–Al–Cu new alloys by inductive sintering, characterization, and corrosion evaluation. *Journal of Materials Research and Technology* 2019;8(5):4302–11. <https://doi.org/10.1016/j.jmrt.2019.07.040>.
- [13] Akinribide OJ, Mekgwe GN, Obadele BA, Ajibola OO, Akinwamide SO, Olubambi PA. Microstructural and phase evolution of spark plasma sintering of graphitized Ti (C0.9N0.1) composites. *International Journal of Refractory Metals and Hard Materials* 2019;78:164–9. <https://doi.org/10.1016/j.ijrmhm.2018.09.013>.
- [14] Muroga T, Nagasaka T, Iiyoshi A, Kawabata A, Sakurai S, Sakata M. NIFS program for large ingot production of a V–Cr–Ti alloy. *Journal of Nuclear Materials* 2000;283-287:711–5. [https://doi.org/10.1016/S0022-3115\(00\)00281-6](https://doi.org/10.1016/S0022-3115(00)00281-6).
- [15] Nastac L, Gungor MN, Ucok I, Klug KL, Tack WT. Advances in investment casting of Ti–6Al–4V alloy: a review. *International Journal of Cast Metals Research* 2006;19(2):73–93. <https://doi.org/10.1179/136404605225023225>.

-
- [16] Dutta B, Froes FH. The Additive Manufacturing (AM) of titanium alloys. *Metal Powder Report* 2017;72(2):96–106. <https://doi.org/10.1016/j.mprp.2016.12.062>.
- [17] Vladimir V. Popov Jr, Anastasia Kolomiets, Gary Muller. Benefits of Additive Manufacturing for Industrial Design Development. Trends, Limitations and Applications. *GJRE* 2018;18(J2):1–8.
- [18] Zhai Y, Lados DA, LaGoy JL. Additive Manufacturing: Making Imagination the Major Limitation. *JOM* 2014;66(5):808–16. <https://doi.org/10.1007/s11837-014-0886-2>.
- [19] Petrovic V, Vicente Haro Gonzalez J, Jordá Ferrando O, Delgado Gordillo J, Ramón Blasco Puchades J, Portolés Griñan L. Additive layered manufacturing: sectors of industrial application shown through case studies. *International Journal of Production Research* 2011;49(4):1061–79. <https://doi.org/10.1080/00207540903479786>.
- [20] Biamino S, Penna A, Ackelid U, Sabbadini S, Tassa O, Fino P et al. Electron beam melting of Ti–48Al–2Cr–2Nb alloy: Microstructure and mechanical properties investigation. *Intermetallics* 2011;19(6):776–81. <https://doi.org/10.1016/j.intermet.2010.11.017>.
- [21] Song B, Zhao X, Li S, Han C, Wei Q, Wen S et al. Differences in microstructure and properties between selective laser melting and traditional manufacturing for fabrication of metal parts: A review. *Front. Mech. Eng.* 2015;10(2):111–25. <https://doi.org/10.1007/s11465-015-0341-2>.
- [22] Yang S, Han Q, Yin Y, Gao J, Zhang Z, Gu Y et al. Effects of micrometer-sized TiB₂ on crack mitigation, mechanical and electrochemical performance of a Ni-based alloy fabricated by selective laser melting. *Optics & Laser Technology* 2021;142:107240. <https://doi.org/10.1016/j.optlastec.2021.107240>.
- [23] Nagarajan B, Hu Z, Song X, Zhai W, Wei J. Development of Micro Selective Laser Melting: The State of the Art and Future Perspectives. *Engineering* 2019;5(4):702–20. <https://doi.org/10.1016/j.eng.2019.07.002>.
- [24] Pacurar R, Pacurar A. Applications of the Selective Laser Melting Technology in the Industrial and Medical Fields. In: Biglino G, editor. *3D Printing Cardiovascular Anatomy: A Single-Centre Experience*. [s.l.]: IntechOpen; 2016.
- [25] Rafi HK, Karthik NV, Gong H, Starr TL, Stucker BE. Microstructures and Mechanical Properties of Ti6Al4V Parts Fabricated by Selective Laser Melting and Electron Beam Melting. *J. of Materi Eng and Perform* 2013;22(12):3872–83. <https://doi.org/10.1007/s11665-013-0658-0>.
- [26] Xu W, Brandt M, Sun S, Elambasseril J, Liu Q, Latham K et al. Additive manufacturing of strong and ductile Ti–6Al–4V by selective laser melting via in situ martensite decomposition. *Acta Materialia* 2015;85:74–84. <https://doi.org/10.1016/j.actamat.2014.11.028>.
- [27] Zhang T, Liu C-T. Design of titanium alloys by additive manufacturing: A critical review. *Advanced Powder Materials* 2022;1(1):100014. <https://doi.org/10.1016/j.apmate.2021.11.001>.
- [28] Dilip JJS, Zhang S, Teng C, Zeng K, Robinson C, Pal D et al. Influence of processing parameters on the evolution of melt pool, porosity, and microstructures in Ti-6Al-4V alloy parts fabricated by selective laser melting. *Prog Addit Manuf* 2017;2(3):157–67. <https://doi.org/10.1007/s40964-017-0030-2>.
- [29] Murr LE, Quinones SA, Gaytan SM, Lopez MI, Rodela A, Martinez EY et al. Microstructure and mechanical behavior of Ti-6Al-4V produced by rapid-layer

- manufacturing, for biomedical applications. *Journal of the mechanical behavior of biomedical materials* 2009;2(1):20–32.
<https://doi.org/10.1016/j.jmbbm.2008.05.004>.
- [30] Yu J, Rombouts M, Maes G, Motmans F. Material Properties of Ti6Al4V Parts Produced by Laser Metal Deposition. *Physics Procedia* 2012;39:416–24.
<https://doi.org/10.1016/j.phpro.2012.10.056>.
- [31] Ahmed T, Rack HJ. Phase transformations during cooling in $\alpha+\beta$ titanium alloys. *Materials Science and Engineering: A* 1998;243(1):206–11.
[https://doi.org/10.1016/S0921-5093\(97\)00802-2](https://doi.org/10.1016/S0921-5093(97)00802-2).
- [32] Xu W, Lui EW, Pateras A, Qian M, Brandt M. In situ tailoring microstructure in additively manufactured Ti-6Al-4V for superior mechanical performance. *Acta Materialia* 2017;125:390–400. <https://doi.org/10.1016/j.actamat.2016.12.027>.
- [33] Wang K, Zhang Q, Zhang J. Evaluation of scale effect of micro electrical discharge machining system. *Journal of Manufacturing Processes* 2019;38:174–8. <https://doi.org/10.1016/j.jmapro.2019.01.005>.
- [34] Kim Y-S, Chu C-N. The Effects of Graphite Powder on Tool Wear in Micro Electrical Discharge Machining. *Procedia CIRP* 2018;68:553–8.
<https://doi.org/10.1016/j.procir.2017.12.121>.
- [35] Kuzin VV, Fedorov SY, Szalay T, Farkas B. Micromachining of a High-Density Current-Conducting Ceramic With the Use of Electrical-Discharge Machining. Part 1. Refractories and Industrial Ceramics 2016;57(2):164–9.
<https://doi.org/10.1007/s11148-016-9948-z>.
- [36] Allegre OJ, Li Z, Li L. Tailored laser vector fields for high-precision micro-manufacturing. *CIRP Annals* 2019;68(1):193–6.
<https://doi.org/10.1016/j.cirp.2019.04.125>.
- [37] Cadot G, Axinte DA, Billingham J. Continuous trench, pulsed laser ablation for micro-machining applications. *International Journal of Machine Tools and Manufacture* 2016;107:8–20. <https://doi.org/10.1016/j.ijmachtools.2016.04.011>.
- [38] Derevyanko DI, Shelkovnikov VV, Orlova NA, Goldenberg BG, Lemzyakov AG, Korolkov VP. Fabrication of High-aspect-ratio Microstructures for LIGA-technology by Synchrotron Radiation Polymerisation of Thetetraacrylate Monomer. *Physics Procedia* 2017;86:122–6.
<https://doi.org/10.1016/j.phpro.2017.01.032>.
- [39] Ma Y, Liu W, Liu C. Research on the process of fabricating a multi-layer metal micro-structure based on UV-LIGA overlay technology. *Nanotechnology and Precision Engineering* 2019;2(2):83–8. <https://doi.org/10.1016/j.npe.2019.07.002>.
- [40] Silvestre CM, Nguyen V, Jansen H, Hansen O. Deep reactive ion etching of ‘grass-free’ widely-spaced periodic 2D arrays, using sacrificial structures. *Microelectronic Engineering* 2020;223:111228.
<https://doi.org/10.1016/j.mee.2020.111228>.
- [41] Li Y, Zhang H, Yang R, Tazrin F, Zhu C, Kaddoura M et al. In-plane silicon microneedles with open capillary microfluidic networks by deep reactive ion etching and sacrificial layer based sharpening. *Sensors and Actuators A: Physical* 2019;292:149–57. <https://doi.org/10.1016/j.sna.2019.04.008>.
- [42] Hamdana G, Puranto P, Langfahl-Klabes J, Li Z, Pohlenz F, Xu M et al. Nanoindentation of crystalline silicon pillars fabricated by soft UV nanoimprint lithography and cryogenic deep reactive ion etching. *Sensors and Actuators A: Physical* 2018;283:65–78. <https://doi.org/10.1016/j.sna.2018.09.035>.

-
- [43] Bogaerts W, Dumon P, Taillaert D, Wiaux V, Beckx S, Luysaert B et al. SOI nanophotonic waveguide structures fabricated with deep UV lithography. *Photonics and Nanostructures - Fundamentals and Applications* 2004;2(2):81–6. <https://doi.org/10.1016/j.photonics.2004.07.002>.
- [44] Jin X, Altintas Y. Prediction of micro-milling forces with finite element method. *Journal of Materials Processing Technology* 2012;212(3):542–52. <https://doi.org/10.1016/j.jmatprotec.2011.05.020>.
- [45] Aurich JC, Bohley M, Reichenbach IG, Kirsch B. Surface quality in micro milling: Influences of spindle and cutting parameters. *CIRP Annals* 2017;66(1):101–4. <https://doi.org/10.1016/j.cirp.2017.04.029>.
- [46] Singh KK, Singh R. Chatter stability prediction in high-speed micromilling of Ti6Al4V via finite element based microend mill dynamics. *Adv. Manuf.* 2018;6(1):95–106. <https://doi.org/10.1007/s40436-018-0210-4>.
- [47] Ma L, Howard I, Pang M, Wang Z, Su J. Experimental Investigation of Cutting Vibration during Micro-End-Milling of the Straight Groove. *Micromachines (Basel)* 2020;11(5). <https://doi.org/10.3390/mi11050494>.
- [48] Hajiahmadi S. Burr size investigation in micro milling of stainless steel 316L. *International Journal of Lightweight Materials and Manufacture* 2019;2(4):296–304. <https://doi.org/10.1016/j.ijlmm.2019.07.004>.
- [49] Yang Y, Han J, Hao X, Li L, He N. Investigation on micro-milling of micro-grooves with high aspect ratio and laser deburring. *Proceedings of the Institution of Mechanical Engineers, Part B: Journal of Engineering Manufacture* 2019;234(5):871–80. <https://doi.org/10.1177/0954405419893491>.
- [50] Mamedov A, Lazoglu I. Thermal analysis of micro milling titanium alloy Ti–6Al–4V. *Journal of Materials Processing Technology* 2016;229:659–67. <https://doi.org/10.1016/j.jmatprotec.2015.10.019>.
- [51] Wissmiller DL, Pfefferkorn FE. Micro end mill tool temperature measurement and prediction. *Journal of Manufacturing Processes* 2009;11(1):45–53. <https://doi.org/10.1016/j.jmapro.2009.06.001>.
- [52] Tarasov LP. Discussion: “The Size Effect in Metal Cutting” (Backer, W. R., Marshall, E. R., and Shaw, M. C., 1952, *Trans. ASME*, 74, pp. 61–71). *Journal of Fluids Engineering* 1952;74(1):71. <https://doi.org/10.1115/1.4015687>.
- [53] Taniguchi N. 1993 ASPE distinguished lecturer. *Precision Engineering* 1994;16(1):5–24. [https://doi.org/10.1016/0141-6359\(94\)90014-0](https://doi.org/10.1016/0141-6359(94)90014-0).
- [54] Aramcharoen A, Mativenga PT. Size effect and tool geometry in micromilling of tool steel. *Precision Engineering* 2009;33(4):402–7. <https://doi.org/10.1016/j.precisioneng.2008.11.002>.
- [55] Vipindas K, Anand KN, Mathew J. Effect of cutting edge radius on micro end milling: force analysis, surface roughness, and chip formation. *Int J Adv Manuf Technol* 2018;97(1):711–22. <https://doi.org/10.1007/s00170-018-1877-1>.
- [56] Wojciechowski S, Matuszak M, Powalka B, Madajewski M, Maruda RW, Królczyk GM. Prediction of cutting forces during micro end milling considering chip thickness accumulation. *International Journal of Machine Tools and Manufacture* 2019;147:103466. <https://doi.org/10.1016/j.ijmachtools.2019.103466>.
- [57] Dib M, Duduch JG, Jasinevicius RG. Minimum chip thickness determination by means of cutting force signal in micro endmilling. *Precision Engineering* 2018;51:244–62. <https://doi.org/10.1016/j.precisioneng.2017.08.016>.

-
- [58] Leo Kumar SP. Measurement and uncertainty analysis of surface roughness and material removal rate in micro turning operation and process parameters optimization. *Measurement* 2019;140:538–47. <https://doi.org/10.1016/j.measurement.2019.04.029>.
- [59] Takács M. Sokkristályos ötvözetek mikroforgácsolása keményfém szármaróval 2006.
- [60] Bissacco G, Hansen HN, Chiffre L de. Micromilling of hardened tool steel for mould making applications. *Journal of Materials Processing Technology* 2005;167(2-3):201–7. <https://doi.org/10.1016/j.jmatprotec.2005.05.029>.
- [61] Balázs BZ, Geier N, Takács M, Davim JP. A review on micro-milling: recent advances and future trends. *Int J Adv Manuf Technol* 2021;112(3-4):655–84. <https://doi.org/10.1007/s00170-020-06445-w>.
- [62] Ezugwu EO, Batista Da Silva R, Falco Sales W, Rocha Machado A. Overview of the Machining of Titanium Alloys. In: Abraham M, editor. *Encyclopedia of sustainable technologies*. Saint Louis: Elsevier Science; 2017, p. 487–506.
- [63] Klocke F, König W, Gerschwiler K. Advanced Machining of Titanium- and Nickel-Based Alloys. In: Kuljanic E, editor. *Advanced Manufacturing Systems and Technology*. Vienna: Springer Vienna; 1996, p. 7–21.
- [64] Dearnley PA, Grearson AN. Evaluation of principal wear mechanisms of cemented carbides and ceramics used for machining titanium alloy IMI 318. *mats. sci. tech.* 1986;2(1):47–58. <https://doi.org/10.1179/026708386790123611>.
- [65] Hartung PD, Kramer BM, Turkovich BF von. Tool Wear in Titanium Machining. *CIRP Annals* 1982;31(1):75–80. [https://doi.org/10.1016/S0007-8506\(07\)63272-7](https://doi.org/10.1016/S0007-8506(07)63272-7).
- [66] Özel T, Thepsonthi T, Ulutan D, Kaftanoğlu B. Micro-Milling of Ti-6Al-4V Alloy with Uncoated and cBN coated Micro-Tools; 2011.
- [67] Hua J, Shivpuri R. A Cobalt Diffusion Based Model for Predicting Crater Wear of Carbide Tools in Machining Titanium Alloys. *Journal of Engineering Materials and Technology* 2005;127(1):136–44. <https://doi.org/10.1115/1.1839192>.
- [68] Zhang S, Li JF, Deng JX, Li YS. Investigation on diffusion wear during high-speed machining Ti-6Al-4V alloy with straight tungsten carbide tools. *Int J Adv Manuf Technol* 2009;44(1-2):17–25. <https://doi.org/10.1007/s00170-008-1803-z>.
- [69] Amin AN, Ismail AF, Nor Khairusshima MK. Effectiveness of uncoated WC–Co and PCD inserts in end milling of titanium alloy—Ti–6Al–4V. *Journal of Materials Processing Technology* 2007;192-193:147–58. <https://doi.org/10.1016/j.jmatprotec.2007.04.095>.
- [70] Sadik MI, Lattemann M, García J. Specific carbide substrate design to enhance tool performance in machining of Ti5553. *Procedia CIRP* 2018;77:598–601. <https://doi.org/10.1016/j.procir.2018.08.203>.
- [71] Özel T, Sima M, Srivastava AK, Kaftanoglu B. Investigations on the effects of multi-layered coated inserts in machining Ti–6Al–4V alloy with experiments and finite element simulations. *CIRP Annals* 2010;59(1):77–82. <https://doi.org/10.1016/j.cirp.2010.03.055>.
- [72] Thepsonthi T, Özel T. Experimental and finite element simulation based investigations on micro-milling Ti-6Al-4V titanium alloy: Effects of cBN coating on tool wear. *Journal of Materials Processing Technology* 2013;213(4):532–42. <https://doi.org/10.1016/j.jmatprotec.2012.11.003>.
- [73] Schueler GM, Engmann J, Marx T, Haberland R, Aurich JC. Burr Formation and Surface Characteristics in Micro-End Milling of Titanium Alloys. In: Aurich JC,

- Dornfeld D, editors. *Burrs - Analysis, Control and Removal*. Berlin, Heidelberg: Springer Berlin Heidelberg; 2010, p. 129–138.
- [74] Mittal RK, Singh RK, Kulkarni SS, Kumar P, Barshilia HC. Characterization of anti-abrasion and anti-friction coatings on micromachining response in high speed micromilling of Ti-6Al-4V. *Journal of Manufacturing Processes* 2018;34:303–12. <https://doi.org/10.1016/j.jmapro.2018.06.021>.
- [75] Aslantas K, Hopa HE, Percin M, Uçun İ, Çicek A. Cutting performance of nano-crystalline diamond (NCD) coating in micro-milling of Ti6Al4V alloy. *Precision Engineering* 2016;45:55–66. <https://doi.org/10.1016/j.precisioneng.2016.01.009>.
- [76] Sui X, Li G, Qin X, Yu H, Zhou X, Wang K et al. Relationship of microstructure, mechanical properties and titanium cutting performance of TiAlN/TiAlSiN composite coated tool. *Ceramics International* 2016;42(6):7524–32. <https://doi.org/10.1016/j.ceramint.2016.01.159>.
- [77] Sousa VFC, Da Silva FJG, Pinto GF, Baptista A, Alexandre R. Characteristics and Wear Mechanisms of TiAlN-Based Coatings for Machining Applications: A Comprehensive Review. *Metals* 2021;11(2):260. <https://doi.org/10.3390/met11020260>.
- [78] Oliaei SNB, Karpát Y. Built-up edge effects on process outputs of titanium alloy micro milling. *Precision Engineering* 2017;49:305–15. <https://doi.org/10.1016/j.precisioneng.2017.02.019>.
- [79] Ziberov M, Da Silva MB, Jackson M, Hung WN. Effect of Cutting Fluid on Micromilling of Ti-6Al-4V Titanium Alloy. *Procedia Manufacturing* 2016;5:332–47. <https://doi.org/10.1016/j.promfg.2016.08.029>.
- [80] Komatsu T, Yoshino T, Matsumura T, Torizuka S. Effect of Crystal Grain Size in Stainless Steel on Cutting Process in Micromilling. *Procedia CIRP* 2012;1:150–5. <https://doi.org/10.1016/j.procir.2012.04.026>.
- [81] Wyen C-F, Wegener K. Influence of cutting edge radius on cutting forces in machining titanium. *CIRP Annals* 2010;59(1):93–6. <https://doi.org/10.1016/j.cirp.2010.03.056>.
- [82] Wyen C-F, Jaeger D, Wegener K. Influence of cutting edge radius on surface integrity and burr formation in milling titanium. *Int J Adv Manuf Technol* 2013;67(1-4):589–99. <https://doi.org/10.1007/s00170-012-4507-3>.
- [83] OBIKAWA T, KANI B. Micro Ball End Milling of Titanium Alloy Using a Tool with a Microstructured Rake Face. *JAMDSM* 2012;6(7):1121–31. <https://doi.org/10.1299/jamdsm.6.1121>.
- [84] Zhao X, Ke W, Zhang S, Zheng W. Potential failure cause analysis of tungsten carbide end mills for titanium alloy machining. *Engineering Failure Analysis* 2016;66:321–7. <https://doi.org/10.1016/j.engfailanal.2016.05.004>.
- [85] Heamawatanachai S, Bamberg E. Cutting force model of orbital single-point micromachining tool. *International Journal of Machine Tools and Manufacture* 2010;50(9):815–23. <https://doi.org/10.1016/j.ijmachtools.2010.05.002>.
- [86] Weber M, Hochrainer T, Gumbsch P, Autenrieth H, Delonnoy L, Schulze V et al. INVESTIGATION OF SIZE-EFFECTS IN MACHINING WITH GEOMETRICALLY DEFINED CUTTING EDGES. *Machining Science and Technology* 2007;11(4):447–73. <https://doi.org/10.1080/10910340701697086>.
- [87] Pratap T, Patra K, Dyakonov AA. Modeling Cutting Force in Micro-Milling of Ti-6Al-4V Titanium Alloy. *Procedia Engineering* 2015;129:134–9. <https://doi.org/10.1016/j.proeng.2015.12.021>.

-
- [88] Lai X, Li H, Li C, Lin Z, Ni J. Modelling and analysis of micro scale milling considering size effect, micro cutter edge radius and minimum chip thickness. *International Journal of Machine Tools and Manufacture* 2008;48(1):1–14. <https://doi.org/10.1016/j.ijmachtools.2007.08.011>.
- [89] Liu X, DeVor RE, Kapoor SG, Ehmann KF. The Mechanics of Machining at the Microscale: Assessment of the Current State of the Science. *Journal of Manufacturing Science and Engineering* 2004;126(4):666–78. <https://doi.org/10.1115/1.1813469>.
- [90] Pratap T, Patra K. Micromilling of Ti-6Al-4V Titanium Alloy Using Ball-end Tool. *IOP Conf. Ser.: Mater. Sci. Eng.* 2017;229:12011. <https://doi.org/10.1088/1757-899X/229/1/012011>.
- [91] Zhao Z, To S, Wang J, Zhang G, Weng Z. A review of micro/nanostructure effects on the machining of metallic materials. *Materials & Design* 2022;224:111315. <https://doi.org/10.1016/j.matdes.2022.111315>.
- [92] Attanasio A, Gelfi M, Pola A, Ceretti E, Giardini C. Influence of Material Microstructures in Micromilling of Ti6Al4V Alloy. *Materials (Basel)* 2013;6(9):4268–83. <https://doi.org/10.3390/ma6094268>.
- [93] Aurich JC (ed.). *Burrs - Analysis, Control and Removal: Proceedings of the CIRP International Conference on Burrs, 2nd-3rd April, 2009, University of Kaiserslautern, Germany*. Berlin, Heidelberg: Springer Berlin Heidelberg; 2010.
- [94] Thepsonthi T, Özel T. Multi-objective process optimization for micro-end milling of Ti-6Al-4V titanium alloy. *Int J Adv Manuf Technol* 2012;63(9-12):903–14. <https://doi.org/10.1007/s00170-012-3980-z>.
- [95] Özel T, Thepsonthi T, Ulutan D, Kaftanoğlu B. Experiments and finite element simulations on micro-milling of Ti-6Al-4V alloy with uncoated and cBN coated micro-tools. *CIRP Annals* 2011;60(1):85–8. <https://doi.org/10.1016/j.cirp.2011.03.087>.
- [96] Bandapalli C, Sutaria BM, Bhatt DV, Singh KK. Experimental Investigation and Estimation of Surface Roughness using ANN, GMDH & MRA models in High Speed Micro End Milling of Titanium Alloy (Grade-5). *Materials Today: Proceedings* 2017;4(2):1019–28. <https://doi.org/10.1016/j.matpr.2017.01.115>.
- [97] Baldo D, Ribeiro Filho, Sergio Luiz Moni, Lauro CH, dos Santos Delfino, Andrea Cristiane, Brandao LC. Analysis of Surface Roughness in Micro Milling of Ti-6Al-4V Titanium Alloy. *Civil, Materials and Computing Engineering* 2014;1079-1080:3–6. <https://doi.org/10.4028/www.scientific.net/AMR.1079-1080.3>.
- [98] Kuram E, Ozcelik B. Optimization of machining parameters during micro-milling of Ti6Al4V titanium alloy and Inconel 718 materials using Taguchi method. *Proceedings of the Institution of Mechanical Engineers, Part B: Journal of Engineering Manufacture* 2017;231(2):228–42. <https://doi.org/10.1177/0954405415572662>.
- [99] Bajpai V, Kushwaha AK, Singh RK. Burr Formation and Surface Quality in High Speed Micromilling of Titanium Alloy (Ti6Al4V). In: *ASME 2013 International Manufacturing Science and Engineering Conference collocated with the 41st North American Manufacturing Research Conference: Volume 2: Systems; Micro and Nano Technologies; Sustainable Manufacturing*. ASME; uuuu-uuuu.
- [100] K V, Mathew J. Wear behavior of TiAlN coated WC tool during micro end milling of Ti-6Al-4V and analysis of surface roughness. *Wear* 2019;424-425:165–82. <https://doi.org/10.1016/j.wear.2019.02.018>.

-
- [101] Ahmadi M, Karpat Y, Acar O, Kalay YE. Microstructure effects on process outputs in micro scale milling of heat treated Ti6Al4V titanium alloys. *Journal of Materials Processing Technology* 2018;252:333–47. <https://doi.org/10.1016/j.jmatprotec.2017.09.042>.
- [102] Wang Y, Zou B, Wang J, Wu Y, Huang C. Effect of the progressive tool wear on surface topography and chip formation in micro-milling of Ti–6Al–4V using Ti(C7N3)-based cermet micro-mill. *Tribology International* 2020;141:105900. <https://doi.org/10.1016/j.triboint.2019.105900>.
- [103] Zhang X, Yu T, Wang W. Prediction of cutting forces and instantaneous tool deflection in micro end milling by considering tool run-out. *International Journal of Mechanical Sciences* 2018;136:124–33. <https://doi.org/10.1016/j.ijmecsci.2017.12.019>.
- [104] Mamedov A, Layegh K. S, Lazoglu I. Machining Forces and Tool Deflections in Micro Milling. *Procedia CIRP* 2013;8:147–51. <https://doi.org/10.1016/j.procir.2013.06.080>.
- [105] Sun Y, LIANG Y, DU R. Simulation and Analysis of Surface Generation in Micro-milling 2006.
- [106] Vogler MP, DeVor RE, Kapoor SG. On the Modeling and Analysis of Machining Performance in Micro-Endmilling, Part I: Surface Generation. *Journal of Manufacturing Science and Engineering* 2004;126(4):685–94. <https://doi.org/10.1115/1.1813470>.
- [107] Zhao Z, To S, Wang J. Effects of grains and twins on deformation of commercial pure titanium in ultraprecision diamond turning. *Journal of Materials Processing Technology* 2019;271:10–22. <https://doi.org/10.1016/j.jmatprotec.2019.03.018>.
- [108] Zhao Z, To S, Sun Z, Ji R, Yu KM. Microstructural effects of Ti6Al4V alloys modified by electropulsing treatment on ultraprecision diamond turning. *Journal of Manufacturing Processes* 2019;39:58–68. <https://doi.org/10.1016/j.jmapro.2019.02.005>.
- [109] Colafemina JP, Jasinevicius RG, Duduch JG. Surface integrity of ultra-precision diamond turned Ti (commercially pure) and Ti alloy (Ti-6Al-4V). *Proceedings of the Institution of Mechanical Engineers, Part B: Journal of Engineering Manufacture* 2007;221(6):999–1006. <https://doi.org/10.1243/09544054JEM798>.
- [110] Oliveira FB de, Rodrigues AR, Coelho RT, Souza AF de. Size effect and minimum chip thickness in micromilling. *International Journal of Machine Tools and Manufacture* 2015;89:39–54. <https://doi.org/10.1016/j.ijmachtools.2014.11.001>.
- [111] Chen N, Chen M, Wu C, Pei X, Qian J, Reynaerts D. Research in minimum undeformed chip thickness and size effect in micro end-milling of potassium dihydrogen phosphate crystal. *International Journal of Mechanical Sciences* 2017;134:387–98. <https://doi.org/10.1016/j.ijmecsci.2017.10.025>.
- [112] Jauregui JC, Resendiz JR, Thenozhi S, Szalay T, Jacso A, Takacs M. Frequency and Time-Frequency Analysis of Cutting Force and Vibration Signals for Tool Condition Monitoring. *IEEE Access* 2018;6:6400–10. <https://doi.org/10.1109/ACCESS.2018.2797003>.

-
- [113] Wang JJ, Uhlmann E, Oberschmidt D, Sung CF, Perfilov I. Critical depth of cut and asymptotic spindle speed for chatter in micro milling with process damping. *CIRP Annals* 2016;65(1):113–6. <https://doi.org/10.1016/j.cirp.2016.04.088>.
- [114] Geier N, Szalay T, Biró I. Trochoid milling of carbon fibre-reinforced plastics (CFRP). *Procedia CIRP* 2018;77:375–8. <https://doi.org/10.1016/j.procir.2018.09.039>.
- [115] Liu J, Li J, Xu C. Interaction of the cutting tools and the ceramic-reinforced metal matrix composites during micro-machining: A review. *CIRP Journal of Manufacturing Science and Technology* 2014;7(2):55–70. <https://doi.org/10.1016/j.cirpj.2014.01.003>.
- [116] Chern GL. Analysis of Burr Formation and Breakout in Metal Cutting. Ph.D. Thesis, University of California at Berkeley 1993.
- [117] Chen MJ, Ni HB, Wang ZJ, Jiang Y. Research on the modeling of burr formation process in micro-ball end milling operation on Ti–6Al–4V. *Int J Adv Manuf Technol* 2012;62(9-12):901–12. <https://doi.org/10.1007/s00170-011-3865-6>.
- [118] Kim D, Lee P-H, Lee S-W. Experimental Study on Machinability of Ti-6Al-4V in Micro End-Milling. *Lecture Notes in Engineering and Computer Science* 2014;2:962–6.
- [119] Kumar P, Bajpai V, Singh R. Burr height prediction of Ti6Al4V in high speed micro-milling by mathematical modeling. *Manufacturing Letters* 2017;11:12–6. <https://doi.org/10.1016/j.mfglet.2016.10.001>.
- [120] Zheng T, Song Q, Du Y, Liu Z. Development of Tool Wear Standards and Wear Mechanism for Micro Milling Ti-6Al-4V Alloy. *Metals* 2022;12(5):726. <https://doi.org/10.3390/met12050726>.
- [121] Colpani A, Fiorentino A, Ceretti E, Attanasio A. Tool wear analysis in micromilling of titanium alloy. *Precision Engineering* 2019;57:83–94. <https://doi.org/10.1016/j.precisioneng.2019.03.011>.
- [122] Dadgari A, Huo D, Swailes D. Investigation on tool wear and tool life prediction in micro-milling of Ti-6Al-4V. *Nanotechnology and Precision Engineering* 2018;1(4):218–25. <https://doi.org/10.1016/j.npe.2018.12.005>.
- [123] Alexander I, Vladimir G, Petr P, Mihail K, Yuriy I, Andrey V. Machining of Thin-walled Parts Produced by Additive Manufacturing Technologies. *Procedia CIRP* 2016;41:1023–6. <https://doi.org/10.1016/j.procir.2015.08.088>.
- [124] Huang X, Bai Q, Li YT, Zhang B. Machining Finish of Titanium Alloy Prepared by Additive Manufacturing. *AMM* 2017;872:43–8. <https://doi.org/10.4028/www.scientific.net/AMM.872.43>.
- [125] Polishetty A, Shunmugavel M, Goldberg M, Littlefair G, Singh RK. Cutting Force and Surface Finish Analysis of Machining Additive Manufactured Titanium Alloy Ti-6Al-4V. *Procedia Manufacturing* 2017;7:284–9. <https://doi.org/10.1016/j.promfg.2016.12.071>.
- [126] Bonaiti G, Parenti P, Annoni M, Kapoor S. Micro-milling Machinability of DED Additive Titanium Ti-6Al-4V. *Procedia Manufacturing* 2017;10:497–509. <https://doi.org/10.1016/j.promfg.2017.07.104>.
- [127] Oliveira Campos F de, Araujo AC, Jardini Munhoz AL, Kapoor SG. The influence of additive manufacturing on the micromilling machinability of Ti6Al4V: A comparison of SLM and commercial workpieces. *Journal of Manufacturing Processes* 2020;60:299–307. <https://doi.org/10.1016/j.jmapro.2020.10.006>.

-
- [128] Le Coz G, Fischer M, Piquard R, D'Acunto A, Laheurte P, Dudzinski D. Micro Cutting of Ti-6Al-4V Parts Produced by SLM Process. *Procedia CIRP* 2017;58:228–32. <https://doi.org/10.1016/j.procir.2017.03.326>.
- [129] Sartori S, Bordin A, Moro L, Ghiotti A, Bruschi S. The Influence of Material Properties on the Tool Crater Wear When Machining Ti6Al4V Produced by Additive Manufacturing Technologies. *Procedia CIRP* 2016;46:587–90. <https://doi.org/10.1016/j.procir.2016.04.032>.
- [130] Sartori S, Moro L, Ghiotti A, Bruschi S. On the tool wear mechanisms in dry and cryogenic turning Additive Manufactured titanium alloys. *Tribology International* 2017;105:264–73. <https://doi.org/10.1016/j.triboint.2016.09.034>.
- [131] Rysava Z, Bruschi S. Comparison between EBM and DMLS Ti6Al4V Machinability Characteristics under Dry Micro-Milling Conditions. *MSF* 2016;836-837:177–84. <https://doi.org/10.4028/www.scientific.net/MSF.836-837.177>.
- [132] Rysava Z, Bruschi S, Piska M, Zidek J. COMPARING THE PERFORMANCE OF MICRO-END MILLS WHEN MICRO-MILLING OF ADDITIVE MANUFACTURED TI-6AL-4V TITANIUM ALLOY. *MM SJ* 2018;2018(04):2543–6. https://doi.org/10.17973/MMSJ.2018_11_201823.
- [133] Oyelola O, Crawforth P, M'Saoubi R, Clare AT. Machining of Additively Manufactured Parts: Implications for Surface Integrity. *Procedia CIRP* 2016;45:119–22. <https://doi.org/10.1016/j.procir.2016.02.066>.
- [134] Varghese V, Mujumdar S. Micromilling-induced Surface Integrity of Porous Additive Manufactured Ti6Al4V Alloy. *Procedia Manufacturing* 2021;53:387–94. <https://doi.org/10.1016/j.promfg.2021.06.041>.
- [135] Rahman Rashid RA, Sun S, Palanisamy S, Wang G, Dargusch MS. A study on laser assisted machining of Ti10V2Fe3Al alloy with varying laser power. *Int J Adv Manuf Technol* 2014;74(1):219–24. <https://doi.org/10.1007/s00170-014-5958-5>.
- [136] Rahman Rashid RA, Sun S, Wang G, Dargusch MS. The effect of laser power on the machinability of the Ti-6Cr-5Mo-5V-4Al beta titanium alloy during laser assisted machining. *International Journal of Machine Tools and Manufacture* 2012;63:41–3. <https://doi.org/10.1016/j.ijmachtools.2012.07.006>.
- [137] Feng Y, Hung T-P, Lu Y-T, Lin Y-F, Hsu F-C, Lin C-F et al. Analytical prediction of temperature in laser-assisted milling with laser preheating and machining effects. *Int J Adv Manuf Technol* 2019;100(9):3185–95. <https://doi.org/10.1007/s00170-018-2930-9>.
- [138] Singh RK, Melkote SN. Laser-assisted Mechanical Micromachining. In: Wang L, Xi J, editors. *Smart Devices and Machines for Advanced Manufacturing*. London: Springer London; 2008, p. 337–365.
- [139] Jeon Y, Pfefferkorn F. Effect of Laser Preheating the Workpiece on Micro end Milling of Metals. *Journal of Manufacturing Science and Engineering* 2008;130(1). <https://doi.org/10.1115/1.2783219>.
- [140] Sun S, Brandt M, Dargusch MS. Thermally enhanced machining of hard-to-machine materials—A review. *International Journal of Machine Tools and Manufacture* 2010;50(8):663–80. <https://doi.org/10.1016/j.ijmachtools.2010.04.008>.
- [141] Dargusch MS, Sivarupan T, Bermingham M, Rashid RAR, Palanisamy S, Sun S. Challenges in laser-assisted milling of titanium alloys. *Int. J. Extrem. Manuf.* 2021;3(1):15001. <https://doi.org/10.1088/2631-7990/abc26b>.

-
- [142] Bermingham MJ, Palanisamy S, Dargusch MS. Understanding the tool wear mechanism during thermally assisted machining Ti-6Al-4V. *International Journal of Machine Tools and Manufacture* 2012;62:76–87. <https://doi.org/10.1016/j.ijmachtools.2012.07.001>.
- [143] Xia H, Zhao G, Li L, Hu M, He N, Ochengo D. Fabrication of high aspect ratio microgroove on Ti6Al4V by laser-induced oxidation assisted micro milling. *Journal of Manufacturing Processes* 2019;45:419–28. <https://doi.org/10.1016/j.jmapro.2019.07.026>.
- [144] Kadivar M, Azrhoushang B, Zahedi A, Müller C. Laser-assisted micro-milling of austenitic stainless steel X5CrNi18-10. *Journal of Manufacturing Processes* 2019;48:174–84. <https://doi.org/10.1016/j.jmapro.2019.11.002>.
- [145] Singh R, Melkote SN. Characterization of a hybrid laser-assisted mechanical micromachining (LAMM) process for a difficult-to-machine material. *International Journal of Machine Tools and Manufacture* 2007;47(7):1139–50. <https://doi.org/10.1016/j.ijmachtools.2006.09.004>.
- [146] Kumar M, Melkote SN. Process capability study of laser assisted micro milling of a hard-to-machine material. *Journal of Manufacturing Processes* 2012;14(1):41–51. <https://doi.org/10.1016/j.jmapro.2011.09.003>.
- [147] Shelton JA, Shin YC. Experimental Evaluation of Laser-Assisted Micromilling in a Slotting Configuration. *Journal of Manufacturing Science and Engineering* 2010;132(2). <https://doi.org/10.1115/1.4001142>.
- [148] Kim T, Kwon K-K, Chu CN, Song KY. Experimental investigation on CO₂ laser-assisted micro-slot milling characteristics of borosilicate glass. *Precision Engineering* 2020;63:137–47. <https://doi.org/10.1016/j.precisioneng.2020.02.004>.
- [149] Kumar M, Melkote SN, M'Saoubi R. Wear behavior of coated tools in laser assisted micro-milling of hardened steel. *Wear* 2012;296(1):510–8. <https://doi.org/10.1016/j.wear.2012.08.011>.
- [150] Hao X, Xu W, Chen M, Wang C, Han J, Li L et al. Laser hybridizing with micro-milling for fabrication of high aspect ratio micro-groove on oxygen-free copper. *Precision Engineering* 2021;70:15–25. <https://doi.org/10.1016/j.precisioneng.2021.01.012>.
- [151] Azarhoushang B, Soltani B, Zahedi A. Laser-assisted grinding of silicon nitride by picosecond laser. *Int J Adv Manuf Technol* 2017;93(5-8):2517–29. <https://doi.org/10.1007/s00170-017-0440-9>.
- [152] Kadivar M, Shamray S, Soltani B, Daneshi A, Azarhoushang B. Laser-assisted micro-grinding of Si₃N₄. *Precision Engineering* 2019;60:394–404. <https://doi.org/10.1016/j.precisioneng.2019.09.004>.
- [153] Paknejad M, Azarhoushang B, Zahedi A, Khakrangin M, Kadivar MA. Investigation of material removal mechanisms of laser-structured Si₃N₄ via single diamond grit scratching. *Int J Adv Manuf Technol* 2023;125(5-6):2759–75. <https://doi.org/10.1007/s00170-022-10793-0>.
- [154] Raj D, Reddy B, Maity SR, Pandey KM. Laser Beam Micromachining of Metals: A Review. *Materials Today: Proceedings* 2019;18:98–103. <https://doi.org/10.1016/j.matpr.2019.06.281>.
- [155] Kiran Kumar K, Samuel GL, Shunmugam MS. Theoretical and experimental investigations of ultra-short pulse laser interaction on Ti6Al4V alloy. *Journal of*

- Materials Processing Technology 2019;263:266–75.
<https://doi.org/10.1016/j.jmatprotec.2018.08.028>.
- [156] Nolte S, Momma C, Jacobs H, Tünnermann A, Chichkov BN, Wellegehausen B et al. Ablation of metals by ultrashort laser pulses. *J. Opt. Soc. Am. B* 1997;14(10):2716. <https://doi.org/10.1364/JOSAB.14.002716>.
- [157] Mannion P, Magee J, Coyne E, O'Connor GM. Ablation thresholds in ultrafast laser micromachining of common metals in air. *Society of Photo-Optical Instrumentation Engineers (SPIE) Conference Series* 2003;4876:470. <https://doi.org/10.1117/12.463744>.
- [158] Zheng B, Jiang G, Wang W, Wang K, Mei X. Ablation experiment and threshold calculation of titanium alloy irradiated by ultra-fast pulse laser. *AIP Advances* 2014;4(3):31310. <https://doi.org/10.1063/1.4867088>.
- [159] Cheng J, Perrie W, Sharp M, Edwardson SP, Semaltianos NG, Dearden G et al. Single-pulse drilling study on Au, Al and Ti alloy by using a picosecond laser. *Appl. Phys. A* 2009;95(3):739–46. <https://doi.org/10.1007/s00339-008-5037-6>.
- [160] Mannion P, Magee J, Coyne E, O'Connor G, Glynn T. The effect of damage accumulation behaviour on ablation thresholds and damage morphology in ultrafast laser micro-machining of common metals in air. *Applied Surface Science* 2004;233(1-4):275–87. <https://doi.org/10.1016/j.apsusc.2004.03.229>.
- [161] Kong MC, Wang J. Surface Quality Analysis of Titanium and Nickel-based Alloys Using Picosecond Laser. *Procedia CIRP* 2014;13:417–22. <https://doi.org/10.1016/j.procir.2014.04.071>.
- [162] Yu Z, Hu J, Li K. Investigating the multiple-pulse drilling on titanium alloy in picosecond laser. *Journal of Materials Processing Technology* 2019;268:10–7. <https://doi.org/10.1016/j.jmatprotec.2018.12.027>.
- [163] Liu D, Chen C, Man B, Meng X, Sun Y, Li F. Evolution and mechanism of the periodical structures formed on Ti plate under femtosecond laser irradiation. *Applied Surface Science* 2016;378:120–9. <https://doi.org/10.1016/j.apsusc.2016.03.229>.
- [164] Ahuir-Torres JI, Arenas MA, Perrie W, Damborenea J de. Influence of laser parameters in surface texturing of Ti6Al4V and AA2024-T3 alloys. *Optics and Lasers in Engineering* 2018;103:100–9. <https://doi.org/10.1016/j.optlaseng.2017.12.004>.
- [165] Zaeh MF, Wiedenmann R, Daub R. A thermal simulation model for laser-assisted milling. *Physics Procedia* 2010;5:353–62. <https://doi.org/10.1016/j.phpro.2010.08.062>.
- [166] Singh R, Alberts MJ, Melkote SN. Characterization and prediction of the heat-affected zone in a laser-assisted mechanical micromachining process. *International Journal of Machine Tools and Manufacture* 2008;48(9):994–1004. <https://doi.org/10.1016/j.ijmachtools.2008.01.004>.
- [167] Yang J, Sun S, Brandt M, Yan W. Experimental investigation and 3D finite element prediction of the heat affected zone during laser assisted machining of Ti6Al4V alloy. *Journal of Materials Processing Technology* 2010;210(15):2215–22. <https://doi.org/10.1016/j.jmatprotec.2010.08.007>.
- [168] Shen X. Numerical modeling and experimental investigation of laser-assisted machining of silicon nitride ceramics 2010.

-
- [169] Tian Y, Wu B, Anderson M, Shin YC. Laser-Assisted Milling of Silicon Nitride Ceramics and Inconel 718. *Journal of Manufacturing Science and Engineering* 2008;130(3). <https://doi.org/10.1115/1.2927447>.
- [170] B. Lesourd. Etude et modélisation des mécanismes de bandes de cisaillement en coupe des métaux. application au tournage assisté laser de l'alliage de titane ta6v (Ph.D. thesis). Ecole Centrale de NANTES 1996.
- [171] Germain G, Dal Santo P, Lebrun JL. Comprehension of chip formation in laser assisted machining. *International Journal of Machine Tools and Manufacture* 2011;51(3):230–8. <https://doi.org/10.1016/j.ijmachtools.2010.11.006>.
- [172] Ayed Y, Germain G, Ben Salem W, Hamdi H. Experimental and numerical study of laser-assisted machining of Ti6Al4V titanium alloy. *Finite Elements in Analysis and Design* 2014;92:72–9. <https://doi.org/10.1016/j.finel.2014.08.006>.
- [173] Ding H, Shen N, Shin YC. Thermal and mechanical modeling analysis of laser-assisted micro-milling of difficult-to-machine alloys. *Journal of Materials Processing Technology* 2012;212(3):601–13. <https://doi.org/10.1016/j.jmatprotec.2011.07.016>.
- [174] Xi Y, Bermingham M, Wang G, Dargusch M. SPH/FE modeling of cutting force and chip formation during thermally assisted machining of Ti6Al4V alloy. *Computational Materials Science* 2014;84:188–97. <https://doi.org/10.1016/j.commatsci.2013.12.018>.
- [175] Xi Y, Zhan H, Rahman Rashid RA, Wang G, Sun S, Dargusch M. Numerical modeling of laser assisted machining of a beta titanium alloy. *Computational Materials Science* 2014;92:149–56. <https://doi.org/10.1016/j.commatsci.2014.05.023>.
- [176] Black SC, Chiles V. *Principios de ingenieria de manufactura*. 1st ed. Mexico: Editorial Continental; 1999.
- [177] Abbasi SA, Feng P, Ma Y, Zhang J, Yu D, Wu Z. Influence of microstructure and hardness on machinability of heat-treated titanium alloy Ti-6Al-4V in end milling with polycrystalline diamond tools. *Int J Adv Manuf Technol* 2016;86(5):1393–405. <https://doi.org/10.1007/s00170-015-8245-1>.
- [178] Denkena B, Grove T. The Effect of Microstructure On the Machinability of Ti-6Al-4V. In: Venkatesh V, editor. *Proceedings of the 13th World Conference on Titanium: Sponsored by Titanium Committee of the Structural Materials Division of the Minerals, Metals et Materials Society (TMS), held August 16-20, 2015, Manchester Grand Hyatt, San Diego, California, USA*. Hoboken, New Jersey: Wiley; 2016, p. 905–910.
- [179] Kushner V, Storchak M. Modelling the material resistance to cutting. *International Journal of Mechanical Sciences* 2017;126:44–54. <https://doi.org/10.1016/j.ijmecsci.2017.03.024>.
- [180] Lauro CH, Brandão LC, Carou D, Davim JP. Specific cutting energy employed to study the influence of the grain size in the micro-milling of the hardened AISI H13 steel. *Int J Adv Manuf Technol* 2015;81(9):1591–9. <https://doi.org/10.1007/s00170-015-7321-x>.
- [181] Milton S, Morandea A, Chalon F, Leroy R. Influence of Finish Machining on the Surface Integrity of Ti6Al4V Produced by Selective Laser Melting. *Procedia CIRP* 2016;45:127–30. <https://doi.org/10.1016/j.procir.2016.02.340>.
- [182] Chern GL. *Analysis of Burr Formation and Breakout in Metal Cutting [PhD]*. Berkeley: University of California 1993.

-
- [183] Soltani B, Azarhoushang B, Zahedi A. Laser ablation mechanism of silicon nitride with nanosecond and picosecond lasers. *Optics & Laser Technology* 2019;119:105644. <https://doi.org/10.1016/j.optlastec.2019.105644>.
- [184] Simon P, Ihlemann J. Machining of submicron structures on metals and semiconductors by ultrashort UV-laser pulses. *Appl. Phys. A* 1996;63(5):505–8. <https://doi.org/10.1007/BF01571681>.
- [185] Krueger J, Kautek W, Lenzner M, Sartania S, Spielmann C, Krausz F. Structuring of dielectric and metallic materials with ultrashort laser pulses between 20 fs and 3 ps. In: Dubowski JJ, editor. *Laser Applications in Microelectronic and Optoelectronic Manufacturing II*. SPIE; 1997, p. 40–47.
- [186] Vorobyev AY, Guo C. Direct observation of enhanced residual thermal energy coupling to solids in femtosecond laser ablation. *Appl. Phys. Lett.* 2005;86(1):11916. <https://doi.org/10.1063/1.1844598>.
- [187] Hohlfeld J, Müller JG, Wellershoff S-S, Matthias E. Time-resolved thermorefectivity of thin gold films and its dependence on film thickness. *Applied Physics B: Lasers and Optics* 1997;64(3):387–90. <https://doi.org/10.1007/s003400050189>.
- [188] Vogel A, Noack J, Hüttman G, Paltauf G. Mechanisms of femtosecond laser nanosurgery of cells and tissues. *Applied Physics B: Lasers and Optics* 2005;81(8):1015–47. <https://doi.org/10.1007/s00340-005-2036-6>.
- [189] Schmidt V, Husinsky W, Betz G. Dynamics of laser desorption and ablation of metals at the threshold on the femtosecond time scale. *Phys Rev Lett* 2000;85(16):3516–9. <https://doi.org/10.1103/PhysRevLett.85.3516>.
- [190] Siegel J, Solis J, Afonso CN, Vega F, Bankmann J, Martínez Sacristán O et al. Evidence for surface initiated solidification in Ge films upon picosecond laser pulse irradiation. *Journal of Applied Physics* 2001;89(7):3642–9. <https://doi.org/10.1063/1.1347958>.
- [191] Rajeev PP, Sengupta S, Das A, Taneja P, Ayyub P, Kaw PK et al. Laser absorption in short-lived metal and nanoplasmas. *Applied Physics B: Lasers and Optics* 2005;80(8):1015–9. <https://doi.org/10.1007/s00340-005-1827-0>.
- [192] Electron emission from metal surfaces exposed to ultrashort laser pulses; 1974.
- [193] Lin Z, Zhigilei LV, Celli V. Electron-phonon coupling and electron heat capacity of metals under conditions of strong electron-phonon nonequilibrium. *Phys. Rev. B* 2008;77(7). <https://doi.org/10.1103/PhysRevB.77.075133>.
- [194] Amoruso S, Bruzzese R, Wang X, O'Connell G, Lunney JG. Multidiagnostic analysis of ultrafast laser ablation of metals with pulse pair irradiation. *Journal of Applied Physics* 2010;108(11):113302. <https://doi.org/10.1063/1.3516491>.
- [195] Linde D von der, Sokolowski-Tinten K, Bialkowski J. Laser–solid interaction in the femtosecond time regime. *Applied Surface Science* 1997;109-110:1–10. [https://doi.org/10.1016/S0169-4332\(96\)00611-3](https://doi.org/10.1016/S0169-4332(96)00611-3).
- [196] Perez D, Lewis LJ. Molecular-dynamics study of ablation of solids under femtosecond laser pulses. *Phys. Rev. B* 2003;67(18). <https://doi.org/10.1103/PhysRevB.67.184102>.
- [197] Yu Z, Yang G, Zhang W, Hu J. Investigating the effect of picosecond laser texturing on microstructure and biofunctionalization of titanium alloy. *Journal of Materials Processing Technology* 2018;255:129–36. <https://doi.org/10.1016/j.jmatprotec.2017.12.009>.

-
- [198] Bonse J, Krüger J, Höhm S, Rosenfeld A. Femtosecond laser-induced periodic surface structures. *Journal of Laser Applications* 2012;24(4):42006. <https://doi.org/10.2351/1.4712658>.
- [199] Dai Y, He M, Bian H, Lu B, Yan X, Ma G. Femtosecond laser nanostructuring of silver film. *Appl. Phys. A* 2012;106(3):567–74. <https://doi.org/10.1007/s00339-011-6705-5>.
- [200] Wynne AE, Stuart BC. Rate dependence of short-pulse laser ablation of metals in air and vacuum. *Appl. Phys. A* 2003;76(3):373–8. <https://doi.org/10.1007/s00339-002-1823-8>.
- [201] Luft A, Franz U, Emsermann L, Kaspar J. A study of thermal and mechanical effects on materials induced by pulsed laser drilling. *Appl. Phys. A* 1996;63(2):93–101. <https://doi.org/10.1007/BF01567635>.
- [202] Nedialkov NN, Atanasov PA. Molecular dynamics simulation study of deep hole drilling in iron by ultrashort laser pulses. *Applied Surface Science* 2006;252(13):4411–5. <https://doi.org/10.1016/j.apsusc.2005.07.096>.
- [203] Vorobyev AY, Guo C. Enhanced absorptance of gold following multipulse femtosecond laser ablation. *Phys. Rev. B* 2005;72(19). <https://doi.org/10.1103/physrevb.72.195422>.
- [204] Vorobyev AY, Kuzmichev VM, Kokody NG, Kohns P, Dai J, Guo C. Residual thermal effects in Al following single ns- and fs-laser pulse ablation. *Appl. Phys. A* 2006;82(2):357–62. <https://doi.org/10.1007/s00339-005-3412-0>.
- [205] Zhao W, Yu Z. Self-cleaning effect in high quality percussion ablating of cooling hole by picosecond ultra-short pulse laser. *Optics and Lasers in Engineering* 2018;105:125–31. <https://doi.org/10.1016/j.optlaseng.2018.01.011>.
- [206] Campo KN, Campanelli LC, Bergmann L, Santos JFd, Bolfarini C. Microstructure and interface characterization of dissimilar friction stir welded lap joints between Ti–6Al–4V and AISI 304. *Materials & Design (1980-2015)* 2014;56:139–45. <https://doi.org/10.1016/j.matdes.2013.11.002>.
- [207] Loksha, Nagaraj PB, Dinesh P. Frictional force during machining process Part 2: Influence of process parameters. *Materials Today: Proceedings* 2021;46:2468–70. <https://doi.org/10.1016/j.matpr.2021.01.401>.